Permeability Studies in Biomimetic Glycosaminoglycan-Hydrogel Membranes

by

Kristin J. Mattern

B.S.E., Chemical Engineering
Princeton University, 2000

M.S., Chemical Engineering Practice
Massachusetts Institute of Technology, 2001

Submitted to the Department of Chemical Engineering
in partial fulfillment of the requirements for the degree of

DOCTOR OF PHILOSOPHY IN CHEMICAL ENGINEERING

at the

MASSACHUSETTS INSTITUTE OF TECHNOLOGY

May 2008

Signature of Author: _____

Department of Chemical Engineering
May 20, 2008

Certified by: _____

William M. Deen
Professor of Chemical Engineering
Thesis Supervisor

Accepted by: _____

William M. Deen
Professor of Chemical Engineering
Chairman, Committee for Graduate Students

Permeability Studies in Biomimetic Glycosaminoglycan-Hydrogel Membranes

by
Kristin J. Mattern

Submitted to the Department of Chemical Engineering on May 20, 2008
in partial fulfillment of the requirements for the degree of
Doctor of Philosophy in Chemical Engineering

ABSTRACT

The rates of water and solute transport tend to be lower in fibrous materials than in bulk solution. This phenomenon of "hindered transport" is caused by steric, hydrodynamic, and electrostatic interactions between the solvent, the solute, and the fibers. In this research the effect of these interactions were studied using charged, fibrous agarose-glycosaminoglycan (GAG) membranes. The work was motivated by current research into the role of the glomerular capillary wall (GCW) in ultrafiltering blood plasma, which is the first step in the processing of blood by the kidney. The GCW is composed of three layers in series: an endothelium, a basement membrane, and an epithelium. Increasing evidence from experimental results and theoretical models of the GCW indicate that the endothelial layer and its associated glycocalyx may significantly limit the transport of macromolecules across the glomerular barrier. The glycocalyx is primarily composed of proteoglycans, a fibrous mixtures of proteins and anionic GAG. GAG fibers are present in many other biological materials, such as basement membranes and cartilage, making the current studies in agarose-GAG relevant to a variety of biological systems.

Agarose-GAG membranes were synthesized by using 1-cyano-4-(dimethylamino)pyridinium tetrafluoroborate (CDAP) to create reactive sites in thin agarose hydrogels. Chondroitin sulfate GAG was then covalently bound to the reactive sites via their terminal amine group. By manipulating the temperature and duration of key reaction steps, the synthesis was optimized to provide high bound GAG yields and a spatially uniform distribution of GAG throughout the membrane. Models of the coupling reaction were developed to guide the synthesis conditions, resulting in 70-115 μm-thick membranes composed of 2-4 v% agarose and 0-0.4 v% GAG.

The Darcy (or hydraulic) permeabilities of the membranes with variable GAG content were measured with buffer solutions over a range of ionic strengths. In 3 v% agarose gels, the addition of even a small amount of GAG (0.4 v%) resulted in a two-fold reduction in the Darcy permeability. Electrokinetic coupling, caused by the flow of ions past the charged GAG fibers, resulted in an additional two-fold reduction in the open-circuit hydraulic permeability when the solution ionic strength was decreased from 1 M to 0.011 M. A microstructural model was used to understand these phenomena, accounting for the charge of the GAG fibers, heterogeneities in the agarose gels, and the mixture of agarose and GAG fibers. Several "mixing rules" from the literature were compared to predict the permeability of a mixture of fibers from structural models for a single fiber type. A fiber volume-weighted averaging of each fiber resistivity was found to be reasonably reliable, with a root-mean-squared error of 24% for 64 cases of fiber

mixtures with differing radii, orientation, and/or charge. The microstructural model, using this mixing rule, accurately predicted the Darcy permeability when charge effects were suppressed at high ionic strengths; however, this model underestimated the reduction in permeability at lower ionic strengths when the effects of the GAG charge were significant. A macroscopic approach to electrokinetic effects using Donnan equilibria better captured the decrease in Darcy permeability with decreasing ionic strength.

Studies of equilibrium partitioning and sieving were performed with BSA (an anionic globular protein) and Ficoll (an uncharged spherical polysaccharide). The effects of charge were studied by varying the ionic strength in experiments with BSA; the effects of solute size were examined by using Ficolls with radii ranging from 2.7 to 5.9 nm. Solute permeability studies were performed in 4 v% agarose gels with 0 or 0.2 v% GAG.

Partition coefficients (Φ) for BSA were measured for ionic strengths of 0.5 to 0.011 M. For BSA in agarose gels with no GAG, $\Phi = 0.65 \pm 0.02$ (standard error) and did not vary with ionic strength. In gels with 0.2 v% GAG, $\Phi = 0.54 \pm 0.02$ at ionic strengths $\geq$ 0.2 M, but decreased by nearly two-fold at 0.011 M. For the same Stokes-Einstein radius (3.5-3.6 nm), the partition coefficients of BSA at neutral conditions and of Ficoll were similar in blank agarose gels, but differed by 15% in agarose-GAG gels. The partition coefficients for Ficolls decreased with increasing solute radius. A microstructural model for partitioning in fibrous materials was evaluated against the experimental observations. The experimental data were most consistent models that had a nearly homogeneous fiber density. The model was in good agreement for partition coefficients of Ficolls with various radii. The decrease in BSA partition coefficient at low ionic strengths was well captured by both microstructural and Donnan models of charge effects.

The sieving coefficient (Θ), or ratio of downstream to upstream solute concentrations, was measured at moderately high Péclet number where $\Theta = \Phi K_c$, where K_c is the convective hindrance factor. It has been hypothesized by others that K_c is independent of charge, such than any charge effects in Θ are caused by Φ. Sieving coefficients were measured under similar conditions as partition coefficients. Like partitioning, ionic strength had little effect on the sieving of BSA through blank agarose, but Θ was decreased by over half from 0.1 M to 0.011 M in gels with 0.2 v% GAG. In these agarose-GAG gels, there was not a statistically significant effect of ionic strength on K_c.

Models used for agarose-GAG membranes were applied to a simple model of the glomerular endothelial glycocalyx. The composition and structure of the glycocalyx are not well characterized, but some of its properties can be inferred from the properties of the entire capillary wall and the other capillary layers. Models of the hydraulic permeability of the endothelium suggest that the glycocalyx may be up to several hundred nanometers thick, but the GAG density is probably less than 4 v%. To determine if sieving through such a layer would contribute to glomerular selectivity, improved models for hindered transport coefficients are needed for fibrous systems where the fiber spacing is on the same scale as the solute size.

Thesis Supervisor: William M. Deen
Title: Carbon P. Dubbs Professor Chemical Engineering

ACKNOWLEDGEMENTS

When I returned to MIT, a collegue told me that graduate school was either one of the best times or one of the worst times in a person's life. I'm fortunate to fall in the former category, and for that I would like to thank many people.

My advisor, Professor Bill Deen, has been a continual source of knowledge and support. His instruction, insights, patience, trust, and encouragement have helped me become a better researcher in so many ways. I have always felt privileged to be part of his lab. I would also like to thank all of the members in the Deen lab, past and present, who have provided a wealth of technical and social support: Matt Lazzara, Kim Kosto, Greg Zugates, Ian Zacharia, Gaurav Bhalla, Panadda Dechadilok, Chang Hoon Lim, Melanie Chim, and Brian Skinn. I owe a large debt of gratitude to two undergrads who have UROPed with me: Chalida (Aey) Nakornchai '07 and Debbie Markham '10 — I would not be writing this thesis now without their help. My thesis committee members, Professors Alan Grodzinsky and Doug Lauffenburger, also provided many insightful comments over the years.

I have been blessed with many supportive teachers over the years. In particular, I want to acknowledge Dr. Schiavone and Mr. Farnsworth at Parkland High School, who provided encouragement and strong foundations in chemistry and math; Professor Sandra Troian at Princeton for showing me the beauty of transport phenomena; Professor T. Kyle Vanderlick at Princeton and Dr. John Markels and Mrs. Colleen Michaels at Merck for encouraging me to pursue graduate school. I hope that I can return the favor to other young scientists in the future.

Graduate school is not just about academics, and I thank all my friends for helping me keep work and life in balance. I'm lucky to have close friends from my "first-first-year" who made coming back to MIT an enjoyable prospect: "The Goon Squad" (Jason, Jason, Nick, and Joe), Heather, Roger, and Greg. Two of my roommates from Princeton also joined me for awhile at roommates in Boston – thanks Marcy and Blair! I also made a number of friends in my "second-first-year": Michelle, Katharina, Andy, Ryan, Ben, Sanjoy, Jane, Kris, Theis, Jake, and many others. Thanks for all the fun times.

I can never thank my parents enough for three decades of support and encouragement. They have never doubted that I could do anything I tried, and have helped in so many ways. Thanks, Mom and Dad!

Finally, I thank Jason. He has been with me since I first set foot at MIT, and has helped to make all of this possible. I look forward to many more years together with him after I become the other Dr. Ploeger.

ꕥ

"The most exciting phrase to hear in science, the one that heralds new discoveries, is not 'Eureka!' but 'That's funny ...'." *- Isaac Asimov (1920 - 1992)*

Table of Contents

List of Figures

List of Tables

Chapter 1. BACKGROUND

The primary function of the kidney is to maintain the composition and volume of the extracellular fluid. This is performed in two stages: ultrafiltration of blood plasma fillowed by selective tubular reabsorption and secretion. The first ultrafiltration step is performed in the glomerulus, where the capillary wall is composed of three distinct layers in series: the fenestrated endothelium, glomerular basement membrane (GBM), and epithelium (Figure 1.1). Due to the low permeability of cellular membranes, most ultrafiltration occurs extracellularly. When properly functioning, a human kidney has the capacity to filter approximately 180 L/day, or the entire blood plasma volume once every 20 minutes. Various forms of kidney disease are associated with changes to the structure of the glomerular capillary wall, which in turn lead to changes in the ultrafiltration properties. The desire to further understand the various types of nephrotic syndromes by correlating the physiological changes in the capillary wall with the changes in measurable properties, such as hydraulic permeability and macromolecular sieving, has provided the motivation over the past 30 years to study the functional properties of the glomerular barrier.

1.1. Glomerular Models

The glomerular barrier is notable for its ability to allow high water fluxes while being very retentive to plasma proteins. These properties can be characterized by the hydraulic permeability, k, and the molecular sieving coefficient, Θ. The hydraulic permeability is defined as the mean fluid velocity divided by the pressure drop across the filter. The sieving coefficient is the ratio of the downstream to upstream solute concentrations, and is affected both by the filtration rate and the structural properties of the filter.

Early studies in glomerular filtration attempted to model the glomerulus with an equivalent pore model for the sieving coefficient, using cylindrical pores in parallel (Maddox et al. 1992). This model had the advantage of being simple to apply to characterize molecular sieving coefficients in various nephrotic conditions, as it separates hemodynamic effects from membrane property effects. However, the effective pore size and density have no correlation with the true glomerular structure. More recent studies have instead employed a structure-based model of the glomerulus, where transport properties such as k and Θ can be calculated from an idealized repeating glomerular unit cell, similar to that represented in Figure 1.1.

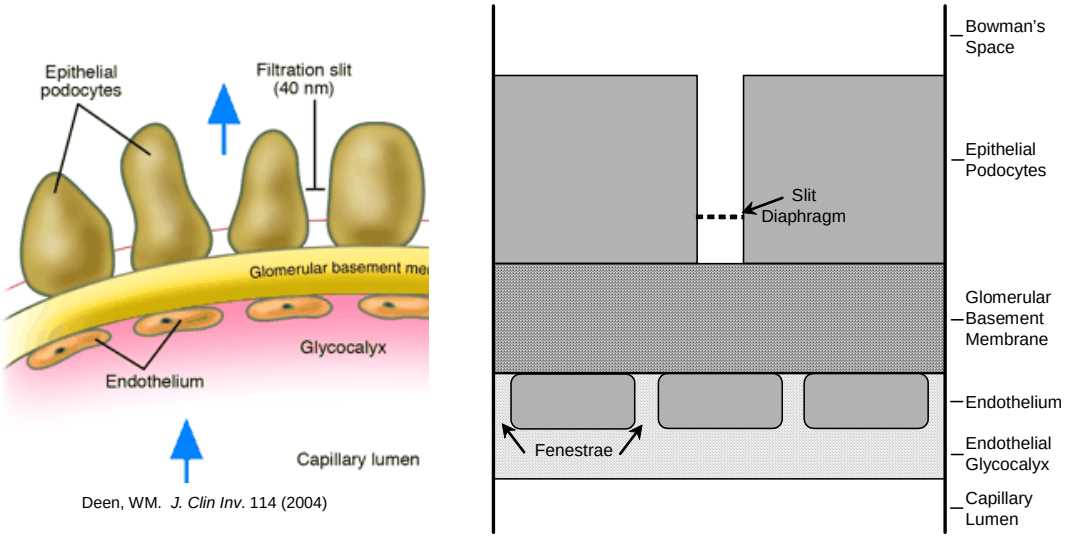

(a) (b)

Figure 1.1 Structure of the glomerular capillary wall, (a) based on physiological observations and (b) in an idealized schematic.

One of the earlier structure-based models was developed by Drumond and Deen (Drumond and Deen 1994) to model the hydraulic permeability, k, of the glomerulus and its individual layers. The approach used computational fluid dynamics to look at velocity and pressure fields within the unit cell, where the total resistance of the capillary wall is the sum of each layer in series.

$$\frac{1}{k} = \frac{1}{k_{endo}} + \frac{1}{k_{GBM}} + \frac{1}{k_{epi}} \tag{1.1}$$

The hydraulic permeability of the GBM was linked to the two bounding layers, since much of the surface of the membrane is blocked by impermeable cells. Knowing the geometry of the layers and the Darcy permeability of isolated GBM, it was shown that that the GBM contributes ~70% of the total hydraulic resistance (Deen et al. 2001). The contributions of the two cellular layers are currently unknown, due to lack of knowledge of the exact structure of the epithelial slit diaphragms and the endothelial fenestrae and glycocalyx.

The hydraulic structure-based model was extended to macromolecular filtration (Edwards et al. 1999). The sieving coefficient, Θ, of a single layer is the ratio of the concentrations on the downstream side to the upstream side. For layers in series, the overall sieving coefficient is simply the product of the individual sieving coefficients.

$$\Theta = \frac{c_{Bowman}}{c_{lumen}} = \Theta_{endo}\Theta_{GBM}\Theta_{epi} \tag{1.2}$$

The sieving properties of GBM were determined from studies of diffusion and convection of neutral Ficoll tracers of various sizes in isolated GBM (Edwards et al. 1997a, Edwards et al. 1997b). However, due to the position of the GBM upstream from the restrictive epithelial slits, the effective Θ_{GBM} for albumin is approximately unity. The overall sieving coefficient for albumin is $6\text{x}10^{-4}$, indicating that one or both of the cellular layers must play a significant role in solute sieving in the glomerular barrier. Since the disruption of either cellular layer may result in proteinuria, it is presumed than both Θ_{endo} and Θ_{epi} must be less than ~0.1 (Deen 2004, Deen et al. 2001). However, the exact contributions of the two layers to charge and size selectivity across the capillary wall are unknown.

1.2. Evidence of Endothelial Role in Glomerular Function

Studies of the intact glomerular wall support that molecular sieving across this barrier is size-selective, and increasing evidence also indicates that it is charge-selective (Blouch et al. 1997, Haraldsson and Sörensson 2004, Ohlson et al. 2000, Sörensson et al. 2001). The individual role of the three barrier layers in this selectivity is still under investigation. In addition to evidence from the previously discussed models that the epithelial and endothelial cell layers interact with the GBM to affect the hydraulic permeability and macromolecular sieving of the glomerulus, numerous other data have been reported that give insight to the roles of the glomerular layers. Bolton et al. characterized GBM isolated from rat glomeruli, demonstrating that it showed size but not change selectivity at physiological ionic strengths (Bolton et al. 1998). However, the results from the models of layers in series show that the actual sieving coefficient in the GBM is approximately unity for albumin, suggest that the role of the GBM in filtration is primarily hydraulic resistance and structural support to the surrounding cell layers.

As suggested by Haraldsson & Sörensson, the above studies of GBM combined with the observation that intact glomeruli show solute selectivity indicate that one or both of the cellular layers play a key role in the size and/or charge selectivity of the glomerulus (Haraldsson and Sörensson 2004). Recent discoveries have shown that Finnish-type congenital nephrosis is characterized by the improper synthesis of nephrin in the slit diaphragms (Tryggvason 1999), which emphasizes the role that the epithelium plays in proper glomerular filtration. However, it is important to remember that the sieving coefficient across the glomerulus is the product of the sieving across each layer; so while damage to the slit diaphragm may be enough to cause proteinuria, proteinuria may also occur without such damage if Θ_{GBM} or Θ_{endo} were increased.

Since the glycocalyx that surrounds the endothelial cell surface is a matrix of highly negatively charged molecules, it seems feasible that the endothelium may play some role in charge and/or size selectivity of proteins. One study that supports this hypothesis was performed by Ryan and Karnovsky, where they visualized the distribution of endogenous albumin in Munich-Wistar rat glomeruli (Ryan and Karnovsky 1976). During normal hemodynamic conditions, negatively charged albumin was found to be largely confined to the glomerular capillary lumen and endothelial fenestra, with only small amounts

detected in the early regions of the GBM. Further evidence of the importance of the endothelial layer in proper glomerular function is the occurrence of proteinuria during pre-eclamptic toxemia (PET) in pregnancy (Lafayette et al. 1998, Maynard et al. 2003). In these patients, a reduction in the density and size of the endothelial fenestrae and accumulation of sub-endothelial fibrinoid deposits was observed. No significant changes were observed in the thickness of the GBM, the frequency of epithelial slits, or the plasma flow rate. However, the subjects affected by preeclampsia showed a significantly decreased glomerular filtration rate and loss of albumin, showing that disruption of the endothelial layer alone is enough to significantly increase $\Theta_{albumin}$. A study by Sörensson et al. focused on the effect of puromycin aminonucleoside (PAN), a nephrosis-inducing agent (Sörensson et al. 2003). When cultures of glomerular endothelial cells in culture were exposed to PAN, the effect was a decrease in the production of glycosaminoglycans (GAGs), which are primary component of the endothelial glycocalyx.

Further evidence of the importance of the endothelium and its glycocalyx in the molecular sieving of proteins can be found in extrarenal (eg- muscle) capillary endothelia. While capillaries in skeletal muscle do not contain an epithelium and the endothelium is not fenestrated, a similar glycocalyx is present between the capillary lumen and the endothelial cell surface. Vink and Duling studied the selectivity of this surface layer in hamster cremaster muscle capillaries, using variously sized and charged tracer molecules (Vink and Duling 2000). Using fluorescent and brightfield microscopy, they found the penetration time of the glycocalyx was an order of magnitude shorter for neutral molecules of 0.4-40 kDa than for anionic tracers of the same size. Size and structural selectivity was also observed, with smaller dextrans (0.4-40 kDa) showing decreased penetration with increasing size, dextrans $\geq$ 70 kDa being fully excluded from the surface layer, and two plasma proteins (67 kDa albumin and 370 kDa fibrinogen) slowly penetrating the surface layer. Another study from the same lab investigated how glycosaminoglycans in the glycocalyx contribute to its size selectivity (Henry and Duling 1999). Using an enzyme to remove hyaluronan from the glycocalyx, the penetration of 70 and 145 kDa dextran tracers increased, while larger tracers remained excluded. A similar study treated arterioles with an enzyme to remove heparin, resulting in an

increased permeability to albumin and lactalbumin across the arteriole wall (Huxley and Williams 2000).

From the body of research summarized above, there is ample evidence that the fenestrated glomerular endothelium and its surrounding glycocalyx have an important effect on the size- and charge-selective properties of the glomerular barrier. Several of these studies indicate that the glycosaminoglycan content of the endothelial cell coat contribute to these properties. The following section will focus on the structure and composition of the glycocalyx.

1.3. The Endothelium and Its Glycocalyx

Endothelial cells are present throughout the body's vasculature. In general, they provide a barrier between blood and tissue, regulate vascular tone, mediate fluid and solute exchange, and participate in coagulation and inflammatory responses (Lindahl and Höök 1978, Pries et al. 2000, Savage 1994). Most of the current knowledge of the properties of endothelial cells comes from studies of cultures of umbilical cord veins (Savage 1994). However, care must be taken when comparing properties of endothelial cells from different locations. In many locations, such as muscle, skin, and connective tissue, intercellular clefts between adjacent endothelial cells form the principle pathway for water and small hydrophilic solutes from the blood to the surrounding tissue (Squire et al. 2001). However, other organs such as the small intestine, stomach, and kidney contain *fenestrated* endothelia, which contain small perforations across the entire cell body to allow for increased rates of transport (Rostgaard and Qvortrup 2002). For example, the glomerular capillaries can filter several hundred times the water and solutes as regular circulatory capillaries (Guyton and Hall 2000). Endothelial cells in different locations also differ in terms of size, shape, intercellular contacts and surface antigens (Zetter 1988). Recently, it was shown that the gene expression between glomerular and aortic endothelial cells is somewhat different (Sengolge et al. 1999).

The transport of water and solutes across glomerular endothelial cells is primarily governed by two features: the fenestra and the glycocalyx. Glomerular fenestrae are circular with a 60-80 nm diameter, extend across the width of the cell, and occupy 20-30% of the luminal surface area (Avasthi and Koshy 1988, Drumond and Deen 1994, Lea

et al. 1989, Rostgaard and Qvortrup 2002). In three dimensions, they take on an approximately hour-glass shape. The glycocalyx is the layer of membrane-bound macromolecules extending from the luminal surface of the endothelial cell. Some references distinguish between this and the endothelial surface layer, which contains both the glycocalyx and additional unbound macromolecules that intertwine to form a thicker layer of macromolecules on the cell surface (Pries et al. 2000); however, this thesis will follow the convention of much of the published research, and use the two terms interchangeably. Cationized ferritin staining of the glomerulus shows an anionic matrix that lines the entire endothelial lumen surface and fills the fenestra (Avasthi and Koshy 1988). It has been proposed that this cell coat extends from the inner part of the fenestra, under the endothelial cells, and partially into the glomerular basement membrane (Latta and Johnston 1976). There is significant debate on the thickness of the cell coat (Weinbaum et al. 2007). Studies have shown that it is a highly deformable surface layer, and measurements of it are subject to the method of visualization used. In various early studies that stained macro- and micro-vessels, the cell coat thickness ranged from 20 to 100 nm (Weinbaum et al. 2007). Studies using hematocrits and reduction in flow velocities compared with open tube flow predict a cell coat of 500-1000 nm (Pries et al. 2000). Measurements in glomerular capillary walls which were rapidly frozen and cross-sectioned showed a 100-200 nm surface layer (Squire et al. 2001). Recent studies that visualized the flow of blood cells, blood plasma, and 70 kDa dextran tracers within capillaries indicated a 400-500 nm surface layer (Vink and Duling 2000). The increasing estimates of the endothelial glycocalyx thickness in recent literature contribute to the motivation to reevaluate the role of this layer in glomerular transport.

Limited information is available on the structure of the glycocalyx (Weinbaum et al. 2007). An analysis of the glycocalyx's effect on microvascular hematocrit suggests that the endothelial cell layer has a hydraulic resistivity of at least 10^{11} N s/m^4 (Pries et al. 2000). Electron microscopy of the glycocalyx showed 10-12 nm fibers with a characteristic spacing of 20 nm (Squire et al. 2001). Other studies have indicated the presence of filamentous sieve plugs 300-400 nm long by 5-10 nm thick in the capillary fenestra of the small intestine, stomach, and peritubular kidneys. However, no sieve plugs were observed in the glomerular capillaries, though a fine 300 nm cell surface coat

was seen to cover the fenestrae and inter-fenestral regions, which was thicker than that observed in other fenestrated endothelia (Rostgaard and Qvortrup 2002). This observation is further supported by the fact that the protein PV-1 that forms the diaphragms in the fenestra of other capillary beds is not present in glomerular endothelia (Sörensson et al. 2003).

The glycocalyx of an endothelial cell contains four type of molecules: proteins, glycoproteins, glycolipids, and proteoglycans (Pries et al. 2000, Sörensson et al. 2003). A glycolipid is a lipid molecule to which a short carbohydrate chain is attached. Due to their hydrophobic nature, they will generally be associated with the cell plasma membrane. Proteins may also be bound to the cell surface, such as those functioning as receptors. In addition, there have been numerous studies on the effects of free plasma proteins, particularly orosomucoid, on the properties of the glycocalyx (Curry et al. 1989, Haraldsson et al. 1992, Huxley and Curry 1991, Schneeberger and Hamelin 1984, Turner et al. 1983). It has been shown that the presence of certain plasma proteins is necessary for maintaining proper permeability of the capillary wall. Their role is likely structural, since it has also been shown that the glycocalyx thickness decreased by two-fold when perfused with protein-free and albumin solutions compared to complete plasma (Adamson and Clough 1992).

The remaining two components of the glycocalyx, glycoproteins and proteoglycans, are similar, being composed of a core protein with carbohydrate side chains. Glycoproteins have short oligosaccharide side chains (2-15 sugar residues) that are often branched and correspond to 1-50 wt% of the molecule. Proteoglycans have much longer glycosaminoglycan (GAG) side chains (~200 sugar residues) that are linear, may have a large number of negatively-charged sulfate groups, and often comprise >50 wt% of the molecule (Kuberan et al. 1999, Pries et al. 2000). When glomeruli are treated with enzymes that digest proteoglycans, large tracer molecules are able to penetrate further into the capillary wall. Similar effects are seen when penetration studies are performed at high ionic molarity or with cation tracers (Kanwar and Venkatachalam 1992). These studies all suggest that these large, negative proteoglycans play a significant role in the transport of molecules across the endothelial glycocalyx. For this reason, the following

section will look at the chemical and structural properties of proteoglycans and their GAG side chains in greater detail.

1.4. Proteoglycans and Glycosaminoglycans

1.4.1. Proteoglycans

As noted in the prior section, proteoglycans (PG) are a class of molecule with several glycosaminoglycan chains attached to a single core protein. They can be found in the extracellular matrix, on the cell surface, or even intracelluarly in nearly all cells throughout the body (Kjellén and Lindahl 1991). Much diversity exists between types of proteoglycans, the predominant variations being core protein length, number of GAG chains, type of GAG chains, and length of GAG chains. The core protein can range from 20 kDa to several hundred kDa (Wight et al. 1991). In most proteoglycans, the core proteins contains 200~600 amino acid groups, corresponding to an extended length of 70-210 nm (Pries et al. 2000). The functional role of the core protein is as a scaffold for the immobilization and spacing of the GAG chains (Kjellén and Lindahl 1991). From 1 to 100 GAG chains may be attached to the core protein, in addition to some smaller oligosaccharides (Kjellén and Lindahl 1991). While GAG chains are generally found attached to protein cores, they occasionally also exist as free polysaccharide chains (Lindahl and Höök 1978). The three types of GAGs that are of interest here are heparan sulfate (HS), chondroitin sulfate (CS), and dermatan sulfate (DS); the properties and distinctions of these molecules will be discussed later. Generally, a single type of GAG is found on a proteoglycan (eg – HS-PG); however, it is possible to have hybrid proteoglycans with various GAG types on a single core protein (Kjellén and Lindahl 1991). For example, the proteoglycan *perlecan*, which is found in most basement membranes, has a 390 kDa protein core, a total weight of 700 kDa, and up to 4 HS chains, which sometimes contain CS or DS substitutes and sometimes contain no GAG chains (Rossi et al. 2003). The widely-studied *syndecan*, which is often found on cell surfaces, contains 3-4 HS chains and 1-2 CS chains on a 32 kDa protein; in contrast, *aggrecan* can contain over 100 CS chains and 100 oligosaccharides on a 210 kDa protein (Wight et al. 1991).

1.4.2. Glycosaminoglycans

Glycosaminoglycans, also referred to mucopolysaccharides in the older literature, are linear polymers with repeating disaccharide units. Each disaccharide unit contains one hexosamine and one hexuronic acid (Kanwar and Venkatachalam, Kjellén and Lindahl 1991, Wight et al. 1991). GAGs, specifically heparin, have the highest negative charge density of any known biological macromolecule, with a heparin average net charge of -5 per kDa (Capila and Linhardt 2002). The negative charge arises from acidic sulfate and/or carboxyl groups on the disaccharide units. Recent research has attempted to use chemical and enzymatic methods to synthesize GAG molecules, though current methods can only produce small oligosaccharides (Karst and Linhardt 2003, Tamura 2001). Instead, nearly all commercially available GAGs are extracted and purified from various animal tissues using organic solvents and/or proteases. Once the PG is extracted, it is further treated enzymatically or with alkali extraction to remove it from the core protein. Finally, the GAG molecules are further purified and separated by precipitation or other fractionation method (Volpi 1996).

GAG molecules are separated into six primary types: heparin (H), heparan sulfate (HS), chondroitin sulfate (CS), dermatan sulfate (DS), keratan sulfate (KS), and hyaluronate (or hyaluronic acid, HA). The names are derived from the tissues in which they were originally extracted; later research has shown that each type of GAG is found in numerous tissues throughout the body (Jaques 1977). The differences between the molecules arise in the combination of hexosamine and hexuronic acids in the disaccharide repeat units (Figure 1.2; Table 1.1). The hexosamine can be either D-galactosamine (GalN) or D-glucosamine (GlcN). The hexuronic acid can be either D-glucuronic acid (GlcA) or L-iduronic acid (IdoA). The differences between CS and DS and between H and HS are subtle and somewhat arbitrary. Chondroitin sulfate generally contains negligible IdoA while dermatan sulfate contains a significant fraction of IdoA. Heparan sulfate has a majority of GlcA while heparin has a majority of IdoA. For these reason, these pairs of molecules are often referred to as a single category.

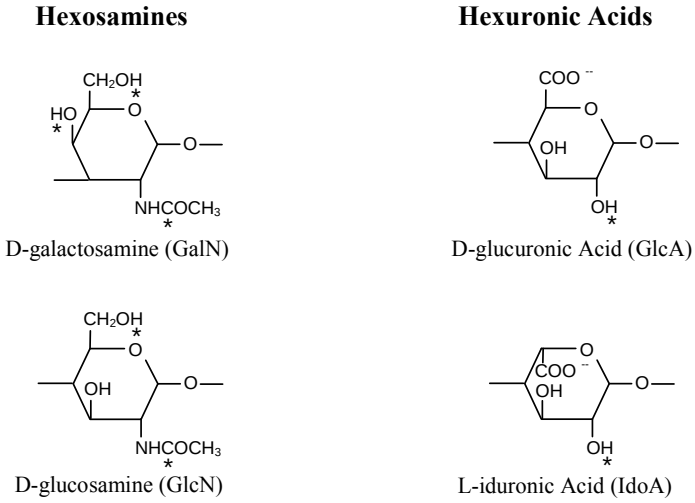

Figure 1.2 Chemical structure of hexosamines and hexuronic acids found in glycosaminoglycan disaccharide repeat units. Potential sites of sulfation are indicated by *. (Kjellén and Lindahl 1991, Lindahl and Höök 1978, Wight et al. 1991)

	Chondroitin Sulfate	Dermatan sulfate	Heparan sulfate	Heparin	Keratan sulfate	Hyaluronic Acid
Hexosamine	GalN	GalN	GlcN	GlcN	GlcN	GlcN
Hexuronic Acid	GlcA	GlcA/IdoA	GlcA/IdoA	GlcA/IdoA	[galactose]	GlcA

Table 1.1 Composition of disaccharide repeat units in each category of glycosaminoglycan: D-galactosamine (GalN); D-glucosamine (GlcN); D-glucuronic acid (GlcA); L-iduronic acid (IdoA) (Kjellén and Lindahl 1991, Lindahl and Höök 1978)

Further variation in GAG molecules exists due to the sulfation of the disaccharide units. The extent of sulfation can vary between types of GAGs, between the tissues in which the GAG was produced, and even between different regions of the same molecule. Sulfation can occur in any of three locations on GlcN and GalN, and on one location on GlcA and IdoA (Figure 1.2) (Kjellén and Lindahl 1991). Heparin has an average of 2.7 sulfate groups per disaccharide; heparan sulfate and chondroitin sulfate an average of ~1 per disaccharide (Capila and Linhardt 2002, Lindahl and Höök 1978, Wight et al. 1991). However, this can be deceiving since the charge may be distributed into high-charge and low-charge segments in a single GAG molecule. The location of sulfation adds additional variation between GAGs. For example, the fraction of chondroitin sulfate known as CS-A contains primarily chondroitin 4'-sulfate, while the fraction known as CS-C contains a larger fraction of chondroitin 6'-sulfate (Volpi et al. 1999). The

composition of these chains has been shown to be stable once synthesized inside the cell, though extended storage in acidic conditions can slightly reduce the extent of sulfation, leaving hydroxyl and amine groups on H/HS and hydroxyl groups only on CS/DS. Only ~2-4% of glucosamino residues in heparin contained a free amino group (Jandik et al. 1996, Volpi et al. 1999).

The GAG chains are connected to the proteoglycan core protein by a unique O-glycosidic linkage, with the exception of hyaluronate which isn't synthesized on a core protein. This structure connects the first disaccharide repeat unit to a serine residue in the core protein. It is composed of a galactosyl-galactosyl-xylosyl-serine segment (Anderson et al. 1964, Wight et al. 1991). This linkage can be cleaved to remove the GAG chain from the core protein by enzyme digestion (xylosidase) or by alkali exposure (Anderson et al. 1964, Kon et al. 1991). The structure of a GAG chain, including the linkage region, is shown in Figure 1.3.

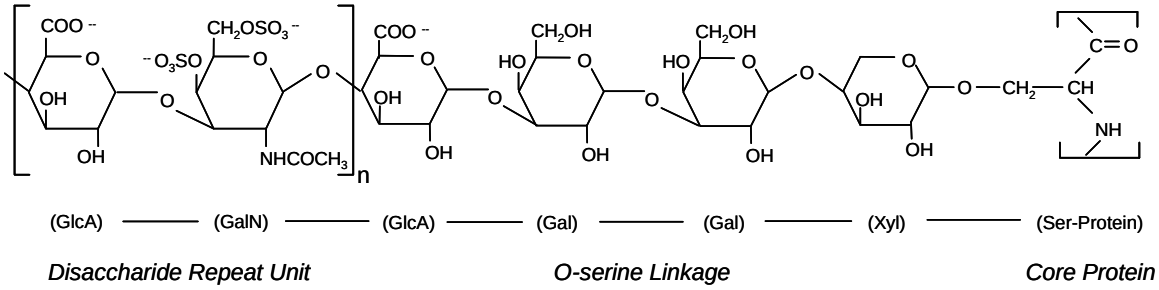

Figure 1.3 Glycosaminoglycan structure, including linkage to protein, for chondroitin sulfate. (Wight et al. 1991)

Glycosaminoglycan chain size can vary over a wide range. HS is usually ≤50 kDa, though it can exceed 100 kDa; CS is usually ≤100 kDa, though it can exceed 300 kDa. In general, a single disaccharide unit (M_W ~ 474 Da) corresponds to approximately 1 nm of chain length, so that the average extended chain length of a 50 kDa GAG is approximately 105 nm (Wight et al. 1991). There is evidence that GAGs exist as helical structures in solution, though it is not known if this structure exists under biological conditions (Capila and Linhardt 2002, Lindahl and Höök 1978). It has been observed that certain GAG chains containing GlcA- and IdoA-containing disaccharide units in alternating sequence can self-associate into aggregates, though most GAGs retain a linear structure (Kjellén and Lindahl 1991).

1.4.3. Renal Glycosaminoglycans

Kjellén and Lindahl have categorized a number of proteoglycans into five basic functional categories of macromolecules with similar structure (core protein length, number and type of GAG substitutions) (Kjellén and Lindahl 1991). This shows that cell types that perform similar roles (eg – regulating blood coagulation or assembling basement membranes) also contain similar proteoglycans. While such similarities between types of GAGs exist between tissues of similar functional types, it is still preferred to have the most direction information available about the composition of the glomerular endothelial glycocalyx. Only a limited number of studies on the proteoglycan and glycosaminoglycan composition of the endothelial glycocalyx have focused specifically on the glomerular endothelium. However, a number of earlier studies were performed under the hypothesis that GAG in the glomerular basement membrane played a major role in glomerular transport properties, especially charge selectivity (Kanwar et al. 1980, Reeves et al. 1980). The presence of GAG chains surrounding the endothelium was neglected, so that GAG characterization of the entire glomerular capillary wall was claimed to represent the GAG character of the GBM alone. These experiments still provide useful information about the types, sizes, and role of GAGs in the overall glomerular barrier, since many of the GAGs present in the GBM were likely synthesized by the endothelium, and are included below.

A number of different proteoglycans have been identified in the glomerulus. A majority of them (~95%) are HS, with ~5% CS. The average weight of these PGs is 130-150 kDa, with ~25 kDa GAG chains and an 18 kDa core protein (Kanwar et al. 1984a, Kanwar et al. 1984b). GAGs extracted from the glomerulus by other groups also contained HS-PGs, though with a larger reported core protein of 140-400 kDa, which is similar to *perlecan* and *agrin* PGs. The CS-PGs *decorin* and *biglycan* were also extracted from the glomerulus. However, staining of the glomerular capillary wall only showed *biglycan* and *perlecan* around the endothelium (Edge and Spiro 1987, Groffen et al. 1998, Klein et al. 1988, Schaefer et al. 2000). *Biglycan* is a 150-240 kDa molecule with a ~45 kDa core protein and 30-40 kDa GAG chains (Wight et al. 1991). Two studies of the PG/GAG content specifically of glomerular endothelial cells in culture have been reported. Kasinath found that both HS-PGs and CS/DS-PGs were produced by

the endothelial cells (Kasinath 1993). Molecular sieving chromatography showed that the PGs were distributed into two sizes, both of which contained 40~45% HS-PGs and the remainder CS/DS-PGs. PGs of similar size and composition were found both attached to the endothelial cell wall and in the surrounding media. More recently, Sörensson *et al.* reported that GAG produced by the endothelial cells was 31% HS, 24% CS, and 23% DS (the remainder classified as residuals) (Sörensson et al. 2003). These GAG molecules had a mean Stokes-Einstein radius of 50-90 Å.

While much variation and speculation exists in the specific composition of the glomerular endothelial glycocalyx, the above studies show that it can assumed that the glycocalyx is approximately composed of proteoglycans that have a high weight fraction of GAG molecules (~80 wt%) with significant anionic charge (~ 1 per disaccharide) distributed over several (3-6) moderately long (80 nm) GAG chains attached to a core protein. This approximate character of the glycocalyx will be used for selecting appropriate GAG molecules in the follow section on the research plan.

Due to the complex nature of the glomerular endothelium and its glycocalyx, it would be desirable to study the transport properties across this barrier with an isolated culture of glomerular endothelial cells. This would require the cells to remain differentiated, express fenestrae, and form a confluent monolayer on an appropriate support. This is challenging since cells taken out of their context tend to lose their shape and function (Daamen et al. 2003). In particular, culturing of glomerular endothelial cells has been limited (Ballermann 1989, Green et al. 1992, Kasinath 1993). It is still infeasible to form a fenestrated, confluent monolayer of glomerular endothelial cells through which transport properties can be measured. For this reason, this research proposes to study the transport properties through a synthetic analog to the glomerular endothelial glycocalyx.

1.5. Thesis Overview

The ultimate goal of this research was to gain insight into the role of the glomerular endothelial glycocalyx in the sieving of blood plasma proteins. In particular, this work investigates the role of charge interactions between GAG fibers and albumin, a blood serum protein. The following chapters describe how an appropriate synthetic analog was created and characterized, how transport properties such as hydraulic permeability and

sieving depended on microstructural properties and solution ionic strength, and how this system could be understood with microstructural models. The work concludes with extensions back to the properties of the physiological glycocalyx; because the structure of the glycocalyx is poorly understood, the physiological conclusions are quite tentative.

The development of an agarose-GAG membrane using cyanogen activation is the topic of Chapter 2, which includes both an experimental investigation into reactions parameters which could increase GAG binding and a model of the competition between GAG diffusion and binding. Portions of that work were published in *Carbohydrate Research* (Mattern and Deen 2007). The hydraulic permeability of agarose-GAG membranes over a range of buffer ionic strengths were investigated in Chapter 3. Of particular interest was a decreased Darcy permeability through charged fibers at low ionic strengths versus high ionic strengths; this electrokinetic effect was investigated with microstructural and Donnan models. An in-depth evaluation of fiber "mixing rules" for the hydraulic permeability of neutral and charged fiber mixtures was published in the *AIChE Journal* (Mattern and Deen 2008). Experimental Darcy permeability through the agarose-GAG membranes and a model of the permeability were published in the *Biophysical Journal* (Mattern et al. 2008).

The permeability of macromolecular solutes in agarose-GAG gels was studied to understand the role of fiber and solute charges in sieving. In Chapter 5, the sieving coefficients of bovine serum albumin (BSA) and monodisperse Ficolls were studied in the agarose-GAG gels over a range of ionic strengths. In Chapter 4, the equilibrium partition coefficients of the macromolecular solutes were also measured in the same gels to compare the charge effects in partition coefficients versus sieving. Electrostatic and excluded volume models were used to understand the charge interactions which affected equilibrium partitioning. This work concludes in Chapter 6 by applying this research to give insight into the potential roles of the glycocalyx in glomerular filtration.

Chapter 2. AGAROSE-GAG MEMBRANE SYNTHESIS

In the following sections, the development and refinement of an agarose-GAG membrane synthesis procedure are presented. The selection of an agarose-GAG system is first presented, followed by a review of agarose functionalization procedures in the literature. An agarose activation procedure using 1-cyano-4-(dimethylamino)-pyridinium tetrafluoroborate (CDAP) is modified from the published procedure for Sepharose® chromatography beads to a procedure for flat agarose membranes. Assay methods for determining viable GAG suppliers for attachment and for measuring the bound GAG content of agarose-GAG gels are summarized. Finally, data is presented on refining the agarose-GAG synthesis to increase the binding yield, including a model for the competing processes governing GAG attachment in membranes.

2.1. Introduction

As discussed in the background, the glycocalyx is a loose matrix that is composed primarily of negatively charged glycosaminoglycan chains bound to core proteins. Since GAG chains contribute the majority of mass and charge to the proteoglycans, the primary objective of this research is to study the transport of fluids and macromolecules through a matrix of GAG. Prior work has considered binding GAG to the walls of nanochannels

(track-etched polycarbonate (TEPC) membranes; diameter ~100nm), which would evoke the structure of the endothelial fenestrae. However, difficulties in determining whether the GAG formed a coating on the channel walls or a film over the membrane surface, combined with sieving data that did not agree with theory, suggested that TEPC membranes were not a suitable substrate for studying transport properties through a GAG matrix.

Instead, this research aims to use a substrate matrix with homogeneously bound GAG. Existing fiber-matrix theories may be used to explain the properties of such a homogeneous fiber system. The following section evaluates the various materials that could be used as the matrix substrate. After selecting agarose as an appropriate substrate, a variety of methods for binding GAG to the agarose fiber matrix are reviewed.

2.1.1. Substrates

Several methods for studying a synthetic assembly of GAGs are available in the literature. Some studies in drug delivery have used cross-linked GAGs; while this method assures that a scaffold membrane does not interfere with the properties of the GAGs, it is unclear how crosslinking GAG chains would affect their properties and if the crosslinked GAG membrane would have sufficient mechanical strength for transport studies (Rubinstein et al. 1992, Salamone 1996, Sintov et al. 1995). Numerous research groups have incorporated GAGs into collagen-I matrices; however, collagen membranes may compress or swell under different pressures and concentrations, making it difficult to study transport phenomena (Daamen et al. 2003, Pieper et al. 2000, Pieper et al. 1999). Similarly, GAGs have been attached to a variety of polymer membranes to create biomedical materials with thromboresistant properties (polymethyl-methacrylate, polyvinylidene-fluoride, and styrene-butadiene, to name a few) (Goosen and Sefton 1979, Karlsson et al. 2000, LaBarre et al. 1974, LaBarre and Jozefowicz 1977, Rea et al. 1971). Prior work in our research group had attached GAG to track-etched polycarbonate membranes; however, non-uniformities in the pores and inability to distinguish between pore- and surface-effects made the substrate unsuitable (Zugates - *unpublished results*). Numerous methods have been published on the use of GAG attached to the surface of Sepharose® (agarose) beads for affinity chromatography and protein separation

(Danishefsky and Tzeng 1974, Danishefsky et al. 1976, Funahashi et al. 1982, Iverius 1971, LaFrance and Dapron 1997, Sasaki et al. 1987, Sepulcre and Moczar 1973). Agarose as a substrate has numerous advantages: its transport properties have been extensively studied in our laboratory; it has relatively constant properties over the pressures and concentrations of interest; it is composed of neutral, rigid fibers; and it can be reproducibly cast into membranes with sufficient strength. For these reasons, an agarose-GAG hydrogel membrane was chosen to study the transport properties of a GAG matrix.

2.1.2. Binding Method for Agarose-GAG

A variety of methods have been published for attaching GAGs to agarose, as reviewed by Funahashi *et al.* and Cuatrecasa (Cuatrecasas 1970, Funahashi et al. 1982). It is desired to attach the GAG molecules to the agarose substrate at a single point, mimicking the end-only attachment found in cell coat proteoglycans. However, most of the attachment methods in the literature use the hydroxyl or carboxyl groups on the GAG chains to react with binding sites synthesized on agarose, which may result in multiple points of attachment. Two categories of covalent GAG attachment remain, which instead use unique functional groups found at the ends of the GAG chain. The first method uses amino-agarose, which reacts with the terminal formyl (carboxyl) group on the reducing end of the GAG chain (LaFrance and Dapron 1997, Sasaki et al. 1987). The second method uses agarose that has been "activated" by cyanogen bromide or similar agents to turn hydroxyl groups into highly reactive cyanate esters, which then react with the primary amine found on the core protein residues at the end of the GAG chain (Axén et al. 1967, Iverius 1971, Kato and Anfinsen 1969, Kohn and Wilchek 1984). In variations of this second method, some procedures bind the amino group on peptides to a N-hydroxysuccinimide, carboxyl or epoxy group on functionalized agarose; however, these methods have varying levels of binding specificity in the presence of competing carboxyl groups on the GAG chains. Of these two end-only attachment methods, the amine-cyanate ester method has been used more extensively and has been studied more thoroughly in the literature; for this reason, a cyanylating-activation procedure to attach GAG chains via their terminal protein residues was chosen.

Since the discovery of the cyanogen halide method for coupling proteins to polysaccharides by Axén, Porath, and Ernback in 1967 (Axén et al. 1967, Porath et al. 1967), a number of improvements and variations on the activation method have been made. An excellent review of the topic has been assembled by Kohn and Wilchek (Kohn and Wilchek 1984); it is briefly summarized here. The conventional activation procedure uses cyanogen bromide (CNBr) in a strongly basic reaction medium to convert the hydroxyl groups on agarose (or any polysaccharide) into a highly-reactive cyanate ester (-OCN). Much of the CNBr is rapidly hydrolyzed into an inert cyanate ion, such that large amounts of the highly toxic CNBr are required to form even moderate levels of active sites. In addition, a majority of the active sites rapidly degrade to an inert carbamate or react with another active site to form cross-linking. The safety of the procedure is also a concern, since CNBr sublimes rapidly at room temperature, is a powerful lachrymator and is highly toxic in even small amounts (Parikh et al. 1974). The conventional method was greatly improved by the addition of triethylamine as a "cyano-transfer agent", whereby the CNBr forms a complex with the triethylamine which decreases the pH at which the reaction is performed and avoids the formation of inert side products. The result is a method that uses less CNBr to achieve a higher activation yield. While this method is still frequently used, several other cyanylating agents were discovered in the early 1980's that pose a less severe health risk and increase the activation yield relative to CNBr. The three of note are N-cyanotriethylammonium tetrafluoroborate (CTEA), p-nitrophenylcyanate (pNPC), and 1-cyano-4-(dimethylamino)-pyridinium tetrafluoroborate (CDAP). While the three reagents are similar in structure (R-C≡N) and reaction sequence, CDAP has the advantage of being used at temperatures slightly above 0°C and resulting in significantly higher activation yields (CDAP: 60-80%, CTEA: 10-20%, pNPC: 10%, CNBr: 1-20%).

The chemistry of the CDAP reaction sequence is presented in Figure 2.1. The repeating units on agarose contain multiple hydroxyl groups which may be activated by CDAP. When CDAP and triethylamine (a cyano-transfer agent) are added, the hydroxyl groups are converted to a pyridinium-isourea derivative. In slightly acidic conditions, the equilibrium of the isourea derivative is shifted towards the cyanate ester. In the presence of primary amines (either the terminal peptide of GAG or a small quench molecule like

ethanolamine), the amine and cyanate ester will form a covalent isourea bond. There are several competing reactions for the active cyanate esters. In aqueous conditions, the cyanate ester can degrade into an inert carbamate group. The cyanate ester can also bind with other activated groups, forming a cyclic imidocarbonate bond between neighboring active groups or a linear imidiocarbonate bond that crosslinks two agarose fibers.

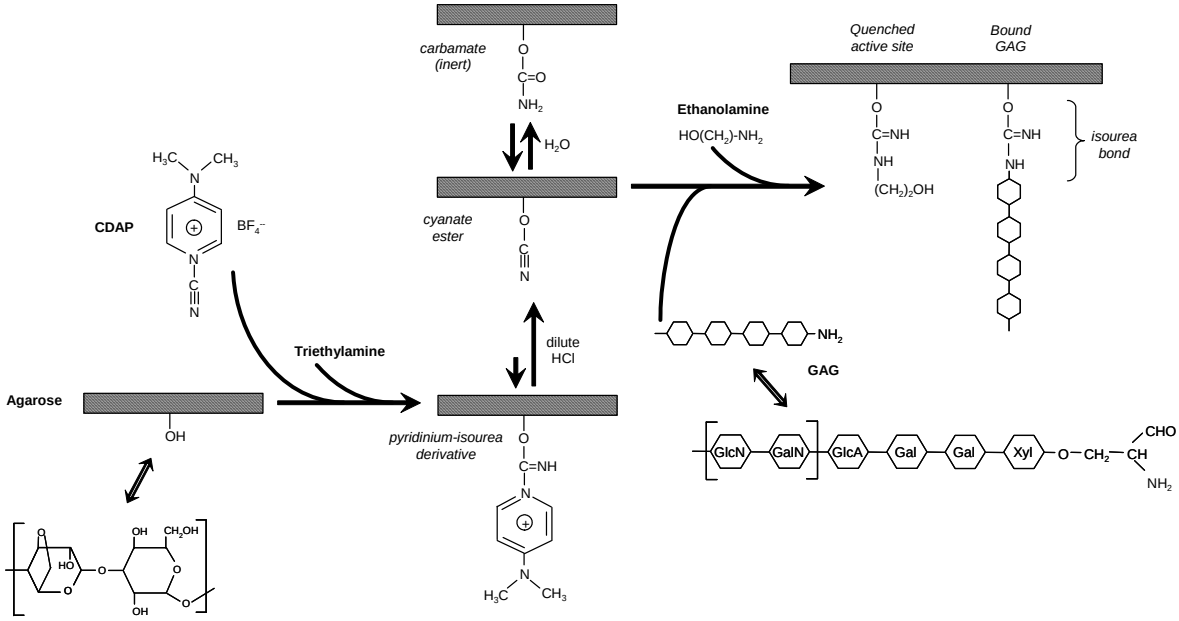

Figure 2.1 Reaction pathway for the activation of agarose by CDAP and the binding of GAG.

2.2. Development of Agarose-GAG Synthesis

This section includes information on the synthesis of agarose-GAG membranes based the published CDAP activation methods for Separose® chromatography beads. The procedure was first modified for flat membranes, then scaled-up to produce batches of 20 membranes. Assay methods for measuring the bound GAG content of the agarose-GAG membranes are reviewed. A brief investigation into the types of GAG which can be used in the synthesis is presented. Finally, the results of this "baseline" synthesis are presented. The following section will aim to improve on the bound GAG content of this baseline.

2.2.1. Method – Agarose-GAG Synthesis

As mentioned previously, the published literature for functionalizing agarose with cyanate esters is based on the use of Sepharose® (agarose) or other polysaccharide resin chromatography beads. For the measurement of transport properties, agarose is instead formed into thin agarose hydrogels based on methods previously developed by our research group (Johnson et al. 1995, Johnston and Deen 1999). A procedure is desired that can create a batch of gels which have uniform properties within the batch and which will not damage gels during the synthesis.

The agarose activation procedure for CDAP is taken from the method by Kohn and Wilchek for polysaccharide resin beads and modified to be appropriate for gel membranes (Kohn and Wilchek 1984). Numerous protocols are available for attaching proteins to cyanate-activated agarose; the procedure here is based on the method used by Iverius (Iverius 1971). Modifications to the procedures included: (1) replacing washes in a sintered glass funnel with multiple equilibrations in an excess volume of the wash solution, (2) keeping each membrane supported and separated in a plastic histology embedding cassette (Figure 2.2), (3) replacing magnetic stir bars with orbital stirring and (4) increasing reagent volumes to assure complete coverage of the gels.

The modified procedure developed to synthesize a batch of twenty agarose-GAG membranes is as follows:

> ***Agarose Gel Casting:*** Suspend agarose (Type IV; Sigma, St. Louis, MO) in KCl-phosphate buffer and heat at 90ºC until it is completely dissolved, forming a 4.1 w/w% (=4 v/v%) solution (or other concentration, as needed). Pour the hot agarose solution onto a 2.5 cm diameter woven polyester support (Spectramesh™ 43 µm opening; #148-248; Spectrum Laboratories, Rancho Dominguez, CA) that was placed on a heated glass plate. Place a second hot glass plate on top and compress the excess agarose away from the mesh. Allow the gel to cool to room temperature and immersed in buffer. Store membranes in buffer and refrigerate until use.
>
> ***Agarose Activation:*** Place each agarose membrane in a plastic histology cassette (Histo-prep Tissue Capsules #15-182-219; Fisher, Hampton, NH). Soak 20 membranes for 15 minutes with gentle agitation in each of the following: 1 L DI water, 1 L 30% acetone (two times) and 1 L 60% acetone (two times). In a beaker surrounded by an ice bath (or ice block), add the washed gels to 200 mL ice-cold 60% acetone. While orbital mixing at 150-200 rpm, add 20 mL of 100 mg/mL

CDAP (#1458C; Research Organics, Cleveland, OH) in dry acetonitrile; wait 1 minute. Dropwise, add 16 mL of 0.2 M triethylamine (TEA) solution over 1-2 minutes; wait 5 minutes while continuing to mix. Rapidly transfer the membranes to 1500 mL of ice-cold 0.05 N HCl (500 mL in each of three jars); wait 30 minutes while continuing to mix. Membranes may be left in the HCl solution up to several hours, if needed. Soak the membranes in 2 L of ice-cold water for 15 minutes (three times).

GAG Attachment: Cover the activated agarose membranes (in their cassettes) with 1 g/L GAG in 0.1M $NaHCO_3$. (Generally, 200 mL can cover five membranes.) Stir with orbital mixing at 4°C for at least 16 hours. To remove the remaining active groups, add 7.5 mL ethanolamine per 100 mL attachment solution and stir for 4 hours at 4°C. Soak the membranes for 15 minutes each with gentle agitation in the following: 2 L DI water (three times), 2 L 0.5 M NaCl (two times) and 2 L DI water (six times). Remove each gel from its cassette, store in ~10 mL 0.1 M KCl-phosphate buffer and refrigerate until use.

All chemicals are reagent grade or higher. The attachment process can use any GAG supply with a primary amine, which will be discussed further in a later section. To produce blank gels as a control for the agarose-GAG gels, the above is followed except for using a 0.1M $NaHCO_3$ attachment solution without GAG.

Figure 2.2 Polypropylene histology cassette used to support agarose membranes during the activation and attachment processes. (Histo-prep Tissue Capsules, #15-182-219; Fisher, Hampton, NH)

2.2.2. Method - GAG Assay

Once the agarose gels have been functionalized with GAG, it is necessary to assay them to determine the GAG content relative to the gel volume and agarose fiber content.

A broad range of assays in the literature can be used to measure GAG concentration. Most of the methods were developed for GAG in solution, though the procedures may be modified to account for the presence of agarose fibers. In the next section, the GAG assays available in the literature are summarized. After selecting the most appropriate assay method for the agarose-GAG membranes, the following section presents some modifications to the assay method to apply it to the agarose-GAG membranes and improve its accuracy.

Selection of Assay Method

The applicable GAG assays in the literature can be divided into five categories: (1) dye assays, (2) end group - primary amine assays, (3) end group - reducing sugar assays, (4) saccharide repeat unit assays, and (5) assays requiring specialized equipment. The available assays are listed in Table 2.1, along with a summary of their range of detection, specialized equipment requirements and procedure difficulty.

While the fluorescamine assay for primary amines has both good sensitivity and a simple procedure, it cannot be used once the amine group has been used for covalent binding to agarose. The Elson-Morgan reaction for glucosamine was used successfully by Funahashi *et al* for measuring the amount of GAG bound to Sepharose; however, it is a difficult procedure requiring acid digestion of both the agarose and the GAG (Funahashi et al. 1982). Of the other methods, the dye-based methods appear to be most attractive in terms of concentration range and simplicity. The methods are simple to perform and only require a spectrometer and basic labware. Metachromatic dye assays use a cationic dye which associates with the negatively charged GAG chain, with the GAG-dye complex absorbing light at a different wavelength than the free dye. It must be remembered that when the GAG is bound to an agarose substrate, the dye-GAG complex will not be in free solution and the measurement of its absorbance using most dye assays is not possible. However, the o-toluidine blue method measures the concentration of *free* dye (versus complexed dye), once the dye-GAG complex has been precipitated. This method can easily be extended to a bound-GAG system for a simple yet precise method for measuring bound GAG concentrations (Smith et al. 1980).

Table 2.1 Summary of GAG assay methods in the literature, with their sensitivity, relative difficulty and specialized equipment requirements.

Assay	Equipment for Measurements	Sensitivity*	Procedure Difficulty	References
Dye-Based Assays				
Dimethyl-methylene blue	spectrometer	10~150 µg/mL	simple	(Whitley et al. 1989)
Acridine orange	fluorometer	5~40 µg/mL	simple	(Diakun et al. 1979)
Alcian blue	spectrometer	50~750 µg/mL	simple	(Gold 1979)
o-Toluidine blue	spectrometer	1~100 µg/mL	simple	(MacIntosh 1941, Smith et al. 1980)
End Group – Primary Amine Assays				
Fluorescamine	fluorometer	5~100 µg/mL	simple	(de Bernardo et al. 1974, Toome et al. 1974, Toome and Manhart 1975)
o-Phthaldialdehyde	fluorometer	5~50 mg/mL	simple/moderate	(Roth 1971)
Fluoraldehyde	fluorometer	1~10 mg/mL	simple	(Jandik et al. 1996)
End Group – Reducing Sugar Assays				
2,2'-Bicinchoninate	spectrometer	1-25 mg/mL	difficult	(Jandik et al. 1996, Waffenschmidt and Jaenicke 1987)
Fluorescent tagging	fluorometer	not reported	moderate	(Hase 1996)
Repeat Unit Assays ***(requires acid/enzymatic digestion of samples)***				
Carbazole Reaction (for hexuronic acid)	spectrometer	10~100 µg/mL	difficult	(Bitter and Muir 1962, Galambos 1967)
Elson-Morgan Reaction (for glucosamine)	spectrometer	30~300 µg/mL	difficult	(Gardell 1953)
UV Detection (for unsaturated uronic acid)	UV spectrometer HPLC column	~100 µg/mL	difficult	(Koshiishi et al. 1998)
Specialized Equipment Assays				
Glucosamine groups	amino acid analyzer	~1 mg/mL	moderate/difficult	(Andersson et al. 1975)
Carboxyl group titration	potentiometer	0.6-20 mg/mL	moderate	(Varshavskaya et al. 1979)
Microscopy (dye staining or immunofluorescence)	microscope	not quantitative	moderate/difficult	(Daamen et al. 2003, van Kuppevelt and Veerkamp 1994)

* - based on 50 kDa GAG

The procedure developed by Smith *et al.* for assaying heparin immobilized on Sepharose beads using o-toluidine blue dye is as follows (Smith et al. 1980):

> ***o-Toluidine Blue Dye Assay:*** Prepare a 50 µg/mL solution of o-toluidine blue dye in 0.01 N HCl with 0.2% (2 mg/mL) NaCl. To each test tube, add 2.5 mL of the dye solution. In the reference test tubes, add 2.5 mL of GAG solution with 1-100 µg/mL GAG in 0.2% NaCl. In the sample test tubes, add a sample membrane and 0.2% NaCl to a total volume of 5 mL (note: Smith *et al.* added 0.025-0.15 mL Sepharose beads; one membrane is ~0.05 mL). Agitate by a Vortex mixer for 30 seconds. Add 5 mL of hexane to each tube and shake vigorously for 30 seconds. Centrifuge the tubes to separate the solvent layers, sample the aqueous layer, dilute the sample 1:10 with absolute ethanol and read the absorbance at 631 nm. The absorbance of the samples is correlated to the absorbance of the reference solutions to determine the GAG content.

This relatively simple procedure can be scaled in volume to assay a larger or smaller GAG content in the agarose-GAG membranes. It is necessary to add the hexane to precipitate the dye-GAG complex in free solution, since the absorbance spectra of the free dye and the bound dye overlap. While it isn't necessary to precipitate the GAG bound to membranes, the solution references and membrane samples are treated identically for consistency. Since the binding between the dye and the GAG molecules isn't covalent, the assay method is non-destructive and the samples may be recovered by washing with a high ionic strength buffer solution. While the reference concentrations used by Smith *et al.* produced a linear response between concentration and absorbance, the binding behavior is actually more complex. As shown by MacIntosh, the GAG concentration-absorbance curve is actually sigmoidal (MacIntosh 1941). The non-linear shape is caused by two factors: a decreased dye-binding efficiency at higher GAG concentrations and a non-linear absorbance curve for toluidine concentrations. However, as long as the GAG concentrations remain moderate and in proper proportion to the dye solution, the concentration-absorbance curve can be well-approximated as linear.

Assay Improvements

While preliminary tests of the o-toluidine assay confirmed that it was able to measure bound GAG at the necessary concentrations, additional tests were performed to determine if the presence of the agarose or the mesh affected the assay, if a minimum time was

required for the dye to diffuse into the membranes, if the assay could be scaled down, if the error on the reference samples could be reduced and if the o-toluidine dye solution was stable over time.

The two largest sources of error in the reference concentration curve were the dilution of the GAG solution to the desired reference concentrations (1-100 μg/mL) and the dilution of the aqueous layer in ethanol before the absorbance measurement. To improve these error sources, a series of stock GAG solutions over the range of concentrations were prepared on a larger scale (~200 mL) and used as a reference for all assays. This improved the accuracy of the assay from ±0.6% to ±0.3% relative error. It was found that dilution of the aqueous sample in ethanol was not necessary for absorbance measurement, so the aqueous layer could be measured directly at 631 nm, reducing the relative error to 0.1%. The assay was able to be scaled down to half-volumes, though there was some increase in error of the measurements. Since the bound GAG content of the membranes was found to be within the range of the full-scale assay, there was no need to pursue further improvements of the small-scale assay.

It was found that when the dye solution is stored in an opaque container for several weeks, there is no significant degradation in color. However, spectrometer readings did vary slightly from week to week, so it is recommended to run a reference calibration curve with each batch of sample assays. There was no significant effect on absorbance over the temperature range 16.5-29.0°C.

Similar to the observations by MacIntosh, the absorbance had a sigmoidal response to the GAG concentration (Figure 2.3) (MacIntosh 1941). Using the assay procedure above, the absorbance had a nearly linear response within the range 5-60 μg/mL (12.5-150 μg/sample). The reference samples used to create the calibration curve for the assay were chosen to fall across this range (0, 5, 10, 20, 30, 40, 50, 60 μg/mL).

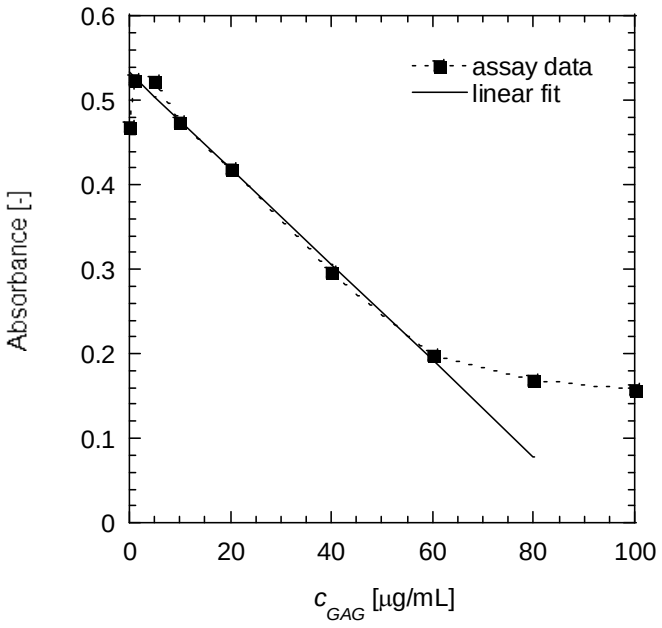

Figure 2.3 Absorbance response for o-toluidine assay for GAG in solution. Absorbance is measured at 631 nm. The linear fit over the range 5-60 μg/mL has R^2=0.994.

Since the membranes have a finite thickness (~70 μm) with GAG distributed throughout, they require at least several characteristic diffusion times (1~2 seconds) to allow the dye to diffuse throughout the thickness. Further tests show that the dye does not reach binding equilibrium with the GAG for several minutes. Therefore, it is necessary to allow the dye solution to equilibrate with the sample for at least 15 minutes prior to measuring the absorbance.

It was found that the assay of a blank agarose membrane was slightly higher (apparent GAG content of 4-14 μg) than a 0 μg/mL reference solution. Partitioning measurements also indicated that there was preferential partitioning of the dye into the membranes (Φ_{dye}=1.5~3). Further studies showed that the assay of the polyester support mesh accounted for most (~90%) of the non-zero reading of the blank, while the additional volume of the hydrogel could cause an apparent GAG concentration of 1.6 μg. To account for these factors, the assay data must be properly interpreted.

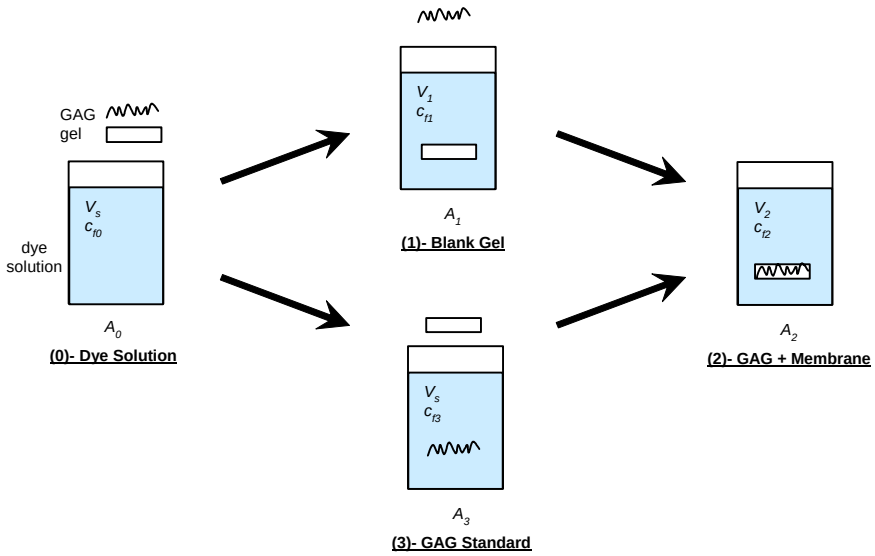

Figure 2.4 Schematic interpretation of GAG assays to account for mesh and gel volume. For each of the four types of samples, the volume (V_i) is known, the absorbance (A_i) is measured and the concentration of free dye ($c_{f,i}$) is assumed proportional to the absorbance by Beer's law.

As shown in Figure 2.4, each sample assayed has a known volume (V_i, which is the sum of solution and gel volumes) and a measured absorbance ($[A]_i$). The absorbance is assumed to follow Beer's law and be linearly related to the concentration of free dye ($c_{f,i}$) by the product of the absorption coefficient (α_{dye}) and the pathlength (l):

$$[A]_i = (\alpha_{dye} l) c_{f,i} \tag{2.1}$$

It is also assumed that the mass of dye bound to GAG ($m_{b,GAG}$) is proportional to the mass of GAG (m_{GAG}) and independent of the concentration of the dye:

$$m_{b,GAG} = \gamma m_{GAG} \tag{2.2}$$

From conservation of mass of the dye during the assay:

$$V_s c_{f,0} = V_1 c_{f,1} + m_{b,mesh} = V_2 c_{f,2} + m_{b,mesh} + \gamma m_{GAG,2} = V_s c_{f,3} + \gamma m_{GAG,3} \tag{2.3}$$

where $m_{b,mesh}$ is the mass of dye bound to the support mesh in the membrane. Rewriting the conservation equation in terms of absorbance:

$$\begin{aligned} V_s (\alpha_{dye} l)^{-1} [A]_0 = V_1 (\alpha_{dye} l)^{-1} [A]_1 + m_{b,mesh} = V_2 (\alpha_{dye} l)^{-1} [A]_2 + m_{b,mesh} + \gamma m_{GAG,2} \\ = V_s (\alpha_{dye} l)^{-1} [A]_3 + \gamma m_{GAG,3} \end{aligned} \tag{2.4}$$

From the reference samples (0) and (3), a calibration curve relating the mass of GAG to the free dye absorbance is generated:

$$m_{GAG,3} = V_s \left(\gamma \alpha_{dye} l\right)^{-1} [A]_0 - V_s \left(\gamma \alpha_{dye} l\right)^{-1} [A]_3 \tag{2.5}$$

which provides values of $V_s \left(\gamma \alpha_{dye} l\right)^{-1}$ and $[A]_0$. From the membrane samples (2) and blank membrane samples (1), the mass of GAG bound in the membrane is expressed by:

$$m_{GAG,2} = V_s \left(\gamma \alpha_{dye} l\right)^{-1} \left(\frac{V_1}{V_s}\right) [A]_1 - V_s \left(\gamma \alpha_{dye} l\right)^{-1} \left(\frac{V_2}{V_s}\right) [A]_2 \tag{2.6}$$

Using Equation (2.6), the mass of GAG bound to any membrane is determined by the absorbance of the membrane, the absorbance of a blank membrane, the constants in the calibration curve and the volumes of the gels. The dye binding to the mesh is accounted for in the absorbance of the blank and the additional volume of the membrane is accounted for in the volume ratios.

2.2.3. Method – GAG Type Selection

It should be noted that the GAG attachment method in Section 2.2.1 requires the presence of a protein residue on the reducing end of the GAG chain. However, prior work in our lab by G. Zugates has indicated that GAG purification methods used by some suppliers (eg – Seikagaku) cleave off the end of the o-serine linkage, leaving no primary amines to attach to the active sites (Zugates - *unpublished results*). From the background information on GAGs and those identified in the glomerular capillary, either heparin sulfate or chondroitin/dermatan sulfate would be representative of the charge and fiber length found in the endothelial glycocalyx. A number of GAGs are commercially available in several fractions of the six GAG types (eg- CS-A, CS-C), each derived from a variety of tissue sources. To confirm that a GAG supply can be used to generate agarose-GAG membranes, it is necessary to test that it contains a terminal primary amine. Additionally, the GAG must have sufficient charge to bind with the o-toluidine dye in the bound GAG assay.

The following sections will outline the assay method used to determine if a GAG supply contains primary amines, then summarize the results of several commercially available GAGs.

Method - Primary Amine Assay

As noted in Table 2.1, there is a category of GAG assays which rely on binding a tag molecule to the primary amine end group on the GAG molecule. Of the three methods reported, the fluorescamine assay is most attractive because of its sensitivity and simplicity. The following procedure has been adapted from several references (de Bernardo et al. 1974, Toome et al. 1974, Toome and Manhart 1975):

> ***Fluorescamine Assay:*** Prepare a 280 μg/mL solution of fluorescamine in acetone; store in a bottled protected from light. Prepare a 0.5M carbonate buffer (pH~9.25), using sodium salts. Prepare aqueous GAG solutions with concentrations of 0-0.2 nmol/mL. To a glass test tube, add 3 mL of the GAG solution and 333 μL of the carbonate buffer; mix on a Vortex mixer. Add 1 mL of fluorescamine solution; mix well. Place a sample in a 4.5 mL cuvette and measure the absorbance at 400 nm (or fluorescence at λ_{ex}=390 nm and λ_{em}=475 nm).

If a GAG supply does not contain a primary amine group, the fluorescamine will not bind and absorb/fluoresce at the given wavelength. If quantitative measurement of the concentration of primary amine groups is required, the samples can be compared to the assay of solutions with known concentrations of glycine or other amine-containing molecule.

Results – Amine Assay and Dye Assay

GAG supplies of several different GAG fractions from various suppliers were tested both for their primary amine content and their response to the o-toluidine dye assay. Suppliers included Calbiochem (La Jolla, CA)), Sigma (St. Louis, MO), MP Biomedicals (Solon, OH) and Seikagaku (Tokyo, Japan); the glycine reference standard was from Mallinkrodt (Phillipsburg, NJ). The results are summarized in Table 2.2.

Table 2.2 Results of fluorescamine primary amine assay and o-toluidine dye assay on various GAG supplies. (n/a indicates 'not assayed')

GAG Type	Supplier *[Product #]*	MW [Da]	Contains 1° Amine?	Binds o-Toluidine?
Chondroitin Sulfate - A	Calbiochem *[#230687]*	50,000	Yes	Yes
	Sigma *[#C9819]*	10-30,000	Yes	n/a
Chondroitin Sulfate – B*	Calbiochem *[#263301]*	30,000	No	n/a
	Sigma *[#C3788]*	10-30,000	No	n/a
	MP Biomedicals *[#194108]*	25,000	No	n/a
Chondroitin Sulfate – C	Calbiochem *[#2307]*	60,000	Yes	No
	Seikagaku *[#400675]*	40-80,000	No**	Yes
Heparin	Calbiochem *[#375095]*	13-15,000	Yes	Yes
Glucosamine Sulfate	Sigma *[#G7889]*	281	Yes	No
Glycine	Mallinkrodt *[#7728]*	75	Yes	n/a

* - Chondroitin Sulfate-B is also known as Dermatan Sulfate

** - From unpublished data by Zugates using the fluorescamine assay (Zugates - *unpublished results*)

As can been seen in Table 2.2, only certain GAG supplies are appropriate for attachment by the CDAP method and assay by the o-toluidine dye method. Of the chondroitin sulfates, only CS-A can be used successfully. The other CS fractions lacked either the amine or the charge to be used in membrane synthesis. Heparin could also be used as a lower molecular weight alternative. Glucosamine sulfate, one of the monomer units in GAG, was too small of a molecule to bind the o-toluidine dye. Based on these results, product availability, and similarity to glomerular GAG, CS-A obtained from Calbiochem was selected as the standard GAG. It was used in all further experiments unless otherwise specified.

2.2.4. Results – "Baseline" Synthesis of Agarose-GAG Membranes

Using the synthesis method described in Section 2.2.1, a batch of twenty gels was produced. The batch used 4 v% agarose gels, of which five were blanks. Using the o-toluidine assay from Section 2.2.2 on four of the agarose-GAG gels, this batch contained 45 ± 2 μg GAG per membrane. Normalizing the GAG content by the gel thickness and mesh volume, the gel within the membranes containd 60 ± 5 μg GAG per mg agarose fibers.

In the paper describing the CDAP activation procedure for Sepharose® 4B beads, Kohn and Wilchek reported that their agarose beads had a coupling capacity of 15 μmol ligand/g resin (based on coupling of ε-aminocaproic acid). Assuming 100% efficiency in coupling GAG, their result is equivalent to 18.8 mg GAG per mg agarose. However, it is likely that the coupling efficiency of GAG would be significantly less, given the much larger size of GAG (~50 kDa) compared to aminocaproic acid (131 Da). Also, it is well known in the literature that the active sites degrade rapidly in aqueous solution, such that many may degrade prior to placement of the membranes in the GAG attachment solution.

While a 4 v% agarose gel with 0.2 w% (~0.25 v%) GAG may not seem adequate to measure the effect of GAG on transport properties, it is also important to consider the relative lengths or surface areas of the two fiber types. Results from slender-body theory for hydraulic flow around rods indicate that it is the fiber length per gel volume, not fiber volume per volume, that is dominant factor governing hydraulic resistance (Clague and Phillips 1997). Assuming GAG fibers are approximately 1 nm per disaccharide unit (474 Da) (Wight et al. 1991), agarose has a density of 1.025 g/mL and agarose has a radius of 1.6 nm (Lazzara and Deen 2004), then the fibers are in a 2:3 length ratio of GAG to agarose.

Since agarose and GAG fibers with equal lengths are predicted by slender-body theory to be sufficient to create a significant change to the properties of agarose gels, CDAP activation is a promising method for GAG membrane synthesis. The next section will discuss modifications of the CDAP method to increase the relative GAG content of the membranes. The effect that the bound GAG has on the transport properties of the agarose membranes will be discussed in Chapters 3-5.

2.3. Synthesis Refinement

Given the potential of the CDAP activation method described in Section 2.2.1, it was desired to improve the synthesis method for binding GAG to agarose to maximize the effect of the GAG on the transport properties of the composite membrane. While several researchers have mentioned reaction conditions that may improve or detract from ligand attachment to Sepharose® beads or dextran, no systematic study has been reported (Kohn and Wilchek 1981, Lees et al. 1996). To increase the relative fraction of bound GAG, it is important to understand what factor(s) are limiting GAG binding in the current procedure. The following sections will first discuss some of the potential limiting factors for GAG binding, then present some additional assays used to characterize the synthesis reactions. The results of the synthesis studies are summarized, then developed into a conceptual model of the limiting factors in the reaction. Finally, the refined conditions for the synthesis are presented, along with the GAG binding results of this improved procedure.

2.3.1. Hypothesized Limiting Parameters

Within the GAG activation and attachment procedures, there are a number of reactions steps which could be either kinetically or transport limited. The kinetics could be limited by reagent concentrations, temperature, or reaction duration. Transport limitations could include external mass transfer, sterically-hindered diffusion, or electrostatically-hindered diffusion. Calculations have shown that none of the reaction steps are stoichiometrically limited, with reagents in 10^1-10^4x excess relative to the bound GAG content. The reaction steps include the formation of the isourea derivative, the protonation to the active cyanate ester, the aqueous wash of the activated gels, and the GAG binding in the attachment solution.

A summary of changes to reactions parameters that could potentially increase the relative bound GAG content is presented in Table 2.3. While the small molecules used during the agarose activation should have little hindrance within the gel, increasing the concentrations of the reagents may increase the activation of the agarose hydroxyl groups. Kohn and Wilchek had shown that increasing the mass of CDAP six-fold also increased their ligand binding capacity six-fold, with a similar increase reported by Less

et al. (though, unlike the proposed process, both their activation conditions may have had stoichiometric limitations) (Kohn and Wilchek 1984, Lees et al. 1996). Lees *et al.* reported that a higher pH during activation increased the binding efficiency, though Kohn and Wilchek found that higher pH also increased the rate of cyanate ester degradation (Kohn and Wilchek 1981, Lees et al. 1996). Using a different fraction of agarose may yield hydroxyl groups which are more reactive with CDAP or may form a hydrogel structure which has lower steric hindrance to GAG diffusion. For dextran and agarose substrates, it has been reported that higher substrate concentrations increase the relative amount of bound ligand (Lees et al. 1996, Porath et al. 1967).

Table 2.3 Potential synthesis parameters for increasing the relative bound GAG content in agarose-GAG membranes.

		CDAP Activation	Cyanate Protonation	Aqueous Wash	GAG Binding
Kinetic	**Reagent Concentration**	• ↑ [CDAP]	• ↑ [H^+]	• ↓ air exposure	• ↕ [GAG] • Buffer type • Buffer pH • Mesh type
	Reaction Duration/Temp.	• ↑ time	• ↕ time • ↕ temp.	• ↓ time • ↓ temp.	• ↑ time • ↕ temp.
Transport	**External Mass Transfer**				• ↑ mixing • No cassette
	Steric Hindrance	• Agarose type			• ↓ ϕ_{GAG} • ↓ gel thickness • ↓ GAG size
	Electrostatic Repulsion				• ↑ ionic strength

Increasing the duration of the activation and protonation reactions may increase the number of binding sites if the reactions have not reached equilibrium. Spectroscopy results by Kohn and Wilchek have indicated that CDAP activation occurs within 90-120 s, though work with CNBr by March *et al.* showed that ligand binding decreased when

the duration of activation was increased from 1 minute to 4 minutes (Kohn and Wilchek 1984, March et al. 1974). Since the protonation reaction and aqueous wash occur in aqueous solutions, decreasing those times or temperatures may help to reduce the degradation of the active sites to an inert carbamate group. However, it has been claimed that the cyanate esters are fairly stable in dilute acid, such that they can be stored in 0.05-0.1N HCl at 0°C for several hours without degradation (Kohn and Wilchek 1984). It is unknown if exposure of the activated gels to air will accelerate the degradation reaction.

The activation of the agarose may not be the limiting factor in binding more GAG to the agarose gels. As the coupling capacities from Kohn and Wilchek indicate, the active sites may be in a large excess compared to the amount of GAG which binds. In this case, improvements to the synthesis would need to focus on the GAG attachment step. The type and pH of the buffer has an unknown role in the binding, though the buffer salt should not contain an amine groups which competes with the GAG for the activated binding sites. Shafer *et al.* reported that increasing the pH during attachment from 5 to 9.5 increased the yield of bound amines, since primary amines (pK_a~9-10) must be depronated to react with the cyanate ester (Shafer et al. 2000). Increasing the GAG concentration in the attachment solution may increase the binding rate, as observed by Lees *et al.* for dextran-protein binding (Lees et al. 1996). However, it is possible that too high of a GAG concentration would result in a dense GAG surface layer which would hinder further diffusion of GAG into the gel interior.

Decreasing the temperature of attachment would slow the rate of active site degradation, but would also slow the diffusion of GAG into the gel. While an attachment duration of 16 hours is significantly longer that the characteristic diffusion time of GAG into the gel (approximately 2 minutes, based on the hindered diffusion of similarly sized dextrans and proteins), it is possible that the attachment reaction is very slow at low temperatures. Lees *et al*. reported that maximum bound ligand was achieved after 3 hours, with 50% binding occurring in about 20 minutes (Lees et al. 1996). The external transport of the GAG from the attachment solution to the gels may be slowed by inadequate mixing or the surrounding cassette. The transport of GAG within the gel may be hindered, with steady-state diffusion reached faster with a lower agarose fiber fraction, a smaller GAG size or a thinner gel. The transport of GAG may also be hindered by

electrostatic repulsion of the flux of GAG by the previously bound GAG at the gel surface; this effect would be diminished at higher ionic strength.

A few other methods were mentioned in the literature which could increase the binding yield. A number of attachment methods make use of a spacer molecule between the substrate and ligand, which helps to overcome steric limitations (Parikh et al. 1974). As an extensions of this idea, a branched spacer could be used to attach multiple ligands to one active site. Similarly, an intact proteoglycan could be attached instead of a single GAG molecule, since the core proteins would contain numerous GAG molecules. However, it is important to note that this would only increase diffusional or steric limitations. It may be possible to add the ligand during the activation or protonation steps, reducing the effect of active site degradation. However, this approach raises concerns over precipitation of GAG in some solvents or activation of hydroxyl groups on GAG with potential cross-linking. Finally, GAG could be bound to ungelled agarose in solution; however, it has been shown that the presence of sugars changes the structure of agarose during gelation (Key and Sellen 1982). These methods were not explored, since the current method yielded adequate bound GAG content.

2.3.2. Methods

The effects of the previously described process parameters can be tested by modifying conditions under which the synthesis reactions are run and assaying the GAG content of the resulting agarose-GAG membranes. However, two additional procedures are available to help gain insight into the intermediate steps of the synthesis process. In the following section, an assay is described for measuring the concentration of activated cyanate esters. Another method is presented for taking cross-sections of the agarose-GAG gels and staining the GAG to provide a visual indication of the distribution of GAG across the gel thickness.

Active Site Assay

The assay for active cyanate esters is based on the method used by Kohn and Wilchek (Kohn and Wilchek 1981). The membrane samples are removed at any point in the

activation or attachment process, briefly washed in DI water to remove any excess reagents, then assayed by the following procedure:

> ***Active Site Assay:*** Prepare a solution of 9 mL cold distilled pyridine, 1 mL DI water and 100 mg N,N' dimethylbarbituric acid (scale volumes as needed). Add 3 mL of the dimethylbarbituric acid solution to 1 activated agarose gel in a 5-20 mL closed test tube. Warm to 40°C in a heating block for 25 minutes with periodic, vigorous mixing. The presence of active cyanate esters should cause the solution to become purple. Remove a 1 mL sample from the test tube, and dilute in 19 mL of water. Measure the absorbance at 588 nm and calculate the active site concentration with an absorbance coefficient of 137,000 L mol^{-1} cm^{-1} in Beer's Law (Equation (2.1)).

Knowing the initial volume of the gel, the assay can be converted from a concentration of active sites in solution to a concentration per mass of agarose fibers. It was confirmed that an unreacted agarose membrane gave a zero reading for this assay.

Cryosectioning

A routine procedure in histology is the removal of thin slices of a tissue for staining of particular molecules. While such sectioning traditionally involves paraffin mounting, another method known as cryosectioning cuts micron-thick sections from a frozen sample. The sample is first placed in O.C.T. media (Tissue-Tek®; Sakura Finetek, Torrance, CA) overnight to exchange out the water and prevent freeze-fracture. The sample is then frozen at -20°C. The Histology Lab in MIT's Division of Comparative Medicine performed the cryosectioning, cutting sections 5 μm thick. Cryosections were successfully taken from gels of various thicknesses and from gels with and without the support mesh. It was possible to take cryosections of samples frozen in 0.1 M KCl-phosphate buffer, though upon thawing, the samples were highly fractured while maintaining their macroscopic shape.

Once the membrane cross-sections were cut, they were mounted to a glass slide and stained. Xylene-based and water-based mountants were tried by the Histology Lab, followed by published procedure for toluidine blue staining and fixation of mucins (Sheehan and Hrapchak 1980). A related method was consulted, which used a slightly different toluidine blue staining and fixing procedure for electrophoresis of GAG through

agarose (Jaques 1977). However, the resulting gels appeared to experience shrinkage during the processes, causing the gel ends curl and make the stain color appear darker. Instead, a "wet staining" procedure was developed for the agarose-GAG cross-sections, where the thawed PBS cross-sections were exposed to several drops of a 500 μg/mL solution of o-toluidine dye in 0.01 N HCl for 30 minutes. The excess dye was pipetted away, then rapidly rinsed (~5 seconds) with DI water. The excess water was blotted away from the slide surrounding the gel, so that the dye would not diffuse away from the stained GAG areas. Using this method (which doesn't require mounting, fixation or dehydration), the bound GAG in the gels was visualized without significant distortion of the gel. The dye stained the bound GAG purple, but areas without bound GAG remained transparent.

2.3.3. Results

Using the previously described assays for bound GAG and activated binding sites, the potential limiting factors in the agarose-GAG membrane synthesis were investigated. The following section presents these results, beginning with the total bound GAG content of the membranes. Then, the effects of several process parameters on the active site content are reported. Finally, cryosections of several gels are shown.

Binding Assay

Given that the GAG binding capacity in the agarose-GAG membranes was significantly lower than the aminocaproic acid binding capacity reported by Kohn and Wilchek for their Sepharose® beads, the process parameters affecting GAG attachment to the activated membranes were first considered. The parameters were varied from the "baseline" process described in Section 2.2.1 except that the baseline gel composition was now 3 v% agarose.

Figure 2.5 shows the effects of various process parameters on the relative bound GAG content of membranes. These are parameters which might affect the binding kinetics. It is seen that there is relative consistency in the attachment process, since three sub-batches which were activated together and attached separately all yielded comparable GAG content. Therefore, any differences between samples are likely due to the changes

in the process parameters and not sample-to-sample variation. Both the temperature and pH of the attachment solution had no significant impact on the bound GAG content within the range considered (0-4°C and pH=8.4-9.0). The type of salt used in the attachment solution did have a strong effect on the bound GAG content, though no salt was found to be more effective than the $NaHCO_3$ in the baseline process. The concentration of GAG in the attachment solution appeared to have some significant effect, though primarily at the lowest concentration of 0.2 g/L; there was minimal increase in bound GAG content above the baseline concentration of 1 g/L. Finally, it was seen that most of the GAG binds with the active sites within the first 30 minutes, so that leaving the gels in the attachment solution overnight (>16 hours) is more than adequate for the attachment reaction to be completed.

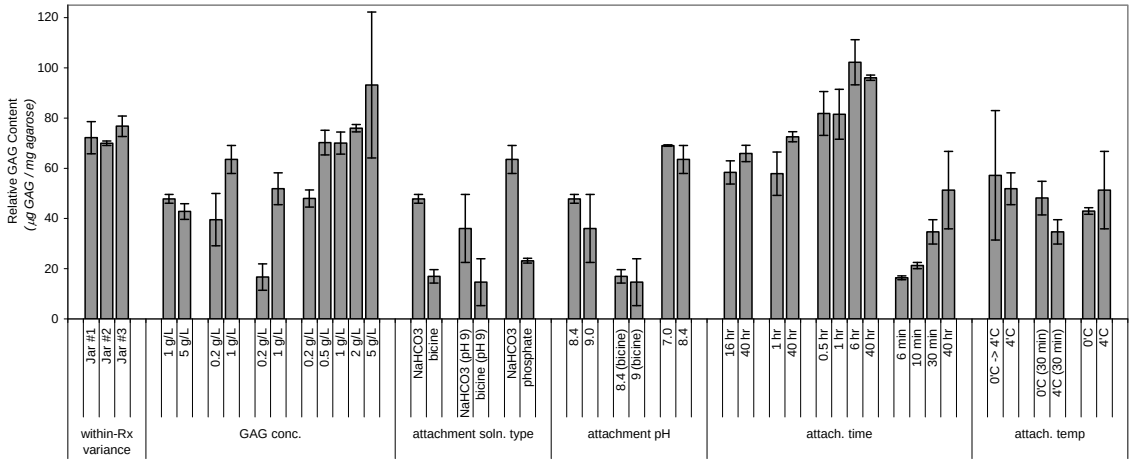

Figure 2.5 Relative bound GAG content of agarose-GAG gels in response to changes in GAG binding process parameters thought to affect the binding kinetics. Error bars represent one standard deviation of n=2-4.

Parameters thought to affect the transport of GAG molecules during GAG attachment were also studied (Figure 2.6). Changes in mixing speed and the use of a plastic cassette to support the gel had no significant effect on the bound GAG content, suggesting that external GAG transport is not limited. While the use of smaller heparin (15 kDa) instead of chondroitin sulfate A (50 kDa) yielded gels with the same GAG content by mass, this actually shows a three-fold increase in the molar bound GAG content. This confirms that there is significant steric hindrance to attachment of GAG molecules within the gel, as

first hypothesized by the higher molar binding yield of Kohn and Wilchek with a small (131 Da) ligand. The slight increase in relative GAG content for gels with a lower agarose concentration also supports the importance of steric hindrance in GAG binding. However, in the range of gels considered (2-4 v%), the change in relative bound GAG content was minor.

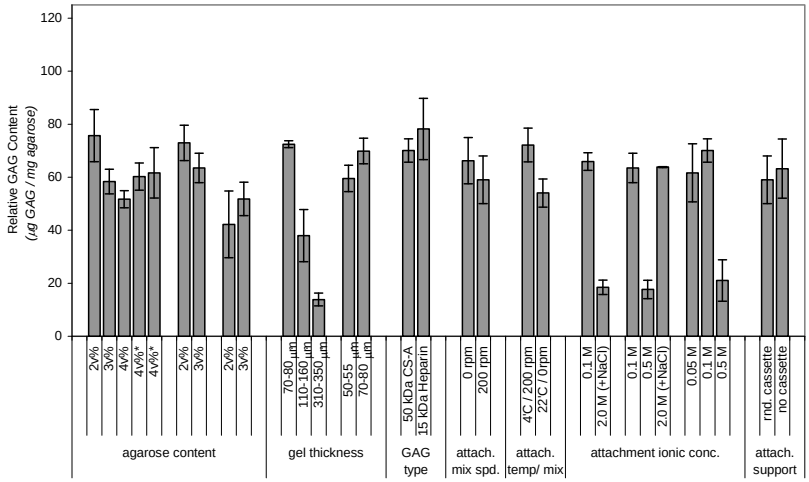

Figure 2.6 Relative bound GAG content of agarose-GAG gels in response to changes in GAG binding process parameters thought to affect GAG transport. Error bars represent one standard deviation of n=2-4. Two samples indicated by '*' used a 2 minute activation after TEA instead of the baseline 5 minutes.

Also in Figure 2.6, the effect of ionic strength on GAG binding (whether by increasing the buffer salt concentration or adding NaCl) had an unclear affect on the bound GAG content. However, since a higher ionic strength resulted in membranes with GAG equal or less than the baseline, it is not likely that electrostatic repulsion of the GAG is limiting binding. Finally, the thickness of the membranes greater than the baseline (70-80 μm) did have a significant impact on the relative GAG content. Based on the previous data on the kinetic rate of binding, even the thickest (310-350 μm) membranes had excess time for diffusion and binding to occur. This implies that some other process may be preventing the homogeneous binding of GAG throughout gels of all thicknesses, such as the formation of a dense GAG surface layer on the membrane or competition of another kinetic rate (e.g. – active site degradation) with the binding reaction. The degradation profile of active sites will be presented in the next section.

While several influential process parameters in the studies of the attachment step were found to cause attachment decreases (salt type, GAG type, GAG concentration, gel thickness), none of these observations led to process changes which could *increase* the relative bound GAG content. Given the limited ability to improve the GAG content during attachment, process parameters were investigated to increase the concentration of active sites generated. As seen in Figure 2.7, there is some variation in the bound GAG content of membranes generated by the "baseline" process conditions. In general, the baseline process conditions with 3 v% agarose yield gels with 60-70 μg GAG/g agarose. Upon investigation of the low outliers from this range, two of the low results occurred when the HCl and aqueous water washes were not allowed adequate time to fully cool from room temperature to 4°C. (This effect is discussed further later in this section.) The agarose fraction used in the gels, the material of the support mesh, and the duration of the activation reaction had no significant effect on the bound GAG content. Increasing and decreasing the CDAP concentration by a factor of two had a slight impact on the bound GAG content, though it was far from the linear relation between CDAP concentration and ligand binding capacity found by Kohn and Wilchek (Kohn and Wilchek 1984). However, the activation process used here for membranes requires a greater volume of all reagents than used by Kohn and Wilchek (0.015 g CDAP/g gel versus 5.7 g CDAP/g gel), suggesting that their binding capacity increase was due to stoichiometric limitations of CDAP while this process has stoichiometric excess.

Process parameters from the protonation of the active sites and the subsequent aqueous wash of reagents out of the membranes were also studied (Figure 2.8). Instead of shifting the reaction equilibrium towards the cyanate ester, increasing the acid concentration during protonation instead resulting in membranes with lower bound GAG content. Decreasing the duration of the protonation reaction to 10 minutes also caused membranes with lower bound GAG content. Based on the previous observation that two of the low outliers of the baseline samples corresponded to syntheses with incompletely cooled water, the affects of wash temperature and duration were measured. While use of partially cooled water (>4°C) had resulted in lowered bound GAG content (48-52 μg GAG/g agarose versus a mean baseline of 68 μg/g), using a well-stirred mixture of ice and water at 0°C resulted in a significantly elevated bound GAG content (105 μg/g).

Similarly, reducing the duration of the aqueous washes also increased the bound GAG content (108-110 µg/g). However, the effects of lower wash temperature and shorter duration were not additive, with the increase from the combined change equal to the increase from a single parameter change. Finally, it was confirmed that exposure of the activated membranes to air did not decrease their GAG binding capacity.

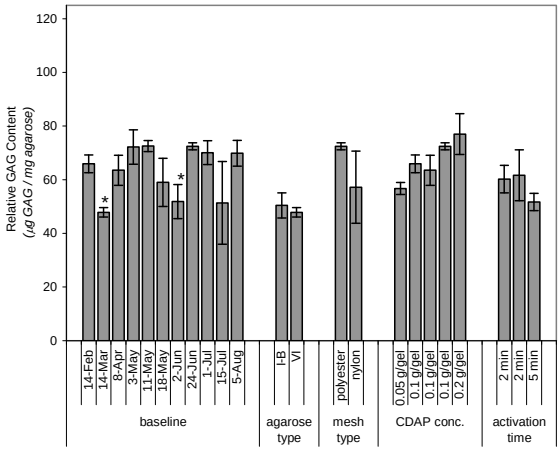

Figure 2.7 Relative bound GAG content of agarose-GAG gels in response to changes in CDAP activation process parameters. Error bars represent one standard deviation of n=2-4. Two baseline samples indicated by '*' used aqueous wash water that was not fully cooled to 4°C.

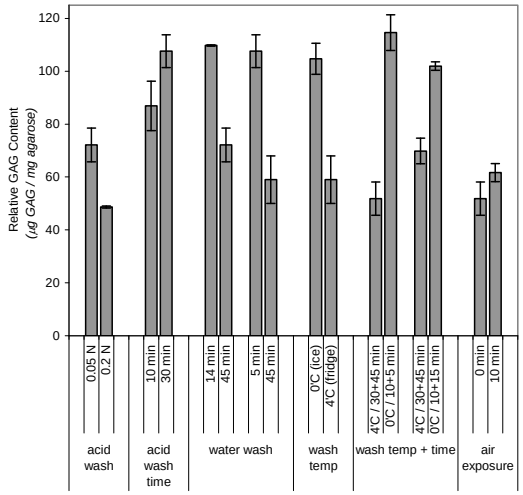

Figure 2.8 Relative bound GAG content of agarose-GAG gels in response to changes in cyanate protonation and aqueous wash process parameters. Error bars represent one standard deviation of n=2-4.

In summary, the results from the bound GAG assays show that the only process parameters with the potential to significantly increase the bound GAG content of the membranes are the temperature and duration of the aqueous wash preceding GAG attachment. The results also indicate the importance of several process parameters in the baseline synthesis procedure which, if changed, could significantly decrease the membranes' bound GAG content: protonation acid concentration, membrane thickness, attachment solution salt type and concentration, GAG concentration and duration of attachment.

Active Site Assay

Based on the apparent importance of active site concentration and rate of degradation to the final bound GAG content of the membranes, the dimethylbarbituric acid assay for active cyanate esters was used to study these properties. Since the temperature and duration of the aqueous wash was found to strongly affect the final bound GAG content, the active sites were assayed to determine their response to these process parameters.

First, the effect of process duration was considered by measuring the active site content of gels during protonation, aqueous wash and GAG attachment at 4°C. As shown in Figure 2.9, the membranes contained over 2000 nmol sites/mg agarose shortly after activation, but contained only two-thirds as many at the beginning of attachment. The degradation of active sites continues in the attachment solution. In a separate experiment, 105±20 nmol sites/mg agarose remained in the membranes after 45 hours in a bath of blank attachment solution (0.1 M $NaHCO_3$). The current data is unable to conclusively show if the rate of degradation during protonation is slower, though it is possible that the acidic conditions during protonation make the degradation into inert carbamate groups less favorable, as shown by Kohn and Wilchek for CNBr-activated gels (Kohn and Wilchek 1981).

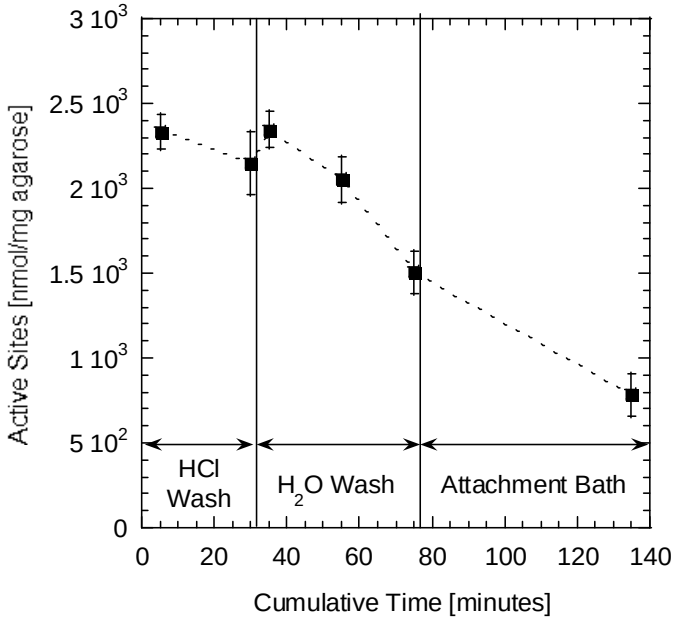

Figure 2.9 Active cyanate ester site degradation during post-activation process steps at 4°C. Error bars are one standard deviation for n=2.

Comparing the active site content of the membranes to the bound GAG content of the resulting membranes shows that only a small number of the actives sites bind with GAG. Further comparisons of stoichiometry confirm that only one in ten hydroxyl groups in agarose become activated, despite the large excess of CDAP in the system (Table 2.4). The active site content is reasonably similar to that reported by Kohn and Wilchek, given the differences in the activation process and assuming that the coupling efficiency of aminocaproic acid will be less than 100% (Kohn and Wilchek 1984).

Table 2.4 Potential binding sites, as determined by active sites, bound GAG, and reagent stoichiometry.

Source	**Binding Sites** *[nmol/mg agarose]*
Published Ligand Binding (Kohn and Wilchek 1984) *(15 µmol/g gel)*	366
Active Sites Prior to Attachment	1,500
Average GAG Binding *(68 µg GAG/mg agarose)*	1.4
Stoichiometry – Agarose *(4 –OH groups per 306 Da repeat unit)*	13,100
Stoichiometry – CDAP *(0.1 g per 3 v% membrane)*	724,000

Next, the effect of temperature on the degradation of active sites was considered. Since the use of 0°C water instead of 4°C water resulted in a 50% increase in the bound GAG content, the kinetics of degradation at these two temperatures were studied. A batch of gels was activated, then split into two groups which were either processed in 4°C (refrigerated) solutions or 0°C (well-mixed ice) solutions. As seen in Figure 2.10, the active sites degraded three times faster in the 4°C solutions than the 0°C solutions. Assuming a first-order rate of decay, the rates of decay in the blank attachment solution were 0.24 hr^{-1} (4°C) and 0.08 hr^{-1} (0°C). These rates of decay should be applicable to agarose activated by any cyanogen method, not just CDAP, since all methods result in active cyanate esters which may degrade into an inert carbamate.

Given the ~10^3-fold excess of active binding sites relative to bound GAG, it appears that the binding of GAG should be independent of any process changes affecting active site concentration. However, the mutual increase of active sites and bound GAG at lower process temperatures suggests that the two properties are not independent. To understand these conflicting observations, it must be considered that not all active sites may be available for reaction, such that the concentration of active sites is stoichiometrically limiting. This idea will be discussed further in the context of other observations.

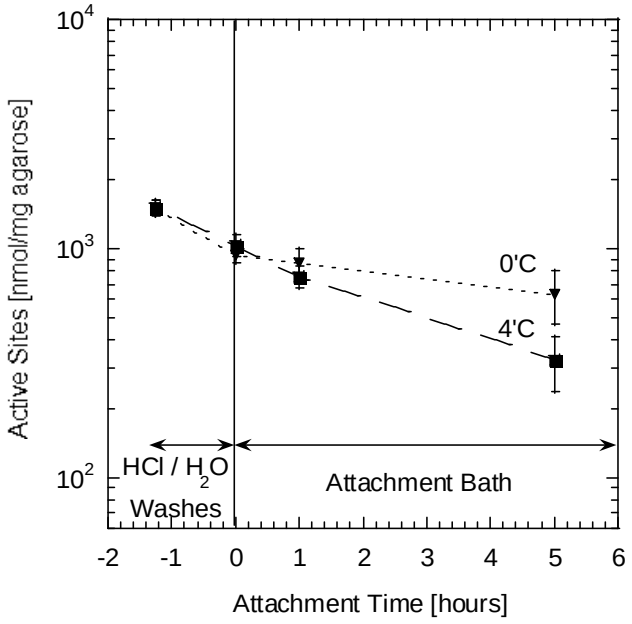

Figure 2.10 Active cyanate ester site degradation at 0°C and 4°C. Error bars are one standard deviation for n=2; all samples were activated in the same batch and treated identically until attachment.

Cryosectioning

Cryosectioning was performed on gels to visually confirm if the GAG attached throughout the gel thickness. Based on the bound GAG content of gels of different thicknesses in Figure 2.6, the average GAG content decreased for membranes thicker than 70 μm. This indicates the bound GAG was not uniform throughout the thickness. However, the bound GAG content of 50 μm and 70 μm-thick gels were statistically indistinguishable, which suggests that GAG heterogeneity may only be present in the larger gels. Cryosections were used to study this problem in two ways. First, the GAG in an average 70 μm-thick gel was stained to determine if the GAG was distributed evenly throughout the gel. Second, a "semi-infinite" agarose membrane was bound with GAG to determine the penetration depth of GAG binding. While toluidine staining may not be appropriate for quantitative histology due to it's non-linear staining at very low GAG concentrations, it is appropriate for indicating where there is a large gradient in the bound GAG content of a gel.

As shown in Figure 2.11, toluidine staining of GAG in a standard 70 μm membrane resulted in a uniform purple color throughout the gel. This confirms that the GAG is not binding purely at the membrane surface and is evenly distributed throughout the thickness. Figure 2.12 shows the staining of a "semi-infinite" 3 mm agarose-GAG gel generated under high-attachment conditions (0°C wash solutions; 10 minute protonation; three 2-minute aqueous washes). The GAG is stained purple along the gel edges but the dye washed away from the gel interior. This confirms that, similar to the toluidine assay in Section 2.2.2, there is no significant binding of the dye to agarose without GAG. The apparent penetration depth of bound GAG is approximately 50-70 μm, based on estimates of the visible color in Figure 2.12 and other similar images.

The penetration depth on the same order as an average membrane thickness supports several observations in the process parameter studies. First, it confirms that GAG is hindered from binding to the core of the membranes for the thicker gels, resulting in a lower average bound GAG content as seen in Figure 2.6. However, this hindrance does not affect average and thinner gels (≤100~140 μm).

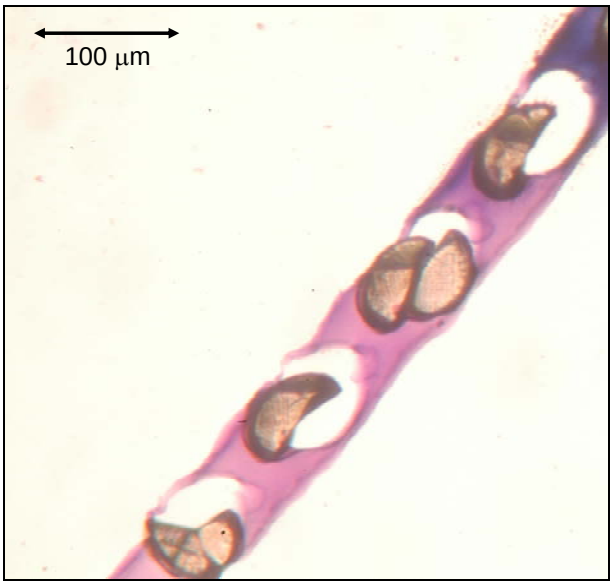

Figure 2.11 Cross-section of an agarose-GAG membrane after toluidine staining of GAG (purple). The holes and oblong objects (brown) are due to the polyester support mesh. The membrane thickness, as determined prior to and after cryosectioning, is 70 μm. The bound GAG content, as determined from other gels from the same batch, was 77±4 μg GAG/mg agarose.

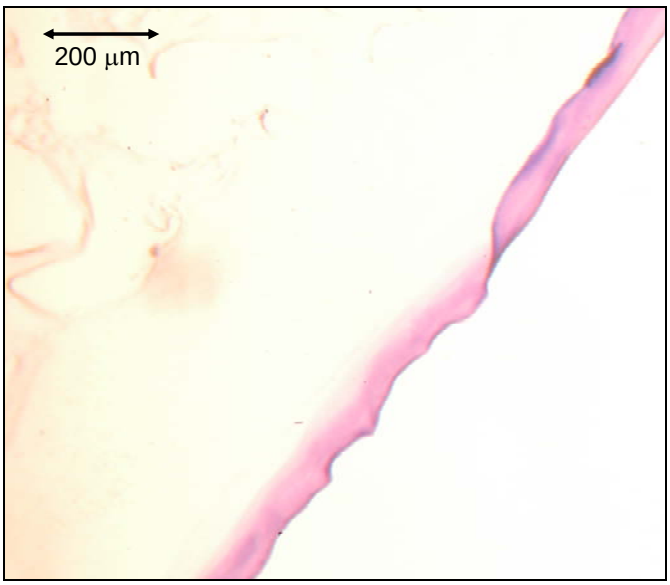

Figure 2.12 Cross-section of agarose-GAG gel after toluidine staining of GAG. The gel was approximately 3 mm thick without a supporting mesh. The bound GAG along the edge of the gel is stained purple, while the toluidine dye washed away from the core of the gel (on the left). The penetration depth of the bound GAG is approximately 70 μm.

2.3.4. Discussion

Based on the results from the bound GAG assays, active site assays and cryosections of the agarose-GAG membranes, a number of process parameters were identified as being important to the GAG-binding process. First, it was observed from the bound GAG assays that the two process parameters which could significantly increase the bound GAG content were the temperature and duration of the aqueous wash preceding attachment. Since these parameters only affect the concentration of active sites, and not the binding of the GAG, they were studied further with the active site assay. This assay confirmed that the degradation rate of $0.24\ hr^{-1}$ at 4°C would reduce the active site content by 20% during the aqueous washes. By shortening the duration of the washes to 15 minutes, only 6% of the active sites would be degraded. The data also showed that the degradation rate of $0.08\ hr^{-1}$ at 0°C would also reduce the active site content by only 6% during the 45 minutes of washes. However, the combination of reducing both the time and temperature should have minimal improvement over reducing time alone, with a predicted decrease of active sites prior to coupling of only 2%. This prediction was confirmed experimentally, since the shortened time and lower temperature increased the bound GAG content from 68 ± 8 μg GAG/mg agarose to 110 ± 1 and 105 ± 6 μg GAG/mg agarose, respectively, but no further increase was measured for the combined effects 0°C and 15 minutes wash time (102 ± 2 μg GAG/mg agarose). (Figure 2.8).

However, the active site assays also showed that there is a 1,000-fold excess of active sites formed relative to the moles of GAG that bind to the membranes. This conflicts with the previous observation that process parameters which increase the active site content also increase the bound GAG content. These observations can be resolved if only a small fraction of the active sites are available for binding. Based on the homogeneous distribution of GAG in the membrane in Figure 2.11, the GAG can access the entire membrane volume and is not limited to the surface active sites. However, agarose is known to form a complex gel structure where two molecules intertwine to form a double helix and multiple (10^1-10^4) helices group together to form each fiber (Attwood et al. 1988, Djabourov et al. 1989, Ratajska-Gadomska and Gadomski 2004, Waki and Harvey 1982). During gelation, the fibers are further intertwined in junction zones that give mechanical stability to the gel network. While 1 in 10 of the hydroxyl groups on agarose

are activated, it is likely that a large fraction of these active sites are sterically inaccessible to the large GAG molecules (50 kDa), thus explaining the 0.1% binding yield. More active sites are sterically accessible to smaller molecules, in agreement with the higher molar binding yields found here for heparin (15 kDa; 0.4% binding yield) and observed by Kohn and Wilchek for aminocaproic acid (131 Da; 24% binding yield) (Kohn and Wilchek 1984).

The second major observation in GAG binding is that both the bound GAG assays and the cryosections showed that GAG is hindered from binding to the core of thick membranes. Possible limitations of binding in the core are the process time, binding kinetics or active site degradation kinetics relative to the diffusion time. The characteristic diffusion time for transient diffusion of GAG (50 kDa) into a slab of thickness δ is

$$\tau_D = \frac{1}{\pi^2}\frac{\delta^2}{D_G} \tag{2.7}$$

which can be estimated from the hindered diffusion of 20-500 kDa proteins and sugars in agarose (D_i~1-8x10^{-7} cm^2/s) (Deen 1998, Key and Sellen 1982, Kosto and Deen 2004). Since the attachment process time (16-40 hours) greatly exceeds that for diffusion of GAG into the core of a 300 μm membrane (~5 minutes), the transport of GAG into the membrane core must instead be competing with the kinetics of the active sites.

The rate of active site degradation (0.24 hr^{-1}) gives a characteristic time of 4 hours at 4°C, indicating that this rate is not the limiting factor relative to the diffusion time. It was shown in Figure 2.5 that the majority of GAG binding occurs within the first 30 minutes, which indicates that the rate of the binding reaction is comparable or somewhat slower than the rate of diffusion of the GAG. When diffusion and first order reaction occur simultaneously, the characteristic time scale can be shown to be:

$$\tau_D = \left(\pi^2 \frac{D_G}{\delta^2} + k_{rxn}\right)^{-1} \tag{2.8}$$

where k_{rxn} is the first order reaction rate constant. Assuming first order binding of GAG with a rate constant of 0.2 min^{-1}, the characteristic time for unbound GAG to reach its steady-state profile is decreased to 2.5 minutes.

However, the reaction is not actually first order, but instead second order with the active sites. The active sites are degrading over time, as well as being stoichiometrically limited due to the previously discussed steric limitations. The result is a complicated system where unbound GAG penetrates into the membrane as active sites become depleted at the edges. The movement of the binding front towards the membrane core slows as the active sites decay, linking the bound GAG content to all three rates (diffusion, binding and degradation). While it is still possible to model these competing effects, the solution can no longer be derived analytically and instead requires numerical methods.

2.3.5. Modeling

Model Development

As just discussed, it is proposed that the rates of GAG diffusion, GAG-active site binding and active site degradation are all involved in determining the bound GAG content of a membrane. The following section outlines the equations which govern the model, the finite difference solution method and a comparison of the model results to the experimental data.

The model contains the concentrations of three species: unbound GAG, bound GAG and active sites. Unbound GAG is subject to both diffusion and second-order reaction with active sites. The corresponding transient conservation equation for the concentration of unbound GAG (c_G) is:

$$\frac{\partial c_G}{\partial t} = \frac{\partial}{\partial x}\left(D_G \frac{\partial c_G}{\partial x} \right) - k_1 c_G \phi_A c_A \tag{2.9}$$

where D_G is the diffusivity of GAG in agarose, k_1 is the second-order binding rate constant, c_A is the concentration of active sites and ϕ_A is the fraction of active sites sterically accessible for binding. The concentration of active sites on the agarose is decreased by both degradation and binding with GAG:

$$\frac{\partial \left(\phi_A c_A \right)}{\partial t} = -k_1 c_G \phi_A c_A - k_2 \phi_A c_A \tag{2.10}$$

where k_2 is the rate of active site degradation. It is assumed that sterically accessible and

inaccessible sites degrade at the same rate. The bound GAG content of the gel (c_b) is given by:

$$\frac{\partial c_B}{\partial t} = k_1 c_G \phi_A c_A \tag{2.11}$$

The concentrations are subject to the initial conditions of no unbound or bound GAG at t=0 and a known initial active site concentration $c_{A,init}$. The unbound GAG concentrations are subject to a symmetry boundary condition at the centerline of the gel and a concentration equal to the bulk solution concentration of GAG ($c_{G,0}$) at the gel edge times the partition coefficient (Φ_G).

The equations can be recast in dimensionless form, as summarized in Table 2.5. The resulting equations contain three dimensionless groups: two Damköhler groups relating the rate of diffusion to the rates of binding (Da_1) and degradation (Da_2) and one group (γ_G) for the ratio of the maximum unbound GAG concentration to maximum active site concentration.

The bound GAG will create additional steric and electrostatic hindrances for the free GAG, which may decrease the values of D_G, Φ_G, and/or k_1 (or, alternately, $k_1\phi_a$). While some models are available to give a relation between the gel fiber content and hindrance to partitioning (such as (Lazzara et al. 2000)) or diffusion (see examples in (Gutenwik et al. 2004)), these relations tend to be developed for a single-fiber or neutral system. Since the exact functional relationship between each of these properties and the bound GAG content is complex for a charged multi-fiber gel, no correlations are available for relating the bound fiber properties to the kinetic and transport properties. However, the effects can be approximated to first order by single-parameter linear or exponential functions to capture the general trends, as given in Table 2.5. As suggested by a model for partitioning in neutral fibers, the decrease in Φ_G takes an exponential form (Lazzara et al. 2000). Diffusivity through neutral polymer gels is also often modeled in an exponential form (though there is variation in the literature about whether the fiber concentration is to the ½ or 1st power) (Masaro and Zhu 1999). For lack of a model to describe the effect of hindrances on the kinetic rate constant, the form was assumed to be approximately linear over the range of interest.

Table 2.5 Dimensionless equations governing the GAG diffusion, binding and active site degradation in agarose-GAG gels.

Dimensionless Variables & Groups

Independent Variables:

$$X = \frac{x}{\left(\delta/2\right)} \qquad \tau = \frac{tD_G(0)}{\left(\delta/2\right)^2}$$

Dependent Variables:

$$\theta_G(X,\tau) = \frac{c_G(x,t)}{\Phi_G(0)c_{G,0}} \qquad \theta_A(X,\tau) = \frac{\phi_A c_A(x,t)}{\phi_A c_{A,init}} \qquad \theta_B(X,\tau) = \frac{c_B(x,t)}{\phi_A c_{A,init}}$$

Dimensionless Groups:

$$Da_1 = \frac{k_1(0)\phi_A c_{A,init}\delta^2}{4D_G(0)} \qquad Da_2 = \frac{k_2\delta^2}{4D_G(0)} \qquad \gamma_G = \frac{\Phi_G(0)c_{G,0}}{\phi_A c_{A,init}}$$

Equations

Unbound GAG:

$$\frac{\partial\theta_G}{\partial\tau} = \frac{\partial f_D}{\partial\theta_B}\frac{\partial\theta_B}{\partial X}\frac{\partial\theta_G}{\partial X} + f_D(\theta_B)\frac{\partial^2\theta_G}{\partial X^2} - Da_1 f_k(\theta_B)\theta_G\theta_A$$

Active Sites:

$$\frac{\partial\theta_A}{\partial\tau} = -Da_1\gamma_G f_k(\theta_B)\theta_G\theta_A - Da_2\theta_A$$

Bound GAG:

$$\frac{\partial\theta_B}{\partial\tau} = Da_1\gamma_G f_k(\theta_B)\theta_G\theta_A$$

Initial & Boundary Conditions

Initial Conditions:

$$\theta_G(\tau=0,X)=0 \qquad \theta_A(\tau=0,X)=1 \qquad \theta_B(\tau=0,X)=0$$

Boundary Conditions:

$$\theta_G(\tau,X=1) = f_\Phi(\Theta_B(\tau,1)) \qquad \frac{\partial\theta_G}{\partial X}(\tau,X=0)=0$$

Bound GAG-Dependent Parameters

Diffusivity:

$$f_D(\Theta_B) = \frac{D_G(\Theta_B)}{D_G(0)} = \exp[-m_D\Theta_B]$$

Partition Coefficient:

$$f_\Phi(\Theta_B) = \frac{D_\Phi(\Theta_B)}{D_\Phi(0)} = \exp[-m_\Phi\Theta_B]$$

Binding Rate Constant:

$$f_k(\Theta_B) = \frac{D_k(\Theta_B)}{D_k(0)} = 1 - m_k\Theta_B$$

The equations were solved by the method of finite differences. The first- and second-order spatial derivatives were linearized using the central difference approximation, and the boundary conditions were incorporated into the equations for the boundary points. The resulting series of non-linear initial value problems was solved using a stiff ODE solver ('*ode23s*') in MATLAB®.

The values of the dimensionless groups and the parameters used to redimensionalize the variables were collected from several sources. The concentration of GAG in bulk solution ($c_{G,0}$) is known for each experiment and the gel thickness (δ) is measured directly with a micrometer. The initial concentration of active sites ($c_{A,init}$) and the rate of active site degradation (k_2) are known from the dimethylbarbituric acid assay described in Section 2.3.2. The diffusivity of GAG within the agarose gel ($D_G(0)$) can be approximated by the hindered diffusivity of other macromolecules in agarose (dextran, Ficolls, and proteins) and adjusted for temperature by the Stokes-Einstein relation. However, most of these macromolecules are spherical or globular, and the conformation of GAG molecules is unknown. The hydrodynamic radii of heparin and dermatan sulfate fractions in solution are almost twice as large as the radii of spherical Ficolls or proteins of similar molecular weight, suggesting that the diffusivity may be lower (Bertini et al. 2005, Johnson et al. 1996, Lebrun and Junter 1993). The fraction of active sites sterically available for binding (ϕ_A) can be estimated by the molar concentration of bound GAG at long times in thin gels relative to the initial active site concentration; note this will somewhat underestimate ϕ_A, since it neglects degradation. Finally, the rate of GAG binding ($k_1(0)$) can be approximated by the amount of GAG bound at moderately short times, when the concentration of active sites is approximately constant at $c_{A,init}$ and the bound GAG content is low. This assumption will underestimate the rate constant, since the concentration of active sites will actually be decreasing from both binding and degradation. The estimated values and ranges of these parameters are summarized in Table 2.6; additional detail is available in the appendix in Table A.6.

Table 2.6 Parameter estimates for baseline values in the diffusion-reaction model of GAG binding.

Parameter	**Value**
$c_{G,0}$	$2\text{x}10^{-8}$ mol/mL
$c_{A,init}$	$4\text{x}10^{-5}$ mol/mL
δ	$7\text{x}10^{-3}$ cm
$D_G(0)$	$10^{-7} - 10^{-8}$ cm^2/s
Φ_G	1
ϕ_A	$1.2\text{x}10^{-3}$
$k_1(0)$	$4\text{x}10^{4}$ mL/mol/s
k_2	$5\text{x}10^{-5}$ s^{-1}
Group	**Value**
Da_1	0.2-2
Da_2	0.006-0.06
γ_G	0.4
$\tau_D = \frac{\left(\delta/2\right)^2}{D_G(0)}$	2-20 minutes

Generalized Scaling Analysis

Some insight into the physical processes can be gained without solving the three coupled model equations. The bound GAG content can be increased by either increasing the number of available active sites ($\phi_A c_{A,init}$) or the binding yield of the active sites (defined as the moles of bound GAG per mole of available active sites, or Θ_B). The experimental results in Section 2.3.3 showed how $c_{A,init}$ could be increased by changing the temperature or duration of the aqueous wash prior to attachment. The binding yield, Θ_B, is increased when the consumption of active sites by GAG binding occurs more rapidly than consumption by degradation. As seen in the active site conservation equation in Table 2.5, this occurs when:

$$\frac{Da_1\gamma_G}{Da_2} = \frac{k_1\Phi_G c_{G,0}}{k_2} \gg 1 \tag{2.12}$$

Using the parameters in Table A.6 with $D_G(0) = 10^{-8}$ cm^2/s, $Da_1\gamma_G/Da_2$ is equal to 16. Since this value satisfies Equation (2.12), no further improvement in the bound GAG content can be expected from the binding yield; instead, further improvement can only be expected from increases in $\phi_A c_{A,init}$. However, when the GAG concentration in the coupling solution was decreased to 0.2 g/L ($0.4 \text{ x } 10^{-8}$ mol/mL), then the ratio $Da_1\gamma_G/Da_2$ is equal to 3. Since the value no longer satisfies Equation (2.12), we expect

there to be a decrease in the binding yield and in the bound GAG content. Increasing the concentration to 5 g/L satisfies Equation (2.12) equally well as 1 g/L, so we do not expect any increase in the binding yield or bound GAG content. Both of these predictions are supported by the experimental results for increased and decreased GAG concentration in the coupling solution (Figure 2.5).

A similar scaling analysis can be done for the spatial homogeneity of the bound GAG concentration. Since diffusion of unbound GAG is the only physical process which affects spatial uniformity, the unbound and bound GAG concentrations will be nearly uniform when diffusion occurs more rapidly than degradation of active sites. The diffusional time scale was used to scale τ in all three equations, so the degradation of active sites can be neglected from the system of equations when:

$$Da_2 = \frac{k_2 \delta^2}{4 D_G(0)} \ll 1 \tag{2.13}$$

Spatial uniformity also requires that the process time be larger than the diffusional time scale, such that coupling is allowed to occur for a time $\tau_{coupling}$ that satisfies:

$$\tau_{coupling} >> \frac{\delta^2}{4 D_G(0)} \tag{2.14}$$

For the baseline parameters in Table A.6 with a GAG diffusivity of 10^{-8} cm/s^2, Da_2 is equal to 0.06 and the diffusional time scale is 20 minutes. Therefore, it was expected that the experimental data would show a uniform bound GAG content in the cross section of a 70 μm membrane (Figure 2.11) and that the bound GAG contents at times less than 30 minutes were lower than the final bound GAG contents (Figure 2.5). It can be expected that the penetration depth into a semi-infinite membrane would occur at a depth $\delta/2$ which causes Da_2 to be equal to one. Using the same parameters, this predicts a penetration depth of 140 μm, which is comparable to the experimental observation of 50-70 μm.

Model Results with Constant Parameters

The reaction-diffusion model for GAG binding was applied to several cases for which there was corresponding experimental data. These include the effects of gel thickness, GAG solution concentration and attachment time on the bound GAG content of the gels,

as well as the penetration depth of bound GAG in gels with "semi-infinite" thickness. The model was first applied with constant parameters (i.e. – all m_i=0) and for a range of GAG diffusivities equal or less than the baseline value of 10^{-7} cm^2/s. The model provides insight into the homogeneity of GAG binding within the agarose-GAG gels and supports the apparent homogeneity in the gel cryosections in Figure 2.11. The model can also be used to determine which process parameters should be modified to synthesize agarose-GAG gels with a "tunable" GAG content.

Experiments were performed with GAG concentrations of 0.2-5 g/L GAG in the attachment solution. As seen in Figure 2.13, the model is in good agreement with the experimental data for GAG diffusivities of 10^{-7}-10^{-8} cm^2/s. The bound GAG content decreases at low GAG concentrations. However, at concentrations above ~1 g/L GAG, the bound GAG content becomes relatively insensitive to the bulk solution GAG concentration. This supports that further increases in the concentration of the attachment solution are not a viable method of increasing the bound GAG content.

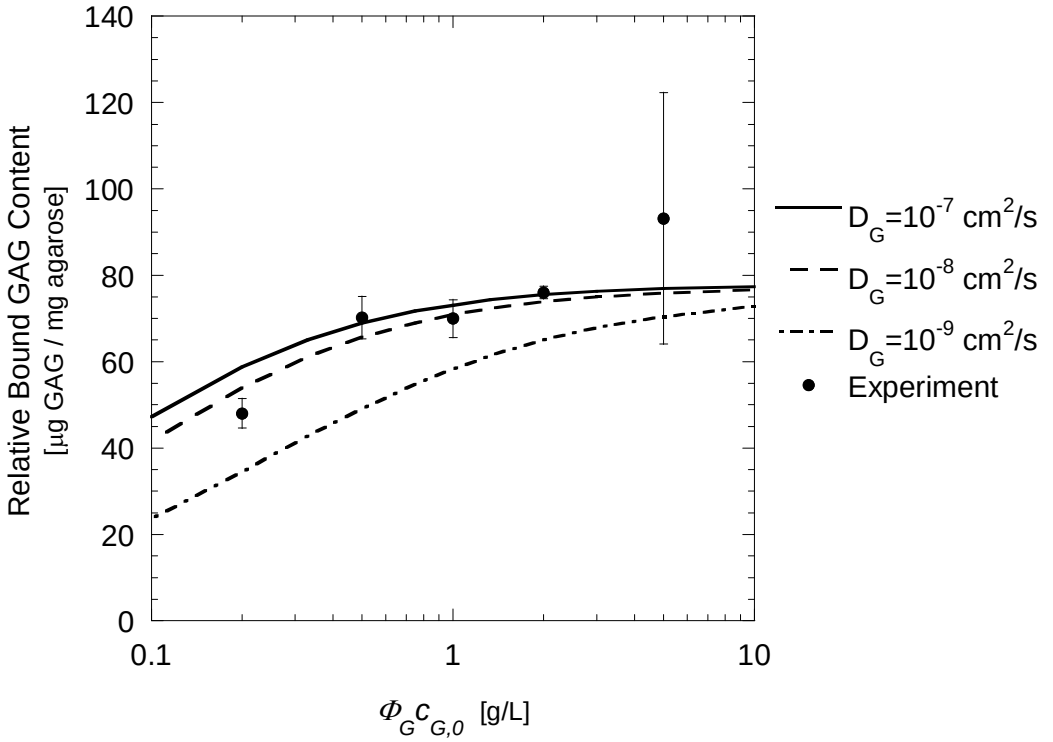

Figure 2.13 Predicted and experimental bound GAG content of agarose-GAG gels for variable GAG concentration in the attachment solution. Error bars represent one standard deviation.

The transient behavior of GAG binding is shown in Figure 2.14. In agreement with experimental observations, a majority of the GAG attachment occurs within the 30 minutes when the GAG diffusivity is 10^{-7}-10^{-8} cm^2/s. While the model deviates somewhat from the experimental data at the longer times, this is attributed to the variability between experimental batches. The two experiments used to study the transient attachment behavior likely contained high- and low-active site contents, as the final bound GAG content of both are outside the average 68 ± 8 μg/mg range observed for baseline attachment conditions. The higher GAG content batch had a shortened aqueous wash prior to attachment, so that the active site content is expected to be approximately 20% higher than baseline. This hypothesis will be tested later in the section, by looking at the model's predictions of transient binding behavior and find bound GAG content for varying $c_{a,init}$. However, the transient model predictions are still in good qualitative agreement with the data, and confirm that a minimum attachment time of two hours is needed reach high bound GAG contents.

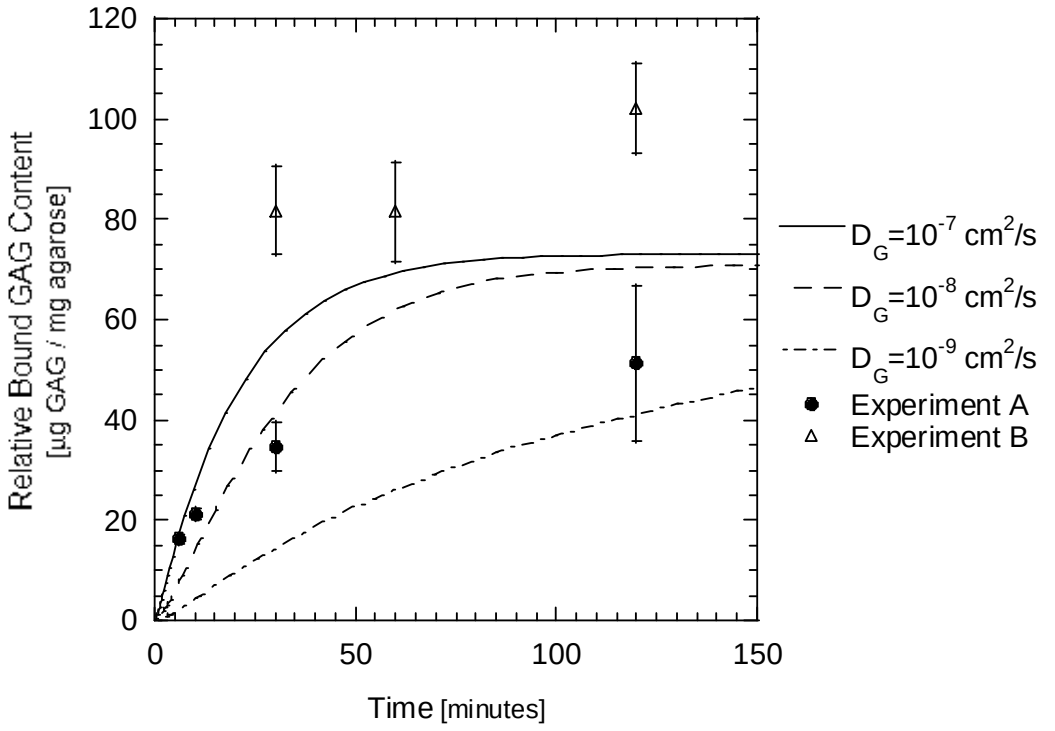

Figure 2.14 Predicted and experimental bound GAG content of agarose-GAG gels for variable attachment times. Error bars represent one standard deviation.

The prediction of bound GAG content for gels of variable thickness (δ) was only captured by the model for a GAG diffusivity of 10^{-9} cm^2/s (Figure 2.15). Even at this very low diffusivity, the bound GAG content is under-predicted for thin (70 μm) gels. For the diffusivities that agree with the transient binding data in Figure 2.14, the model overestimates the ability of GAG binding to occur in the central region of gels hundreds of microns thick.

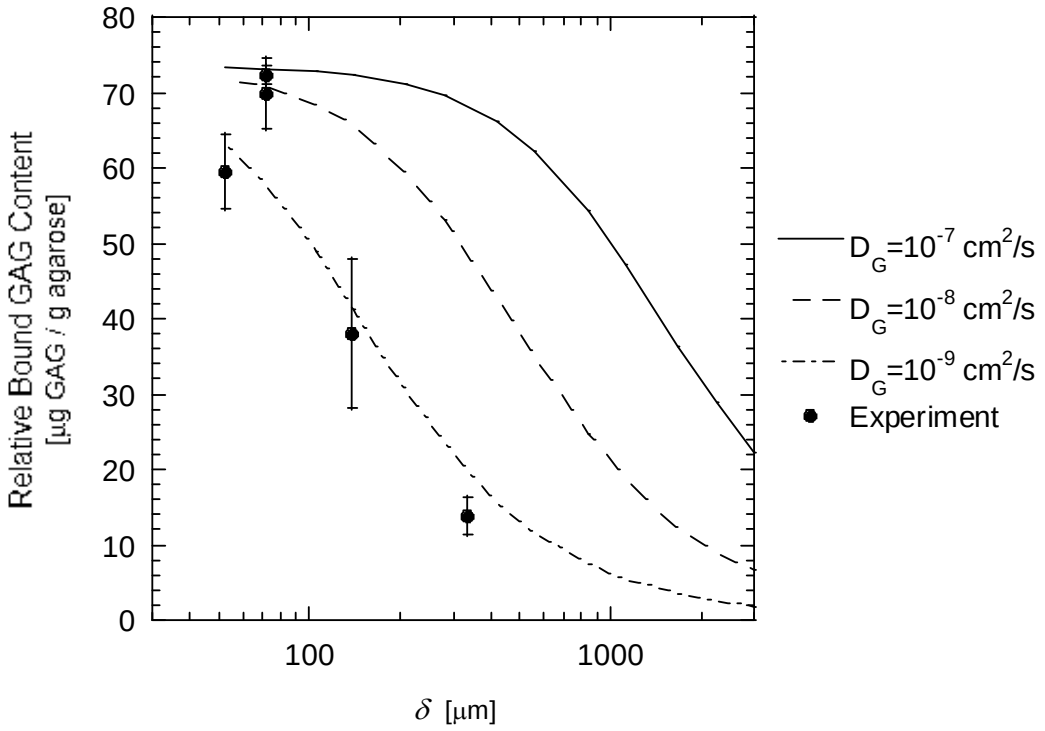

Figure 2.15 Predicted and experimental bound GAG content of agarose-GAG gels for variable gel thickness (δ). Error bars represent one standard deviation.

In addition, as seen in the cryosections in Figure 2.12, the penetration depth of GAG binding in gels of "semi-infinite" thickness is approximately 70 μm. Assuming that the depth at which the bound GAG content is half of the surface content is approximately the penetration depth, the model predicts that expected penetration depth for a diffusivity of 10^{-8}-10^{-9} cm^2/s (Figure 2.16). A "semi-infinite" depth in the model is defined as one for which the final bound concentration at the centerline is approximately zero (at least two orders of magnitude smaller than the concentration at the outer surface).

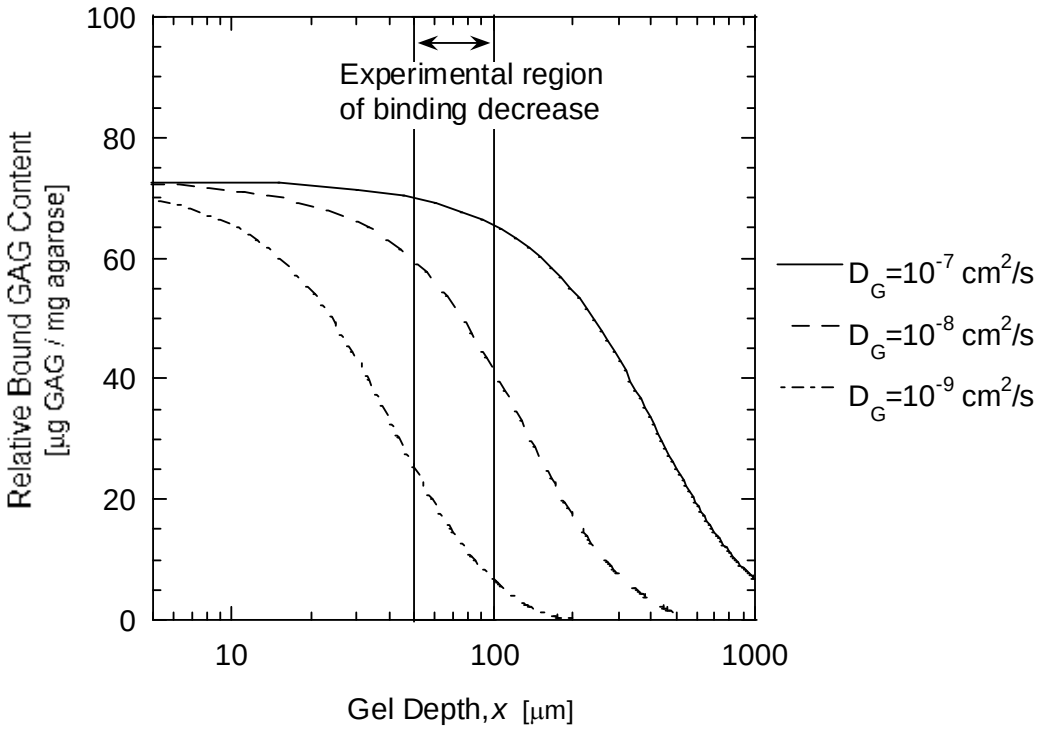

Figure 2.16 Predicted bound GAG profile as a function of depth for agarose-GAG gels of "semi-infinite" gel thicknesses. The depth refers to the distance from the outer surface of the gel, and the "semi-infinite" thickness was such that the final bound GAG content at the centerline was at least two orders of magnitude smaller than the bound GAG content at the outer surface.

While the model is able to correctly predict the qualitative response to the four experimental parameters, it is unable to do so with a single value of the GAG diffusivity. The bound GAG contents at short times and for low solution GAG concentrations are best predicted when the diffusivity is 10^{-7}-10^{-8} cm^2/s. These diffusivities are at or slightly below that assumed in Table 2.6 for spherical macromolecules of similar weight. However, the final bound GAG content for gels of larger thicknesses or the penetration depth into a semi-infinite gel is best predicted by a lower diffusivity (~10^{-9} cm^2/s). These observations suggest that the diffusivity may be a function of bound GAG content. The diffusivity would be larger when there is little bound GAG (at short times or low GAG concentrations) and would be hindered by steric and electrostatic interactions when more GAG has bound (at long times).

As previously discussed, there is some uncertainty of the diffusivity of GAG in agarose because of its large hydrodynamic radius relative to other molecules of a similar

molecular weight. Based on the results so far, it is assumed that the diffusivity of GAG in 3v% agarose is on the lower end of the estimated range, or approximately 10^{-8} cm^2/s. This makes $Da_1 = 2$ for 70 μm-thick gels and $Da_1 >> 1$ for thicker gels. This large value of the Damköhler indicates that there should be transport limitations to GAG binding in thicker gels, as experimentally observed.

The further reduction of the diffusivity by an order of magnitude due to GAG binding is also reasonable. The addition of any type of fiber will create steric hindrances to the free diffusion of a molecule. It has been shown that the addition of less than 1 v% of dextran fibers to 4v% agarose reduced the diffusivity of macromolecules to half of that in agarose alone (Kosto and Deen 2004). The electrostatic interactions of negatively charged GAG molecules could further hindered the diffusion. A similar effect of charge was observed in the reduction of myoglobin diffusivity through agarose and carrageenan gels of different charge and at different ionic strengths (Hirota et al. 2000).

Model Results with Parameters as a Function of Bound GAG

As described previously, simplified relations between the bound GAG content and the transport and kinetic properties can be included in the model. Based on the previous observations with constant properties, it appears the functional dependence of the diffusivity on bound GAG is significant. The model is therefore applied to the case when $m_D \neq 0$. Based on prior results, the initial diffusivity is taken to be 10^{-8} cm^2/s. Initially, it is assumed that the binding rate constant and GAG partitioning were constants ($m_k = m_\Phi = 0$); this assumption is supported in the following section since the variable diffusivity was able to improve agreement with experimental results without introducing the other variable parameters. The diffusivity parameter m_D was adjusted to provide reasonable agreement with the data. Since the relative root mean squared (RMS) error between the model and the data provided conflicting fits for different values of m_D (Table 2.7), the final value was selected on a visual basis. At the selected value of $m_D = 3$, the ratio of the diffusivity with maximum bound GAG ($\Theta_B = 1$) to the diffusivity with no bound GAG would be 0.05.

Table 2.7 Relative root mean squared (RMS) error between model and experimental data for different values of m_D.

Variable Parameter	m_D 0	3	4	5	6	7	8
δ	2.7	1.5	1.0	0.8	0.6	0.3	1.7
$c_{G,0}$	0.2	0.2	0.3	0.3	0.4	0.5	2.2
t (Expt. A)	1.1	1.1	1.1	1.1	1.1	1.1	- -
t (Expt. B)	1.0	1.0	1.0	0.9	1.0	0.9	- -

Using the binding model with a bound-GAG-dependent diffusivity, the bound GAG content for binding with different GAG solution concentrations is relatively unchanged from the model prediction with a constant diffusivity (Figure 2.17). Similarly, the transient binding behavior is unaffected at short times and only slight slowed at moderate times (Figure 2.18). To evaluate the previous hypothesis that the higher bound GAG content of the second set of experimental data was due to a higher initial active site concentration, the model was run with several increased values of $c_{a,init}$. As seen in Figure 2.18, the model does provide good agreement with the data at long times for a 50% increase $c_{A,init}$, which is similar to the 20% increase predicted from the shortened aqueous wash time. However, there is no ready explanation for the deviation of the data from the model predictions and the first data set at intermediate times (30-60 minutes).

The model prediction for the bound GAG content of gels of different thicknesses showed significant improvement by including the bound GAG-dependent diffusivity (Figure 2.19). While the bound GAG content remains higher for thin gels ($\leq$ 70 μm), the reduced diffusivity caused significantly less binding in thicker gels. Decreased GAG binding in thick gels is also observed in the plot of bound GAG as a function of position in a semi-infinite gel (Figure 2.20), where the penetration depth decreased from 120 μm with constant diffusivity to 46 μm for reduced diffusivity. The model predicts that a 70 μm-thick gel would have an 18% bound GAG content decrease between the gel surface and centerline. This is a relatively small decrease, and is understandably not observable in the gel cryosections.

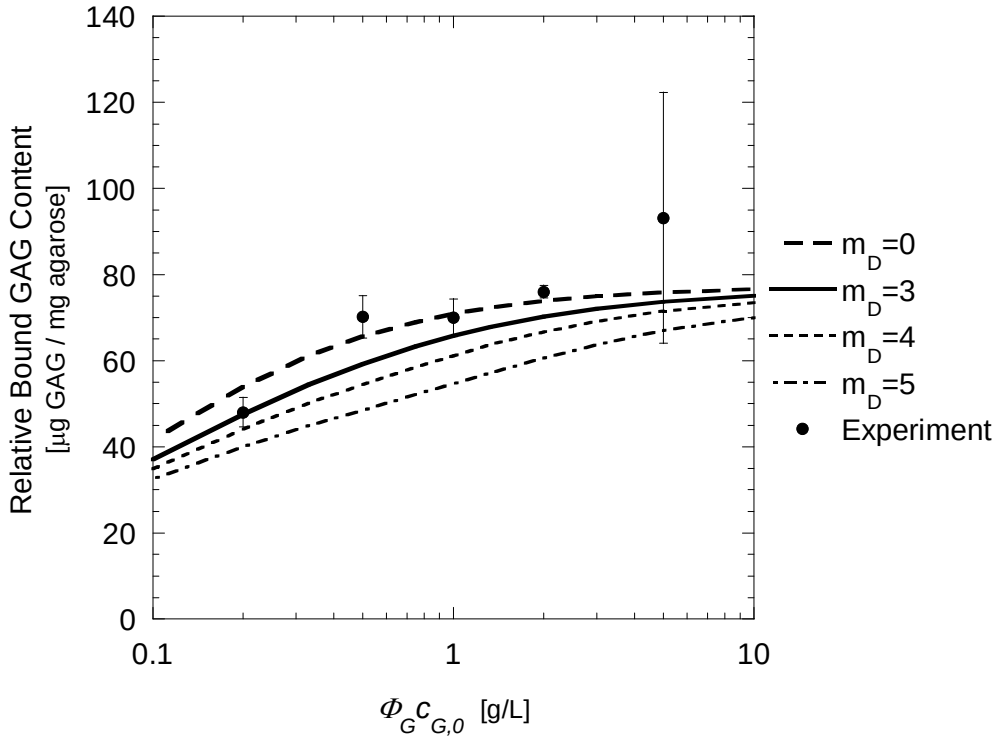

Figure 2.17 Predicted and experimental bound GAG content of agarose-GAG gels for variable GAG concentration in the attachment solution. Error bars represent one standard deviation.

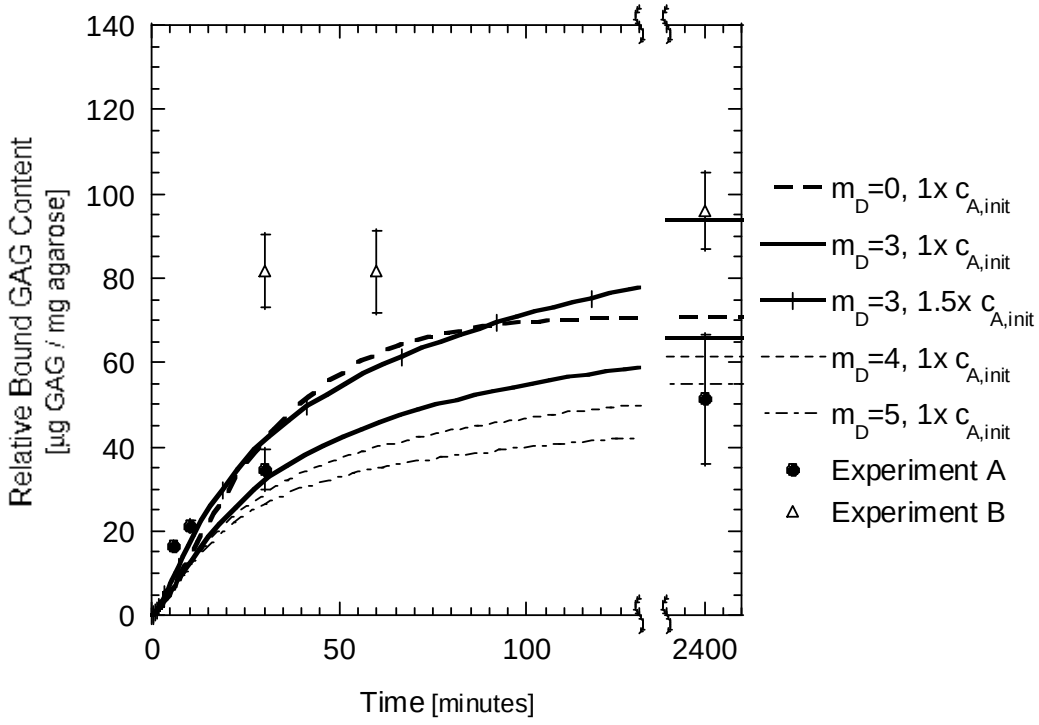

Figure 2.18 Predicted and experimental bound GAG content of agarose-GAG gels for variable attachment times and two different initial active site concentrations (1x and 2x the baseline value). Error bars represent one standard deviation.

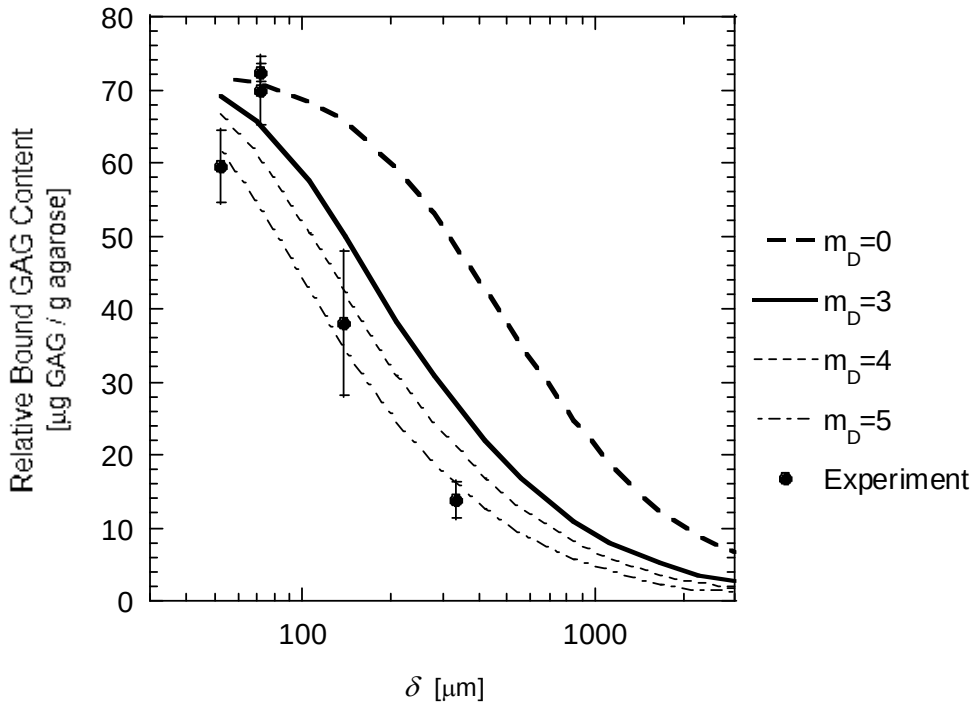

Figure 2.19 Predicted and experimental bound GAG content of agarose-GAG gels for variable gel thickness (δ). Error bars represent one standard deviation.

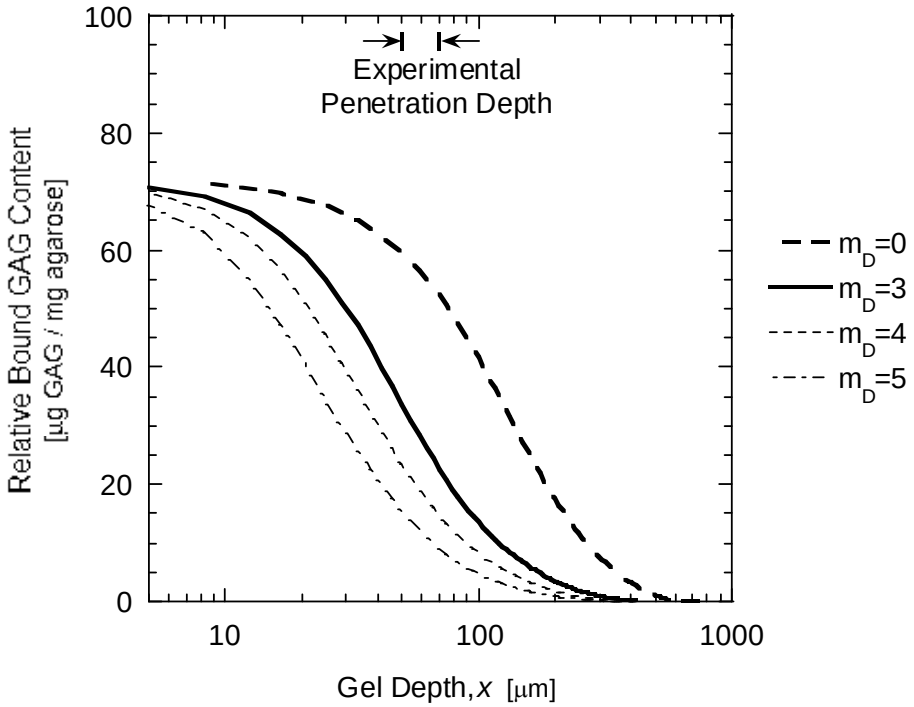

Figure 2.20 Predicted bound GAG profile as a function of depth for agarose-GAG gels of "semi-infinite" gel thicknesses. The depth refers to the distance from the outer surface of the gel, and the "semi-infinite" thickness was such that the final bound GAG content at the centerline was at least two orders of magnitude smaller than the bound GAG content at the outer surface.

The agreement between the experimental data and the model confirms that the dominant physical processes are included in our conceptual model of GAG attachment to activated agarose. While the functional relation between bound GAG content and diffusivity was approximated by a single-parameter exponential function with an experimentally fit parameter, it appears this is adequate to capture the effects seen from different diffusivities at short and long times. Other than the diffusivity parameter, all other model parameters were determined from independent experiments. Given this, the model is in good quantitative agreement with all the sets of experimental data.

2.4. Conclusions

The previous sections described the choice of agarose as a substrate for attaching GAG and the choice of the CDAP method for generating active sites for attachment. A number of experiments determined that the temperature and duration of the aqueous wash were the primary process variables which could be used to increase the bound GAG content of the agarose-GAG gels. Further experiments showed that these two process parameters have a significant impact on the fraction of active sites which degrade prior to GAG attachment.

A conceptual model of the GAG attachment step was developed to give insight into the homogeneity of the bound GAG and effect of process parameters on the attachment. While some aspects of the process were approximated, such as the effect of bound GAG on diffusional hindrance, the model was able to explain many of the experimental observations. Cryosections confirmed the model prediction that the bound GAG content is relatively uniform across the thickness of a 70 μm membrane.

Based on experimental and model results, the process parameters best suited to creating a "tunable" bound GAG content in agarose-GAG gels are the acid and aqueous wash temperatures and durations. Since these parameters affect the initial concentration of active sites during attachment, any changes in these parameters will more uniformly affect the gel (as compared to low GAG concentrations or short binding times, which could lead to a heterogeneous core region). As seen in Table 2.5, the relation between initial active sites to final bound content is not purely proportional. However, experiments have shown that the use of 0°C wash conditions results in a bound GAG

content approximately 50% greater than the "baseline" reaction conditions. Use of the active site degradation kinetics from Section 2.3.3 and the attachment model in this section provide a predictive tool for synthesizing agarose-GAG gels with a target bound GAG content.

The following is a summary of the agarose-GAG membrane synthesis which includes modification to increase the final bound GAG content:

> ***Agarose Activation:*** Place each 3v% agarose membrane in a plastic histology cassette (Histo-prep Tissue Capsules #15-182-219; Fisher, Hampton, NH). Soak 20 membranes for 15 minutes with gentle agitation in each of the following: 1 L DI water, 1 L 30% acetone (two times) and 1 L 60% acetone (two times). In a beaker surrounded by an ice bath (or ice block), add the washed gels to 200 mL ice-cold 60% acetone. While orbital mixing at 150-200 rpm, add 20 mL of 100 mg/mL CDAP (#1458C; Research Organics, Cleveland, OH) in dry acetonitrile; wait 1 minute. Dropwise, add 16 mL of 0.2 M triethylamine (TEA) solution over 1-2 minutes; wait 5 minutes while continuing to mix. Rapidly transfer the membranes to 1500 mL of 0.05 N HCl and ice (500 mL in each of three jars); wait 10 minutes while continuing to mix. Soak the membranes for 3-5 minutes in 2 L of well-mixed cold water and ice (three times).
>
> ***GAG Attachment:*** Cover the activated agarose membranes (in their cassettes) with 1 g/L GAG solution (Chondroitin sulfate A, *#230687*; Calbiochem,La Jolla, CA) in 0.1M $NaHCO_3$ and a small volume of ice. (Generally, 200 mL can cover five membranes.) Stir with orbital mixing at 0°C for at least 2-4 hours (stir in a refrigerated area to minimize ice melting). To remove the remaining active groups, add 7.5 mL ethanolamine per 100 mL attachment solution and stir for 4 hours at 4°C. Soak the membranes with gentle agitation in the following for 15 minutes each: 2 L DI water (three times), 2 L 0.5 M NaCl (two times) and 2 L DI water (six times). Remove each gel from its cassette, store in ~10 mL 0.1 M KCl-phosphate buffer and refrigerate until use.

The procedure above resulted in gels with a bound GAG content of 102±2 µg GAG/mg agarose. Gels activated in the same batch, but otherwise following the baseline synthesis procedure outlined in Section 2.2.1, had a bound GAG content of 70±5 µg GAG/mg agarose. The 4v% gels initially synthesized (Section 2.2.4) had a bound GAG content of 60±5 µg GAG/mg agarose. Therefore, modifications to the agarose-GAG attachment procedure resulted in a 70% increase in the bound GAG content compared to these initial membranes. As described in Section 2.2.4, the GAG

and agarose fiber now have a 1:1 length ratio. This indicates that the GAG component of the composite membrane should have a significant contribution to the permeability properties of membrane. The following chapters will evaluate the GAG contribution for the hydraulic permeability, partitioning, and sieving of agarose-GAG membranes.

Chapter 3. HYDRAULIC PERMEABILITY

3.1. Introduction

In the work presented here, the hydraulic permeabilities of agarose-GAG gels are determined by both experimental and modeling methods. First, the applicable models for permeability in the literature are reviewed, then developed into a unified model for the permeability of a heterogeneous, charged composite gel. The model predictions are then compared to the experimentally measured hydraulic permeability of gels with variable GAG content for a range of ionic strengths.

3.1.1. Darcy Permeability

General

For a porous material, Darcy's law is used to describe the macroscopic relation between the fluid velocity (<**v**>) and pressure gradient (∇p):

$$\langle \mathbf{v} \rangle = \frac{-\kappa}{\mu} \nabla p \tag{3.1}$$

where μ is the fluid viscosity and κ is the Darcy permeability. Equivalently, the

permeability may be given as the hydraulic permeability (k), which is the Darcy permeability divided by the viscosity.

Fiber Permeability

The hydraulic permeability of fibrous materials, including hydrogels, has been studied by many people. Early models were for simple systems with flow parallel or perpendicular to an ordered array of fibers; these include the models developed by Happel, Kuwabara, Hasimoto, Drummond and Tahir, and Sangani and Acrivos (Drummond and Tahir 1984, Happel 1959, Hasimoto 1959, Kuwabara 1959, Sangani and Acrivos 1982). The Drummond and Tahir solution for flow parallel to a square array of fibers is:

$$\frac{\kappa}{r_f^2} = \frac{1}{4\phi}\left(-\ln\phi - 1.476 + 2\phi - 0.5\phi^2 + O\left(\phi^4\right)\right) \tag{3.2}$$

where r_f is the fiber radius and ϕ is the fiber volume fraction. The Sangani and Acrivos solution for flow perpendicular to a square array of fibers is:

$$\frac{\kappa}{r_f^2} = \frac{1}{8\phi}\left(-\ln\phi - 1.476 + 2\phi - 1.774\phi^2 + 4.076\phi^3 + O\left(\phi^4\right)\right) \tag{3.3}$$

Numerous other researchers have developed hydraulic permeability models for fibrous systems with more complex properties than the periodic arrays described above. These include fibers with 3-dimensional or random orientations, fibers with multiple radii, and charged fibers. These will each be discussed in more detail in the following sections.

3.1.2. Charged Fiber Models

Background

The hydraulic permeability of a charged fiber system is dependent on both hydrodynamic and electrical forces. The electrokinetic coupling occurs because of the net charge in solution near a charged surface, which results in an electric field that is a body force within the Navier-Stokes equation. This effect is denoted by the electrokinetic coupling coefficients (k_{ij}) for the system, which relate the area-averaged

velocity ($\langle \mathbf{v} \rangle$) and area-averaged current density ($\langle \mathbf{j} \rangle$) to macroscopic applied gradients in pressure and voltage (V):

$$\begin{bmatrix} \langle \mathbf{v} \rangle \\ \langle \mathbf{j} \rangle \end{bmatrix} = \begin{bmatrix} -k_{11} & k_{12} \\ k_{21} & -k_{22} \end{bmatrix} \begin{bmatrix} \nabla p \\ \nabla V \end{bmatrix} \tag{3.4}$$

By Osager reciprocity, k_{12} will be equal to k_{21} (Onsager 1945).

The closed-circuit permeability, k_{11}, occurs when there is no macroscopic gradient in voltage. However, the open-circuit permeability (k_{oc}) is more relevant to most experimental systems where there is a non-zero streaming potential but no macroscopic current. The open circuit permeability is defined as:

$$k_{oc} = k_{11} - \frac{k_{12}k_{21}}{k_{22}} \tag{3.5}$$

All future references to the hydraulic permeability for a charged system will be for the open-circuit permeability, unless otherwise noted.

Electrokinetic coupling is often studied with macroscopic continuum models which involve average properties, with assumptions such as Donnan equilibrium (see reference in (Eisenberg and Grodzinsky 1988)). However, two microcontinuum models have been developed for charged fibers. Such models include molecular-level structural properties and allow for a spatial distribution of the charge double layer. Both models assume that the fibers are oriented in an ordered cubic array with flow occurring parallel or perpendicular to the fiber axis; to date, no model for the permeability of a charged random fiber matrix has been developed. A solution for the coupling coefficients is derived from a unit cell around a single fiber. The variable parameters in both models are the fiber surface charge, fiber radius, fiber volume fraction and solution bulk ion concentration.

Donnan Model

In the Donnan model for macroscopic charge behavior, the charge of the system is treated as being continuous though the volume, rather than contained only on the fiber surface. The permeability through neutral fibers is determined by any method (microcontinuum, experimental, etc.) and the fiber charge is treated as uniformly distributed through the membrane. No net flux of ions across the membrane,

electroneutrality, and concentration equilibrium at the membrane-solution interface are used to determine the ion concentration and electrical potential fields within the membrane (see, for example, (Deen et al. 1980, Lakshminarayanaiah 1969, Ohshima 1994)). Given that the concentrations of salt ions are equal on both sides of the membrane, then the concentration of each ion within the membrane will be constant. The expression for the streaming potential across the membrane is then:

$$\Delta\psi = \frac{\delta c_b v_x \left(D_+ - D_-\right) - \delta v_x \left[c_+^{'}\left(D_+ - D_-\right) - c_m D_+\right]}{D_+ D_- \left(2c_+^{'} - c_m\right)} \tag{3.6}$$

where c_b is the ionic strength of the bulk solution, c_m is the fixed charge concentration in the membrane, δ is the membrane thickness, v is the magnitude of the fluid velocity normal to the membrane surface, and c_+' is the positive ion concentration inside the membrane given by:

$$c_+^{'} = \frac{c_m}{2} + \sqrt{\frac{c_m^2}{4} + c_b^2} \tag{3.7}$$

The expression for volumetric fluid flux can be rewritten in a form similar to Darcy's law:

$$v_x = -k_n\left[\frac{\Delta P}{\delta} + RTc_m\Delta\psi\right] = -k\frac{\Delta P}{\delta} \tag{3.8}$$

where the neutral permeability through the membrane (k_n) is related to the charged permeability through the membrane (k) by:

$$k = k_n\left[1 + \frac{k_n RTc_b\left(c_b\left(D_+ - D_-\right) - c_+^{'}\left(D_+ - D_-\right) + c_m D_+\right)}{D_+ D_- \left(2c_+^{'} - c_m\right)}\right]^{-1} \tag{3.9}$$

Helmholtz Double Layer Model

Eisenberg and Grodzinksy derived analytical results for the coupling coefficients by making several simplifying assumptions (Eisenberg and Grodzinsky 1988). The results were derived for the limit of a small Debye length relative to both the fiber radius and the fluid region between fibers. Electromechanical coupling is then limited to the boundary layer around the fiber, and fluid flow in the bulk region can be solved independent of electrical forces. The boundary layer occurs at one Debye length away from the surface

with no electrical potential and an impenetrable slip plane at that boundary. The Debye length (λ_D) is calculated from:

$$\lambda_D = \sqrt{\frac{\varepsilon RT}{F^2 \sum_i z_i^2 c_i}} \tag{3.10}$$

where ε is the dielectric permittivity of the solvent, R is the ideal gas constant, T is the absolute temperature, F is Faraday's constant, z_i is the valence charge of species i and c_i is the molar concentration of species i. The unit cell is approximated as a cylinder surrounding a single fiber.

The coupling coefficients for flow perpendicular to the fiber axes are given by:

$$k_{11} = \frac{b^2}{4\mu G_2}\left[\ln\left(\frac{b}{a}\right) - \frac{1}{2}\frac{b^4 - a^4}{b^4 + a^4}\right] \tag{3.11}$$

$$k_{12} = k_{21} = \frac{\sigma_s \lambda_D}{\mu}\frac{b^4 - a^4}{b^4 + a^4}\left[1 + \frac{\sigma_s^2 \lambda_D}{a\mu\sigma_o} + \frac{|\sigma_s|\mu_+}{a\sigma_o} + 2\frac{\lambda_D}{a}\left(\frac{b^4 - a^4}{b^4 + a^4}\right)\left(1 + \frac{|\sigma_s|\mu_+}{a\sigma_o}\right)\right]^{-1} \tag{3.12}$$

$$k_{22} = \sigma_o \frac{1 - \xi}{1 + \xi} \tag{3.13}$$

where σ_s is the fiber surface charge density, μ is the fluid viscosity, b is the unit cell radius, a is the radius of the boundary layer and σ_o is the fluid conductivity. The radii and conductivity are defined by:

$$\begin{aligned} a &= r_f + \lambda_D \\ b &= \frac{r_f}{\sqrt{\phi}} \\ \sigma_o &\equiv F c_b \left(\mu_+ + \mu_-\right) \end{aligned} \tag{3.14}$$

where c_b is the bulk solution ionic strength and $\mu_\pm$ are the positive and negative ion mobilities. The constants G_2 and ξ are defined as:

$$\begin{aligned} G_2 &= \frac{1 - \dfrac{\sigma_s^2 \lambda_D}{a\mu\sigma_o + \mu|\sigma_s|\mu_+} + 2\dfrac{\lambda_D}{a}\left(\dfrac{b^4 - a^4}{b^4 + a^4}\right)}{1 + \dfrac{\sigma_s^2 \lambda_D}{a\mu\sigma_o + \mu|\sigma_s|\mu_+} + 2\dfrac{\lambda_D}{a}\ln\left(\dfrac{b}{a}\right) G_1} \\ G_1 &= \left(\frac{b^4 - a^4}{b^4 + a^4}\right)\left[\ln\left(\frac{b}{a}\right) - \frac{1}{2}\left(\frac{b^4 - a^4}{b^4 + a^4}\right)\right]^{-1} \end{aligned} \tag{3.15}$$

$$\xi = \frac{a^2}{b^2}\frac{1-\frac{\sigma_s^2\lambda_D}{a\mu\sigma_o}-\frac{|\sigma_s|\mu_+}{a\sigma_o}+2\frac{\lambda_D}{a}\left(\frac{b^4-a^4}{b^4+a^4}\right)\left(1-\frac{|\sigma_s|\mu_+}{a\sigma_o}\right)}{1+\frac{\sigma_s^2\lambda_D}{a\mu\sigma_o}+\frac{|\sigma_s|\mu_+}{a\sigma_o}+2\frac{\lambda_D}{a}\left(\frac{b^4-a^4}{b^4+a^4}\right)\left(1+\frac{|\sigma_s|\mu_+}{a\sigma_o}\right)} \tag{3.16}$$

The coupling coefficients for flow parallel to the fiber axes are given by:

$$k_{11} = \frac{1}{8\mu b^2}\left[4b^2\ln\left(\frac{b}{r_f}\right)-3b^4+4{r_f}^2b^2-{r_f}^4\right] \tag{3.17}$$

$$k_{12} = k_{21} = \frac{\sigma_s\lambda_D}{\mu}\left(1-\frac{{r_f}^2}{b^2}-\frac{1}{2}\frac{\lambda_D}{r_f}\frac{{r_f}^2}{b^2}\right) \tag{3.18}$$

$$k_{22} = \sigma_o\left[1-\frac{{r_f}^2}{b^2}+2\frac{{r_f}^2}{b^2}\left(\frac{\sigma_s^2\lambda_D}{r_f\mu\sigma_o}+\frac{|\sigma_s|\mu_+}{r_f\sigma_o}\right)\right] \tag{3.19}$$

Diffuse Double Layer Model

The assumptions made by Eisenberg and Grodzinksy limit the applicability of their model to systems where the double layers surrounding the fibers are non-interacting. Chammas, Federspiel and Eisenberg developed a more rigorous model that includes diffuse double layers which may be overlapping (Chammas et al. 1994). The problem is cast as a perturbation of the static electric field caused by the imposed flow. The electrical and hydrodynamic equations are coupled throughout the unit cell:

$$\nabla p = \mu\nabla^2\mathbf{v} + \varepsilon\nabla^2\psi\nabla\psi \tag{3.20}$$

$$0 = \nabla\cdot\mathbf{v} \tag{3.21}$$

$$0 = \overline{\nabla}\cdot\left(-D_i\nabla c_i - \frac{z_i}{|z_i|}\mu_i c_i\nabla\psi + c_i\mathbf{v}\right) = \overline{\nabla}\cdot\mathbf{n}_i \tag{3.22}$$

$$\nabla^2\psi = \frac{Fz}{\varepsilon}\left(c_- - c_+\right) \tag{3.23}$$

Here, $\mathbf{v}$ is the velocity vector, ψ is the electrical potential, c_i is the concentration of species i, $\mathbf{n}_i$ is the flux of species i,D_i is the diffusivity of species i, F is Faraday's constant, and ε is the dielectric permittivity of the solvent. These equations were solved with a finite difference method in a transformed curvilinear grid. The details of the coupled electrokinetic equations and the perturbation solution will be presented later in section 3.2.1.

3.1.3. Orientation and Population Averaging

Most of the available models for hydraulic permeability discussed so far have considered an ordered array of a single type of fiber, which can be solved using the symmetry of the system. However, such solutions become difficult or impossible when the system contains two different populations of fibers. The fiber populations could have different orientations (parallel and perpendicular to the flow), different radii, or different surface charges.

Random Fiber Arrays

Simulations of ordered 3-dimensional fiber arrangements were done by Hidgon and Ford and Koponen *et al.* (Higdon and Ford 1996, Koponen et al. 1998). This approach has only recently become feasible, since it is not simplified by symmetry and instead involves numerical simulations which require significant computing power. An analogous approach could be used for systems with random fiber orientations instead of an ordered array. By finding the permeability of a fiber oriented at some angle relative to the direction of applied pressure, the result can be spatially averaged over all orientations to find the random fiber permeability. This method was used by Clague and Phillips and Clague *et al.* (Clague et al. 2000, Clague and Phillips 1997). Clague *et al.* empirically fit their results for random fiber permeabilities with the equation:

$$\frac{\kappa}{r_f^2} = \left[\frac{1}{2}\sqrt{\frac{\pi}{\phi}} - 1\right]^2 \left[0.71407 \exp\left(-0.51854\phi\right)\right] \tag{3.24}$$

Prior to these computational results, several approximations were used to estimate the permeability of random fibers. Spielman and Goren used swarm theory for a single rod in a porous medium (Spielman and Goren 1968). Jackson and James assumed that random fibers could be approximated by a cubic lattice of fibers, which could be found by averaging flow past a population that was oriented one-third parallel to the flow and two-thirds perpendicular to the flow (Figure 3.1) (Jackson and James 1982, 1986). Their averaging of these populations was:

$$\frac{1}{k_{avg}} = \frac{1}{k_{\parallel}\left(\frac{1}{3}\phi_{total}\right)} + \frac{1}{k_{\perp}\left(\frac{2}{3}\phi_{total}\right)} \tag{3.25}$$

where k_{avg} is the average hydraulic permeability through the fibers, $k_{\parallel}$ is the permeability parallel to a periodic fiber array, $k_{\perp}$ is the permeability perpendicular to a periodic fiber array and ϕ_{total} is the fiber volume fraction of all fibers in the system. Eisenberg and Grodzinksy and Chammas *et al.* also approximated flow through a random matrix of charged fibers by averaging flow past a one-third parallel and two-thirds perpendicular fiber system (Chammas et al. 1994, Eisenberg and Grodzinsky 1988). However, their averaging took the linear form:

$$k_{avg} = \frac{1}{3}k_{\parallel}\left(\phi_{total}\right) + \frac{2}{3}k_{\perp}\left(\phi_{total}\right) \ . \tag{3.26}$$

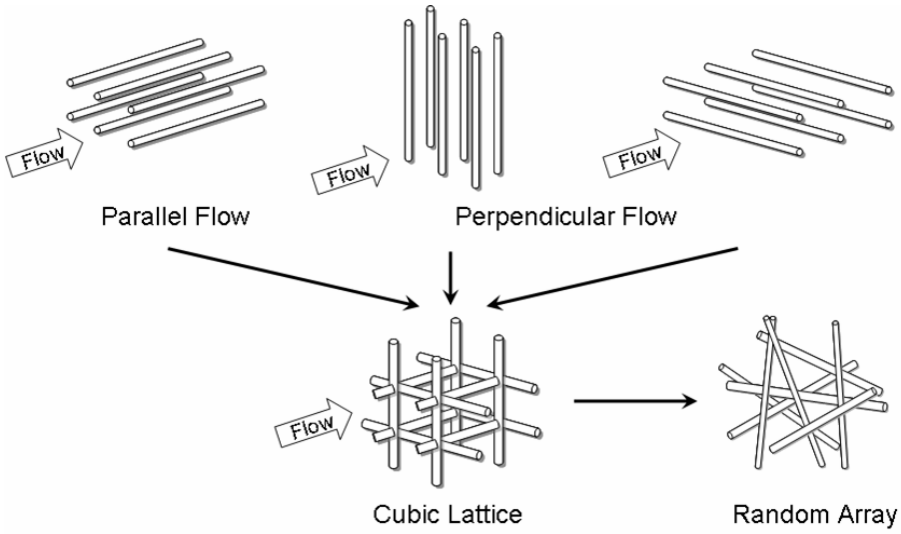

Figure 3.1 Diagram of periodic two-dimensional fiber arrays combined into a cubic lattice arrangement. The cubic lattice has been used by several authors as an approximation for modeling the hydraulic permeability of a random three-dimensional array.

Jackson and James proposed the cubic lattice structure based on the drag force acting on a rod oriented obliquely to low Reynolds number flow (Jackson and James 1982, 1986). The drag force is inversely related to the hydraulic permeability of an array of the fiber. The force vector can be separated into three perpendicular components, which Jackson and James claim are equivalent to the forces on three rod segments in the same three directions. Extending this to a large system of random fibers or a randomly-coiled

chain, the rod segments can be arranged into a cubic lattice with one-third of the segments oriented parallel to each of the directions.

A more rigorous derivation of the one-third parallel / two-thirds perpendicular arrangement of fibers is found by extension to orientation averaging of fibers in heat conduction and electrophoresis. This derivation was done by De Keizer *et al.* and Stigter for electrophoresis of fibers oriented as an angle θ relative to an imposed electric field, as well as by Deen (Problem 4-14) for heat conduction through a fibrous composite with an imposed temperature gradient (De Keizer et al. 1975, Deen 1998, Stigter 1978). When the result is averaged over all spatial orientations, the result is equal to the linear sum of one-third of the parallel result plus two-thirds of the perpendicular result. Stigler has shown that this result is true for any vector field that is linearly related to an applied field.

Bimodal Fiber Arrays

For systems with bimodal fiber radii, Ethier derived an analytical solution for fibers with highly dissimilar fiber radii, such that the fine fibers formed a homogeneous region between the larger fibers (Ethier 1991). Maroudas *et al.* used a highly simplified view of a system of collagen and GAG as two fiber regions in parallel, which results in a variant of Equation (3.26) (Maroudas et al. 1987):

$$k_{avg} = \frac{A_1 k_1 + A_2 k_2}{A_1 + A_2} \tag{3.27}$$

where A_1 and A_2 are the areas of fiber regions 1 and 2.

For systems with fiber radii of similar magnitude, solutions to the permeability have been found by numerical simulations by Edwards *et al.* for ordered systems and by Clague and Phillips for random systems (Clague and Phillips 1997, Edwards et al. 1990). Clague and Phillips proposed an analytical mixing rule for bimodal fibers, which was in good agreement with their simulations:

$$\frac{1}{k_{avg}} = \frac{\phi_1}{\phi_{total}} \frac{1}{k_1(\phi_{total})} + \frac{\phi_2}{\phi_{total}} \frac{1}{k_2(\phi_{total})} \tag{3.28}$$

where ϕ_1 and ϕ_2 are the volume fractions of fiber types 1 and 2, respectively. Levick cites a similar semi-empirical mixing rule developed by Ethier for a GAG-protein system

(Ethier 1983, Levick 1987). The inverse permeability of the two fibers is weighted by their relative fiber lengths instead of their relative fiber volumes:

$$\frac{\left(\phi_1/r_{f,1}^2\right)+\left(\phi_2/r_{f,2}^2\right)}{k_{avg}}=\frac{\left(\phi_1/r_{f,1}^2\right)}{k_1\left(\phi_{total}\right)}+\frac{\left(\phi_2/r_{f,2}^2\right)}{k_2\left(\phi_{total}\right)} \tag{3.29}$$

No models have been developed for the permeabilities of fiber systems with different fiber charges or with more than two fiber radii.

3.1.4. Non-Homogeneous Fiber Models

Background

There is significant evidence that the fibers in agarose gels can not be considered homogeneously distributed. Disagreement of hydraulic permeability measurements of agarose with homogeneous random fiber models by several researchers has indicated that a more complex fiber structure is likely present (Clague and Phillips 1997, Johnson and Deen 1996b, White and Deen 2002). Studies of macromolecule sieving through agarose also concluded that the results could only be explained if the agarose gels contained high- and low- fiber density regions (Kosto and Deen 2005). Electron microscopy, dynamic light scattering and turbidity measurements of agarose have also shown an uneven distribution of fiber spacing (Aymard et al. 2001, Bulone et al. 2004, Waki and Harvey 1982). It has been hypothesized that the agarose fibers tend to aggregate in cross-linked regions during gelation, leaving the surrounding regions fiber-depleted (Djabourov et al. 1989, Manno et al. 1999). This can be seen in microscopy images of agarose gels, such as Figure 3.2.

An agarose gel contains up to three characteristic length scales: molecular, intermolecular, and supramolecular. Molecular lengths apply to the length and radius of an individual agarose molecule or multi-molecule fiber. Intermolecular lengths describe lengths between fibers or cross-linked junctions; this is often described as the gel's inter-fiber spacing, pore diameter or correlation length. Supramolecular length scales have been reported by some researchers for fiber density variations over many fiber lengths. The exact length scales of a gel are difficult to specify, since they have been reported to be a function of the total fiber content, rate of cooling, solution ionic strength, and agarose type (Aymard et al. 2001, Bettelheim et al. 1966, Foord and Atkins 1989, Griess

et al. 1993a, Maaloum et al. 1998, Waki and Harvey 1982). However, once the gel has formed, changes in solution ionic strength, solution sugar content and gamma irradiation were not reported to have a significant effect on the fiber spacing (Griess et al. 1993a, Key and Sellen 1982, Maaloum et al. 1998).

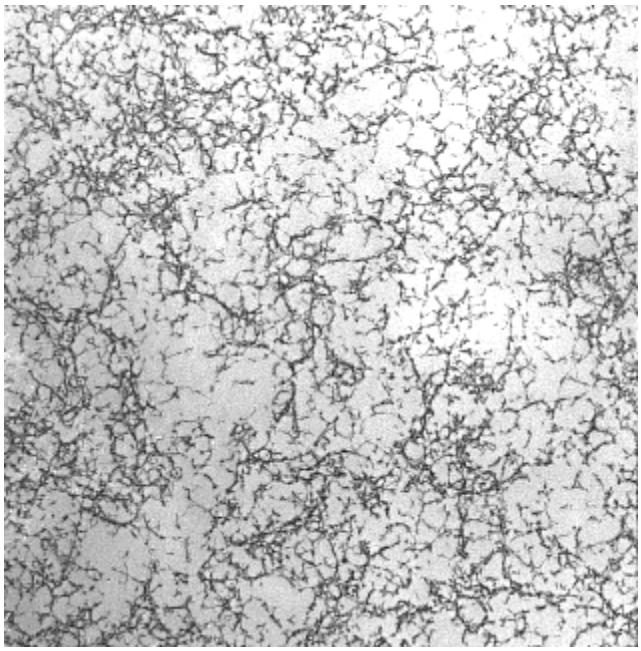

Figure 3.2 Transmission electron micrograph of a 2% agarose gel; image is approximately 7 x 7 μm [from Aymard *et al.* (Aymard et al. 2001)]

A wide range of molecular and intermolecular length scales have been reported in the literature for agarose, likely due to variations in agarose type, agarose concentration, cooling rate, solution composition and method of analysis. The mean fiber radius of 1-4 w/v% agarose has been reported in the range of 0.7-4.4 nm, where a fiber may contain 6-100+ agarose helices (Arnott et al. 1974, Attwood et al. 1988, Chui et al. 1995, Djabourov et al. 1989, Ratajska-Gadomska and Gadomski 2004, Waki and Harvey 1982, Whytock and Finch 1991). Wytock and Finch found that the mean fiber diameter increases with increasing agarose concentration in the range 0.3-2 w/v% (Whytock and Finch 1991). Djabourov *et al.* showed that the fiber diameters in 2.4 w/w% gels contain at least two distributions, with 87% of fibers with a 1.5 nm mean radius and 13% with a 4.1 nm mean radius (Djabourov et al. 1989). The reported values for inter-fiber spacing are similarly diverse, with pore diameters of 37-300 nm for 1-4 w/v% agarose (Attwood

et al. 1988, Griess et al. 1993b, Maaloum et al. 1998, Ratajska-Gadomska and Gadomski 2004, Xiong et al. 2005). Maaloum *et al.* found that the mean pore diameter was proportional to $\phi_a^{-0.6}$, which is in between the predictions from theories for random arrangements of straight and flexible chains (Maaloum et al. 1998).

The presence of supramolecular length scales in agarose gels has been noted by several researchers. In a phase diagram for agarose, there is spinodal gel formation for concentrations above ~1.5 w/v%; below this concentration, there is a direct transition from sol to gel (Manno et al. 1999). Other theories of agarose gelation include competing forces between cross-linking nucleation and aggregation, which are both affected by the fiber concentration and the cooling rate and temperature. These theories are all supported by a number of experimental observations of large-scale heterogeneity at agarose concentrations >1 w/v% and at relatively high (35~45°C) gelation temperatures. Griess *et al.* proposed that fiber heterogeneity in two zones would explain the difference in the distribution of fiber spacing in electron micrographs of 2.5% gels versus the spacing predicted by a homogeneous random fiber distribution (Griess et al. 1993b). Pines and Prins observed closely packed spherical regions of ~4.9 μm radius in 1% gels with their microscope (though Djabourov *et al.* and Waki & Harvey both noted they were not able to repeat these observations) (Djabourov et al. 1989, Pines and Prins 1973, Waki and Harvey 1982). Aymard *et al.* observed fiber-rich and -poor regions in electron micrographs of 2% gels cured ≥ 35°C, which was supported by their turbidity measurements which estimated the size of these regions at 300~6,000 nm (Aymard et al. 2001). Attwood *et al.* also observed fiber-poor regions in Sepharose® 4 beads (4% agarose) on the order of ~300 nm diameter (Attwood et al. 1988). Manno *et al.* studied 2 w% agarose gels with a variety of techniques (optical rotation, dispersion, small- and large-angle light scattering), and found that demixed droplets occurred on lengths of 3.7-12.5 μm depending on the quench temperature (40-46.5°C). However, at lower quench temperatures (≤31.5°C), the demixing appeared to be hindered by more rapid cross-linking, such that supramolecular features were not observed (Manno et al. 1999).

Instead of attempting to characterize and model the full distribution of fiber densities and fiber radii for the gels synthesized in our lab, a simpler model of agarose

heterogeneity is preferred. In the following section, several models for fiber systems with two regions of different hydraulic permeability are considered for modeling agarose.

Models

The simplest models of two regions with different hydraulic permeabilities are layers in series and layers in parallel (Figure 3.3). Even if the composite contains many thin layers, it is mathematically equivalent to two layers with a volume fraction equal to the sum of the thin layers. The effective hydraulic permeability of the composite, k_{eff}, relative to the permeability of region 1, k_1, is given by:

$$\text{Parallel}: \quad \frac{k_{eff}}{k_1} = 1 - \varepsilon_2 + \varepsilon_2 \frac{k_2}{k_1} \tag{3.30}$$

$$\text{Series}: \quad \frac{k_{eff}}{k_1} = \left[1 - \varepsilon_2 + \varepsilon_2 \frac{k_1}{k_2} \right]^{-1} \tag{3.31}$$

where ε_2 and k_2 are the volume fraction and hydraulic permeability of region 2, respectively. The parallel model can be interpreted as a material with pores which extend through the entire thickness; the series model would be a striated material. Sieving studies in agarose used a parallel layer model to help explain the results (Kosto and Deen 2005).

Extensions of these models have been published which combine the regions in a "checker board" arrangement of unit cells of alternating regions. Yu and Soong did a simple averaging of this system using the sum of resistances in series and parallel to predict the overall permeability (Yu and Soong 1975). The results from such models are bounded by the limits of a system that has just a parallel or just a series arrangement. Schweers and Löffler did a more rigorous numerical simulation of the same system, allowing there to be flow both parallel and perpendicular to the applied pressure due to pressure variations between adjacent regions (Schweers and Löffler 1994). However, both of these "checker board" models are limited by needing accurate dimensions and properties of each of the cells.

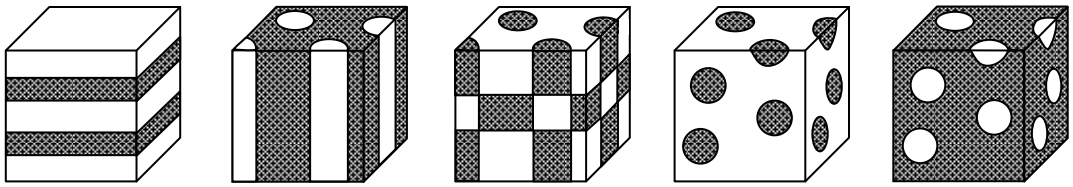

Figure 3.3 Schematics of five idealized models of heterogeneity in fiber density

A more tractable model that allows for interspersed fiber regions is spherical regions within a surrounding matrix. This isotropic system has been studied in numerous other contexts, such as electrical and thermal conductivity, with the governing equations having the same form as Darcy's law for hydraulic permeability. The resulting permeability (conductivity) of the composite was first described by the Maxwell solution (also known as the Lorentz-Lorenz solution or Clausius-Mossotti solution, depending on the field of research):

$$\frac{k_{eff}}{k_1} = \frac{1+2\beta\varepsilon_2}{1-\beta\varepsilon_2} \tag{3.32}$$

$$\beta \equiv \frac{(k_2/k_1)-1}{(k_2/k_1)+2} \tag{3.33}$$

where region 2 refers to the spherical regions and region 1 to the surrounding matrix (Fricke 1924). The solution is derived for the dilute case when the sphere diameter is small relative to the sphere spacing. The solution was extended by Fricke for spheroids and by Meredith and Tobias for higher sphere volume fractions (Fricke 1924, Meredith and Tobias 1961). A more rigorous derivation of higher sphere volume fractions was done by Jeffrey (Jeffrey 1973), of which the first six terms in the power series solution are given by:

$$\frac{k_{eff}}{k_1} = 1 + 3\beta\varepsilon_2 + {\varepsilon_2}^2\left(3\beta^2 + \frac{3\beta^3}{4} + \frac{9\beta^3}{16}\frac{(k_2/k_1)+2}{2(k_2/k_1)+3} + \frac{3\beta^4}{64} + \ldots\right). \tag{3.34}$$

Bonnecaze and Brady showed by numerical simulations that the Jeffrey model has reasonable accuracy up to a volume fraction of ε_2=0.2~0.5 and for systems larger than

several sphere diameters (Bonnecaze and Brady 1991). Note that if the system dimension is several times larger than the sphere diameter, then the effective permeability is independent of the sphere diameter and only a function of ε_2.

3.2. Model Development

The following sections describe the evaluation and application of the various hydraulic permeability models to agarose-GAG gel membranes.

3.2.1. Charged Fiber Models

Diffuse Double Layer Model

The diffuse double layer model developed by Chammas *et al.* was replicated in COMSOL Multiphysics® (v. 3.2), with several changes (Chammas et al. 1994). Multiphysics® automatically generates a finite element mesh, so there was no need to transform to a curvilinear coordinate system. Additionally, the model was solved using a velocity vector and pressure formulation of the equations, instead of stream function and vorticity. The square array of fibers was modeled with a half-fiber unit cell, with a dimensionless fiber radius, R_f, and unit cell width, B (Figure 3.4). The fiber radius is non-dimensionalized by the Debye length ($R_f=r_f/\lambda_D$) and the dimensionless unit cell width is related to the fiber volume fraction by:

$$B = R_f \sqrt{\frac{\pi}{4\phi}} \tag{3.35}$$

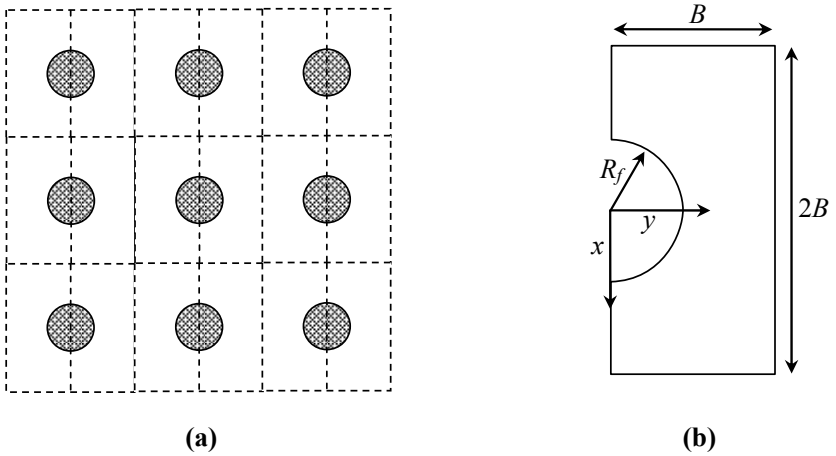

Figure 3.4 (a) Square array of charged fibers with unit cell boundaries. (b) Single unit cell for a fiber with radius R_f and unit cell width B.

The system contains five dimensionless field variables: pressure (P), fluid velocity ($\mathbf{u}$), positive and negative ion concentration ($C_{\pm}$) and electrical potential (Ψ). The unperturbed system of equations includes the Navier-Stokes equation, the continuity equation, species conservation equations for positive and negative ions, and Poisson's equation:

$$\nabla P = \beta_E \nabla^2 \mathbf{u} + \nabla^2 \Psi \nabla \Psi \tag{3.36}$$

$$0 = \nabla \cdot \mathbf{u} \tag{3.37}$$

$$0 = \nabla \cdot \left(-\left(\nabla C_+ + C_+ \nabla \Psi - \beta_E \alpha C_+ \mathbf{u} \right) \right) = \nabla \cdot \mathbf{N}_+ \tag{3.38}$$

$$0 = \nabla \cdot \left(-\left(\nabla C_- - C_- \nabla \Psi - \beta_E \alpha \frac{D_+}{D_-} C_- \mathbf{u} \right) \right) = \nabla \cdot \mathbf{N}_- \tag{3.39}$$

$$\nabla^2 \Psi = \frac{1}{2}\left(C_- - C_+ \right) \tag{3.40}$$

where the dimensionless variables are related to the dimensional variables by:

$$\begin{aligned} \nabla &= \lambda_D \overline{\nabla} \\ \Psi &= z_+ \psi / V_{th} = zF\psi / RT \\ C_{\pm} &= c_{\pm} / c_b \\ \mathbf{N}_{\pm} &= \mathbf{n}_{\pm} \lambda_D / D_{\pm} c_b \\ P &= p / \pi_b = p / 2RTc_b \\ \mathbf{u} &= \mathbf{v} / u_s \end{aligned} \tag{3.41}$$

Here, λ_D is the Debye length, c_b is the external bulk concentration, π_b is the bulk osmotic pressure, u_s is the superficial fluid velocity, V_{th} is the thermal voltage, z ($=z_+=-z_-$) is the absolute value of the ion charge for a binary electrolyte and $\mathbf{N}_{\pm}$ are the dimensionless ion fluxes. The two dimensionless groups are:

$$\beta_E = \frac{z\left(u_s \mu \big/ \varepsilon V_{th} \right)}{\left(V_{th} \big/ \lambda_D \right)} = \frac{zE_s}{E_{DL}} \tag{3.42}$$

which is the relative strength of the flow-induced electric field (E_s) compared to the characteristic electric field across the double layer (E_{DL}) and:

$$\alpha = \frac{\mathrm{Pe}}{\beta_E} = \frac{\varepsilon V_{th}/\mu}{z\mu_+} = \frac{\varepsilon V_{th}^2}{z^2 \mu D_+} \tag{3.43}$$

which is the relative strength of the effective electrophoretic mobility to the positive ion mobility. Here, μ is the fluid viscosity, μ_+ is the positive ion mobility and Pe is the Peclet number based on the superficial velocity:

$$\mathrm{Pe} = \frac{u_s \lambda_D}{D_+} \tag{3.44}$$

The diffusivity of the ions are related to their mobility by Einstein's relation:

$$D_\pm = \frac{RT}{zF}\mu_\pm \tag{3.45}$$

For a typical superficial velocity (u_s) of 10^{-7} m/s in an aqueous 0.1 M monovalent salt solution, the dimensionless groups are $\beta_E \approx O\left(10^{-7}\right)$ and $\alpha \approx O(1)$, which suggests a perturbation solution using the parameter β_E. The five field variables are expressed as a power series in the perturbation parameter β_E, in the form:

$$\Psi = \Psi^{(0)} + \beta_E \Psi^{(1)} + \beta_E^2 \Psi^{(1)} + \ldots \tag{3.46}$$

The zero-th (O(1)) and first order (O(β_E)) systems of equations are discussed below.

Order-0 Model

The zero-th order solution corresponds to the case of $\beta_E = 0$, when **u**=0 everywhere and there is no flow-induced electric field. As shown by Chammas *et al.*, the equations of motion are decoupled from the electric field and concentration equations. As a result, the ion concentrations are described by a Boltzman distribution:

$$c_\pm^{(0)} = \exp\left(\mp\Psi^{(0)}\right) \tag{3.47}$$

and the potential is given by the Poisson-Boltzman equation:

$$\nabla^2 \Psi^{(0)} = \sinh \Psi^{(0)} \tag{3.48}$$

As will be seen in the following sections, it is not necessary to solve for the unperturbed pressure ($p^{(0)}$).

The boundary conditions for the system assume that the fields are confined to the *x*-*y* plane and are independent of *z*. The boundary conditions are summarized in Table 3.1. There is symmetry at the *y*=0 and *y*=*B* surfaces. In the absence of an external perturbing

field, there is also symmetry at the $x=\pm B$ surfaces. The fiber surface boundary condition at $r=R_f$ is given by Gauss' Law for a charged surface with surface charge density σ_s.

Table 3.1 Boundary conditions for the dimensionless electrokinetic equations for a periodic unit cell around a charged fiber with applied pressure and electric fields

	$y=0,B$	$x=\pm B$	$r=R_f$
0^{th}-Order	$n\cdot\nabla\Psi^{(0)}=0$	$n\cdot\nabla\Psi^{(0)}=0$	$n\cdot\nabla\Psi^{(0)}=-\dfrac{\sigma_s\lambda_D}{\varepsilon V_{th}}$
1^{st}-Order: Perpendicular	$n\cdot\nabla P^{(1)}=0$ $n\cdot\mathbf{u}^{(\mathbf{0})}=0$ $n\cdot\nabla\mathbf{N}_{\pm}^{(\mathbf{1})}=0$ $n\cdot\nabla\Psi^{(1)}=0$	let $P^{(1)}(x=+B,y)=0$ then $P^{(1)}(x=-B,y)=\dfrac{2B\lambda_D}{\beta_E\pi_b}\dfrac{dp}{dx}$ $t\cdot\mathbf{u}^{(\mathbf{0})}=0$ $C_{\pm}^{(1)}=0$ let $\Psi^{(1)}(x=+B,y)=0$ then $\Psi^{(1)}(x=-B,y)=\dfrac{2Bz\lambda_D}{\beta_E V_{th}}\dfrac{dV}{dx}$	$\mathbf{u}^{(\mathbf{0})}=0$ $n\cdot\nabla\mathbf{N}_{\pm}^{(\mathbf{1})}=0$ $n\cdot\nabla\Psi^{(1)}=0$
1^{st}-Order: Parallel	$n\cdot\nabla u_z^{(\mathbf{1})}=0$	$n\cdot\nabla u_z^{(\mathbf{1})}=0$	$u_z^{(\mathbf{1})}=0$

1^{st}-Order Model – Perpendicular Flow

This section considers the 1^{st}-order ($O(\beta_E)$) system of equations for macroscopic gradients in pressure (dp/dx) and voltage (dV/dx) applied perpendicular to the fiber axes. A perpendicular field will induce transverse flow with u_x and u_y components; all field variables are assumed to functions of x and y only. The 1^{st}-order perturbation of equations (3.36)-(3.40) yields the following set of equations:

$$\nabla P^{(1)}=\nabla^2\mathbf{u}^{(\mathbf{0})}+\nabla^2\Psi^{(1)}\nabla\Psi^{(0)}+\nabla^2\Psi^{(0)}\nabla\Psi^{(1)} \tag{3.49}$$

$$0=\nabla\cdot\mathbf{u}^{(\mathbf{0})} \tag{3.50}$$

$$0=\nabla\cdot\left(-\left(\nabla C_+^{(1)}+C_+^{(0)}\nabla\Psi^{(1)}+C_-^{(1)}\nabla\Psi^{(0)}-\alpha C_+^{(0)}\mathbf{u}^{(\mathbf{0})}\right)\right)=\nabla\cdot\mathbf{N}_+^{(1)} \tag{3.51}$$

$$0=\nabla\cdot\left(-\left(\nabla C_-^{(1)}-C_-^{(0)}\nabla\Psi^{(1)}-C_-^{(1)}\nabla\Psi^{(0)}-\alpha\frac{D_+}{D_-}C_-^{(0)}\mathbf{u}^{(\mathbf{0})}\right)\right)=\nabla\cdot\mathbf{N}_-^{(1)} \tag{3.52}$$

$$\nabla^2\Psi^{(1)}=\frac{1}{2}\left(C_-^{(1)}-C_+^{(1)}\right) \tag{3.53}$$

The boundary conditions for this system are summarized in Table 3.1. There is symmetry at the y=0 and y=B surfaces. The fiber surface boundary conditions at r=R_f include no-slip, no ion flux, and Gauss' Law for an unperturbed charged surface. The boundary conditions at the x=±B surfaces relate the gradients across the period unit cell to the macroscopic gradients across the fiber matrix. The pressure and electric field gradients across the unit cell must be equal to the macroscopic gradients. Since the 0^{th}-order solution describes the unperturbed system, the macroscopic gradients must be related to the 1^{st}-order solutions. Both of these properties are defined relative to a reference value, which for convenience can be defined to be zero at one of the boundaries. In the absence of macroscopic concentration gradients, the concentrations must be equal at the x=±B boundaries; periodic nature of the system requires that the concentrations are unperturbed. By the symmetry of the system, there can be no tangential flow at these boundaries.

1^{st}-Order Model – Parallel Flow

This section considers the 1^{st}-order system of equations for macroscopic gradients in pressure (dp/dz) and voltage (dV/dz) applied parallel to the fiber axes. For applied gradients parallel to the fiber axes, the only non-zero velocity component is $u_z(x,y)$. Similarly, the only non-zero components of the perturbed ion fluxes and electric potential are $\mathbf{N}_{z,\pm}^{(1)}(x,y)$ and $\Psi^{(1)}(z)$, which decouple the electrokinetic equations. The local gradients in pressure and electrical potential are only dependent on the macroscopically applied gradient. The result is the simplified equation for $u_z(x,y)$:

$$\frac{\lambda_D}{\beta_E \pi_b}\left(\frac{dp}{dz}\right) = \nabla^2 u_z^{(\mathbf{0})} + \frac{1}{2}\left(C_-^{(0)} - C_+^{(0)}\right)\frac{z\lambda_D}{\beta_E V_{th}}\left(\frac{dV}{dz}\right) \tag{3.54}$$

The ion fluxes for parallel flow are evaluated from:

$$N_{z,+}^{(1)} = -\left(C_+^{(0)}\frac{z\lambda_D}{\beta_E V_{th}}\left(\frac{dV}{dz}\right) - \alpha C_+^{(0)} u_z^{(\mathbf{0})}\right) \tag{3.55}$$

$$N_{z,-}^{(1)} = -\left(-C_-^{(0)}\frac{z\lambda_D}{\beta_E V_{th}}\left(\frac{dV}{dz}\right) - \alpha\frac{D_+}{D_-}C_-^{(0)} u_z^{(\mathbf{0})}\right) \tag{3.56}$$

The boundary conditions for the *z*-velocity are symmetry at the unit cell boundaries and no-slip at the fiber surface.

Coupling Coefficients

The coupling coefficients from Equation (3.4) are evaluated from the area-averaged velocity and current density in the cases of no applied pressure gradient or no applied voltage gradient:

$$k_{11} \equiv \frac{-\langle \mathbf{v} \rangle\big|_{dV/dx=0}}{\left(\frac{dp}{dx}\right)} \qquad k_{12} \equiv \frac{-\langle \mathbf{v} \rangle\big|_{dp/dx=0}}{\left(\frac{dV}{dx}\right)}$$
$$k_{21} \equiv \frac{-\langle \mathbf{j} \rangle\big|_{dV/dx=0}}{\left(\frac{dp}{dx}\right)} \qquad k_{22} \equiv \frac{-\langle \mathbf{j} \rangle\big|_{dp/dx=0}}{\left(\frac{dV}{dx}\right)} \tag{3.57}$$

For perpendicular flow, the macroscopic velocity and current density are evaluated by:

$$\langle \mathbf{v} \rangle = \frac{u_s}{B} \int_0^B u_x^{(0)}\big|_{x=\pm B}\, dy \tag{3.58}$$

$$\langle \mathbf{j} \rangle = \frac{zF\beta_E}{B} \int_0^B \mathbf{e}_x \cdot \left(\frac{D_+ c_b}{\lambda_D} \mathbf{N}_+^{(1)} + \frac{D_- c_b}{\lambda_D} \mathbf{N}_-^{(1)} \right)_{x=\pm B} dy \tag{3.59}$$

For parallel flow, the macroscopic properties are evaluated by:

$$\langle \mathbf{v} \rangle = \frac{u_s}{\left(2B^2\right)} \int_0^B \int_{-B}^B u_z^{(0)} dx dy \tag{3.60}$$

$$\langle \mathbf{j} \rangle = \frac{zFc_b D_+ \beta_E}{2B^2 \lambda_D} \int_0^B \int_{-B}^B \left(N_{z,+}^{(1)} - \frac{D_-}{D_+} N_{z,-}^{(1)} \right) dx dy \tag{3.61}$$

The exact value of the macroscopic gradients *dp/dx* and *dV/dx* used in the model are unimportant, since the coupling coefficients are constants that indicate a response proportional to any unit gradient.

Numerical Methods

The finite element grid in COMSOL Multiphysics® was generated with a maximum element size scaling factor of 0.55, creating maximum element lengths approximately 4% of 2*B*. The grid density was increased at the cylinder surface to a maximum element size

of 0.005-0.03 in response to the larger field gradients near the surface. This resulted in approximately 3000-15000 elements within the unit cell, which is comparable to the 8080 unit grid used by Chammas *et al*. (Chammas et al. 1994). Increasing the grid size confirmed numerical convergence of the coupling coefficients to within 0.1%. The model was solved with the nonlinear UMFPACK solver using default solver parameters from the Navier-Stokes model with a relative error tolerance of $1x10^{-5}$.

The values of the physical constants used in the model are summarized in Table 3.2, assuming an aqueous sodium chloride solution. The variable parameters in the model include fiber volume fraction, fiber radius, fiber surface charge density and bulk solution ionic strength.

Table 3.2 Physical constants used in the diffuse double layer and Helmholtz double layer hydraulic permeability models, assuming an aqueous sodium chloride solution at room temperature.

Constant	Value
ε	$= 7.08 \times 10^{-10}$ F/m
$V_{th}=RT/F$	$= 2.5 \times 10^{-2}$ V
F	$= 9.648 \times 10^{4}$ C/mol
R	= 8.314 J/mol-K
μ	$= 1 \times 10^{-3}$ Pa-s
$z_+=-z_-=z$	= 1
D_+	$= 1.3 \times 10^{-9}$ m^2/s
D_-	$= 2.0 \times 10^{-9}$ m^2/s

Model Results

Results were validated against the coupling coefficients provided in P. Chammas' thesis for an extracellular matrix system (Chammas 1989). Consistent with her approach, the parallel and perpendicular results are averaged into a single random fiber value using a weighted linear average. As shown in Figure 3.5, there is good agreement between values of k_{ij} from the prior and current models. The values of k_{12} and k_{21}, which should be equal by Onsager reciprocity, agree more closely in the current model. This is perhaps due improvements in computational methods in the last twenty years which provide a more accurate convergence to the true solution. The discrepancy between the values for k_{22} is exactly accounted for if Chammas' results did not include the conductive flux of ions due to an applied voltage gradient in the current density for the parallel k_{22}.

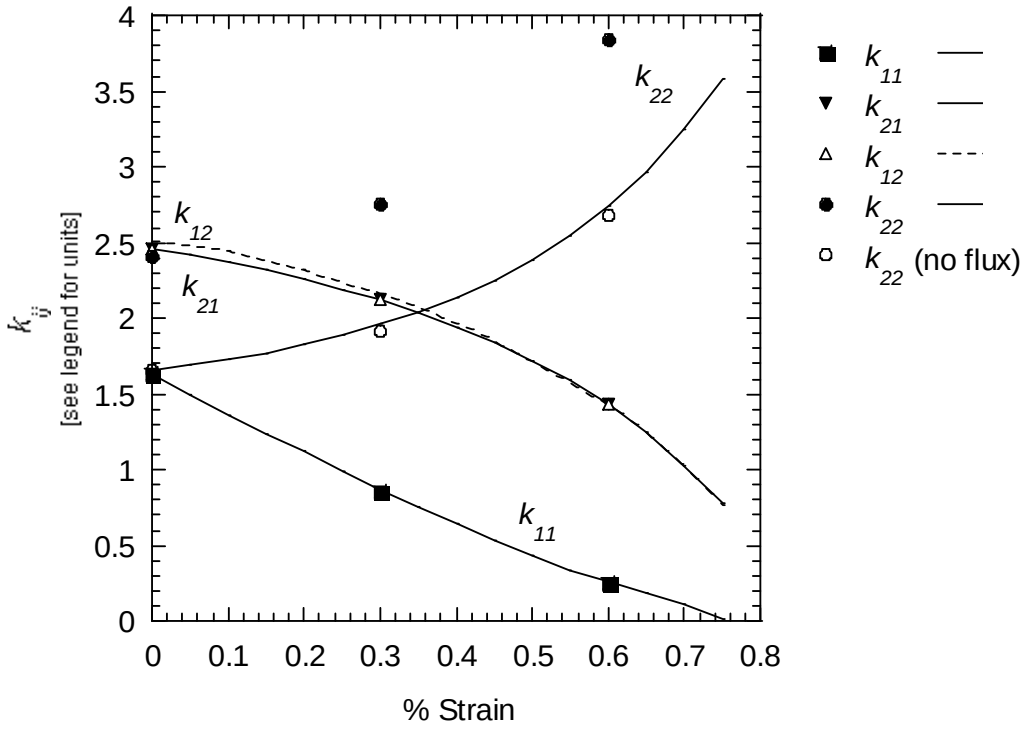

Figure 3.5 Coupling coefficients for a system of GAG fibers with $r_f = 0.9$ nm, $\sigma_s = -120$ mC/m^2, $c_b = 0.15$ M NaCl and $\phi = 0.09/(1\text{-}\%\ \text{strain})$. Curves are results from (Chammas 1989); symbols are data generated from the model. Coupling coefficients are scaled in the following units: k_{11} [x10^{-15} m^4/N-s] (■,—), k_{21} [x-10^{-8} m^2/V-s] (▼,—), k_{12} [x-10^{-8} m^2/V-s] (△,- - -), k_{22} [N/V^2-s] (●,—), k_{22} without the conductive flux for flow parallel to fibers [N/V^2-s] (○,—)

The open circuit permeability (k_{oc}) from the diffuse double layer model was compared against the Helmholtz double layer and neutral fiber models in Figure 3.6. The open circuit hydraulic permeability was evaluated from the four coupling coefficients for flow parallel and perpendicular to the fiber axes, as given by Equation (3.5). The figure compares the three model predictions for fiber volume fractions comparable to the bound GAG fiber densities. The neutral fiber model used the results by Sangani and Acrivos and Drummond and Tahir for periodic arrays of neutral fibers; see equations (3.2) and (3.3). The parallel and perpendicular fiber permeabilities from each of the three models were then averaged into a random fiber system using weighted linear averaging. As seen in Figure 3.6, the Helmholtz double layer model did not asymptotically approach the predictions of the neutral fiber model at high ionic strengths due to assumptions in the model about an impenetrable slip plane at the double layer. The Helmholtz model also

deviated from the diffuse double layer model at low ionic strengths, where the half-distance between the fibers was only twice the Debye length. This deviation indicates that the interactions between the double layers become important at large Debye lengths, so the diffuse double layer model must be used for modeling the GAG-agarose gels. The diffuse double layer model did asymptotically approach the neutral fiber model at high ionic strengths, as was expected for a system with highly screened charges.

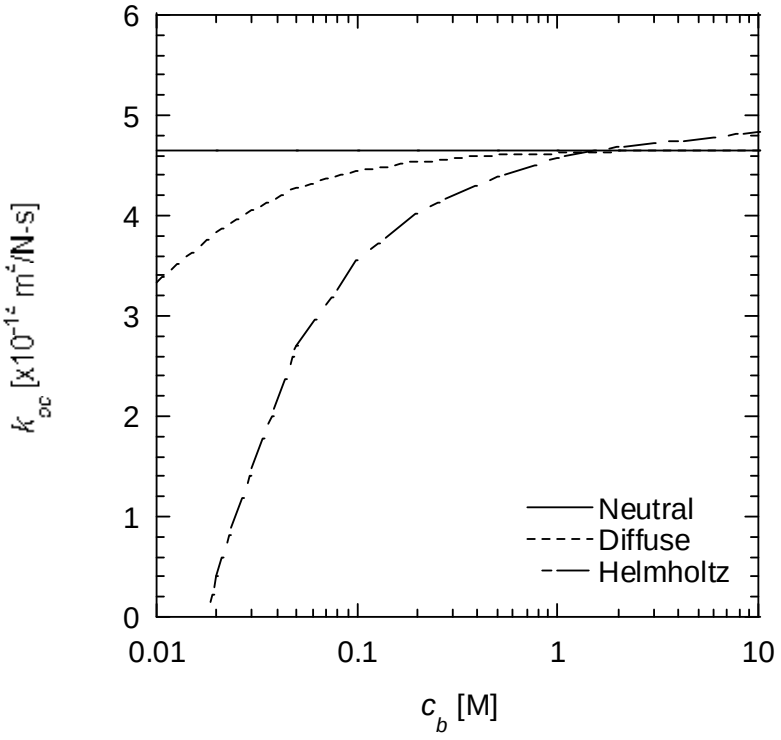

Figure 3.6 Three models for open-circuit hydraulic permeability for 0.37v% system of GAG with r_f=0.5 nm and σ_s=-120 mC/m^2. The neutral fiber model (—) is from Equations (3.2) and (3.3); the Helmholtz model (- —) is based on work by Eisenberg and Grodzinksy (Eisenberg and Grodzinsky 1988); the diffuse model (- - -) is based on the work by Chammas *et al*. (Chammas et al. 1994). Parallel and perpendicular results are combined using weighted linear averaging from Equation (3.26).

As shown in Figure 3.7, the charge effects in the closed-circuit hydraulic permeability (k_{11}) only account for a portion of the charge effects in the open-circuit permeability (k_{oc}) found by the diffuse double layer model in Figure 3.6. The k_{12}, k_{21} and k_{22} coefficients were responsible for the remainder of the charge effect. The neutral hydraulic permeability ($k_{11,neutral}$) has no charge effects and remains constants at all ionic strengths.

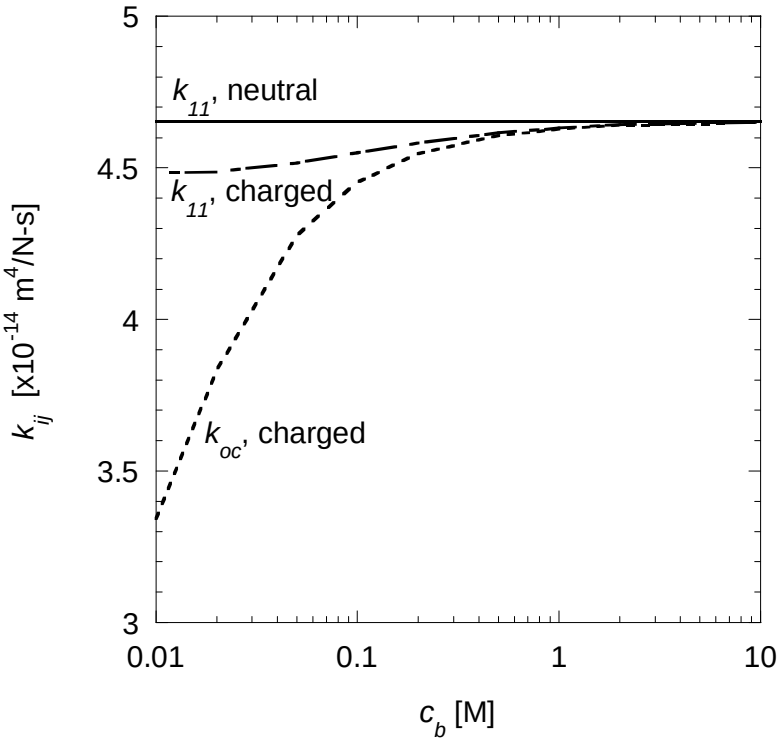

Figure 3.7 Comparison of the open-circuit (k_{oc}, - - -), closed-circuit (k_{11}, - —) and neutral (—) hydraulic permeability for 0.37v% system of GAG with r_f=0.5 nm and σ_s=-120 mC/m^2 with the diffuse double layer model and weighted linear averaging. Models were identical to those used in Figure 3.6.

The values of the individual coupling coefficients used in the previous two figures are shown in Figure 3.8. As seen in Figure 3.8(a), the closed-circuit permeability (k_{11}) for flow parallel to the fibers is independent of ionic strength. The closed-circuit permeability for perpendicular flow in Figure 3.8(b) does decrease slightly (approximately 7%) at lower ionic strengths. However, the coefficients k_{21}, k_{12}, and k_{22} have a strong ionic strength dependence for both fiber orientations. From electrokinetic coupling of the coefficients as given by Equation (3.5), the open-circuit permeability (not shown) decreased by 30% for parallel flow and 20% for perpendicular flow at 0.01 M ionic strength. Using Equation (3.26) to find the permeability of randomly oriented fibers, the resulting open-circuit permeability (previously shown in Figure 3.6 and Figure 3.7) decreased by 28% at 0.01 M relative to high ionic strengths.

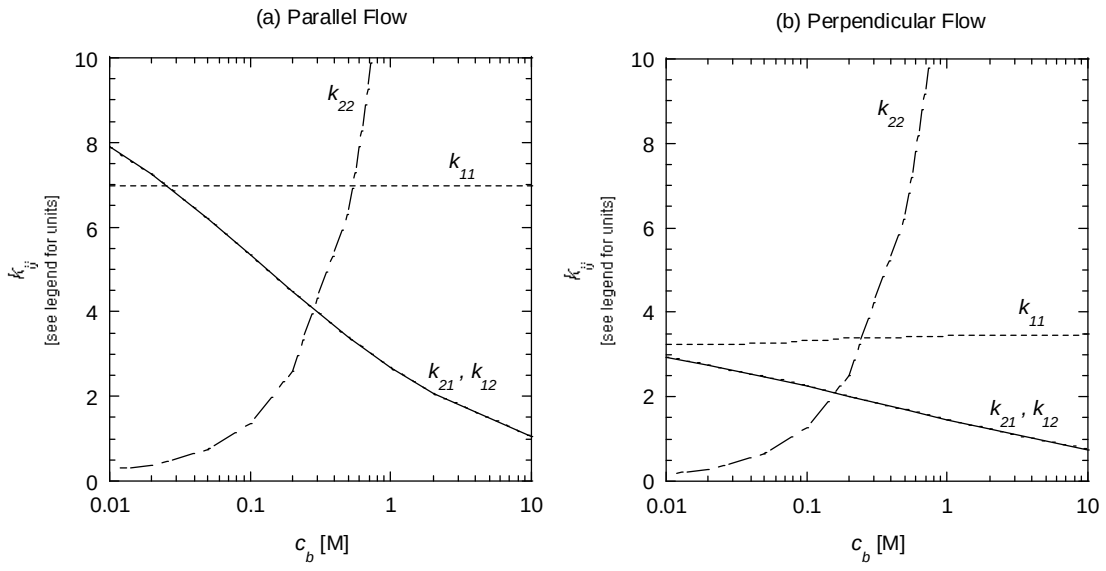

Figure 3.8 Coupling coefficients for a system of 0.37v% GAG with r_f=0.5 nm and σ_s=-120 mC/m^2 based on the diffuse double layer model. (a) Flow parallel to the fiber axes; (b) flow perpendicular to fiber axes. Coupling coefficients are scaled in the following units: k_{11} [x10^{-14} m^4/N-s](- - -), k_{21} and k_{12} [x-10^{-8} m^2/V-s] (—), k_{22} [N/V^2-s] (- —).

Structural versus Donnan Models

The diffuse double layer model and Helmholtz double layer model described in Sections 3.1.2 and 3.2.1 calculate the permeability based on the charge contained on the fiber surface. However, the charge can instead be treated as a uniform concentration throughout the membrane, as done in the Donnan equilibrium model. Such an assumption is most applicable when the spacing between the charged fibers is of the same magnitude as the radius of the fibers. Assuming a unit cell model, the center-to-center distance between two GAG fibers is 15 times the fiber diameter for a 0.37v% gel.

While the GAG fiber spacing in the system cannot fully justify the use of the Donnan model, the comparison in Figure 3.9 between the double layer models and the Donnan model shows that Donnan model does capture the charge effects in the system. The figures show the open-circuit permeability for a periodic array of 0.37v% GAG using the diffuse double layer model and the Donnan model (using Equations (3.2) and (3.3) for the neutral permeability). The Donnan model agrees with the diffuse double layer model to within 18% for perpendicular flow and 31% for parallel flow. While not as precise as the structural models, the Donnan model does provide a reasonable estimate of decreased permeability due to charge with much less computational effort than the diffuse double

layer model and without the breakdown of model assumptions at low ionic strengths found in the Helmholtz double layer model.

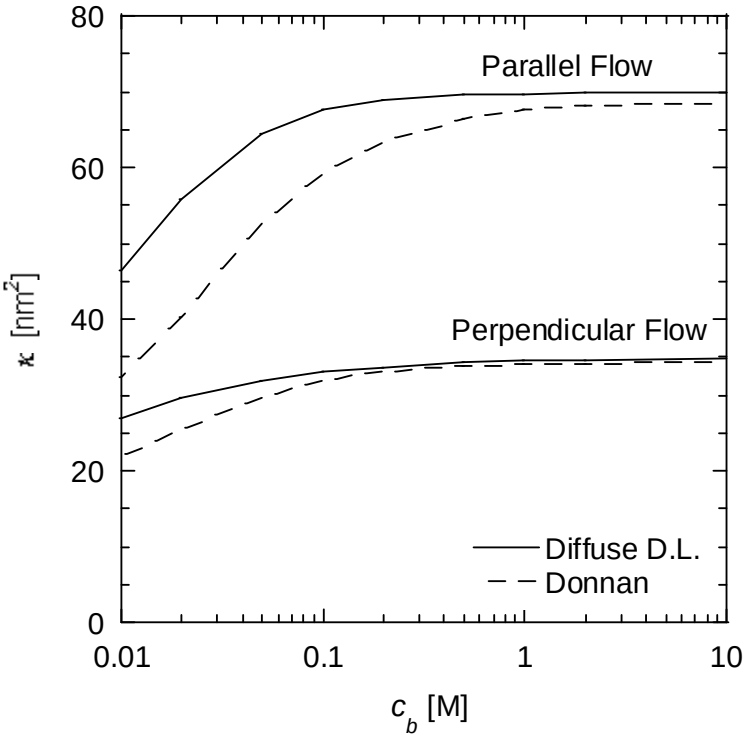

Figure 3.9 Diffuse double layer and Donnan equilibrium models for open-circuit Darcy permeability of a square array of charged fibers. The two sets of curves represent flow parallel and perpendicular to the axis of a system GAG with ϕ=0.00375, r_f=0.5 nm and σ_s=-120 mC/m^2. The Donnan model used Equations (3.2) and (3.3) for the neutral fiber permeability.

3.2.2. Orientation and Population Averaging

Averaging Methods

As reviewed in section 3.1.3, the current literature provides several methods for averaging the hydraulic permeability of different fiber populations, which can yield very different results if the fiber populations are dissimilar. All approaches assume that the fibers are sufficiently dilute that they do not interact, which is virtually impossible to achieved (Mackplow et al. 1994). Even if the limit of infinite dilution were reached, there is no exact solution to the Stokes equation for flow around an isolate cylinder, leading to the so-called "Stokes paradox" (Deen 1998).

The four averaging methods presented in the literature include the inverse averaging used by Jackson and James (Equation (3.25)), the weighted inverse averaging proposed

by Clague and Phillips (Equation (3.28)), the length-weighted inverse averaging developed by Ethier (Equation (3.29)) and weighted linear averaging used by Chammas *et al*. (Equation (3.26)) (Chammas et al. 1994, Clague and Phillips 1997, Ethier 1983, Jackson and James 1982). This section will consider the derivations of these averaging methods, while the following sections will compare their ability to predict permeabilities in various multi-fiber systems.

The averaging methods in Equations (3.25) and (3.28) can both be derived from a force balance on the fibers. The pressure drop across the fibers is equal to the force per area acting on the system, which allows Darcy's Law to be rewritten as:

$$\frac{1}{\kappa_{avg}} = \frac{F_{total}}{\mu\langle \mathbf{v} \rangle \phi_{total} V_{total}} = \frac{F_1 + F_2}{\mu\langle \mathbf{v} \rangle \phi_{total} V_{total}} \tag{3.62}$$

where F_{total} is the total force acting on the fibers, <**v**> is the macroscopic imposed velocity, V_{total} is the total unit volume of the system and F_1 and F_2 are the force acting on fibers of populations 1 and 2, respectively. Letting each population i of fibers contain n_i number of fibers of length $l_{f,i}$ and radius $r_{f,i}$ with a volume fraction ϕ_i, we can define a dimensionless force per fiber length:

$$\tilde{f}_i = \frac{F_i}{n_i l_{f,i} \mu\langle \mathbf{v} \rangle} \tag{3.63}$$

where the fiber length is related to the fiber volume fraction by:

$$\phi_i = \frac{n_i l_{f,i} \pi r_{f,i}^2}{V_{total}} \quad . \tag{3.64}$$

This allows Darcy's Law to be written as:

$$\frac{1}{\kappa_{avg}} = \left(\frac{\phi_1}{\phi_{total}} \frac{\tilde{f}_1}{\pi r_{f,1}^2} + \frac{\phi_2}{\phi_{total}} \frac{\tilde{f}_2}{\pi r_{f,2}^2} \right) \quad . \tag{3.65}$$

For a single fiber system, the dimensionless force per length is equal to:

$$\frac{\tilde{f}}{\pi r_f^2} = \frac{\phi_{total}}{\phi} \frac{1}{\kappa(\phi)} = \frac{1}{\kappa(\phi)} \tag{3.66}$$

where $\kappa(\phi)$ is a function derived for the specific fiber orientation. The question arises if the equivalent expression for one fiber population in a multi-fiber system is:

$$\frac{\tilde{f}_i}{\pi r_{f,i}^2} = \frac{\phi_{total}}{\phi_i \, \kappa_i(\phi_i)} \tag{3.67}$$

or

$$\frac{\tilde{f}_i}{\pi r_{f,i}^2} = \frac{1}{\kappa_i(\phi_{total})} \tag{3.68}$$

There is no rigorous proof that one expression is more valid than the other. If Equation (3.68) is substituted into Equation (3.65), then Equation (3.28) results. This is equivalent to a macroscopic arrangement of single fiber-type layers in series, with both layers at a fiber density ϕ_{total} and with the layer thickness in proportion to ϕ_i. Alternately, if Equation (3.67) is substituted into Equation (3.65), then a generalized expression for Equation (3.25) results:

$$\frac{1}{k_{avg}} = \frac{1}{k_1(\phi_1)} + \frac{1}{k_2(\phi_2)} \quad . \tag{3.69}$$

These results can easily be extended to systems with more than 2 populations of fibers. It should be noted that in the limit of both fiber properties becoming identical, Equation (3.28) will correctly reduce to the single fiber expression; however, Equation (3.69) will not.

Ethier's derivation of Equation (3.29) begins with the assumption that the pressure drops are additive instead of the forces being additive. The length over which each pressure drop occurs is proportional to the number of fibers of type *i*. The resulting system is equivalent to two single-fiber systems in series, which allows Ethier to find the resulting length-weighted inverse averaging. If both fibers have the same radius, then equations (3.29) and (3.28) are identical.

The averaging method in Equation (3.26) is developed by extension to orientation averaging of fibers in heat conduction and electrophoresis. As discussed in Section 3.1.3, when heat conduction or electrophoresis of a randomly-oriented rod is averaged over all spatial orientations, the result is one-third of the parallel result plus two-thirds of the perpendicular result. Stigler has shown that this result is true for any vector field that is linearly related to an applied field. The equivalent generalized averaging formula is:

$$k_{avg} = \frac{\phi_1}{\phi_{total}} k\left(\phi_{total}\right) + \frac{\phi_2}{\phi_{total}} k\left(\phi_{total}\right) \quad . \tag{3.70}$$

It should be remembered that an exact derivation of Equation (3.70) from flow around a randomly oriented fiber is not possible, and Equation (3.70) is only formulated by analogy to electrophoresis or heat conduction. Equation (3.70) is equivalent to a system with layers of a single fiber-type arranged parallel to the flow, each layer with a fiber density ϕ_{total} and a cross-sectional area proportional to ϕ_i.

Critique of Averaging Methods – Orientation and Radius

The four averaging methods presented are: inverse averaging (3.69), weighted inverse averaging (3.28), length-weighted inverse averaging (3.29) and weighted linear averaging (3.70). Each averaging method has been applied to specific situations in the literature, without evaluation if one method is more appropriate than another. Since all of these averaging methods assume a dilute fiber system, they will be an approximation to the true system behavior. The following section will evaluate the applicability of the averaging methods for systems with random fibers (multiple orientations), multiple fiber radii, and multiple fiber surface charges.

For fibers in random orientations, they can be idealized as a population of fibers with one-third of the fibers oriented along each of the *x*, *y*, and *z* axes. The basis of this assumption was reviewed in Section 3.1.3. Assuming a fiber population with one-third parallel and two-thirds perpendicular to the applied flow, Figure 3.10 compares the three averaging methods against the numerical simulation results of Clague and Phillips and Clague *et al.* (Clague et al. 2000, Clague and Phillips 1997). The curves show the predicted permeability based on each averaging methods, while the symbols are permeabilities reported from the simulations. Equations (3.2) and (3.3) were used for modeling the 2-dimensional periodic fiber arrays. All models agree well with the simulation data and deviate by at most 40%.

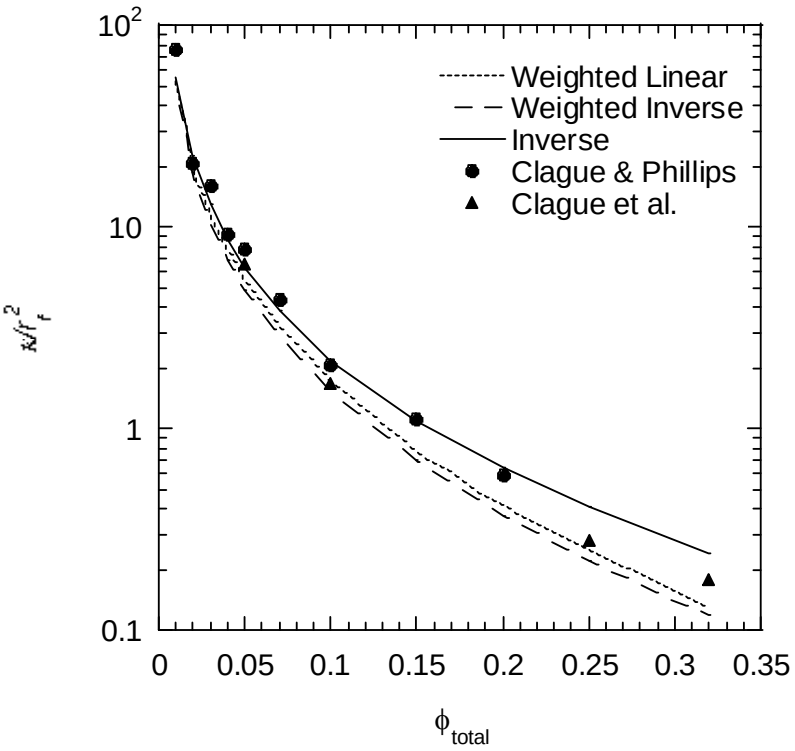

Figure 3.10 Dimensionless Darcy permeability of randomly oriented fibers. Lines for three averaging methods for periodic arrays of one-third parallel and two-thirds perpendicularly-oriented fibers are compared to the Clague and Phillips (●)(Clague and Phillips 1997) and Clague *et al.* (▲)(Clague et al. 2000) numerical simulations for a random system.

In addition to orientation averaging, averaging between fibers of different radii is also important for the hydraulic permeability of the agarose-GAG membranes. Clague and Phillips performed simulations of the hydraulic permeability of bimodal fibers in ordered and random orientations (Clague and Phillips 1997). They first considered a periodic 2-dimenionsal array of small and large fibers with flow perpendicular to their axes. The fibers were present in equal numbers, and the radius of the large fiber to the small fiber was 2:1. The results of their simulation are compared to the four averaging methods in Figure 3.11. The permeabilities of the monomodal fibers used in the averaging methods were found from Equation (3.3) for a periodic square array with perpendicular flow. The difference between the averaging methods is less than 70%, though the simulation appears to agree most closely with the inverse and weighted-inverse models.

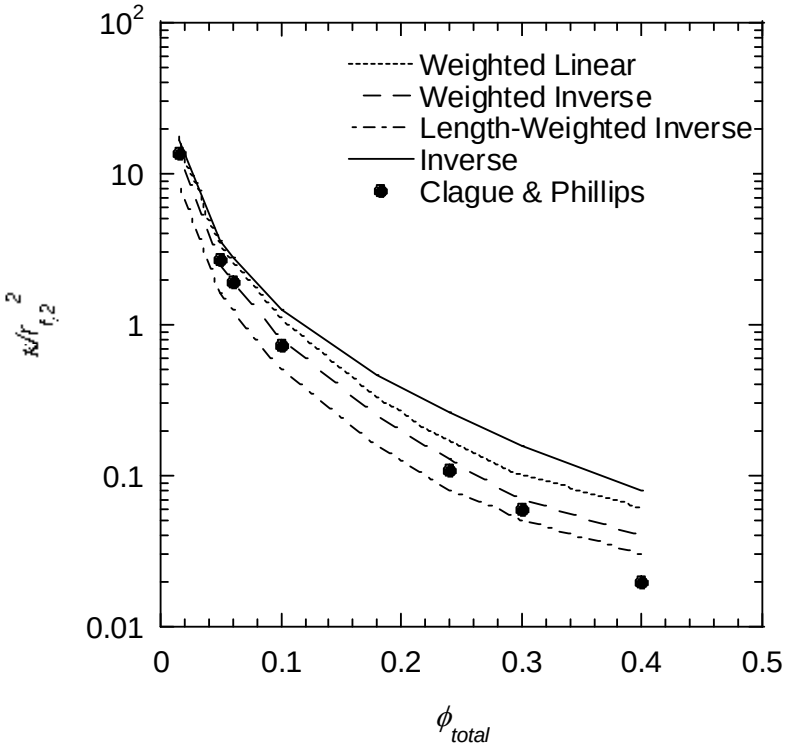

Figure 3.11 Dimensionless Darcy permeability of flow perpendicular to a periodic, bimodal fiber array. The radius of the larger fiber ($r_{f,2}$) is twice the radius of the smaller fiber; fibers are present in a 1:1 number ratio. Lines for four averaging methods are compared to the Clague and Phillips (●)(Clague and Phillips 1997) numerical simulations.

The averaging methods are also compared for a random fiber system similar to that reported for agarose. The matrix is composed of 87% of fine fibers with a 1.5 nm radius and 13% of coarse fibers with a 4.5 nm radius. The simulation results from Clague and Phillips in Figure 3.13 are compared to the four averaging methods with Equation (3.24) for random monomodal fibers. For this system, there is nearly a five-fold difference between averaging methods. The simulation results fall in the middle of the range. As in the ordered fiber system in Figure 3.11, the bimodal random fiber simulations are most closely matched by the inverse and weighted-inverse averaging methods.

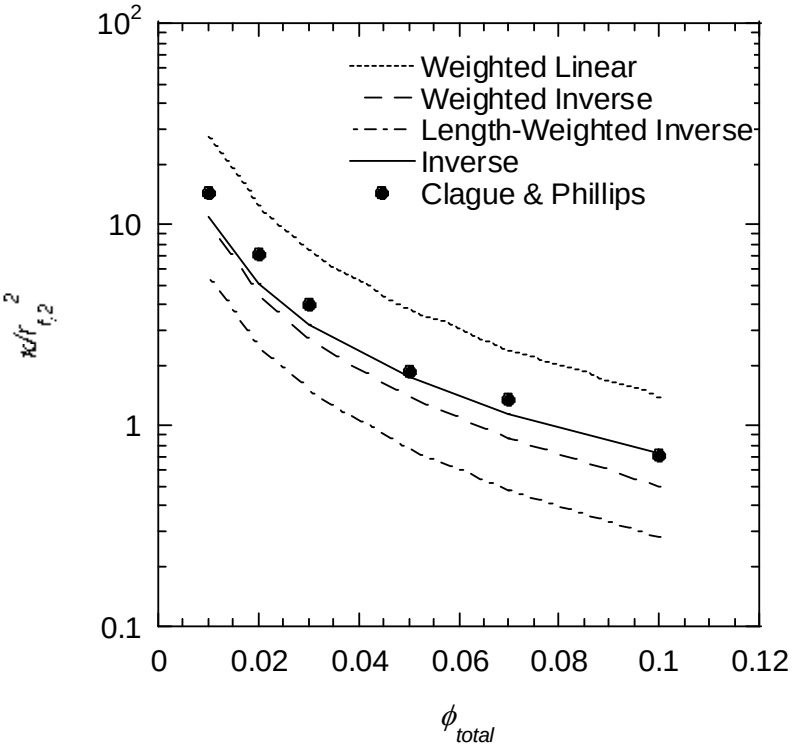

Figure 3.12 Dimensionless Darcy permeability of flow a random, bimodal fiber array. The radius of the coarse fiber ($r_{f,2}$) is 4.5 nm and the fine fiber is 1.5 nm; the fibers are 13% coarse and 87% fine, by number. Lines for four averaging methods are compared to the Clague and Phillips (●)(Clague and Phillips 1997) numerical simulations.

A second bimodal, random fiber system similar to a collagen/proteoglycan gel was also simulated by Clague and Phillips. The collagen ($r_{f,2}$ = 20 nm) had a fixed composition of ϕ_2 = 0.05, while the proteoglycan ($r_{f,1}$ = 3 nm) constituted the balance of the total fiber volume fraction. As shown in Figure 3.13, the averaging methods again span over an order of magnitude, with the simulation results falling in the middle. Similar to the prior to bimodal fiber examples in Figure 3.11 and Figure 3.12, the inverse and weighted-inverse averaging methods provide the best estimate of the simulation results.

(Note that correspondence with the authors of (Clague and Phillips 1997) confirmed several typographic errors in their paper. In their Figure 9, the ordinate is normalized by the larger fiber radius. In Figure 10, the ordinate was incorrectly labeled as k/r_f^2; it should be k (nm^2). In Figure 11, the ordinate is mislabeled by a factor of ten; it should range from 0.1 to 10.0.)

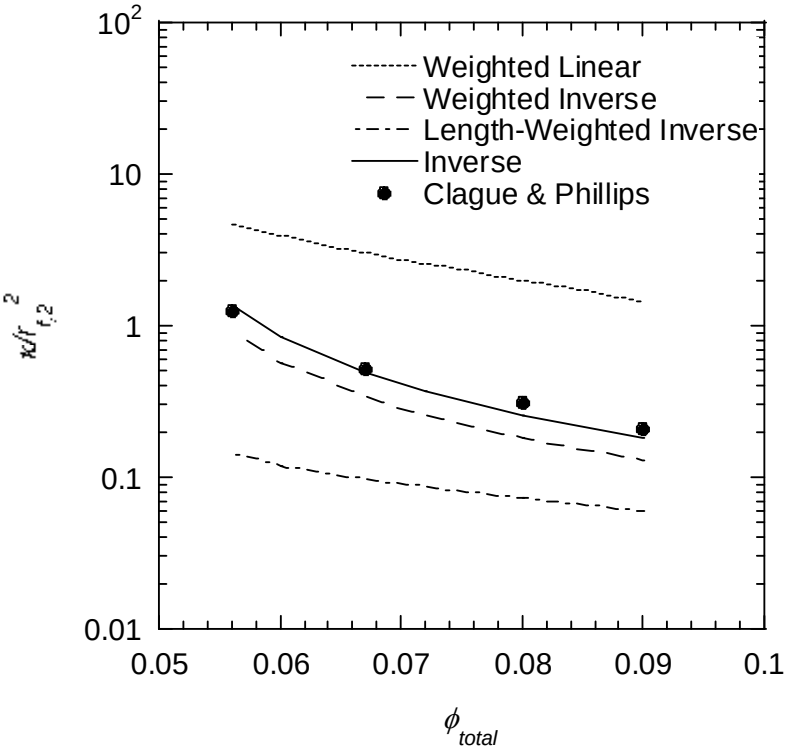

Figure 3.13 Dimensionless Darcy permeability of flow through a random, bimodal fiber array. The radius of the coarse fiber ($r_{f,2}$) is 20 nm and the fine fiber is 3 nm; the coarse fiber volume fraction is constant at $\phi_2 = 0.05$. Lines for four averaging methods are compared to the Clague and Phillips (●)(Clague and Phillips 1997) numerical simulations.

Critique of Averaging Methods – Charge

Based on the simulations by Clague and Phillips for random and bimodal fiber arrays, a neutral multi-fiber system can be well-represented by either an inverse or weighted-inverse average of the individual fiber populations. However, there is no published data on permeability in charged multi-fiber systems. To confirm that the inverse and weighted-inverse averaging methods are still appropriate for charged fiber systems, the diffuse double layer model presented in Section 3.2.1 was adapted to model a 2-fiber system with different surface charge densities and/or different fiber radii.

Since the model depends on having a unit cell that is both symmetric and repeating, the geometry of the 2-fiber array is limited. However, a square lattice can be easily generated that has a one-to-one ratio between two fiber types, shown in Figure 3.14. The boundary conditions at both fiber surfaces are the same as those for the single fiber in

Table 3.1, though the charge can be different between the $R_{f,1}$ and $R_{f,2}$ surfaces. The unit cell width B is found by using ϕ_1 and $R_{f,1}$.

The combined 2-fiber model is compared to the averages of single-fiber models using the diffuse double layer simulation in Section 3.2.1 for charged ordered fibers and the Equations (3.2) and (3.3) for square arrays of neutral fibers.

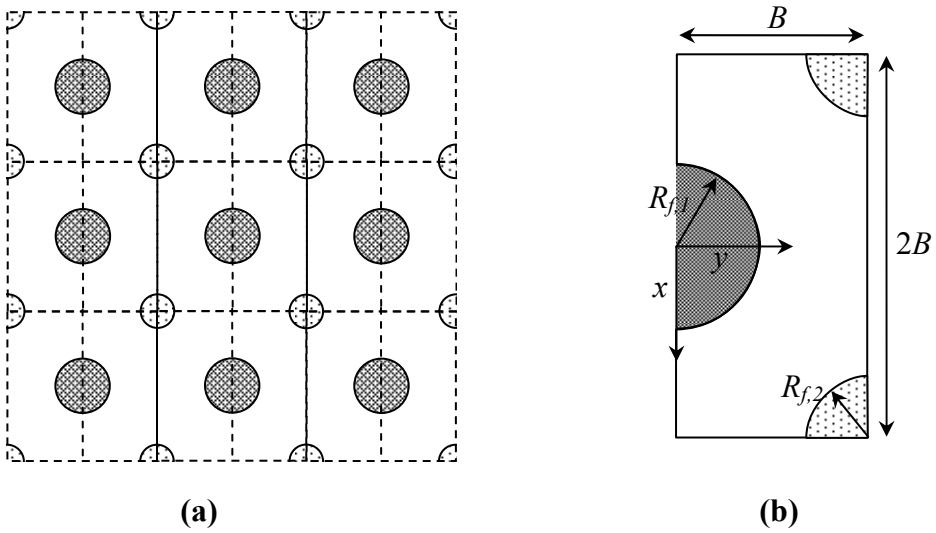

Figure 3.14 (a) Square array of two fiber populations with unit cell boundaries. (b) Single unit cell for fibers with radii $R_{f,1}$ and $R_{f,2}$ and unit cell width B.

The first case considers two fiber populations with the same radius and different charge. Fiber population *1* has a surface charge of -120 mC/m^2 and fiber population *2* is uncharged, while both fibers have $r_{f,1}$=$r_{f,2}$=0.9 nm and ϕ_1=ϕ_2. The open-circuit hydraulic permeability of the square array was simulated for flow parallel and perpendicular to the fiber axis. Figure 3.15 (with ϕ_1=0.09) and Figure 3.16 (with ϕ_1=0.02) compare the open-circuit permeability from the simulations (symbols) with the permeability predicted by the three averaging methods (lines). The results are shown in each Figure for flow both perpendicular and parallel to the fiber axes. For both fiber volume fractions, the weighted-linear and weighted-inverse averaging methods provide good agreement for both parallel and perpendicular flow. Unlike the prior results for neutral fibers, the inverse averaging method no longer appears to provide a good fit to the charged fiber simulations.

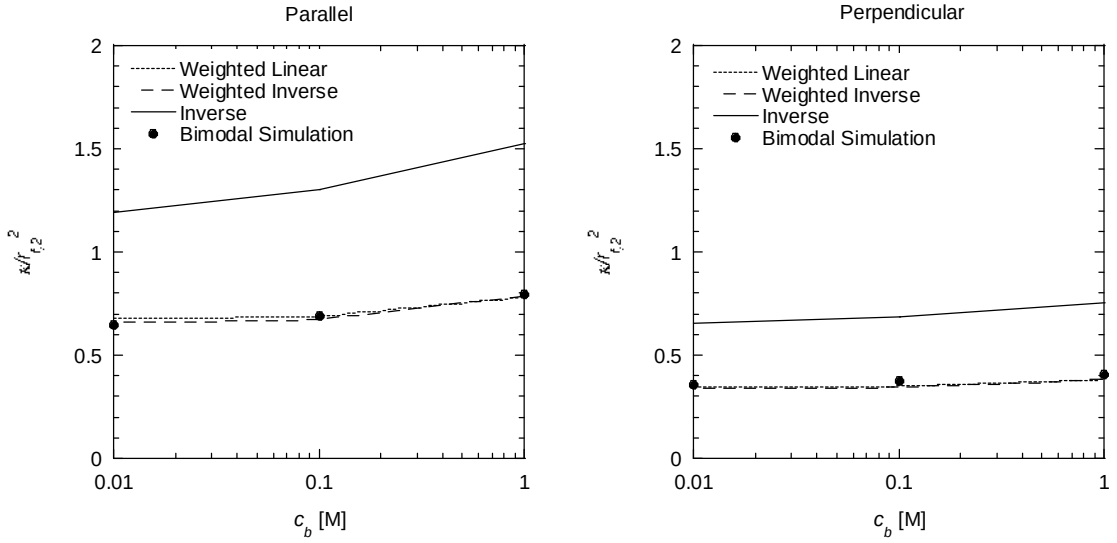

Figure 3.15 Open-circuit hydraulic permeability for a square array of fibers with radii $r_f = 0.9$ nm and $\phi_{total} = 0.18$ ($\phi_1 = 0.09$) with an equal number of neutral fibers (σ_s=0 mC/m^2) and charged fibers (σ_s = -120 mC/m^2). Lines for three averaging methods are compared to the numerical simulations (●) of the system.

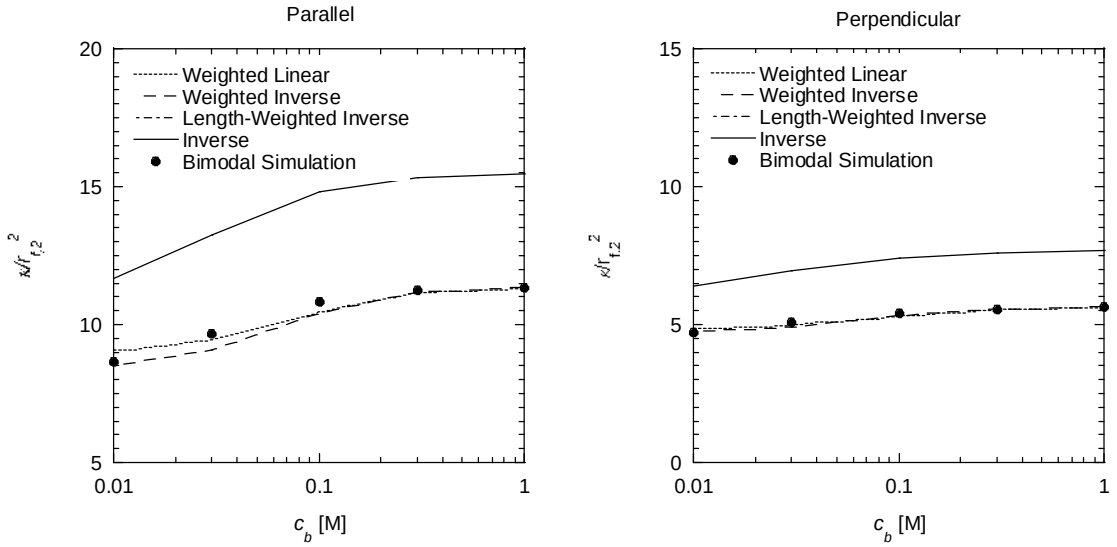

Figure 3.16 Open-circuit hydraulic permeability for a square array of fibers with radii $r_f = 0.9$ nm and $\phi_{total} = 0.04$ ($\phi_1 = 0.02$) with an equal number of neutral fibers ($\sigma_s = 0$ mC/m^2) and charged fibers (σ_s = --120 mC/m^2). Lines for three averaging methods are compared to the numerical simulations (●) of the system.

As suggested by the differences between the simulation results in Figure 3.15 and Figure 3.16, the decrease in the permeability due to charge effects is a function of both ionic strength and fiber volume fraction. The decrease in open circuit permeability relative to neutral permeability is shown in Figure 3.17 for periodic fiber arrays with either all-charged or half-charged/half-neutral fibers ("1 Fiber" and "2 Fiber", respectively). In general for a given ionic strength, charge will cause a larger decrease in permeability in systems with denser fibers. A minimum values of $\kappa_{oc}/\kappa_{neutral}$ occurred for 0.01 M. The minimum is a result of competition between the increased in neutral permeability at higher ϕ and the corresponding increase in fixed charge density. A similar results is found with the Donnan model, as discussed in more depth in my published work (Mattern and Deen 2008). While the two-fiber system contains half the total charge in the single-fiber system (with other properties held constant), the decrease in the permeability of the two-fiber system is not simply half that of the single-fiber system.

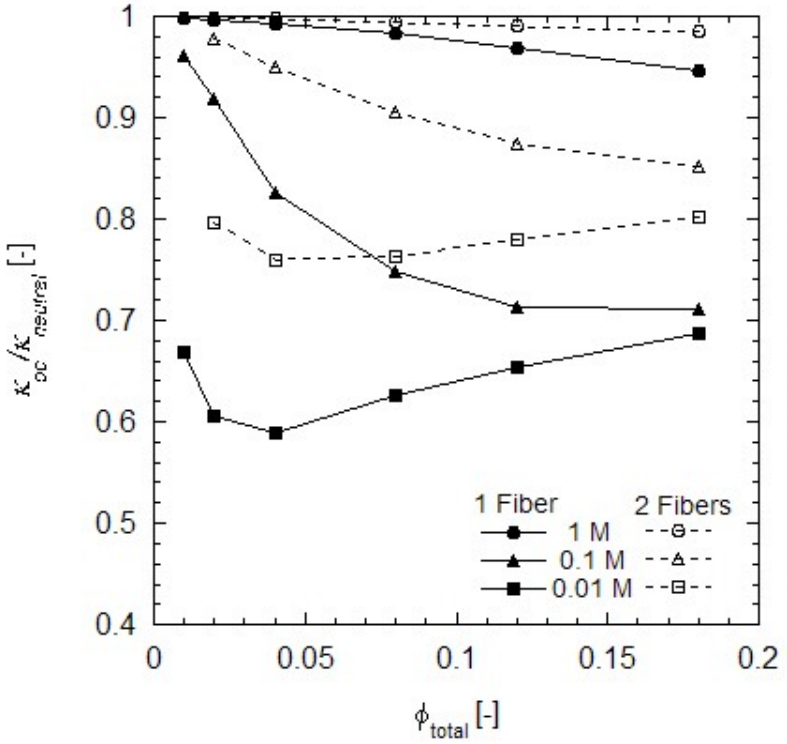

Figure 3.17 Open circuit Darcy permeability relative to neutral permeability for axial flow through arrays of charged and neutral fibers. Closed symbols are the permeability through an array of charged fibers with r = 0.9 nm and σ_s = -120 mC/m^2. Open symbols are the permeability through a two fiber array with $r_1 = r_2$ = 0.9 nm, $\sigma_{s,1}$ = -120 mC/m^2 and $\sigma_{s,2}$ = 0. The open circuit permeability used the diffuse double layer model, and the neutral permeability was calculated with Equation (3.2).

The second case considered for a charged multi-fiber array involved charged fibers in a square array with fine charged fibers and coarse neutral fibers. The fine fibers (population 1) have a radius $r_{f,1}$=0.5 nm, a volume fraction ϕ_1=0.004, and a surface charge density $\sigma_{s,1}$=-120 mC/m^2. The coarse fibers (population 2) have a radius $r_{f,2}$=1.6 nm, a volume fraction ϕ_2=0.041, and no surface charge. As will be discussed in later sections, this idealized model is comparable to the agarose-GAG membranes used for experiments. The open-circuit permeability of this two-radii array is shown in Figure 3.18, along with the permeabilities from the four mixing rules. Similar to the charged single-radii system in Figure 3.15, the permeability from the bimodal simulation is bracketed by the four averaging methods. However, the different averaging methods now span a much larger range (±75% of the two-radii simulation for perpendicular flow) than the previous results for equal fiber radii (±35% of the simulation). Similar to the neutral bimodal fiber arrays in Figure 3.11 and Figure 3.13, the inverse and weighted-inverse averaging methods most closely predict the permeability of the charged bimodal fiber array.

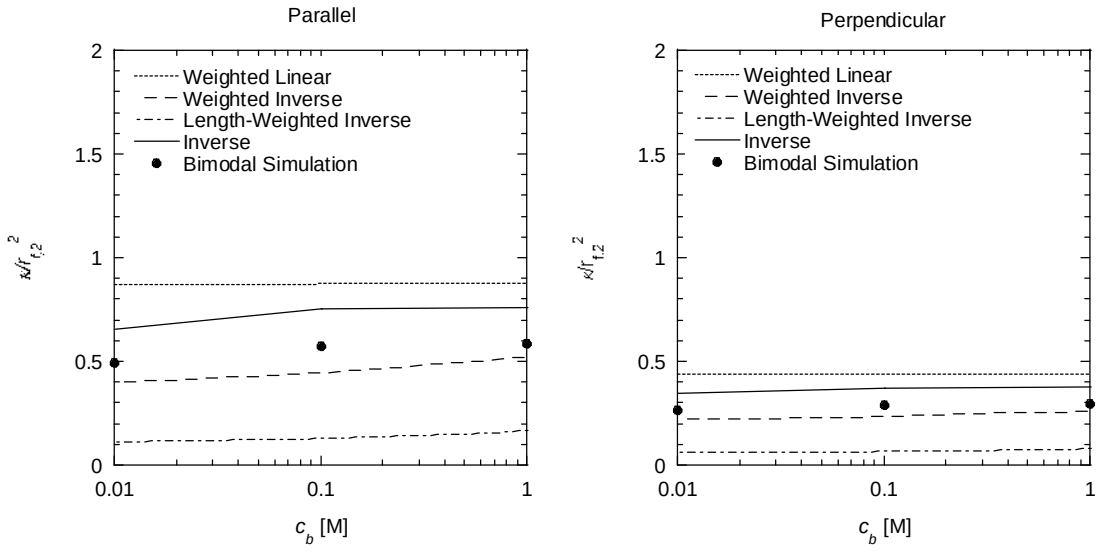

Figure 3.18 Open-circuit hydraulic permeability for a square array of fibers similar to an agarose-GAG membrane. Fiber population *1* ("GAG") has $r_{f,1}$=0.5 nm, ϕ_1=0.004 and $\sigma_{s,1}$=-120 mC/m^2. Fiber population *2* ("agarose") has $r_{f,2}$=1.6 nm, ϕ_2=0.041 and σ_{s2}=0 mC/m^2. Lines for four averaging methods are compared to the numerical simulations (●) of the system.

There is no data in the literature for the hydraulic permeability of a random array of charged fibers. Therefore, any speculations about orientation averaging of charged fibers must be based on the previous data for periodic charged fibers or random neutral fibers.

Critique of Averaging Methods – Conclusions

The comparisons of the four averaging methods for single fiber populations to the corresponding results for multi-fiber systems show that no single averaging method can fully predict the hydraulic permeability of the composite system. All averaging methods involve assumptions of how the interactions between the fiber populations can be approximated by single-fiber models. For example, the weighted-inverse averaging method is algebraically equivalent to a 2-region gel with each fiber type separated into a region with a fiber density ϕ_{total}, with the regions arranged in series. The weighted linear average is the same, expect the regions would be arranged in parallel. The inverse averaging method assumes that fiber interactions only occur between similar fiber types, rather than interactions with the nearest fiber neighbor based on ϕ_{total}.

To determine the most appropriate averaging method to use for evaluating the hydraulic permeability of multi-fiber systems, the accuracy of the method for systems with fibers of different orientations, radii and/or charge must all be considered. The root mean square (RMS) error of each averaging method, as a percentage of the simulation, provides a normalized way of comparing the averaging methods across the different multi-fiber systems. The RMS error of the averaged permeability relative to the composite simulation permeability is summarized in Table 3.3 for the various fiber arrays presented previously in this section. Here, the relative RMS error is defined by:

$$s = \sqrt{\frac{1}{n}\sum_{i=1}^{n}\left(\frac{\kappa_{averaged}(x_i)}{\kappa_{simulation}(x_i)} - 1\right)^2} \times 100\% \tag{3.71}$$

where x_i is the abscissa variable, n is the number of points, $\kappa_{averaged}$ is the permeability based on averaging single fiber permeabilities and $\kappa_{simulation}$ is the permeability based on the simulation of the composite.

Table 3.3 Root mean squared relative error of averaging models compared to simulation results for fiber systems with multiple orientations, radii, and/or surface charges.

	Weighted Linear	Weighted Inverse	Length-Weighted Inverse	Inverse
Orientation *(Figure 3.10)*				
vs. Clague & Phillips	25%	32%	- *	14%
vs. Clague et al.	19%	25%	- *	10%
Radius				
Figure 3.11	76%	38%	33%	138%
Figure 3.12	87%	32%	62%	19%
Figure 3.13	485%	36%	80%	13%
Charge *(Figure 3.15)*				
Parallel	3%	2%	- *	88%
Perpendicular	6%	6%	- *	83%
(Figure 3.16)				
Parallel	4%	4%	- *	36%
Perpendicular	2%	2%	- *	36%
Charge+Radius *(Figure 3.18)*				
Parallel	61%	19%	76%	31%
Perpendicular	55%	16%	74%	29%
All Neutral Simulations (*n=30*)	**186%**	**33%**	**48%**	**69%**
All Charged Simulations (*n=34*)	**24%**	**8%**	**32%**	**49%**
All Simulations (*n=64*)	**128%**	**24%**	**40%**	**59%**

** - Model identical to weighted inverse method under the given conditions.*

For most conditions, the RMS error between the weighted-inverse and inverse models and the simulation results is less than 35%. However, there was significant deviation with inverse averaging for the periodic bimodal array (Figure 3.11) and the charged fibers in Figure 3.15. Weighted inverse averaging provides a more consistent prediction of the multi-fiber permeability for a variety of fiber types, including charged fibers. This can be seen in Figure 3.19, which graphically shows the deviations of the averaging rules from

simulation results. The weighted linear and length-weighted inverse have several instances of significantly over- or under-estimating the permeability, respectively. The inverse averaging method over-estimated the permeability of some of the neutral fibers and nearly all of the charged fiber cases. The weighted-inverse averaging tends to fall closest to the simulation results for a wide range of neutral and charged fibers.

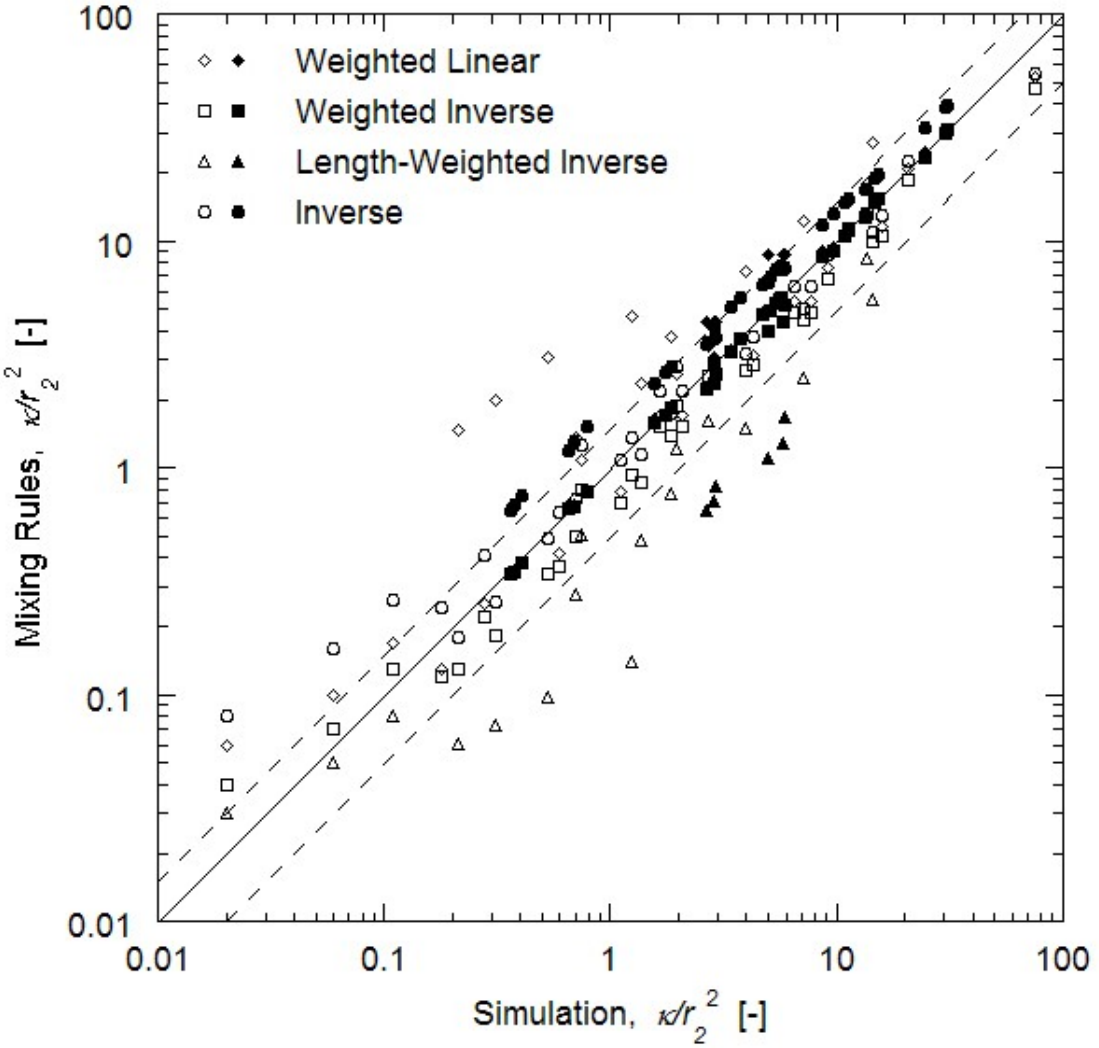

Figure 3.19 Darcy permeability of complex fiber systems as predicted by single-fiber mixing rules and multi-fiber simulations. The solid line is the unity line and the dashed lines are ± 50%. Open symbols are data for neutral fiber systems from the literature (Clague et al. 2000, Clague and Phillips 1997) and solid symbols are charged fiber systems using the diffuse double layer model.

Based on these results, the weighted-inverse averaging method will be used for predicting the permeability of a composite of multiple fibers with differing radii and/or charge and for predicting the permeability of a random fiber array based on parallel and perpendicular flow models.

Charge Averaging – Diffuse Double Layer versus Donnan Models

The comparisons of averaging methods for charged fibers discussed above use the structurally-based diffuse double layer model. However, as seen in Figure 3.15 and Figure 3.18, the choice of averaging method can change how the permeability decreases with decreasing ionic strength. An alternate approach for modeling charge effects in multi-fiber systems is to use the Donnan model In this approach, both fiber types are treated as neutral. Then a fiber averaging method is used to account for the combined steric effects and the Donnan model can be used to account for charge effects.

This Donnan approach was applied to the two-fiber system used in Figure 3.15, where both fibers have the same radius but only one is charged. In the neutral case, the system is composed of only a single fiber type with r_f=0.9 nm. The neutral permeability was calculated with Equations (3.2) or (3.3) for a neutral square array; no fiber averaging method was necessary. The surface charge of -120 mC/m^2 on half the fibers was converted into an equivalent homogeneous volumetric charge of c_m=-250 meq/L for the Donnan model. A comparison of the permeabilities predicted by the diffuse double layer model and the Donnan model are shown in Figure 3.20. Results are shown for two total fiber volume fractions: (a) ϕ_{total}=0.18 and (b) ϕ_{total}=0.04. The Donnan model agrees well with the diffuse double layer results for flow perpendicular to the fiber axes at both fiber volume fractions. For flow parallel to the fiber axes, the Donnan model provides good agreement at high volume fractions, though it slightly over predicts the charge effect at low volume fractions. A similar over prediction was observed in the single-fiber array in Figure 3.9 at lower fiber volume fractions, when the spacing between the charged fibers was much larger than the fiber radius.

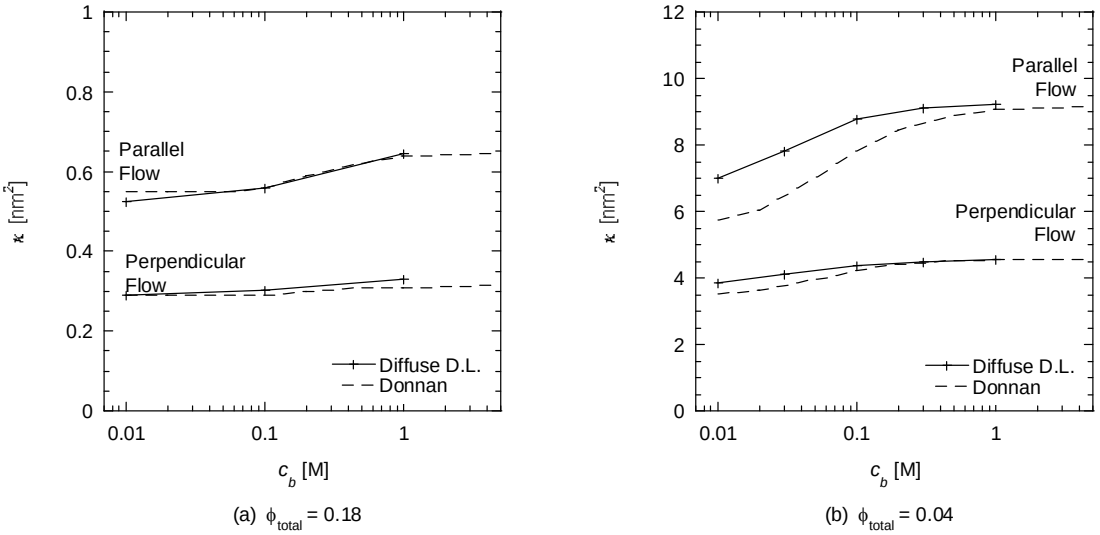

Figure 3.20 Diffuse double layer and Donnan models for the open-circuit Darcy permeability through a square array of fibers with radii r_f=0.9 nm and an equal number of neutral fibers (σ_s=0 mC/m^2) and charged fibers (σ_s=-120 mC/m^2). The graphs show results for flow parallel and perpendicular to the fiber axes for a total fiber volume fraction of (a) ϕ_{total}=0.18 and (b) ϕ_{total}=0.04.

The Donnan model was also applied to the charged bimodal system in Figure 3.18, where the charged fibers have a different radius ($r_{f,1}$=0.5 nm, $\sigma_{s,1}$=-120 mC/m^2) than the neutral fibers ($r_{f,2}$=1.6 nm). The fibers volume fractions were ϕ_1=0.004 and ϕ_2=0.041. The Donnan model used weighted-inverse averaging of Equations (3.2) or (3.3) to model the neutral permeability. The Donnan model for the charged bimodal system is shown in Figure 3.21, as well as two approaches for the diffuse double layer model. The "2 Fiber" model included both charged and neutral fibers in one simulation, as diagrammed in Figure 3.14; these results were considered the most accurate since it includes interactions between the two fiber types. The "1 Fiber" model used the diffuse double layer model for a single charged fiber (as shown in Figure 3.4), then used weighted-inverse averaging add the permeability of the neutral fibers (given by Equation (3.2) or (3.3)).

As seen in Figure 3.21, the Donnan model and the double layer models all approach the same neutral limit at high ionic strengths. Even though the charged fiber spacing does not formally allow the charge to be considered homogeneous, the Donnan model appears to capture the effect of charge fairly accurately at lower ionic strength. However, there was relatively poor agreement between the 1-Fiber and 2-Fiber diffuse double layer models at intermediate ionic strengths. This suggests that the fiber mixing rule in the 1-

Fiber model may distort the effect of charge on permeability in a multi-fiber system. Both the Donnan model and the fiber mixing rule in the 1-Fiber model employ simplifying assumptions to estimate the hydraulic permeability. The errors associated with these assumptions may make one model more appropriate than the other for a given fiber system. For the agarose-GAG-like fiber system in Figure 3.21, both models provide useful insight into the role of charge.

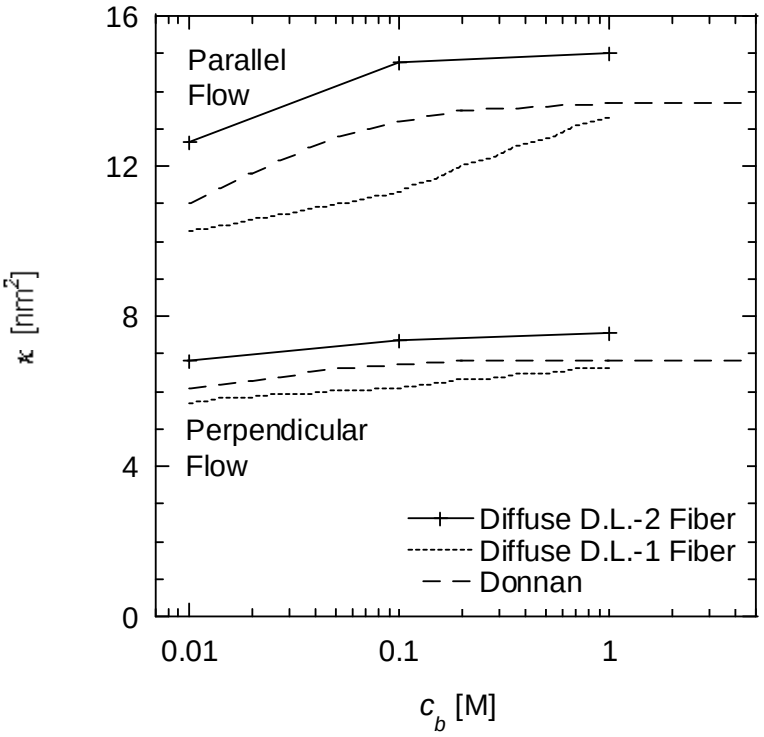

Figure 3.21 Diffuse double layer and Donnan models for the open-circuit Darcy permeability through a square array of fibers similar to an agarose-GAG membrane. The graphs show results for flow parallel and perpendicular to the fiber axes where fiber population *1* ("GAG") has $r_{f,1}$=0.5 nm, ϕ_1=0.004 and $\sigma_{s,1}$=-120 mC/m^2 and fiber population *2* ("agarose") has $r_{f,2}$=1.6 nm, ϕ_2=0.041 and σ_{s2}=0 mC/m^2. The diffuse double layer "2 Fiber" model uses the model in Figure 3.14, the "1 Fiber" model uses the model in Figure 3.4 plus weighted-inverse averaging of Equation (3.2) or (3.3), and the Donnan model uses weighted-inverse averaging of Equation (3.2) or (3.3).

3.2.3. Non-Homogeneous Fiber Models

Model Selection

Using a homogeneous fiber model, such as the empirically-fit model by Clague *et al.* for randomly oriented fibers (Equation (3.24)), the hydraulic permeability of a gel can be predicted from the volume fraction of fibers and the fiber radius (Clague et al. 2000).

However, as discussed in Section 3.1.4, observations of agarose structure and discrepancies between homogeneous models and experimental data suggest that a heterogeneous model for agarose may be needed. Hydraulic permeability and macromolecule sieving can be explained if the gel has multiple regions with higher and lower fiber densities. Microscopy and other techniques show uneven distributions of fiber spacing, which is consistent with the theories of fiber aggregation during gelation.

Five two-region models for agarose heterogeneity were proposed in Section 3.1.4: series, parallel, checker-board, spherical clumps and spherical voids (Figure 3.3). For a given heterogeneous region model and homogeneous fiber model, the permeability through the entire system is fully specified by the total fiber volume fraction ϕ_{total} and the two parameters ϕ_2/ϕ_{total} and ε_2. The volume fraction of fibers in region 1 can be found by volume conservation for the entire system:

$$\frac{\phi_1}{\phi_{total}} = \frac{1-\left(\phi_2/\phi_{total}\right)\varepsilon_2}{1-\varepsilon_2}. \tag{3.72}$$

Figure 3.22 compares the effective hydraulic permeability of the heterogeneous system (k_{eff}) to the hydraulic permeability of a homogeneous fiber system (k_{homog}) with the same total fiber volume fraction. The abscissa is the ratio of the fiber density in region 1 relative to region 2; at $\phi_1/\phi_2=1$, the system is homogeneous and $k_{eff}/k_{homog}=1$. Based on previously published experimental data for 1.9v% and 3.8v% agarose gels, the effective permeability was 3-4 times higher than that predicted by homogeneous fiber models (Johnson and Deen 1996b). As shown in Figure 3.22, the permeability of two layers in series does not exceed the permeability of a homogeneous system with the same total fiber volume fraction (i.e. $k_{eff}/k_{homog}\leq 1$ for series). Both the parallel and spherical models can yield a permeability higher than the equivalent homogeneous permeability, which is in agreement with the experimental observations of agarose. However, the spherical model has a permeability only slightly higher than the homogeneous system when matrix fiber density is higher than the spherical density ($\phi_1/\phi_2>1$), which suggests that a model of lower density "voids" within agarose cannot explain the observed permeability. Both spherical "clumps" of fibers and parallel "pores" through the agarose could explain the 3-to-4-fold higher permeability. The predictions of these two models are very similar, differing by less than 11% for the conditions in Figure 3.22. The images

of agarose structure, the description of gelation kinetics and the likelihood of an isotropic medium suggest a random clump structure is more physically plausible than parallel pores.

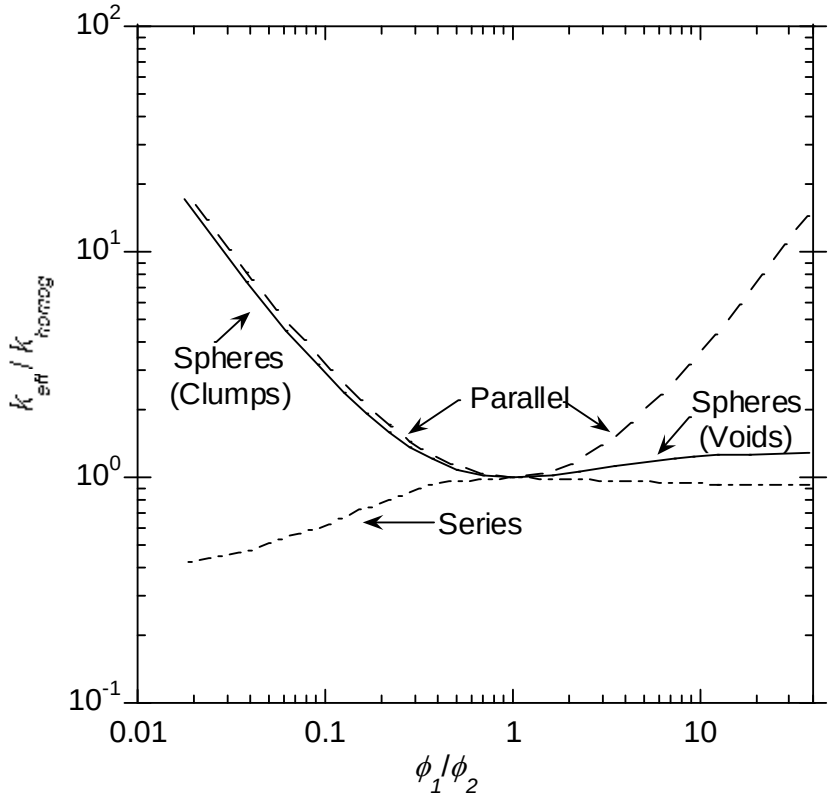

Figure 3.22 Effective hydraulic permeability of a two region composite compared to the permeability for a homogeneous system with the same total fiber volume fraction. Here, ϕ_{total}=0.03 and ε_2=0.1. The parallel model is described by Equation (3.30) (- - -); the series model is described by Equation (3.31) (- · -). The spherical model (—) is Equation (3.34), with region 2 referring to the spheres. The homogeneous fiber permeability is given by Equation (3.24).

As described previously, several models are available for the effective permeability of a material with spherical heterogeneities. The Maxwell solution (Equation (3.32)) has the simplest form. The expression by Jeffrey has more accuracy at higher volume fractions, though full power series solution contains more terms than those shown in Equation (3.34). Results of numerical simulations are also available from Bonnecaze and Brady for a limited number of conditions. For clumps with κ_s/κ_m = 0 and 0.01, the results from Maxwell, Jeffrey (both truncated and full expressions), and Bonnecaze and Brady differed by 2.2% or less over the full range of ε_2 = 0-0.5. These conditions are

representative of those implied by the experimental agarose results; using the methods that are described in the following sections, 3v% agarose yields values of $\kappa_s/\kappa_m = 10^{-2}$-$10^{-4}$ with ε_2 = 0.05-0.5. Accordingly, the Maxwell expression was used for all calculations involving spherical voids.

Model Application

The heterogeneous models require that ϕ_{total}, ϕ_2/ϕ_{total}, and ε_2 be specified. Knowing the total fiber volume fraction, this leaves two adjustable parameters which are fit to the agarose hydraulic permeability. Since agarose structure likely varies with different fiber volume fractions, values of ϕ_2/ϕ_{total}, and ε_2 are assumed to different for different values of ϕ_{total}. For a given ϕ_{total}, the value of blank agarose hydraulic permeability for a can be used to fit one of the two parameters. The degrees of freedom require that the other parameter be independently specified. This is illustrated in Figure 3.23 for 3 v% agarose gels, where the curve shows all parameter combinations of ϕ_2/ϕ_{total} and ε_2 that result in a permeability of κ = 453 nm^2.

The values that the parameters ϕ_2/ϕ_{total}, and ε_2 can take are bounded. The sphere volume fraction ε_2 can have a minimum value of 0 and a maximum value of ~0.5 where the model breaks down and the system approaches the sphere cubic packing density of 0.52. The volume fraction ϕ_2 is bounded by a minimum value of 0 and a maximum value of 0.78 when the fibers are cubic packed. Further, ϕ_2 is also limited through volume conservation by the bounds of ϕ_1, which also has a minimum of 0 and a maximum of 0.78. These bounds on parameter space are illustrated in Figure 3.23, where the dashed line shows all parameter combinations which predict a permeability of 453 nm^2 for 3 v% agarose, while the solid line indicates parameter combinations which fall within physical bounds.

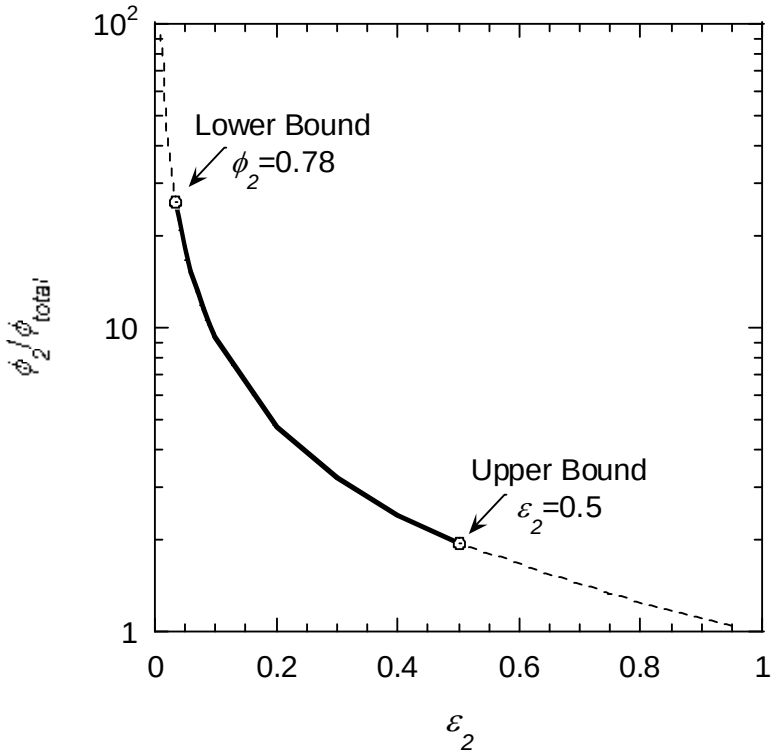

Figure 3.23 Range of parameters for the spherical heterogeneity model for 3v% agarose with κ = 453 nm^2. The homogeneous fiber permeability is given by Equation (3.24) with r_f = 1.6 nm. The dotted line (- - -) represents all combinations of parameters which predict a 453 nm^2 permeability; the solid line (—) is the range of parameters which fall within physical bounds.

For systems with both GAG and agarose, it is assumed that GAG binds in proportion to the number of active binding sites, and the number of these sites are proportional to the volume of fibers. Therefore, the heterogeneity of GAG is given by the same ϕ_2/ϕ_{total} and ε_2 as the agarose substrate to which it binds. Fitting these two parameters to the permeability of agarose without bound GAG and knowing the total GAG volume fraction from the GAG assay, the permeability of the composite is modeled with no additional fitted parameters. In Figure 3.24, the composite permeability (κ_{eff}) of 3v% agarose with neutral GAG fibers was calculated over a range of ε_2. In this example, the permeabilities of both fibers are given by Equation (3.24) and are combined with weighted inverse averaging from Equation (3.28). As illustrated in the figure, the composite permeability is a very weak function of ε_2, changing by less than 0.5% over the bounded range of ε_2. Therefore, the model is effectively only fit to the parameter ϕ_1/ϕ_{total}. It will be shown in

the following section that the composite permeability is also a very weak function of the choice of ε_2 for charged fiber models.

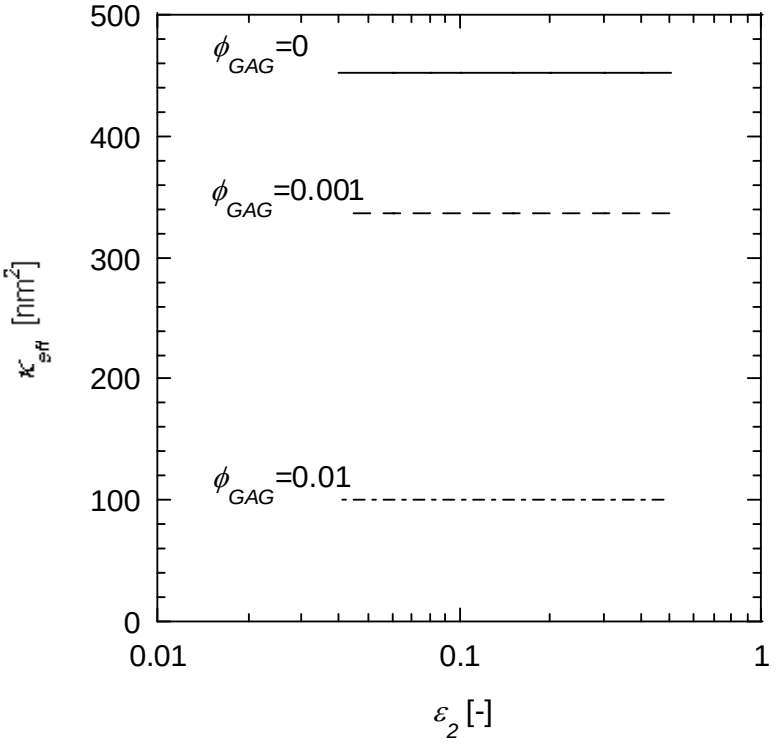

Figure 3.24 Effective hydraulic permeability of a heterogeneous, neutral agarose-GAG composite as a function of ε_2 and ϕ_{GAG}. The ϕ_2/ϕ_{total} parameter for the spherical heterogeneity model was fit to a 3v% agarose gel with $\kappa = 453$ nm^2 (—). The neutral homogeneous fiber permeabilities are given by Equation (3.24) with $r_{f,agarose} = 1.6$ nm and $r_{f,GAG}$=0.5 nm. The effective permeabilities changes less than 0.5% over the range of ε_2 for both gels with low GAG (ϕ_{GAG} =0.001; - - -) and high GAG (ϕ_{GAG} =0.01; - · -) contents.

3.2.4. Composite Agarose-GAG Hydraulic Permeability Model

The agarose-GAG composite gel has a mixture of charged GAG and neutral agarose fibers in a matrix with heterogeneous fiber density. As summarized in Figure 3.25, the model for charged and neutral fibers and fiber heterogeneity can be combined to predict the hydraulic permeability of an agarose-GAG membrane. As discussed in Section 3.2.1, the hydraulic permeability for the charged fibers should be modeled with a diffuse double layer model. The model results for flow parallel and perpendicular to the charged fibers are averaged into a random GAG fiber open-circuit permeability using weighted inverse averaging from Equation (3.28). The permeability of the agarose fibers is modeled by the

Clague *et al*. Equation (3.24) for randomly oriented neutral fibers. The permeability of the composite is found by averaging the agarose and GAG permeabilities using weighted inverse averaging. The heterogeneous structure of the agarose is approximated by spherical, dense fiber clumps within a lower density matrix using the results from Maxwell in Equation (3.32). Since GAG binds to active sites on agarose fibers, it is assumed that the GAG fibers will be present in a constant proportion to agarose fibers ($\phi_{GAG,i}/\phi_{agarose,i}$ is a constant).

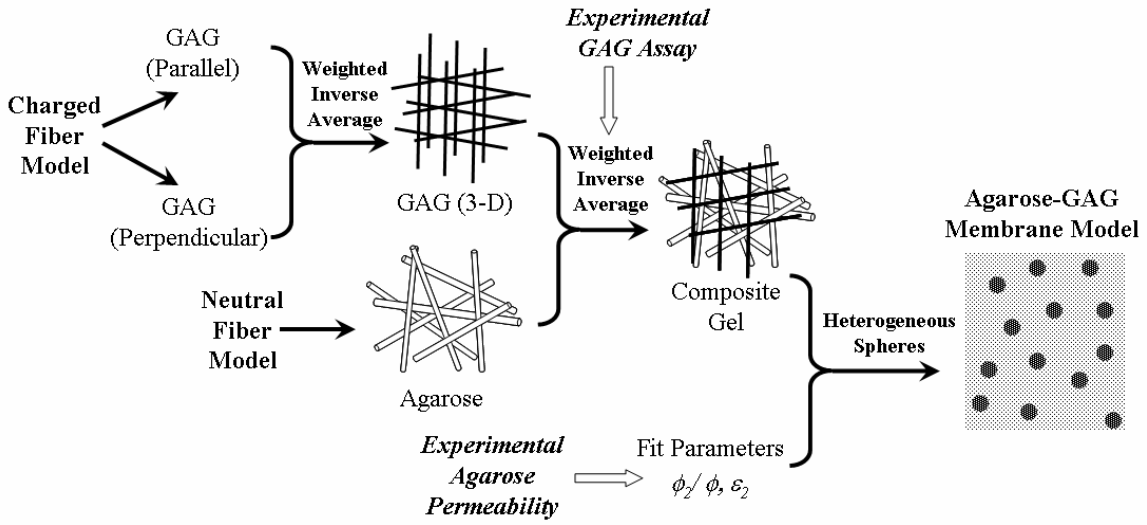

Figure 3.25 Composite model for the hydraulic permeability of an agarose-GAG membrane. The composite model includes a periodic charged fiber model for GAG, a random neutral fiber model for agarose, an averaging method to combine the permeabilities of multiple fiber types and a heterogeneous permeability model to account for variations in the agarose fiber density. The model also includes experimental data on the bound GAG content of the agarose-GAG membranes and the hydraulic permeability of agarose membranes without GAG.

The parameters in the model include physical properties, experimental variables, experimental results and fit model parameters. As discussed in previous sections, this composite model contains known physical properties for the ions in solution and the charge and dimensions of agarose and GAG fibers. As discussed in Chapter 1, the physical properties of GAG fibers (radius, length, charge) have values cited within a narrow range. Most references cite the GAG radius as 0.5-1.0 nm, the length as 1 nm per disaccharide (105-132 nm for 50 kDa chondroitin sulfates with 0-1 sulfate substitutions/disaccharide) and the surface charge as -65 – -195 mC/m^2 (Chammas et al.

1994, Dea et al. 1973, Eisenberg and Grodzinsky 1988, Ogston and Wells 1972, Wight et al. 1991). Unless otherwise noted, the properties of GAG and agarose fibers used in the models are the values in Table 3.4.

Table 3.4 Fiber properties for GAG (CS-A) and agarose

	GAG (CS-A)	**Agarose**
Fiber radius	0.5 nm	1.6 nm
Fiber charge	-100 mC/m^2	0 mC/m^2
Fiber length	105 nm/50kDa	- -
Fiber density	1.00 g/mL *(based on values above)*	1.025 g/mL

The total volume fraction of the agarose fibers and the solution concentration are controlled experimental variables. The total volume fraction of GAG fibers is experimentally determined by the GAG assay, the GAG fiber radius and the GAG fiber length. The hydraulic permeability of an agarose gel without bound GAG is also experimentally determined.

For a given GAG assay and agarose hydraulic permeability, the only adjustable parameter in the model is the sphere volume fraction, ε_2. Once ε_2 is selected, then the ratio ϕ_2/ϕ_{total} is fit to the blank agarose hydraulic permeability. All other parameters are known, and the composite gel model predicts the hydraulic permeability for an agarose gel with any GAG content.

Figure 3.26 compares the predicted hydraulic permeability of an agarose-GAG membrane to the permeability of a blank agarose gel. The model considers a membrane with 3 v% agarose and 129 mg GAG/g agarose ($\phi_{GAG} = 0.0039$). Three values of ε_2 across the physically bounded range were used to predict the agarose-GAG hydraulic permeability. As shown in the figure, the composite gel model predicts a significant decrease in hydraulic permeability for the modest amounts of GAG which can be bound to agarose. The model predicts a slight decrease in the permeability at ionic strengths below 0.1 M. It is also seen that varying ε_2 within its bounded range has a minor effect on the predicted permeability of the composite system. This insensitivity to ε_2

strengthens the predictions of the model, since they are primarily a function of only the physical properties and the one fit parameter for agarose.

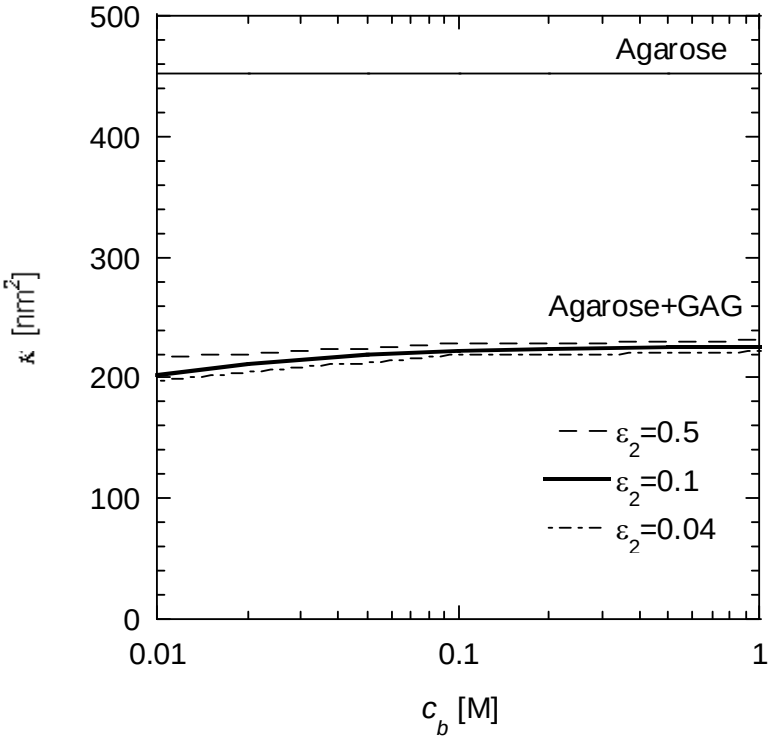

Figure 3.26 Darcy permeability (κ) of a composite agarose-GAG fiber system and the sensitivity to model parameters. Composite gel is 3v% agarose with $r_{f,a}$ = 1.6 nm and 129 mg/g GAG (ϕ_{GAG} = 0.0039) with $r_{f,GAG}$ = 0.5 nm and $\sigma_{s,GAG}$ = -100 mC/m^2. The thin solid line (—) shows the permeability of agarose without GAG. The other lines show the predicted permeability of the agarose-GAG membranes. The thick solid line (—) is the middle of the range for ε_2; the two dashed lines show the predictions for the upper (- - -) and lower (- · -) limits of ε_2.

The sensitivity of the model to the physical properties of GAG is shown in Figure 3.27. For the extreme case of a five-fold increase in GAG charge, there is minimal change in the permeability of agarose-GAG at low ionic strengths. Changes in the GAG fiber radius affect both the hydraulic permeability and GAG volume fraction (the GAG surface charge density could also be affected, depending if the GAG charge per monomer or per surface area is assumed to be a known constant). Since $\phi \propto r_f^2$ and $\kappa \sim -(r_f^2/\phi)\ln\phi$, the hydraulic permeability has only a moderate dependence on the GAG fiber radius. At the high end of cited GAG fiber radii, the permeability is increased by approximately 50% relative to r_f=0.5 nm.

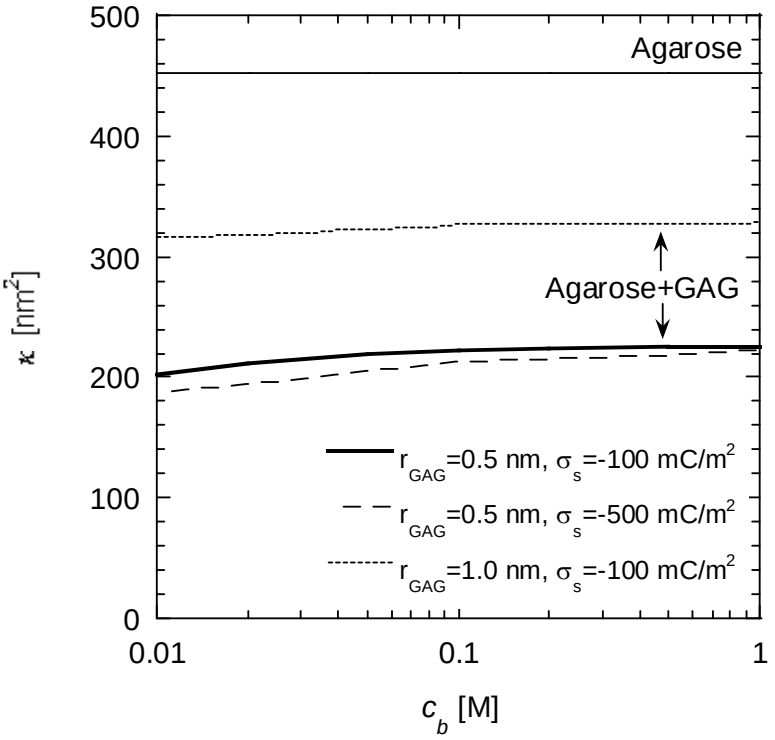

Figure 3.27 Darcy permeability (κ) of a composite agarose-GAG fiber system and the sensitivity to GAG properties. Composite gel is 3v% agarose with $r_{f,a}$ = 1.6 nm and 129 mg/g GAG with radius and surface charge specified in the legend. The thin solid line (—) shows the permeability of agarose without GAG. The other lines show the predicted permeability of the agarose-GAG membranes for various combinations of GAG radius and charge. All models use ε_2=0.1.

Model Variations

Several variations of the composite model were considered, with the model previously described by Figure 3.25 considered the "baseline" model. Since the GAG binds to active sites on agarose, it was assumed in the baseline model that the spatial distribution of GAG fibers would be in proportion to the distribution of agarose fibers. However, it is possible that GAG fibers would preferentially bind in the low-density regions of agarose, due to decreased steric hindrance from agarose and to avoid electrostatic interactions with other bound GAG in high density areas. In the extreme of this model, the GAG is *only* present in the low-density agarose matrix and is absent in the high-density clumps. This preferential GAG binding model is shown in Figure 3.28. Unlike the baseline model, the mixing rule to find the permeability of an agarose-GAG mixture is not used in the clumps (Region 1), which are assumed to be only agarose in the preferential binding model. There is a higher volume fraction of GAG in the matrix

(Region 2) in the preferential model than the baseline model. The membrane heterogeneity was treated the same as in the baseline model.

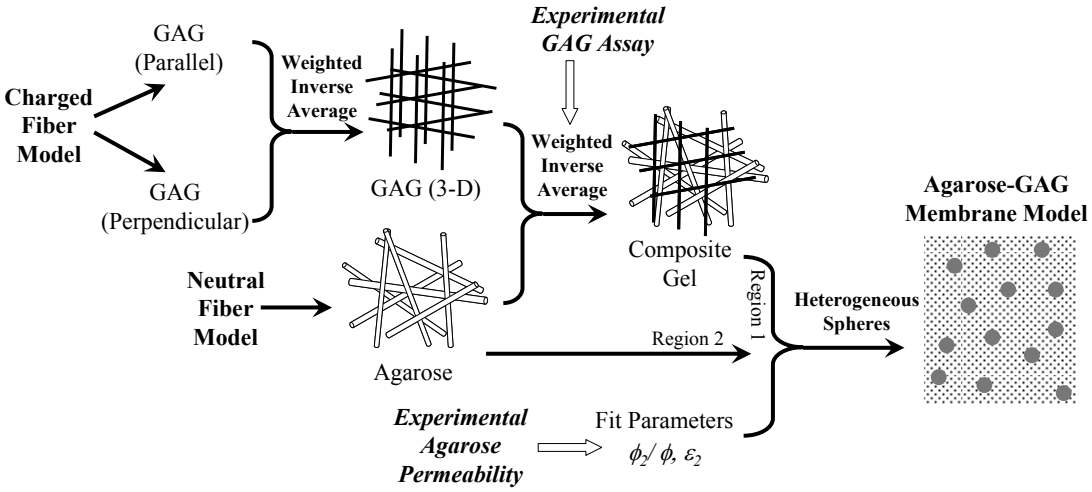

Figure 3.28 Preferential GAG binding model: Alternate composite model for the hydraulic permeability of an agarose-GAG membrane. This alternate model considers that the GAG may not bind in proportion to agarose but instead binding more highly in the low-density agarose matrix. This model considers the extreme case where all the GAG binds in only the low-density matrix ('Region 1').

A second variation on the composite model makes use of the charged two-fiber model described in Section 3.2.2. The two-fiber model simulates the permeability through a periodic array of charged and uncharged fiber, so that, unlike the baseline model, a mixing rule is not needed to find the permeability of an agarose-GAG mixture. This two-fiber model is illustrated in Figure 3.29. Using the two-fiber model to calculate the permeability of ordered arrays agarose-GAG, the weighted-inverse mixing rule was used to find the permeability of randomly oriented fibers. The membrane heterogeneity was treated the same as in the baseline model.

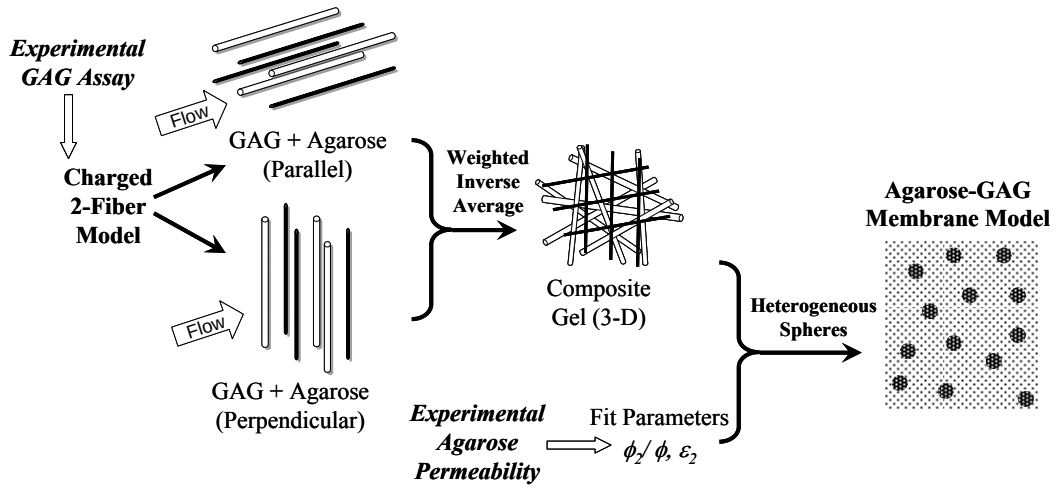

Figure 3.29 Two-fiber model: Alternate composite model for the hydraulic permeability of an agarose-GAG membrane. This alternate model uses the model for flow past a 1:1 ordered array of two types of charged fibers, as shown in Figure 3.14. The model is limited to certain ratios of GAG fibers to agarose fibers; for a 1:1 ratio this is equivalent to 0.3 v% GAG and 3 v% agarose.

The third variation assumes that the open-circuit permeability is calculated across the entire membrane, not in each region. In the baseline model in Figure 3.25, all permeabilities used in the fiber mixing rules and heterogeneity models were open-circuit permeabilities. The implicit assumption in that approach is that there is no net current across each spherical region. This assumption may be over restrictive, since it is only necessary to have no net current across entire membrane. As shown in Figure 3.30, a model was developed which calculates the coupling coefficients for a heterogeneous material before applying Equation (3.5) to calculated the open-circuit permeability. This approach enforces no net current across the entire membrane, but not necessarily within each heterogeneous region (clumps and surround matrix). The electrokinetic coupling coefficients (k_{ij}) for GAG were calculated. Then the Maxwell equation for heterogeneity was applied to each coupling coefficient, giving values of k_{ij} for a system with spherical clumps. These values of k_{ij} for the heterogeneous material were then combined into an open circuit permeability. Finally the weighted-inverse mixing rule was used to combine the GAG open circuit permeability with the heterogeneous agarose permeability.

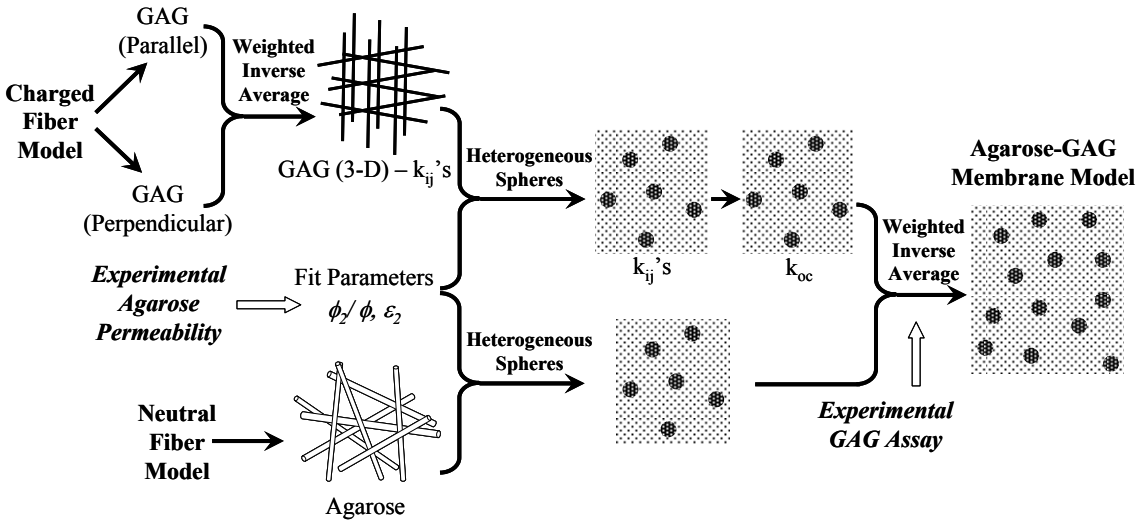

Figure 3.30 Clumped coupling coefficients model: Alternate composite model for the hydraulic permeability of an agarose-GAG membrane. This alternate model considers that the condition of no current in the open-circuit permeability is valid only over the composite membrane, not necessarily over each heterogeneous region.

The permeability predicted by these three model variations are compared to the baseline model. In Figure 3.31, the baseline model is compared to the preferential GAG binding and heterogeneous coupling coefficient models for 3 v% agarose with 0.39 v% GAG. It is clear from the figure that preferential GAG binding in only the low-fiber density region results in a Darcy permeability that is an order of magnitude lower than when GAG binds in proportion to agarose. However, the choice of combining the electrokinetic coupling coefficients before or after accounting for the fiber heterogeneity has virtually no affect on the predicted permeability.

In Figure 3.32, the baseline model is compared to the two-fiber model for 3 v% agarose with 0.29 v% GAG (a different GAG volume fraction was necessary since the two-fiber model requires a one-to-one ratio of the number of fibers). The use of the two-fiber model from Figure 3.14 to predict the agarose-GAG permeability differs by 25-35% from the reference model, even at neutral conditions. This deviation is unsurprising, as similar deviations due to the fiber mixing rule were also present in the homogeneous two-fiber model in Figure 3.18.

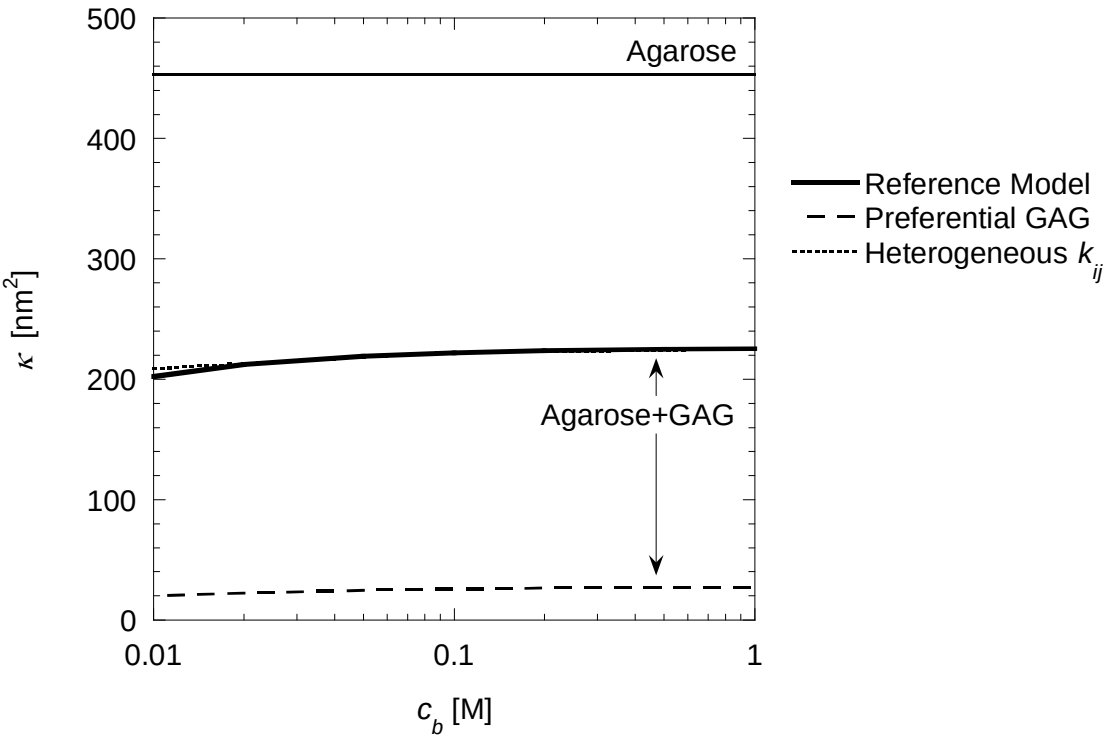

Figure 3.31 Darcy permeability (κ) of variations to the composite agarose-GAG model: preferential GAG binding, heterogeneous coupling coefficient, and baseline reference models. The composite gel is 3v% agarose ($r_{f,a}$ = 1.6 nm and ε_2=0.1) and 129 mg/g GAG (ϕ_{GAG} = 0.0039, $r_{f,GAG}$ = 0.5 nm, and $\sigma_{s,GAG}$ = -100 mC/m^2). The heterogeneous coupling coefficient model is nearly identical to the reference composite model.

The differences between these model variations indicate that baseline model should be relatively reliable, even with the assumptions about internal electrokinetic coupling and the use of fiber mixing rules. The large difference in permeability between the baseline and preferential GAG binding models provide an explanation if the experimental hydraulic permeability is lower than the model predictions.

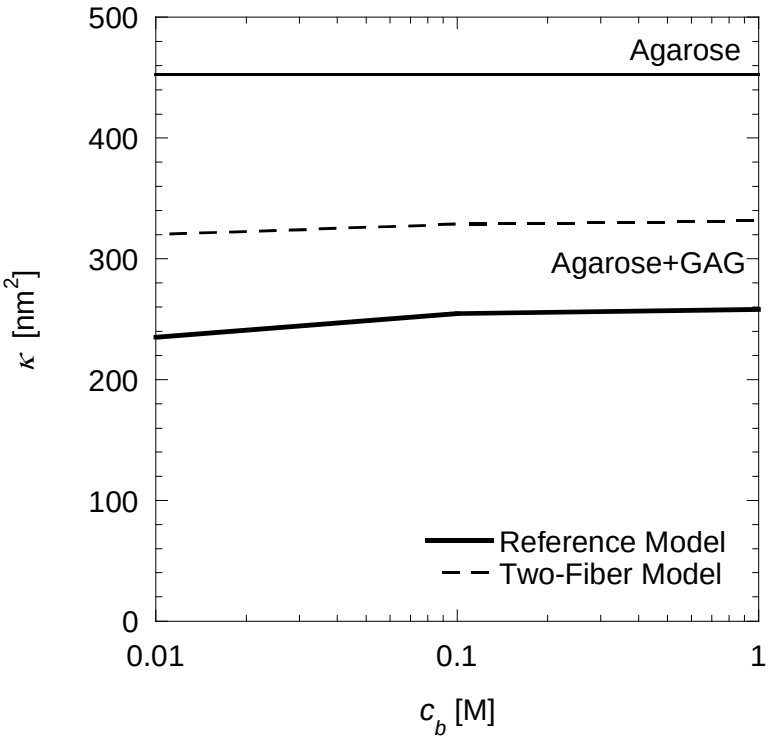

Figure 3.32 Darcy permeability (κ) of variations to the composite agarose-GAG model: two-fiber and baseline reference models. The composite gel is 3v% agarose ($r_{f,a}$ = 1.6 nm and ε_2=0.1) and ϕ_{GAG} = 0.0029 ($r_{f,GAG}$ = 0.5 nm and $\sigma_{s,GAG}$ = -100 mC/m^2).

Model Application to Agarose-Dextran

The composite model in Figure 3.25 can also be applied, with slight modification, to the agarose-dextran gels previously characterized in our lab (Kosto and Deen 2005, White and Deen 2002). Since dextran is a randomly-oriented neutral fiber, it can be modeled with equation (3.24) instead of the charged fiber models with orientation-averaging. Using a dextran radius of $r_{f,dex}$ = 0.33 nm, the composite model was applied to 4 v% and 8 v% agarose gels with variable dextran contents (Figure 3.33) (Kosto et al. 2004). Since the 500 kDa dextran equilibrates within the gel and is then irradiated to create cross-linkages with the agarose fibers, it is unclear if the dextran is spatially distributed in proportion to the agarose (Figure 3.33a) or if it is spatially homogeneous (Figure 3.33b). Note that the volume fractions of dextran reported in White and Deen have been reinterpreted with the improved values of dextran immobilization efficiency reported by Kosto and Deen. However, the reinterpreted data uses the dextran partition

coefficients reported by White, which deviate from the values reported by Kosto, leading to additional uncertainty in the experimental abscissa values (Kosto and Deen 2005, White and Deen 2002).

As can be seen in the figure, the composite model captures the decrease in hydraulic permeability with increasing dextran volume fraction. The heterogeneous model also more accurately captures the magnitude of the hydraulic permeability, which is an order of magnitude larger than predicted by homogeneous fiber permeability models. The assumption of proportional or homogeneous dextran has relatively little impact on the predictions at higher agarose content, though the homogeneous model appears to have a better fit for 4 v% agarose. Again, it should be noted that there is some uncertainty in the abscissa value, and that the size of dextran and method of binding is very different than that used for synthesizing agarose-GAG gels.

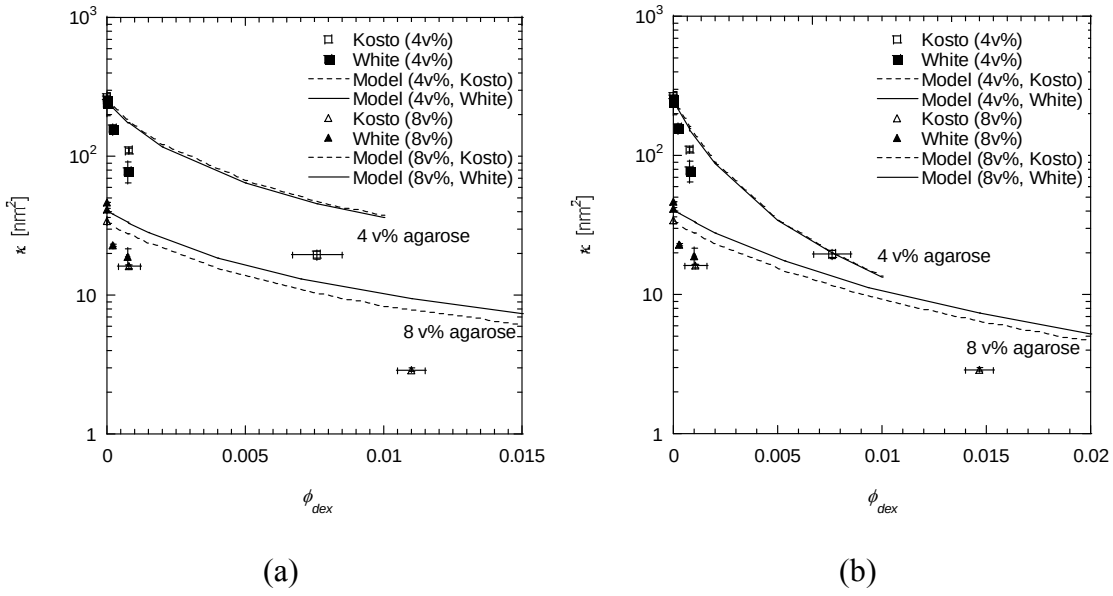

Figure 3.33 Darcy permeability (κ) of a composite agarose-dextran fiber system for (a) heterogeneous dextran and (b) homogeneous dextran (500 kDa). The gels are 4 v% agarose (■,□) and 8 v% agarose (▲,△); open symbols are data from Kosto and Deen (Kosto and Deen 2005), closed symbols are data from White and Deen with corrected values of ϕ_{dex} based on the binding efficiency from Kosto (White and Deen 2002). The composite model predictions are indicated by the corresponding lines for each content; solid lines are fit to the agarose data from White and Deen (—) and dashed lines are fit to the agarose data of Kosto and Deen (- - -). The model parameters are $r_{f,a}$ = 1.6 nm, $r_{f,dex}$ = 0.33 nm and ε_2=0.1.

Composite Model Using Donnan Equilibrium

The composite model for agarose-GAG described previously can be adapted to use the Donnan equilibrium model instead of structural models to account for the charge of GAG fibers. One approach is to assume the charge is distributed in proportion to the GAG and apply the Donnan model to each region of fiber density. Since the "clumps" are impermeable relative to the surrounding matrix (k_2/k_1~0.001), this is equivalent to applying the charge density in the matrix to the entire membrane. Alternately, one could assume that the macroscopic average charge density, based on the total GAG charge per total membrane volume, should be used in the Donnan model. Both of these results are shown in Figure 3.34. Equation (3.24) was used for both agarose and GAG fibers, with weighted inverse averaging and the spherical clump model used to create the neutral composite permeability. The assumption of -1.3 meq/L (matrix charge density) versus -16.6 meq/L (macroscopic charge density) is seen to have a strong effect on the permeability at low ionic strengths. The use of the Donnan model instead of the diffuse double layer may improve the model predictions if the effect of charge on permeability occurs on a length scale much larger than the fiber spacing (i.e. – if the charge in the dense "clumps" affects the electrical potential field or ion flux in the surrounding matrix).

The following section will describe the approach for experimentally measuring the hydraulic permeability of agarose-GAG gels, then compare the experimental results to the predictions of the composite model.

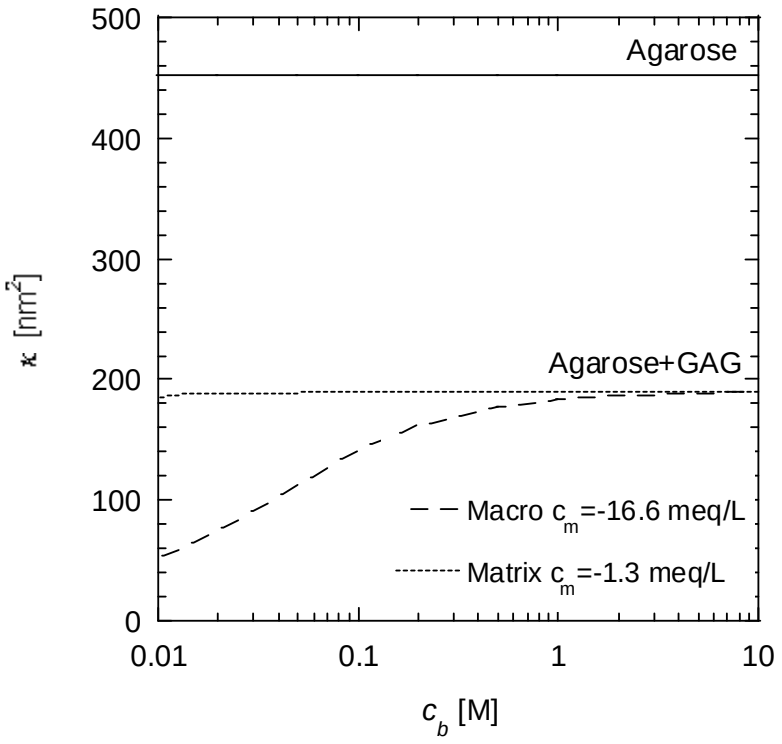

Figure 3.34 Darcy permeability (κ) of the composite agarose-GAG model using Donnan equilibrium. The composite gel is 3v% agarose ($r_{f,a}$ = 1.6 nm and ε_2=0.1) and ϕ_{GAG} = 0.0039 ($r_{f,GAG}$ = 0.5 nm). The charge density in the matrix uses a fixed charge density of -16.6 meq/L and the macroscopic charge density uses -1.3 meq/L.

3.3. Experimental

The method for experimental determination of the hydraulic permeability of a gel membrane is described in the following sections, along with new information about the support mesh correction factor. Results on the pressure dependence of permeability measurements, osmotic swelling of the gels and wash-out of the bound GAG are presented. Finally, hydraulic permeability measurements for several GAG contents and solution ionic strengths are compared to the predictions of the previously developed composite model.

3.3.1. Method

The Darcy permeability of each mesh-reinforced gel was measured as described previously (Johnson and Deen 1996b, Johnston and Deen 1999, White and Deen 2002). The gel membrane was placed in a 10 mL ultrafiltration cell (Model 8010, Millipore,

Bedford, MA). The cell reservoir was filled with a KCl-phosphate buffer solution at pH 7.4. The buffer was 0.01 M sodium phosphate with a balance of potassium chloride to create solutions with an ionic strength of 0.1 M to 1 M. For solutions with an ionic strength below 0.1 M, the buffer was 0.005 M sodium phosphate with the balance as potassium chloride. All buffers contained approximately 0.001 w/v% (0.00015 M) sodium azide to inhibit microbial growth. All gels used type VI agarose (Product #A3893, Sigma, St. Louis, MO) and chondroitin sulfate A from bovine trachea (Product # 230687, Calbiochem, La Jolla, CA).

The ultrafiltration cell was pressurized with nitrogen to achieve a transmembrane pressure drop of approximately 10 kPa. The pressure drop was monitored using a pressure transducer (Model CP379, Validyne Engineering, Northridge, CA), and corrections were made to account for hydrostatic pressure. Samples of the filtrate were collected over timed intervals and weighed to determine the steady-state volumetric flow rate (Q). The cross-sectional exposed area of the membrane (A_m) was determined to be 366 mm^2 by measuring the fritted diameter of the ultrafiltration cell membrane support. This was further confirmed by measuring the area of a stained gel after filtration of a toluidine dye solution. The thickness of the gel (δ) was determined by confining the membrane between two microscope slides of known thickness and measuring the combined thickness with a micrometer (Model 293-766-30, Mitutoyo, Aurora, IL). Gel thicknesses were generally in the range of 70-75 μm. The Darcy permeability was then calculated by:

$$\kappa = \mu \frac{\delta}{\Delta P} \frac{Q}{\beta_m A_m} \tag{3.73}$$

where ΔP is the pressure drop across the membrane and β_m is a correction factor that accounts for the increased flow resistance due to the polyester mesh support within the gel. The β_m mesh correction factor will be discussed further in the following section.

3.3.2. Applied Pressure Corrections

As noted in the Methods (Section 3.3.1), the pressure drop measured by the pressure transducer was adjusted to determine the transmembrane pressure drop. Within the ultrafiltration cell, the applied pressure is increased by the hydrostatic head of the

solution above the membrane. The pressure then drops to atmospheric pressure across the membrane and the outlet tube (Figure 3.35).

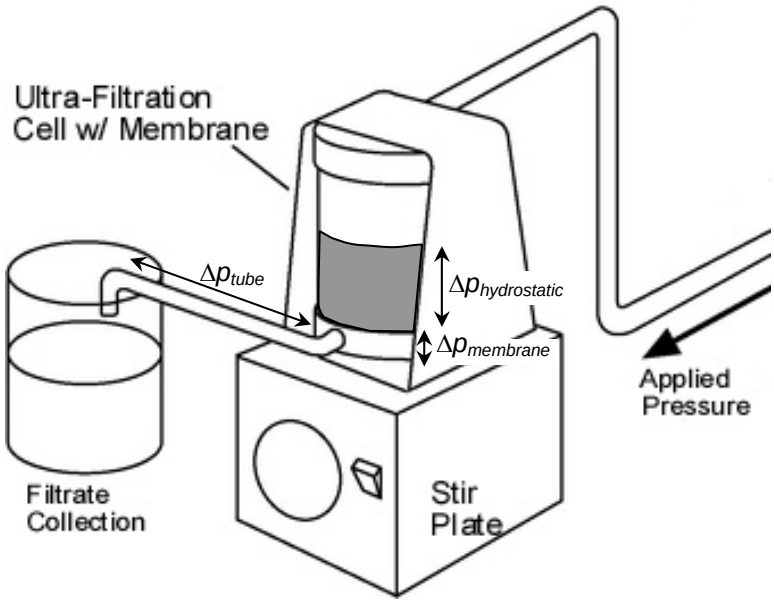

Figure 3.35 Schematic of pressure changes in the ultra-filtration apparatus. The hydrostatic head increase, the transmembrane pressure drop, and the outlet tube pressure drop sum to the applied pressure measured by the upstream pressure transducer.

The contributions of each pressure change for the hydraulic permeability measurements of a blank agarose membrane at 10 kPa are summarized in Table 3.5. A typical hydrostatic head in the ultra-filtration cell is 25 mm. This results in a 2.5% increase to the applied pressure, which is why it is important to adjust for the effect in determining the transmembrane pressure. Since the liquid height decreases by approximately 10 mm during a permeability measurement, the hydrostatic pressure is based on the average of the initial and final solution heights during the steady state measurements. The transmembrane pressure drop is found by inverting Equation (3.73). A blank agarose gel has an average permeability of 453 nm^2 and is typically 70 μm thick. With a 10 kPa applied pressure, a typical flow rate is approximately 0.5 mL/minute. The resulting transmembrane pressure drop account for nearly all of the upstream applied pressure. Poiseuille's solution for pipe flow is used to estimate the pressure drop across the outlet tube:

$$\Delta p_{tube} = \frac{8\mu Q z_{tube}}{\pi R_{tube}^4} \tag{3.74}$$

where z_{tube} and R_{tube} are the length and inner radius of the outlet tube. The tube is nearly horizontal, so there is no need to adjust for hydrostatic pressure changes across the tube. In the current ultra-filtration cells, the tubes are 10 cm long with a 1.2 mm inner radius. The resulting pressure drop across the tube is negligible (0.01%) and does not need to be accounted for when determining the transmembrane pressure drop. The maximum pressure drop across the droplet due to surface tension (assuming a hemispherical droplet) is:

$$\Delta p_{droplet} = \frac{2\gamma}{R_{tube}} \tag{3.75}$$

where the surface tension, γ, between air and water at room temperature is 72.75 dynes/cm. However, this is the maximum pressure when the drop is nearly fully formed, and actual pressure from surface tension periodically fluctuates from zero (no droplet) to this maximum (fully formed droplet).

Table 3.5 Characteristic pressure changes across the ultra-filtration apparatus for the hydraulic permeability measurement of a blank agarose membrane.

$\Delta p_{applied}$	$\Delta p_{hydrostatic}$	$\Delta p_{transmembrane}$	Δp_{tube}	$\Delta p_{droplet}$
10 kPa	0.25 kPa	10.24 kPa	0.001 kPa	0.12 kPa

3.3.3. Mesh Correction Factor, β_m

Using a correlation developed by Johnson and Deen, the mesh correction factor (β_m) can be calculated if the dimensions of the fiber mesh are known (Johnson and Deen 1996b). These dimensions include the fiber radius (R_m), the center-to-center fiber spacing (W), the total gel thickness (δ) and the gel thickness upstream of the mesh (δ_1). The mesh correction factor is a function of three dimensionless parameters: the ratio of open area to total area (α_m), the ratio of membrane thickness to fiber radius (λ_m), and the fraction of gel upstream of the fiber (γ_m):

$$\alpha_m = \left(1 - \frac{2R_m}{W}\right)^2$$
$$\lambda_m = \delta / R_m \tag{3.76}$$
$$\gamma_m = \frac{\delta_1}{\delta - 2R_m}$$

Johnson found that the effect of γ_m on the correction factor is negligible and that the correction factor is primarily a function of α_m and λ_m. So although the real meshes consist of three-dimensional woven fibers, the mesh correction factor was calculated with the fibers aligned in a single plane in the center of the gel.

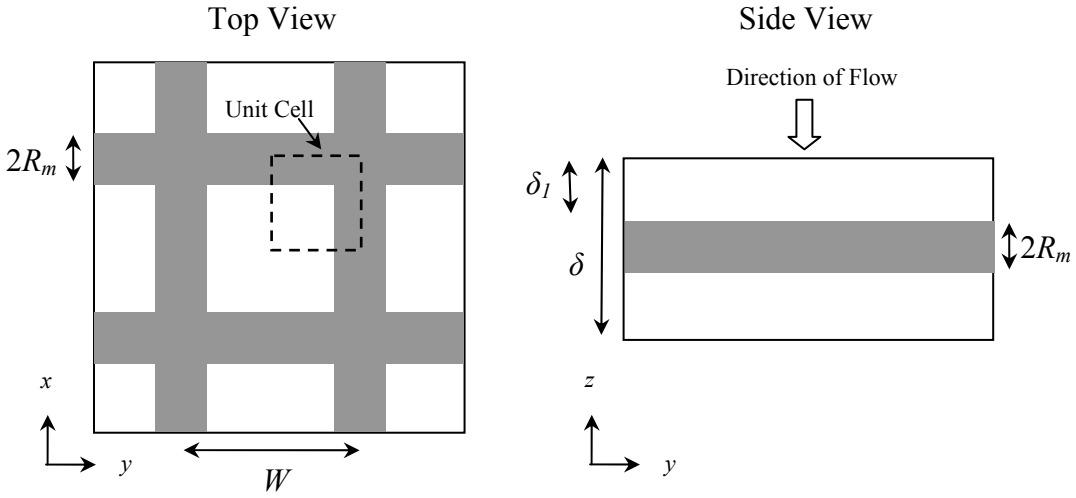

Figure 3.36 Model geometry and dimensions used for calculating the mesh correction factor

Prior researchers have calculated β_m from the mesh dimensions given by the mesh manufacturer and a plot of Johnson's model results. However, inspection under a microscope showed that the true mesh dimensions were significantly different from those claimed by the company. The following sections will report the true dimensions of the meshes, then determine the beta correction factor for the corrected geometry using a finite element model.

Microscopy and Mesh Dimensions

To determine the true dimensions of the fiber meshes, two meshes were randomly selected from each of four lots of Spectra/Mesh® 43 µm Polyester Filters (Part No. 148-248, Spectrum Laboratories, Rancho Dominguez, CA). Each mesh was digitally photographed under a compound optical microscope at 10x magnification with a 0.001" scale bar slide underneath (Figure 3.37). The dimensions of the mesh were determined by comparing pixel length of a mesh dimension to the pixel length of the scale bar. To confirm there was no image compression, an equal number of measurements were taken perpendicular to each other.

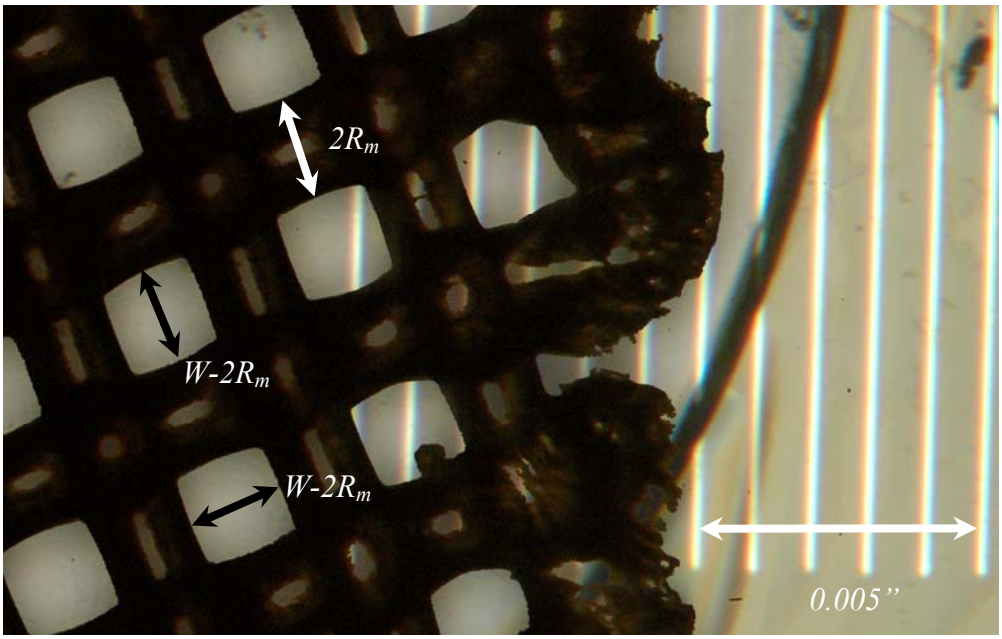

Figure 3.37 Sample microscope image of a mesh with measured dimensions. The fiber diameters corresponds to $2R_m$ and the mesh openings correspond to W-$2R_m$. Scale bars in the background are spaced at 0.001" (25 µm).

Spectrum Laboratories reported the mesh properties as 43 µm mesh openings, 29% open area, 70 µm thickness and 25 mm mesh diameter. Assuming the thickness of the mesh consists of two woven fibers, the fiber diameter equals half of the mesh thickness, or 35 µm. This diameter is consistent with the claim of 29% open area. Microscope images of the meshes agree with the manufacturer's claim of a mesh opening of 43 µm; however the fiber diameter of 45 µm is significantly larger than the 35 µm supported by

the mesh thickness or % open area (Table 3.6). Without three-dimensional imaging, it is difficult to reconcile the 70 μm mesh thickness with a 45 μm fiber diameter. It is possible that the mesh fibers are compressed during weaving, giving them an elliptical profile.

Table 3.6 Mesh dimensions compared to manufacturer's claimed dimensions. Standard deviation based on n=8-12 measurements from two meshes within each lot.

	Measured					Manufacturer's
	Lot # 3213522	Lot # 3214715	Lot # 3215683	Lot # 3218305	Average	Claimed
Fiber Diameter ($2R_m$)	45.7 μm *± 2.6 μm*	43.3 μm *± 2.5 μm*	44.1 μm *± 2.1 μm*	46.8 μm *± 2.1 μm*	45 μm	35 μm
Mesh Opening (W-$2R_m$)	42.0 μm *± 1.9 μm*	44.5 μm *± 1.7 μm*	43.6 μm *± 1.7 μm*	41.7 μm *± 2.1 μm*	43 μm	43 μm
% Open Area	23%	26%	25%	22%	24%	29%

Finite Element Modeling

The mesh correction factor using the revised dimensions in Table 3.6 was determined by a three-dimensional finite-element simulation in COMSOL Multiphysics®. For a series of solid mesh fibers with a homogeneous gel filling the interstices, the flow through the gel is described by Darcy's law. Combining Darcy's law (Equation (3.1)) with the continuity equation, the governing equation for flow around the fibers is:

$$\nabla^2 p = 0 \tag{3.77}$$

The system was modeled by the unit cell indicated in Figure 3.36. The boundary conditions include symmetry on the four unit cell sides and no-penetration on the fiber surface:

$$n \cdot \nabla p = 0 \tag{3.78}$$

as well as a unit applied pressure at the top surface and no pressure on the bottom surface (Δp = -1). The mesh correction factor is evaluated as the average local pressure gradient over the bottom mesh surface relative to the applied pressure gradient:

$$\beta_m = \frac{\int\int \frac{dp}{dz} dxdy}{\frac{\Delta p}{\delta} \int\int dxdy} \tag{3.79}$$

The geometry of the mesh was the same as used by Johnson and Deen, with a grid of cylindrical fibers aligned on a single place and centered at half the gel thickness. For comparison, two other geometries were considered to more accurately reflect the woven nature of the mesh (Figure 3.38). These include cylindrical fibers which are arranged on two planes and fibers which are angled. While all arrangements preserve the fiber dimensions and fractional open area, the fibers occupy a larger volume in the second two models.

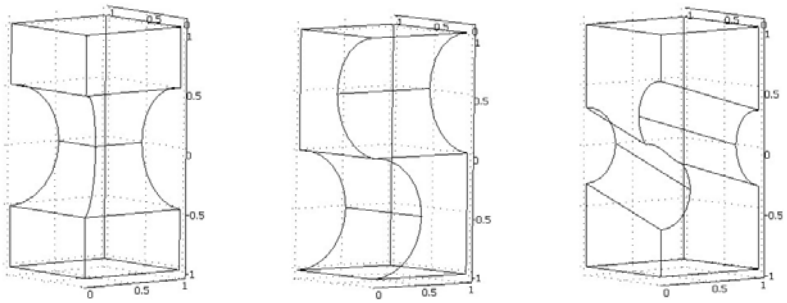

(a) (b) (c)

Figure 3.38 Three models of fiber alignment for a woven mesh: (a) single-plane mesh, (b) double-plane mesh and (c) angled mesh.

First, simulations of the single-plane mesh were run to validate the current model against Johnson and Deen's and Johnston's results (Johnson and Deen 1996b, Johnston 1999). For a mesh with $\lambda_m = 3.75$ and $\gamma_m = 0.5$, the models were in agreement within 0.5% over the range of $\alpha_m = 0.1\text{-}0.7$. The models were in equally good agreement for $\alpha_m = 0.4$ and $\lambda_m = 2.5\text{-}7.5$.

After validation of the model, β_m was calculated for the revised mesh dimensions, comparing the effect of fiber orientation on the results. As illustrated in Table 3.7, the mesh correction factor decreases with increasing gel thickness. The correction factors from the double-planed mesh are 20-25% higher than the ones from the single-plane mesh model. However, the woven mesh model has a correction factor 3% lower than the single-plane mesh model. These differences may be influenced by the larger excluded volume of the double-plane and angled meshes relative to the single-plane mesh (21%

and 35% larger, respectively). However, due to the similarity of the single-plane and angled mesh results, excluded volume is not the primary factor that caused the correction factors to differ.

Table 3.7 Mesh correction factor (β_m) for three models of fiber alignment and three gel thicknesses. Mesh used revised dimensions of W = 88 μm and R_m = 22.5 μm (α_m = 0.24, γ_m = 0.5 and λ_m = 3-6).

	Single-Plane	Double-Plane	Angled
δ = 70 μm	0.363	- *	- *
δ = 90 μm	0.416	0.521	0.403
δ = 130 μm	0.505	0.580	0.488

* - β_m could not be calculated due to the apparent diameter of fibers exceeding the gel thickness

Based on the measurements of the meshes, the corrections factors for the support meshes are based on fibers with a 45 μm diameter and 43 μm opening. This results in an excluded volume of 17.7 μL per mesh based on the double-plane fiber arrangment. Using the single-plane mesh geometry which was used by previous researchers, the mesh correction factor is taken as $\beta_m = 0.3627$ for a 70 μm-thick gel; the correction factors for other gel thicknesses are included in Table 3.8. The results from the single-plane mesh model are in good agreement with the angled fibers, without being limited by the apparent discrepancy between fiber diameter and mesh thickness. The correction factor for the single-plane mesh with $W = 88$ μm, $R_m = 22.5$ μm, and $\gamma_m = 0.5$ is fit by the polynomial:

$$\beta_m = -7\times10^{-6}\delta^2 + 0.0038\,\delta + 0.1298, \text{ where } \delta[nm]. \tag{3.80}$$

Table 3.8 Mesh correction factor (β_m) for multiple gel thicknesses. Mesh used revised dimensions of W = 88 μm and R_m = 22.5 μm (α_m = 0.24, γ_m = 0.5 and λ_m = 3-6) and the single-plane fiber geometry.

δ [μm]	65	70	75	80	85	90	95	100
β_m [-]	0.349	0.363	0.376	0.390	0.403	0.416	0.428	0.441
δ [μm]	105	110	115	120	125	130	140	150
β_m [-]	0.452	0.464	0.475	0.485	0.495	0.505	0.523	0.541

3.3.4. Results

The following sections evaluate the suitability of agarose-GAG gels for hydraulic permeability measurements. This includes the pressure-dependence of the permeability measurements, potential wash-out of GAG after extended filtration, selection of a GAG-free control gel for comparison to agarose-GAG gels and potential osmotic swelling or hysteresis at different solution ionic strengths. The section concludes by comparing the hydraulic permeability of the agarose-GAG gels to the composite model developed in Section 3.2.4 for several GAG contents and over a range of ionic strengths.

Pressure Dependence

Several previous studies in our laboratory have investigated the dependence of agarose hydraulic permeability on pressure. Johnson and Deen reported a decrease in κ of approximately of 2%/kPa for 1.9-7.2 v% agarose gels with 3-20 kPa applied pressure, where the decrease is defined as the slope divided by the 0 kPa intercept (Johnson and Deen 1996b). Johnston repeated similar experiments on 4-8 v% agarose gels and found less of a dependence of κ on the applied pressure (0.5-1.4%/kPa) (Johnston 1999). However, White and Deen reported no clear pressure dependence of agarose-dextran gels over the range 6.7-20 kPa (White and Deen 2002). This result was confirmed by Kosto and Deen over a wider range of conditions (4-8 v% agarose, 0-1 v% dextran, 1-31 kPa) (Kosto and Deen 2005).

Due to the discrepancies in these reports, the pressure dependence of the hydraulic permeability of agarose and agarose-GAG gels was measured. First, the Darcy permeability of 4 v% agarose gels was measured over the range 1.5-20 kPa (Figure 3.39). Measurements were performed with 0.1 M buffer and pressures were tested in a random order. Similar to the results of Johnston, there was an average decrease in permeability of 1.3%/kPa. However, most of this pressure decrease occurred at very low applied pressures, such that the average decrease above 5 kPa was negligible (<0.6%/kPa).

The Darcy permeability of agarose-GAG gels was also measured at 1.5-20 kPa in a random order, shown in Figure 3.40. The composite gels showed a similar pressure dependence as the agarose gels, with an average pressure dependence of 1.0-1.2%/kPa but little change at higher pressures.

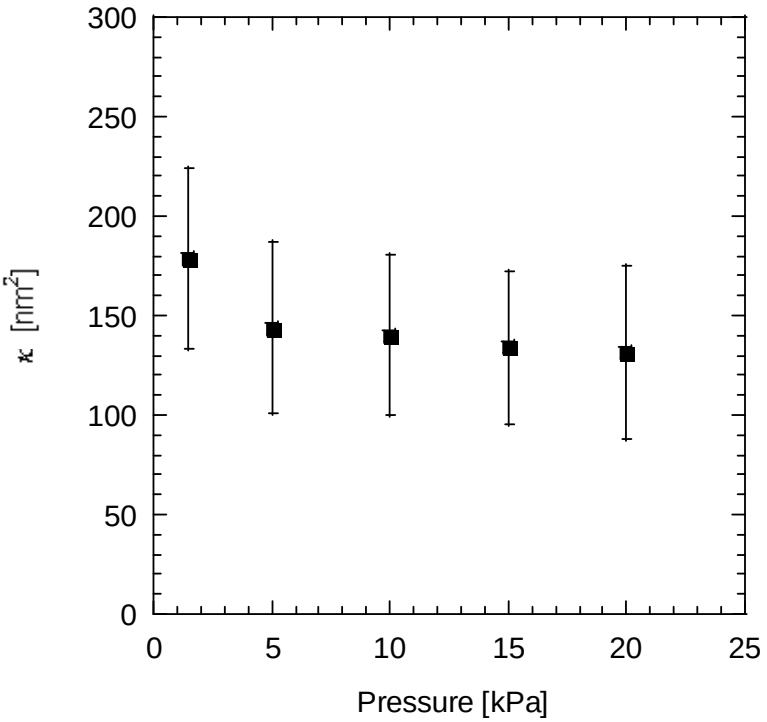

Figure 3.39 Transmembrane pressure-dependence of the Darcy permeability of 4 v% agarose gels. Error bars are the standard deviation for n=9 gels (except n=7 at 1.5 kPa and n=6 at 20 kPa).

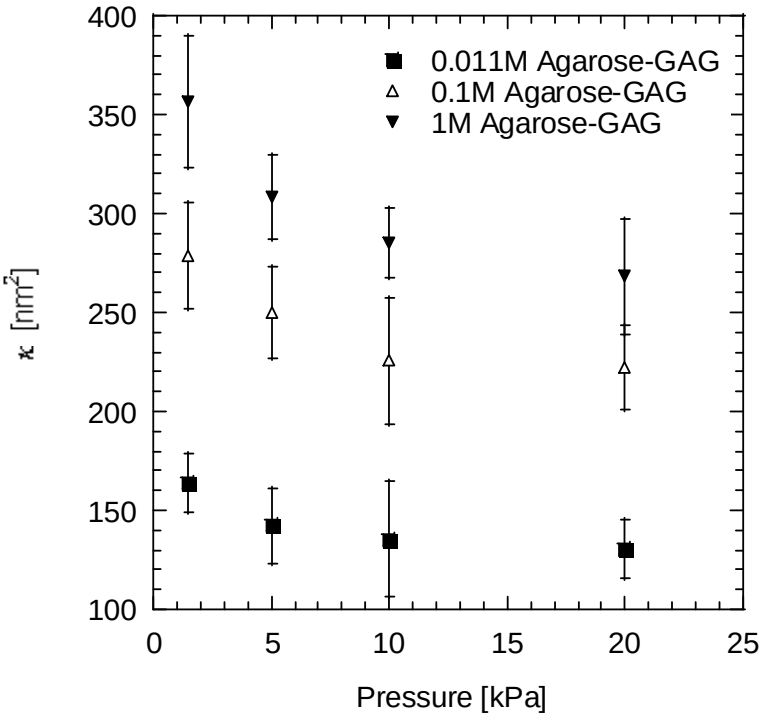

Figure 3.40 Transmembrane pressure-dependence of the Darcy permeability of agarose-GAG gels. Gels are 3 v% agarose and 129 mg GAG/g agarose (0.37 v% GAG). Measurements were performed with phosphate buffered saline solutions of 0.011 M (■), 0.1 M (△) and 1 M (▼) ionic strength. Error bars are the standard deviation for n=4 gels.

The agarose gels showed a pressure dependence similar to prior results, and the covalent binding of the GAG does not appear to modify this dependence. The change in hydraulic permeability with pressure is relatively small, with a majority of the change occurring at pressures below 5 kPa. This suggests that the fibers within the gel are not being compressed into a higher fiber density at elevated pressures. To achieve a moderate flow rate and work at pressures with constant properties, future hydraulic permeabilities are measured at approximately 10 kPa, unless otherwise noted.

GAG Wash-Out

The GAG assay on most agarose-GAG gel membranes is performed shortly after GAG attachment. To confirm that the assay is measuring the amount of covalently bound GAG and not residual un-bonded GAG, the GAG content and Darcy permeability of agarose-GAG gels was measured over 11 hours of filtration of 0.1 M buffer. The properties reported in Table 3.9 represent measurements from a single pair of gel membranes (with the exception of the initial GAG content assay, which was measured for three other gels from the same batch). As can be seen, the GAG content is virtually unchanged during extended filtration. The change in Darcy permeability is also minimal relative to the error in the measurements. It can be concluded that the wash procedure at the end of the membrane synthesis is adequate for removing unbound GAG molecules, and that there is no further wash-out of GAG during permeability measurements.

Table 3.9 Darcy permeability and GAG content of agarose-GAG gels during extended filtration (n=2, except n=3 for 0 hr GAG content)

Filtration Time [hr]	κ [nm^2]	GAG Content [mg GAG/g agarose]
0	253 ± 49	72.6 ± 6.3
1	249 ± 47	
4.5	235 ± 40	
8	238 ± 42	
11	240 ± 44	70.0 ± 8.3

Blank Agarose Gels

To study the effects of the charged GAG molecules on the membrane properties, gels were produced with variable GAG content. As a control, the properties of these gels are compared to agarose gels with no bound GAG. However, the question arises if the appropriate blank gel is unreacted agarose, agarose which has been exposed to the activation reagents or agarose which as been activated and bonded with small, neutral molecules instead of GAG. It has been reported that activated cyanate esters can form imidocarbonate cross-links between fibers (Kohn and Wilchek 1984). It is generally known that a change in solvents can affect the physical cross-linking between the agarose chains. For these reasons, the permeability of the three potential blanks was compared to determine which is most appropriate as the blank control sample.

The Darcy permeability of 3 v% agarose gels was measured for four batches prior to the activation reaction. After activation, three of the batches were placed in 0.1 M $NaHCO_3$ solutions with no GAG. The fourth batch was placed in 0.1M $NaHCO_3$ and 10^{-4} M ethanolamine (the molar equivalent to 5 g/L GAG). The samples were otherwise treated identically to gels placed in GAG attachment solutions. Following the attachment procedure, the permeability of the gels was measured.

The Darcy permeability of the blank gels before and after reaction are shown in Figure 3.41. The hydraulic permeability of the agarose gels increased by an average of 25% after exposure to the activation reactions. This confirms that either imidocarbonate cross-linking or solvent exposure does change the properties of agarose gels during activation. However, there is no significant difference between gels exposed to ethanolamine during the attachment step. This suggests that the binding of GAG, ethanolamine or other molecule should not significantly change the gel properties after activation. Therefore, the activated blank gels exposed to only $NaHCO_3$ solutions appear to be an appropriate control for GAG-agarose gels.

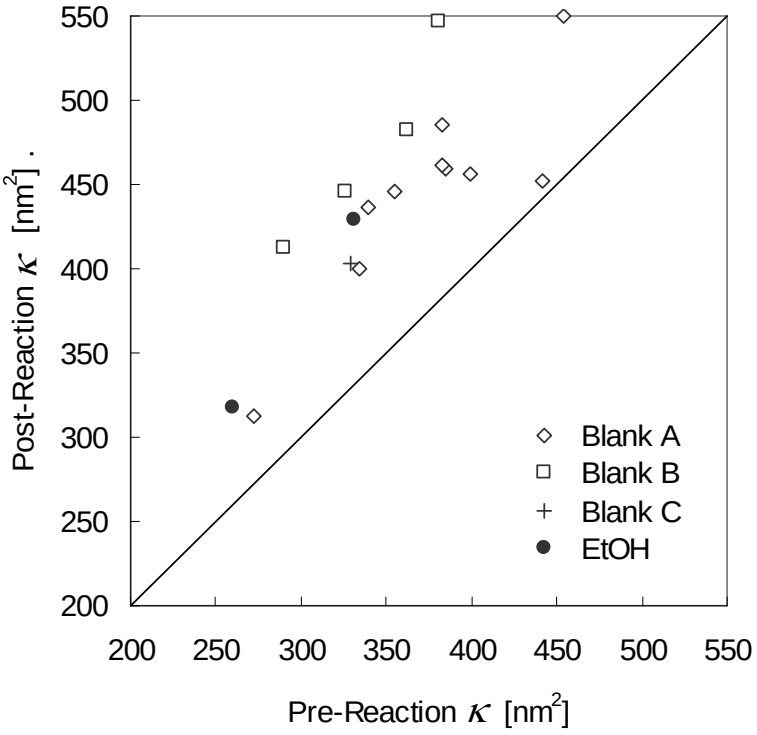

Figure 3.41 Darcy permeability of blank 3 v% agarose gels before and after exposure to activation reagents. Blank gels (Batches A ◇, B □ and C +) refer to activated agarose exposed to carbonate solution; EtOH gels (●) were exposed to ethanolamine instead of GAG during attachment.

Ionic Strength Hysteresis and Osmotic Swelling

While the gel structure is primarily determined by the physical cross-linking of the neutral agarose fibers, it is possible that electrostatic interactions between the charged GAG fibers may change the gel properties. These interactions are screened at high ionic strengths and strongest at low ionic strengths. To study the potential effects of the fiber charge interactions, the agarose-GAG membranes were tested for osmotic swelling and hysteresis of permeability measurements.

To investigate osmotic swelling, two groups of 3 v% agarose gels with high GAG content (129 mg GAG/g agarose) were equilibrated overnight in approximately 20-25 mL of buffer. Each group was placed in different ionic strengths in a random order. The gel thicknesses were measured as previously described, with two glass slides and a micrometer. As seen in Table 3.10, there was no change in the thickness of agarose-GAG gels with ionic strengths in the range of interest.

Table 3.10 Agarose-GAG gel thickness over a range of ionic strengths. Gels are 3 v% agarose and 129 mg GAG/g agarose. Standard deviations are based on n=5 (Group 1) and n=4 (Group 2).

	Ionic Strength		
	0.011 M	0.1 M	1.0 M
Group 1			
Trial A	72.6 ± 1.7	72.0 ± 1.2	73.2 ± 2.9
Trial B	71.2 ± 1.3	72.4 ± 1.3	71.2 ± 1.1
Group 2			
Trial A	71.5 ± 4.8	73.0 ± 1.2	72.8 ± 1.3
Trial B	72.0 ± 0.8	71.0 ± 1.4	71.8 ± 1.0

To determine if the hydraulic permeability of the gels is dependent on the previous ionic strength exposure, the permeabilities of two high-GAG gels were measured for a random sequence of ionic strengths. The gels were equilibrated in two 10 mL baths of buffer for 5 minutes each between ionic strengths, in addition to approximately 2 minutes (approximately 2 mL) of buffer filtered before the steady-state permeability measurements. As seen from the hysteresis paths in Figure 3.42, there is no apparent hysteresis between permeability measurements based on the previous ionic strength. The variation between permeability measurements is comparable for all ionic strengths.

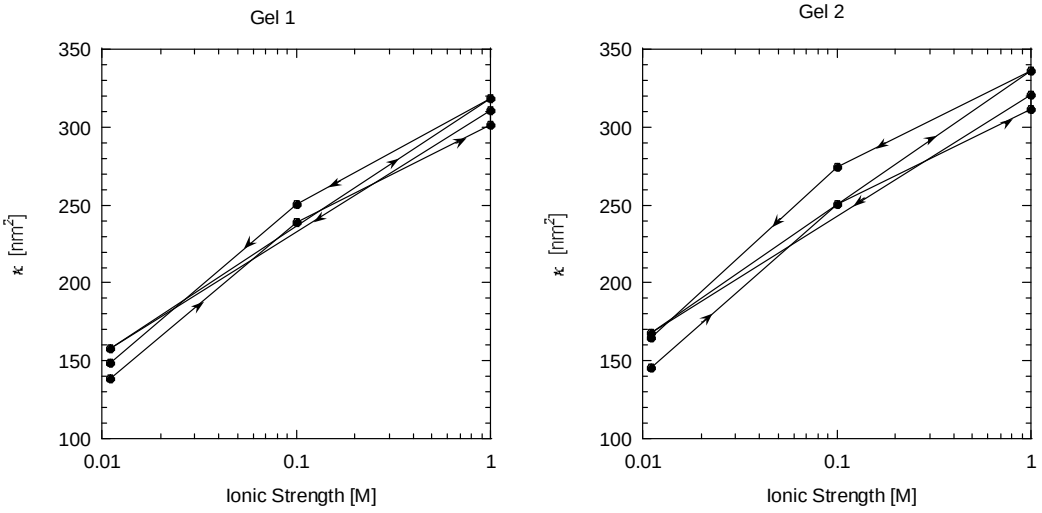

Figure 3.42 Hysteresis of Darcy permeability with ionic strength. Gels are 3 v% agarose and 129 mg GAG/g agarose.

It is concluded that the effect of solution ionic strength on the charged GAG-agarose gels does not result changes in the gel structure that affect the Darcy permeability through either changes in gel thickness or measurement hysteresis.

Experimental Permeability for GAG Content and Ionic Strength

After completing the experiments in the previous sections to verify suitable conditions for measuring the Darcy permeability of agarose-GAG gels, the permeability was measured for a range of ionic strengths and GAG contents. Six 3 v% agarose gels with no GAG, medium GAG and high GAG were tested. To eliminate the possibility that differences in the permeability are caused by variations in the agarose instead of the bound GAG, the agarose gels were pre-selected to have comparable distributions of permeabilities (Table 3.11). As seen in Figure 3.41, the permeability of a gel after reaction is proportional to its pre-reaction permeability. The permeabilities at different ionic strengths were performed in a random order for each gel.

Table 3.11 Darcy permeability of unreacted 3 v% agarose gels. Three subsets of the agarose gels were activated to created gels with high GAG (Group 1), medium GAG (Group 2) and blanks (Group 3).

	All Gels	Group 1	Group 2	Group 3
Mean κ [nm^2] ± std. dev.	376 ± 53	382 ± 39	382 ± 59	376 ± 41
# gels	51	6	6	6

To generate gels with differing GAG contents, the GAG attachment process was modified. For the high GAG gels, the activated gels were placed in a 0.05N acid bath with ice, then washed in three ice baths for 5 minutes each before being placed in the 4°C 1 g/L GAG attachment solution. For the medium GAG gels, the activated gels were placed in a refrigerated (0-4°C) acid bath, washed in three refrigerated water bathes for 15 minutes each, then placed in an ambient (~15°C) water bath for 20 minutes prior to being placed in the 4°C 1 g/L GAG attachment solution. The blank gels were treated the same as the medium GAG gels, except they were placed directly in a refrigerated 0.1M $NaHCO_3$ solution after the three washes. The result was agarose gels with

0 mg GAG/g agarose for no GAG, 54 ± 0.3 mg GAG/g agarose for medium GAG and 129 ± 14 mg GAG/g agarose for high GAG.

The Darcy permeability of these gels is reported in Figure 3.43 for solution ionic strengths of 0.011 1.0 M. The presence of GAG fibers, even at the low concentrations of 54 mg GAG/g agarose and 129 mg GAG/g agarose, decreased the permeability of the gels by over 29% and 41%, respectively. Assuming a GAG radius of 0.5 nm, a GAG fiber length of 1 nm per dissacharride and a dissacharride weight of 474 Da for chondroitin sulfate with one sulfate substitution, the GAG has a volume fraction of ϕ_{GAG}=0.0017 for medium GAG (54 mg GAG/g agarose) and ϕ_{GAG}=0.0039 for high GAG (129 mg GAG/g agarose). Assuming an agarose fiber radius of 1.6 nm, the ratio of GAG fiber length to agarose fiber length is 0.57:1 and 1.35:1 for medium and high GAG, respectively. As noted by Clague and Phillips, slender body theory predicts that hydraulic permeability is primarily a function of the fiber length per unit volume (Clague and Phillips 1997). It is therefore not surprising that a low volume fraction of GAG fibers produced a significant decrease in the permeability, since they have a comparable fiber length to agarose.

Figure 3.43 also shows that the permeability of the blanks gels was independent of the ionic strength of the buffer solution passed through them, confirming that agarose has negligible net charge. This agrees with the product information supplied by Sigma for agarose (Product # A3893, Sigma, St. Louis, MO), which reports a sulfate content of <0.20%. However, both the medium GAG and high GAG gels had a decrease in permeability of 32% and 49%, respectively, over the range of 1.0 M to 0.01 M buffer solution. This is due to the electrokinetic coupling in the open-circuit permeability of the highly-charged GAG fibers.

The curves in Figure 3.43 are the predictions of the composite model for hydraulic permeability which was presented in Section 3.2.4 (Figure 3.25). Both the decrease in permeability due to GAG fibers and the decrease in permeability at low ionic strength are well-captured by the model. The model assumes a GAG fiber charge density ($\sigma_{s,GAG}$) of -100 mC/m^2 and agarose heterogeneity parameter of ε_2=0.1. The decrease in permeability predicted by the addition of GAG fibers is in excellent agreement with the data. However, the relative decrease in permeability due to diminished charge screening

at low ionic strengths is underestimated by the model. This is possibly due to the assumptions in the fiber mixing models, which are coarse approximations to the interactions between multiple fiber types. Such approximations may underestimate the electrokinetic coupling which occurs between the two fiber types, and would be more pronounced at low ionic screening. As noted in Table 3.3, the weighted inverse averaging method often underpredicts the hydraulic permeability of charged systems with a root mean squared error of 20-30%.

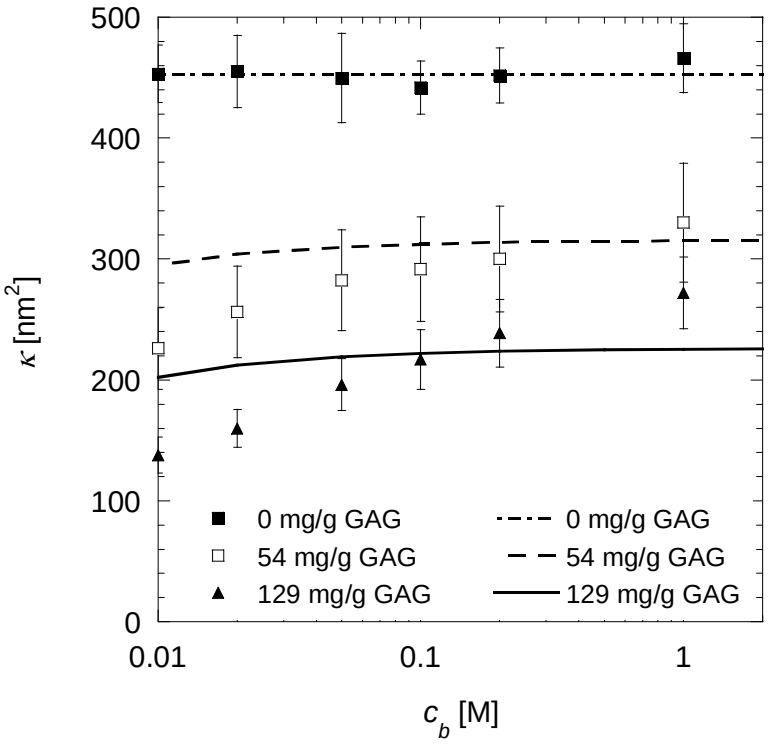

Figure 3.43 Darcy permeability (κ) of agarose-GAG gels over a range of ionic strengths of phosphate buffered saline solution. All gels are 3v% agarose and 0 mg GAG/g agarose (■), 54 mg GAG/g agarose (□) or 129 mg GAG/g agarose (▲). The composite model predictions are indicated by the lines for the corresponding GAG content: ϕ_{GAG}=0 (- · -), ϕ_{GAG}=0.0017 (- - -) and ϕ_{GAG}=0.0039 (—). The model parameters are $r_{f,a}$ = 1.6 nm, $r_{f,GAG}$ = 0.5 nm, $\sigma_{s,GAG}$ = -100 mC/m^2, $l_{f,GAG}$=105.5 nm/molecule, MW$_{GAG}$=50 kDa and ε_2=0.1. Error bars are one standard deviation for n=6.

Alternately, a more likely problem is the way in which charge is treated in the agarose "clumps". In the modular clump approach, a zero current conditions as necessarily imposed separately within each region (matrix and spheres). In an actual heterogeneous material, zero *overall* current is all that is required under open-circuit conditions. Thus, flow in the two regions may be coupled electrically in ways that could be captured only

by a more complex model, where the charge of GAG in the fiber "clumps" influences the electrical potential in the surrounding fiber matrix. In a simplified version of such a model, the effect of charged inclusions within a neutral gel were shown to have long-range effect on the electrokinetic coupling, even when Debye lengths were 1-2 orders of magnitude smaller than the charged inclusions (Hill 2006).

If charge effects occur on a scale larger than a "clump", then the Donnan equilibrium model may provide a more appropriate way to approximate the charge behavior. The Donnan model predictions of hydraulic permeability for the high GAG gels are shown in Figure 3.44. The two curves in the figure show the Donnan model using a neutral fiber permeability calculated from the neutral composite model (Equation (3.24) with inverse weighted averaging and spherical heterogeneities), as well as from the experimental permeability at high ionic strength. While the diffuse double layer composite model *underpredicted* the permeability decrease at low ionic strengths, the Donnan model with a macroscopic charge density *overpredicts* the decrease.

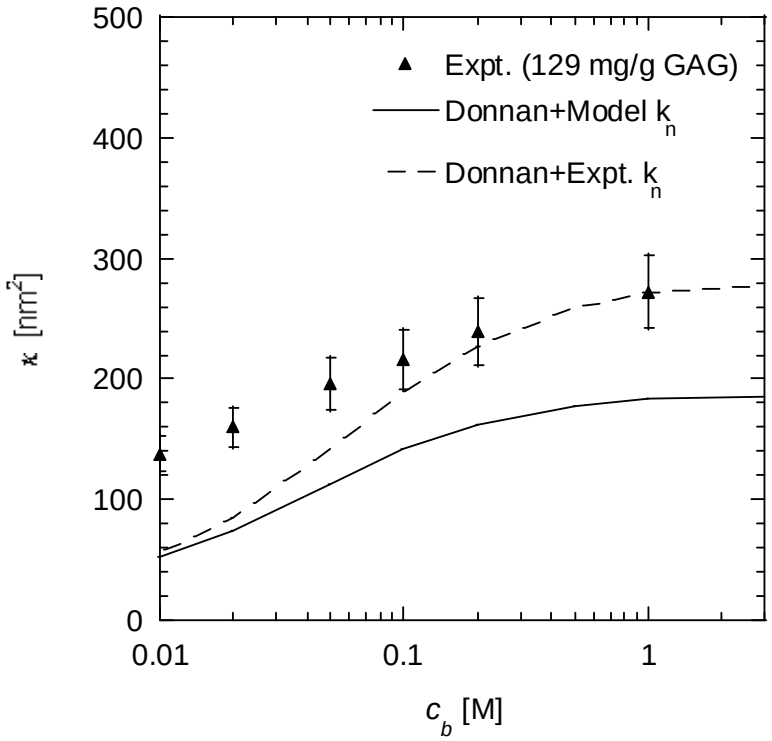

Figure 3.44 Darcy permeability (κ) of agarose-GAG gels over a range of ionic strengths of phosphate buffered saline solution. Experimental data is from gels with 3v% agarose and 129 mg GAG/g agarose (▲). The Donnan composite model predictions are indicated by the lines using the experimental neutral fiber permeability (- - -) and the model neutral permeability (—). The model parameters are $r_{f,a}$ = 1.6 nm, $r_{f,GAG}$ = 0.5 nm, $\sigma_{s,GAG}$ = -100 mC/m^2, ϕ_{GAG}=0.0039, and ε_2=0.1. The Donnan model uses the macroscopic fixed charge density of c_m=-16.6 meq/L. Error bars are one standard deviation for n=6.

The choice of fixed charge density in the Donnan model is bounded by the macroscopic charge density (-16.6 meq/L) and the matrix charge density (varies with ε_2; -1.3 meq/L for ε_2=0.1) (Figure 3.45). If the GAG binding is not proportional to the agarose density (e.g. – there is preferential binding in regions of lower steric or electrostatic hindrance) or if the charge effects occur on length scales larger than the fiber spacing (i.e. – the electrical potential in the matrix is affected by the highly-charged clumps), then the effective fixed charge density in the Donnan model will fall between these two bounds. As seen in Figure 3.45, the charge density that minimizes the relative root mean squared error is -8.7 meq/L, which is equivalent to a matrix GAG density of $\phi_{1,GAG}$=0.0021. However, using this $\phi_{1,GAG}$ in the Donnan composite model predicts a decrease of ~90% in the neutral permeability due to the addition of 129 mg GAG/g agarose to 3 v% agarose, which is much larger than the 40% reduction observed experimentally. Therefore it appears that the charge effects occur over a large length scale, which is not captured by the heterogeneous clump model.

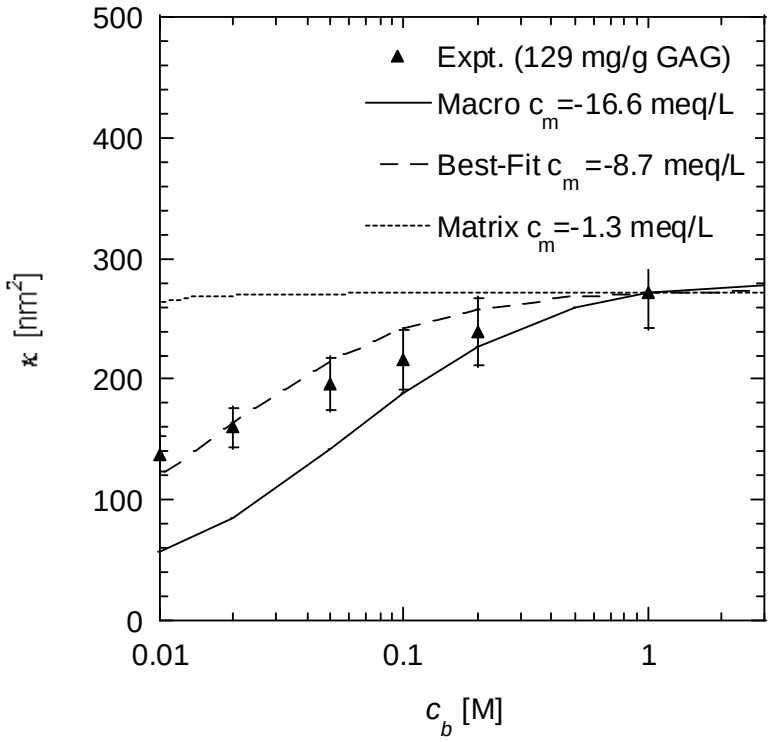

Figure 3.45 Darcy permeability (κ) of agarose-GAG gels over a range of ionic strengths of phosphate buffered saline solution. Experimental data is from gels with 3v% agarose and 129 mg GAG/g agarose (▲). The Donnan composite model predictions using the experimental neutral fiber permeability are indicated by the lines using a fixed charge density based on the macroscopic GAG content (—), the GAG content in the Region 1 matrix (with ε_2=0.1) (····) and the best-fit to the experimental data (- - -). Error bars are one standard deviation for n=6.

The Donnan composite model was also applied to Darcy permeability data collected from 4 v% agarose gel with 0 and 53 mg GAG/g agarose (ϕ_{GAG} = 0, 0.0022) (Figure 3.46). The synthesis of these gels will be discussed further in later chapters. The Donnan composite model used the neutral fiber permeability predicted by fiber models and a fixed charge density based on the macroscopic GAG content. This is the same model used to generate the solid curve in Figure 3.44. Fortuitously, the model more closely matches the experimental data for the 4 v% agarose gels in Figure 3.46 than the 3 v% gels in Figure 3.44. The results were insensitive to the choice of the heterogeneity parameter, with the 0.2 v% GAG curve changing by less than 0.1% for ε_2 = 0.1-0.5.

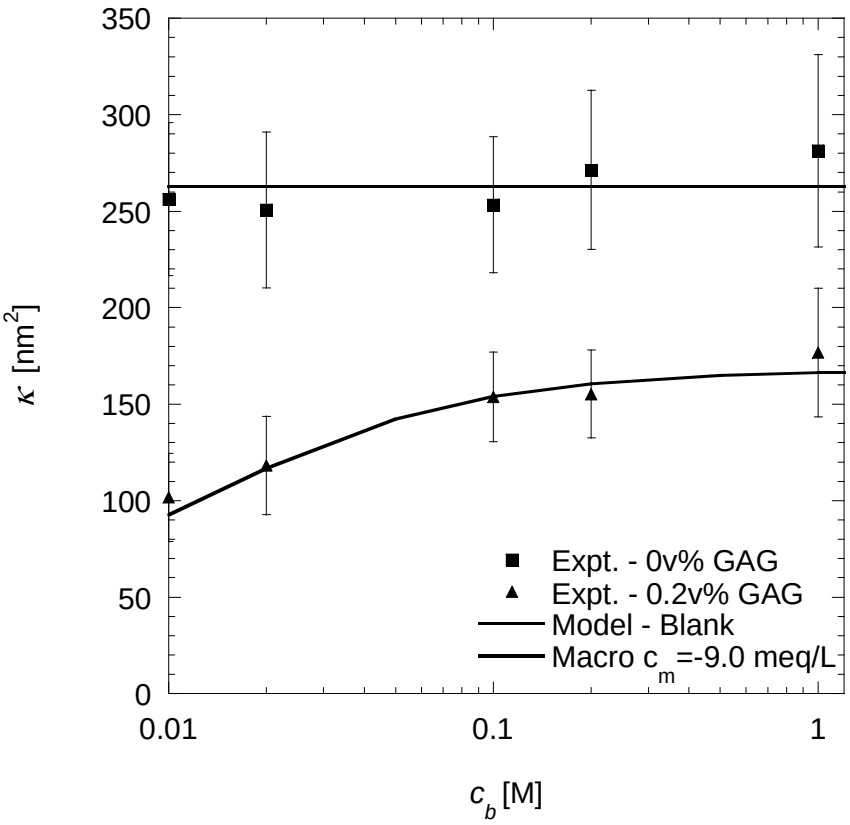

Figure 3.46 Darcy permeability (κ) of agarose-GAG gels with 4v% agarose over a range of ionic strengths of phosphate buffered saline solution. The Donnan composite model predictions are indicated by the lines using the model neutral permeability and the macroscopic fixed charge density (c_m = -9.0 meq/L). The model parameters are $r_{f,a}$ = 1.6 nm, $r_{f,GAG}$ = 0.5 nm, $\sigma_{s,GAG}$ = -100 mC/m^2, ϕ_{GAG}=0.0022, and ε_2=0.1. Experimental data is from gels with 0 mg GAG/g agarose (■) or 53 mg GAG/g agarose (0.2 v% GAG) (▲). Error bars are one standard deviation for n=6.

Further research is required to determine the correct way to model the open-circuit hydraulic permeability through a membrane with heterogeneous charge distribution. However, until such a rigorous approach is developed, the Donnan equilibrium model and the neutral composite fiber model provide a rationalization of the effect of GAG fibers and solution ionic strength on the hydraulic permeability of agarose-GAG membranes.

3.4. Conclusions

The Darcy permeability of 3 v% agarose membranes was observed to decrease by almost half with the addition of 129 mg GAG/g agarose (0.4 v% GAG). The Darcy permeability was further reduced by half when the ionic strength of the solution was reduced from 1 M to 0.01 M. A number of additional characterizations of the membranes confirmed that these effects were not due to transient changes in permeability, order of ionic strengths, gel swelling, selection of blank gel type, pressure effects, or variation between gel prior to GAG attachment. The value of the correction factor, β_m, was improved with revised dimensions of the membrane support mesh and three-dimensional modeling of the woven fiber arrangement of the mesh.

No single model was available in the literature to predict the hydraulic permeability of the agarose-GAG membranes. A model was developed that captured the presence of two types of randomly-oriented fibers with different radii, the charge affect of the GAG fibers, and the heterogeneous density of the agarose fibers. A number of charged fiber models and fiber mixing rules were evaluated. Since the heterogeneity of the agarose fibers appears to result in heterogeneity of GAG charge, it was difficult to implement the no-net-current restriction of open-circuit permeability to the heterogeneous regions. The Donnan model was able to rationalize the effect of solution ionic strength on the macroscopic permeability, while structural permeability models and fiber mixing rules predicted the decrease in permeability from the addition of GAG fibers.

Chapter 4. MACROMOLECULE PARTITIONING

4.1. Introduction

One of the properties which characterizes the permeation of a solute *i* through a hydrogel is the equilibrium partition coefficient, Φ_i. It relates the concentration of the solute within the gel (c_i') to the concentration in the surrounding bulk solution (c_i) at equilibrium:

$$\Phi_i = \frac{c_i'}{c_i} \tag{4.1}$$

where c_i' is based on the total gel volume, including solids.

Due to its relevance to gel chromatography, a number of studies have investigated how macromolecules partition into agarose gels. Solutes have included Ficoll (a crosslinked surcrose), dextran, and proteins (ribonuclease, chymotrypsinogen A, ovalbumin, bovine serum albumin, aldolase, and thyroglobulin) (Laurent 1967, Lazzara and Deen 2004, Moussaoui et al. 1992, White and Deen 2000). Several studies have considered charge interactions in partitioning, such as protein-protein interactions (Buck et al. 2001), protein-agarose (Sepharose^{TM}) interactions (Crone 1974), protein- modified

agarose (Superose^{TM}) interactions (Edwards and Dubin 1993), and protein-sulfated agarose interactions (Johnson et al. 1995). Less studied is partitioning into composite gels with two or more types of fibers. One study looked at the partitioning of monodisperse Ficolls into agarose-dextran gels (Kosto et al. 2004), which is of particular relevance to the current work because of the structural similarity between dextran and GAGs.

The following sections present partition coefficients for BSA and monodisperse Ficolls into agarose-GAG gels. Partition coefficients were measured over a range of ionic strengths to study the electrostatic interactions between solutes and fibers. The partitioning of Ficolls with several hydrodynamic radii was also studied. Relevant partitioning theories are summarized, combined into a composite model for agarose-GAG membranes, and compared to the experimental data.

4.2. Theory

The partitioning of macromolecules into gels typically models cross-linked polymers as randomly oriented rigid rods, similar to models for Darcy permeability. Early theoretical work was done by Ogston, who derived an expression for the partitioning of a dilute solution of spheres into an array of randomly oriented rods:

$$\Phi_i = \exp\left[-\phi\left(1+\frac{r_{s,i}}{r_f}\right)^2\right] \tag{4.2}$$

where ϕ is the volume fraction of fibers, $r_{s,i}$ is the radius of the solute i, and r_f is the radius of the rod. The fiber model for equilibrium partitioning was extended to concentrated solutions of spheres (Fanti and Glandt 1990), solutions of spheroids (Lazzara et al. 2000), mixtures of multiple types of fibers (Lazzara et al. 2000), and charged solutes or fibers (Johnson and Deen 1996a).

Similar to the model for hydraulic permeability in Chapter 3, the agarose-GAG membranes can be viewed as a mixture of two fiber types with two regions of different fiber densities to account for the heterogeneity in agarose fiber distributions. The following sections will discuss the relevant theories for a composite model for agarose-GAG membranes.

4.2.1. Multi-Fiber Models

An excluded-volume model was developed for partitioning in neutral systems with interactions between any number of spheroidal solutes and rigid rods (Lazzara et al. 2000). The model is applicable for both dilute and concentrated solutions. The partition coefficient is calculated by summing the volumes excluded to a solute due to its finite size, the size of other solutes, and the presence of fixed fibers. For a membrane with two fibers (types 1 and 2) and a spherical solute (*i*), the partition coefficient is given by

$$\Phi_i = \exp\left[-\phi_1 \left(1 + \frac{r_s}{r_{f,1}} \right)^2 - \phi_2 \left(1 + \frac{r_s}{r_{f,2}} \right)^2 + 8\chi_i \left(1 - \Phi_i \right) \right] \tag{4.3}$$

where χ_i is the volume fraction of solute *i* (for dilute solutions, this last term is negligible relative to the fiber excluded volume terms).

It can be seen that the dilute form of Equation (4.3) ($\chi_i = 0$) is simply the product of the partition coefficients for each fiber type. This form is because the interactions of the solute with a fiber type *j* are assumed to be independent of the solute interactions with all other fiber types. We hypothesized that this multiplicative form can be extended to mixtures of agarose and GAG fibers, where the exclusion effects of the GAG are independent of the exclusion effects of agarose:

$$\Phi_i \approx \Phi_{i,a} \Phi_{i,GAG} \ . \tag{4.4}$$

In this form, only the partition coefficient in GAG ($\Phi_{i,GAG}$) includes charge interactions between GAG and solute *i*; the partition coefficient in agarose ($\Phi_{i,a}$) uses neutral fiber models.

4.2.2. Charge Models

Similar to the models for Darcy permeability, the charged fibers can either be accounted for by a microstructural model or a macroscopic Donnan equilibrium model.

Donnan Equilibrium

In the macroscopic model, the negative charge is assumed to be uniformly distributed throughout the membrane volume with a concentration c_m ($c_m > 0$, assuming negative

fixed charge). The charge induces a jump in potential at the membrane surface, know as the Donnan potential (ψ_D):

$$\psi_D = \psi_{mem} - \psi_{bulk} = \frac{-RT}{F} \ln\left(\frac{c_+^{'}}{c_b}\right) \quad . \tag{4.5}$$

Using a reference state of zero potential in the bulk solution, the Donnan potential with a symmetric, monovalent salt is evaluated as

$$\psi_D = \frac{-RT}{F} \ln\left(\frac{-c_m}{2c_b} + \sqrt{\frac{c_m^{\,2}}{4c_b^{\,2}} + 1}\right) . \tag{4.6}$$

The Donnan potential will have the same sign as the fixed charge, with $\psi_D < 0$ for a negatively charged membrane.

To find how a finite-sized solute partitions into the membrane, it is assumed that the steric and electrostatic effect are independent and can be superimposed (Bhattacharjee et al. 1999). Solving the linearized Poisson-Boltzmann equation for a charged sphere in a uniform potential field (ψ_∞), the potential at the sphere surface is

$$\psi = \psi_\infty + \frac{r_s}{\varepsilon} \frac{\sigma_s}{\left(1 + r_s / \lambda_D\right)} \tag{4.7}$$

where σ_s is the surface charge density of the solute and λ_D is the Debye length. Using the approach in Johnson and Deen for evaluating the partition coefficient (Johnson and Deen 1996a), the Boltzmann factor is independent of position and the expression becomes

$$\Phi_i = \Phi_{i,0} \exp\left(-\frac{z_i F}{2RT} \psi_D\right) \tag{4.8}$$

where $\Phi_{i,0}$ is the partition coefficient for the neutral system and z_i is the valance charge of the solute.

Microstructural

Johnson and Deen developed a structural model for the partitioning of dilute solutes into a charged fiber membrane (Johnson and Deen 1996a). The model uses the linearized Poisson-Boltzmann equation, which has minimal errors for potentials of <2-4 *RT*/*F*. In the current system, the GAG surface charge at 0.01 M gives an electrostatic potential of 5.5 *RT*/*F*, which makes applicability of the model borderline at the lowest ionic strength but reasonable for the majority of conditions (a minimum of 1.3 *RT*/*F* at 1 M).

In the microstructural model, the partition coefficient is evaluated by a steric function (g) weighted by a Boltzman factor, which is integrated over space:

$$\Phi_i = \int_0^\infty \exp\left(-E(h)\right) g(h)\, \mathrm{d}\, h \tag{4.9}$$

where h is the distance from the sphere surface to the fiber surface. The steric and electrostatic functions are evaluated by

$$g(h) = \frac{2\phi(h + r_s + r_f)}{r_f^2} \exp\left[\frac{-\phi(h + r_s + r_f)^2}{r_f^2}\right] \tag{4.10}$$

$$E(h) = \left(\frac{RT}{F}\right)^2 \frac{\varepsilon r_s}{kT}\left[A_1\sigma_s\sigma_f + A_2\sigma_s^2 + A_3\sigma_f^2\right] \ . \tag{4.11}$$

The dimensionless surface charge densities for the solute ($\tilde{\sigma}_s$) and fiber ($\tilde{\sigma}_f$) are related to the dimensional surface charge density (σ_i) by

$$\tilde{\sigma}_i = \frac{r_s F}{\varepsilon RT}\sigma_i \tag{4.12}$$

The parameters A_1, A_2, and A_3 were found through numerical simulations and fit to the form

$$A_i = a_i \beta^{b_i} \tau^{-c_i} \exp\left[-d_i \eta\right] \tag{4.13}$$

where $\beta = r_f/r_s$, $\tau = r_s/\lambda_D$, and $\eta = h/\lambda_D$. The coefficients a_i, b_i, c_i, and d_i are given in Table 4.1.

Table 4.1 Constants in the free energy correlation for the microstructural partitioning model

i	a_i	b_i	c_i	d_i
1	2.3523	0.7599	1.2472	1.0956
2	0.3570	0.5052	0.9512	3.7684
3	0.4473	0.9310	1.1512	2.4987

In model results in the following sections, the integration in Equation (4.9) was done numerically, with a step size small enough that the solution converged (generally ~1500 steps was more than adequate) and infinity was approximated by the greater of 10 Debye lengths or 10 times r_f^2/ϕ (such that exponential terms in both $g(h)$ and A_i had negligible contribution to the integral).

4.2.3. Heterogeneity

Unlike the Darcy permeability or other analogous transport properties (Bonnecaze and Brady 1991), the equilibrium partition coefficient in a heterogeneous material with multiple regions does not depend on the shape or distribution of those regions. Instead, the effective partition coefficient of the entire material ($\Phi_{i,eff}$) is simply found by adding the partition coefficient in each region j ($\Phi_{i,j}$) weighted by the volume fraction of that region:

$$\Phi_{i,eff} = \sum_j \varepsilon_j \Phi_{i,j} \quad . \tag{4.14}$$

The measured partition coefficients discussed in the following sections, denoted as Φ for simplicity, are equivalent to $\Phi_{i,eff}$.

4.3. Experimental Materials & Methods

4.3.1. Membrane Modifications

The hydraulic permeability experiments in Chapter 3 focused on 3 v% agarose gels of approximately 70 μm thickness. However, for several reasons which are explained here and in the following chapter on solute sieving, it was beneficial to change the membranes to 4 v% agarose and 95 μm thickness. The 3 v% gels provided minimal steric hindrance to the solutes of interest, like bovine serum albumin. The thinness of the membranes corresponded to small gel volumes, which resulted in higher errors in partitioning measurements and lower solute concentrations that were difficult to measure with conventional assays.

The agarose-GAG gels were prepared in the same way as described in Chapter 2. However, the glass plates had ~100 μm spacers (made from overhead transparency film) glued in the corners. The result was gels with a mean thickness of 95 μm (80-115 μm). GAG was attached following the conditions for "high GAG" gels in Chapter 3, which resulted in gels with 53 ± 11 mg GAG/g agarose ($\phi_{GAG} = 0.0022$).

4.3.2. Test Solutes

As stated previously, the objectives of this research were to determine the roles of solute size and charge on equilibrium partitioning into fibrous agarose-GAG membranes.

Following previous studies in our lab on solute size effects, narrow fractions Ficolls of several molecular weights were used (Johnson et al. 1996, Kosto et al. 2004). Several options were considered for exploring the role of charge in proteins: comparison of native proteins to charge-neutralized proteins, comparison of globular proteins to equivalently sized neutral Ficolls, and comparison of proteins at high and low ionic shielding.

Ficolls

Ficolls are neutral polymers of sucrose and epichlorohydrin that are highly branched and cross-linked, forming a nearly spherical structure. Four narrow fractions of Ficoll were previously obtained (special order from Pharmacia LKB, Piscataway, NJ) and labeled with 5-(4,6-dichlorotriazinyl)aminofluorescein (DTAF) (Barskii et al. 1968, De Belder and Granath 1973). The Ficolls contain ~1 fluorescein per molecule, which is insufficient to give the Ficoll a significant charge (Johnson et al. 1996).

There are slight discrepancies between previous researchers on the value of the Stoke-Einstin radius (r_s) for each Ficoll fraction. The radii have been determined from a correlation of Ficoll molecular weight and hydraulic radius generated by quasielastic light scattering (Oliver et al. 1992), as well as by two sets of free-solution diffusivities measured by fluorescence-recovery after photobleaching (FRAP) (Johnson et al. 1996, Kosto and Deen 2004). The Ficoll properties are summarized in Table 4.2. In the following work, we use the Stokes-Einstein radii reported by Kosto and Deen (Kosto and Deen 2004).

Table 4.2 Properties of Ficolls. Molecular weight and polydispersity (M_w/M_n) were reported by Pharmacia; Stokes-Einstein radii are from referenced sources.

Sample	M_w [Da]	M_w/M_n	r_s [nm] (Kosto and Deen 2004)	r_s [nm] (Johnson et al. 1996)	r_s [nm] (Oliver et al. 1992)
Ficoll 21K	21,290	1.22	2.7	3.03	2.97
Ficoll 37K	37,360	1.18	3.5	3.80	3.77
Ficoll 61K	60,710	1.15	4.5	4.82	4.64
Ficoll 105K	105,210	1.13	5.9	6.23	5.87

Proteins

Many types of globular proteins are available for study. Bovine serum albumin (BSA; 69 kDa) is the most biologically relevant for renal filtration due to its high concentrations in blood. It is well characterized due to its prevalence in other biological studies, with a Stokes-Einstein radius of ~3.6 nm and native charge of -21 at physiological conditions (Johnson et al. 1995, 1996, Vilker et al. 1981).

Several smaller, related proteins are also readily available, such as ovalbumin (45 kDa, r_s = 2.7~3.1 nm), lactalbumin (14 kDa; ~2.3 nm), and parvalbumin (12 kDa). Other globular proteins (some of which are di/tri/tetra-meric) include chymotrypsinogen A (25 kDa; 2.2 nm), horseradish peroxidase (HRP; 40 kDa, 3.0 nm), hexokinase (54 kDa, 3.6 nm), lactic dehydrogenase (140 kDa, ~4.3 nm), aldolase (158 kDa, 4.8 nm), catalase (250 kDa, 5.2 nm), immunoglobulin G (IgG; 150 kDa, 5.2~5.6 nm), physobiliproteins (104 & 240 kDa), and thyroglobulin (670 kDa, 8.5 nm). However, many of the proteins considered did not have a well-characterized hydraulic radius or net charge, or the charge varied between different clonal forms. It was preferred to work with an anionic protein, to avoid complex binding interactions between a cationic protein and the anionic GAG. Previous work by Dr. Kim Kosto in the Deen Lab found significant differences between the hydraulic radius of IgG from size-exclusion chromatography versus FRAP diffusivity, which raised concern over the experimental suitability of IgG. Other proteins were not readily available in the quantities needed for the experiments described in the following sections. Further, it was found that the agarose-GAG gels were not selective to proteins significantly smaller than BSA, such as ovalbumin. Due to the these limitations, it was decided to only use BSA (Sigma #A2153; St. Louis, MO) in the following sieving studies.

It is possible to neutralize the native charge on BSA if the buffer solution pH is at the protein's isoelectric point; however, this would complicate the experiments by also affecting the charge of the GAG fibers. It is also possible to neutralize BSA with a graded modification of the carboxyl groups to yield a zero net charge protein (Hoare and Koshland 1967). However, personal communications with J. (Sörensson) Nystrom and B. Haraldsson noted that such charge-modified BSA needed to be used shortly after synthesis, since it tended to lose a significant fraction of the charge modification after

several weeks. Another charge-modifying procedure exists for adding negative charge by succinylation of native (neutral) HRP (Sörensson et al. 1998), which they noted was charge-stable for at least a year. However, the smaller size of HRP made it of less interest in the current study. Due to the limitations of charge-modified proteins, they were not included in the following studies.

As noted previously, the charge behavior of proteins can be compared to the behavior of similarly-sized neutral Ficolls. While a number of studies have found similar transport properties for proteins and Ficolls in agarose under neutral conditions (Johnson et al. 1996, Johnston and Deen 2002, Kosto and Deen 2004), differences have been observed in track-etched membranes and *in vivo* renal studies (Venturoli and Rippe 2005). It was hypothesized that Ficolls may have an open, slightly deformable structure that makes them deviate from results for hard spheres. This theory was supported by permeability studies with Ficoll and well-defined pores, where Ficolls deviated from hard-sphere model predictions when the solute radius approached or exceeded the pore radius (Fissell et al. 2007).

"Dilute" Solutions

It was desired to perform all experiments in the dilute limit, where solute-solute interactions could be neglected in the solution. Using Equation (4.3) in the limit of no fibers, the partition coefficient for a BSA molecule in a 1 g/L solution relative to an infinitely dilute solution is 0.991, or a 0.9% difference from solute-solute interactions. However, the interaction between BSA molecules at low ionic strengths was of most concern, where charge interactions are strongest. The strengths of any solute-solute interactions at low ionic strengths were estimated by virial expressions for BSA diffusivity and osmotic pressure as a function of concentration.

The osmotic pressure for BSA at pH 7.4 was reported at ionic strengths of 0.01, 0.05, and 0.15 M over a range of BSA concentrations (DiLeo 1982). The results were curve-fit to a virial form, where at 0.01 M the expression was

$$\Pi = 0.7662 c_{BSA} + 5.93 \times 10^{-3} c_{BSA}^2 + 1.89 \times 10^{-5} c_{BSA}^3 \qquad (4.15)$$

where the osmotic pressure (Π) is in units of mmHg and the BSA concentration is in g/L.

A virial expansion was also reported for the diffusivity of BSA for ionic strengths of 0.0005-0.1 M (Anderson et al. 1978). The expression at 0.01 M was

$$D = D_0\left[1 + 0.0170 c_{BSA}\right] \tag{4.16}$$

with the BSA concentration in g/L. From these expression, the solute-solute interactions in a 1 g/L solution were 0.8% of the osmotic pressure dilute value and 2% of the diffusivity dilute value. These second-order effect were small enough to consider all solutions ≤ 1 g/L as dilute over the range 0.01-0.5 M.

4.3.3. Method

The partition coefficient was measured similarly to the method described previously (Kosto et al. 2004), with slight modifications to the rinse procedure prior to equilibration in buffer. If the membrane was being changed to a solution of a different ionic strength from the previous measurement, it was first equilibrated in several milliliters of buffer of the new ionic strengths for at least 2 minutes to rinse out excess salt. Each membrane then was placed into a vial with approximately 10 mL of macromolecule solution of known concentration in the buffer of interest (1 g/L for proteins or 0.5 g/L for Ficolls). The large solution volume (relative to the gel volumes of ~0.03 mL) ensured that the solute concentration in the solution remained nearly constant. The phosphate buffers (0.011-0.5 M, pH 7.4) were identical to those used for measuring the hydraulic permeability, whose compositions are summarized in Appendix B. The membrane was allowed to equilibrate for 1 hour. Using a BSA diffusivity in 3.9 v% agarose of $3\text{x}10^{-7}$ cm^2/s (Johnson et al. 1996), the equilibration time was many times longer than the 75 second characteristic diffusion time for a 95 μm membrane.

After the membrane equilibrated, it was removed from the solute solution, the excess solution was rinsed off, and the membrane was placed in a vial with a small volume of solute-free buffer (generally 1 mL for proteins or 2 mL for Ficolls). The membrane was again allowed to equilibrate for 1 hour. Unlike previous partitioning methods, it was found that due to the small volume of the gel relative to its surface area, agarose-GAG gels were particularly sensitive to the method used to remove excess solute solution prior to the second equilibration. To fully wash the excess solute solution off the gel surface without allowing significant solute to diffuse out from the gel, each membrane was

placed between two coarse stainless steel meshes separated by ~6 mm spacers, such that the membrane could freely move in the volume between the meshes. The mesh-membrane assembly was then dipped in 400 mL of buffer. The membrane was quickly removed from the mesh, shaken, and blotted lightly on its edge to remove excess buffer.

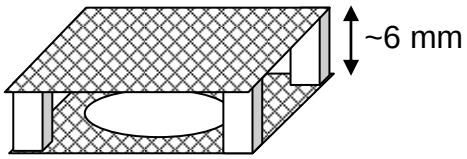

Figure 4.1 Diagram of mesh "basket" used for rinsing membrane between partitioning equilibrations.

The concentrations of the solute in the initial solution ($c_{i,1}$) and the buffer after equilibration ($c_{i,2}$) were measured using the assays outlined in Section 4.3.4. Using a mass balance on the solute, the partition coefficient was calculated from

$$\Phi_i = \frac{V_2}{V_g\left(\frac{c_1}{c_2}-1\right)} \approx \frac{V_2 c_2}{V_g c_1} \tag{4.17}$$

where V_2 is the volume of buffer and V_g is the total volume of hydrogel in the membrane. The volume of the gel (22-39 μL) was determined from the membrane thickness as measured by micrometers, the mesh radius (12.5 mm), and the volume of the mesh fibers (17.7 μL, based on the average mesh dimensions reported in Chapter 3).

4.3.4. Solute Assays

Several solute assays were utilized depending on the type and concentration of the solute.

Fluorescence

For fluorescein-labeled Ficoll, either of two spectrofluorometric detectors with an excitation at 488 nm and emission at 515 nm was used to measured the relative concentrations. The detector in the Deen Lab (Shimadzu RF-551 PC; Columbia, MD) could generally detect fluorescent-Ficoll concentrations of 10^{-5}-10^{-4} g/L; the detector in the Hatton Lab (Photon Technology International, Inc.; Birmingham, NJ) could detect

10^{-5}-10^{-3} g/L. Since only the relative concentrations (c_1/c_2) were needed and the fluorescence was directly proportional to the concentration, no standard curves were used. The corresponding ionic strength buffer was used to measure the blank readings on the fluorometer and to dilute samples into the detectable concentration range.

UV Absorbance

Solutions of BSA were measured in a spectrophotometer (Shimadzu BioSpec 1601; Columbia, MD) for concentrations of 0.1-2 g/L in either a UV-transparent or quartz cuvette with buffer in the reference cell. Proteins follow Beer's Law, with a linear correlation between their concentration (c_{BSA}, in g/L) and their absorbance at 280 nm:

$$\mathrm{Abs}_{280\,\mathrm{nm}} = 0.667 c_{BSA} \tag{4.18}$$

assuming a 1 cm path length through the sample (Fasman 1989).

Bradford Assay

Unlike prior work in our lab, a new method was needed for measuring the dilute concentrations of proteins that result from the equilibration of thin gels in the buffer. We chose not to add a fluorescent tag to the protein, since it disrupted the UV absorbance and could change the native charge. Methods in which a fluorescent reagent binds to the protein (fluorescamine, fluoraldehyde, o-phthalaldehyde, or Sigma FlurorProfile®) were considered, but generally had less sensitivity than dye-complex assays (Bradford, Lowry, and bicinchronic acid). Of the dye-complex assays, the Bradford (aka Coomassie Blue) assay was selected because of its robustness at higher salt concentrations.

The procedure was followed for the Coomassie Protein Assay Kit (Pierce #23200; Rockford, IL) using the Micro Microplate Protocol, which has a working range of 3-30 mg/L. Briefly, standard BSA solutions were prepared over the range 0-35 mg/L. In a 96-well plate, 150 μL of a standard or unknown sample was placed in each well. Then 150 μL of the Coomassie Reagent was added to each well and lightly shaken. After incubating the plate for 10-45 minutes at room temperature, the absorbance at 595 nm was measured with a plate reader (Ying lab's Versamax Plate Reader, Molecular Devices, Sunnyvale, CA; or Stephanopoulos lab's Fusion Plate Reader, Packard BioScience/PerkinElmer, Waltham, MA). The standards curve is not linear, so the

concentration of each sample was linearly interpolated between the nearest standard points. Standard curves were indistinguishable for buffer ionic strengths $\leq$ 0.1 M; individual standard curves were generated for each ionic strength higher than 0.1 M.

4.4. Results & Discussion

4.4.1. Experimental

Method Verification

As noted earlier, modifications to earlier partitioning methods (Kosto et al. 2004) were required to yield accurate results for the thin agarose-GAG gels. Attempted methods included rinsing the excess solution off with a squirt bottle (the previous method), dipping the membrane into a beaker of buffer (using either forceps or a mesh platform), blotting the solution off with a KimWipe, or compressing away excess solution between two glass slides. The result of each method was compared against previous results for the partitioning of BSA into 4 v% agarose in 0.1 M PBS, as well as for similarly-sized Ficoll into 4 v% agarose; these results are shown in Table 4.3. While the previous rinsing method resulted in Φ_{BSA} = 0.42 ± 0.05 (standard error for n = 6), the mesh platform dipping method yielded Φ_{BSA} = 0.63 ± 0.01 (n = 19; average thickness = 88 μm). The precision of this method and its consistency with previous agarose results confirmed that it was appropriately washing away excess surface solution without removing solute from the gel interior.

Table 4.3 Partition coefficients for BSA and Ficoll into 4 v% agarose

	Φ_0	Ref.
Published Results		
BSA (3.6 nm) in 4v% agarose	~0.58 ~0.67	(Buck et al. 2001) (Lazzara and Deen 2004)
Ficoll (3.5 nm) in 4 v% agarose	~0.63	(Kosto et al. 2004)
Current Results		
BSA - Prior rinsing method	0.42 ± 0.05	
BSA - Mesh rinsing method	0.63 ± 0.01	

Additional experiments measured the partition coefficient of the polyester support mesh in the absence of agarose, which resulted in no detectable protein in the equilibrated buffer. This finding, and the similarity between the current results and previous mesh-free results in Table 4.3, verified that the presence of the polyester mesh within each membrane did not affect the partitioning results. Protein solutions of known concentrations were placed in glass vials, with volumes and concentrations similar to those present during partitioning experiments. Assay of these solutions over time showed no change in concentrations, indicating that there was negligible adsorption of the BSA to the walls of the glass vials during the experiment.

Similar to the hydraulic permeability data for 3 v% agarose in the previous chapter, the 4 v% agarose gels were characterized by their hydraulic permeability prior to GAG attachment to reduce random biases between the blank and GAG-containing groups due to sample-to-sample variability. The unreacted agarose gels were divided into two groups that were functionalized to produce blanks (unreacted averages: $\kappa = 166 \pm 21$ nm^2, $\delta = 96 \pm 10$ μm, $\phi_{GAG} = 0$) and GAG-containing gels ($\kappa = 165 \pm 25$ nm^2, $\delta = 96 \pm 10$ μm, $\phi_{GAG} \sim 0.0022$).

To verify that the solution concentrations were in the dilute regime, the partition coefficients were measured with initial solution concentrations of 0.5 g/L and 1.0 g/L BSA in 0.011 M PBS. Partitioning theory predicts that solute-solute interactions in the bulk solution would result in a partition coefficient higher than the dilute limit. The experimental partition coefficients (Table 4.4) had no statistical difference between the two BSA concentrations based on a Student's t-test ($\alpha = 0.05$). This confirms the prediction from osmotic pressure and diffusivity virial expression that 1 g/L BSA solutions at 0.011 M can be treated as dilute.

Table 4.4 Partition coefficients for BSA in 4 v% agarose gels with GAG contents and variable solute concentrations in 0.011 M PBS.

	$c_1 = 0.5$ g/L	$c_1 = 1.0$ g/L
$\phi_{GAG} = 0$	0.66 ± 0.08	0.62 ± 0.05
$\phi_{GAG} = 0.002$	0.33 ± 0.07	0.32 ± 0.04

Experimental Results

Equilibrium partition coefficients were measured in 4 v% agarose gels without GAG and with 0.2 v% GAG. The findings are discussed in the following section, as well as tabulated in Appendix C.

The partition coefficients for Ficolls of four different Stokes radii were measured in 0.1 M PBS, shown in Figure 4.2 as a function of the solute radii. As expected, the partition coefficients decreased when additional GAG fibers were present and decreased for larger solute radii. These trends were consistent with previous partition coefficients measured for the same Ficoll fractions in 4 v% agarose-dextran gels (Kosto et al. 2004). The results for blank agarose (without a second fiber) are ~15% lower in the previous study, likely because of slight changes in the agarose structure due to the treatment of blank gels. In the previous study, the blank gels were treated with electron beam irradiation which could lead to further fiber cross-linking.

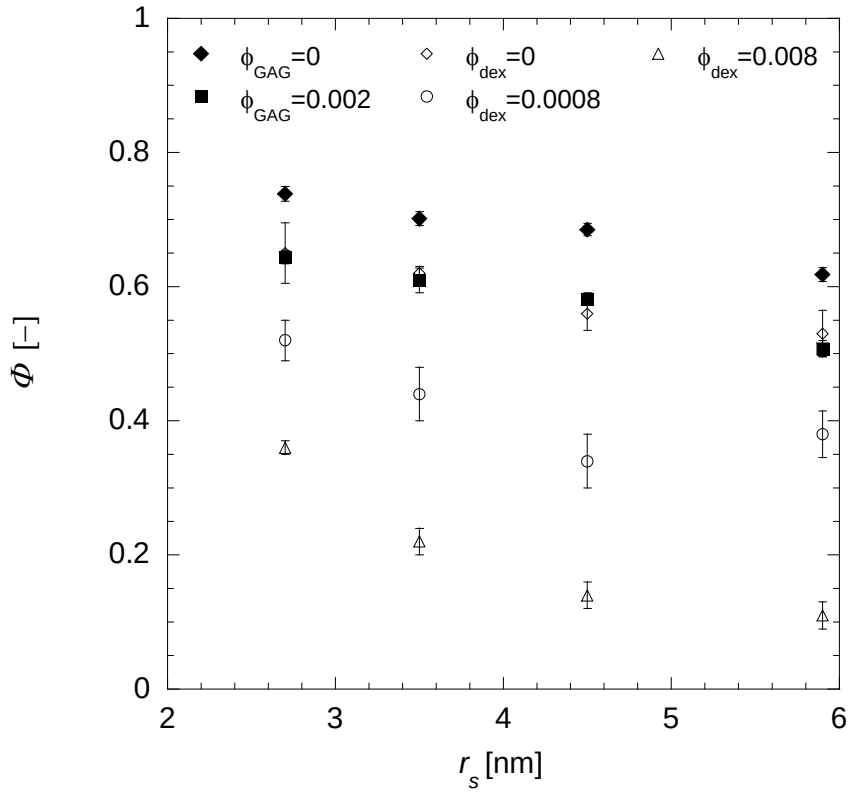

Figure 4.2 Partition coefficients (Φ) of Ficoll of various Stokes-Einstein radii in 4 v% agarose membranes. Data from the current study are indicated with solid symbols for gels with 0 v% and 0.2 v% GAG. Previous partitioning results for gels with variable dextran content are indicated with open symbols. All experiments were conducted in 0.1 M PBS. Error bars are one standard error with n = 10-11 samples in the current study and n = 4 in the previous dextran study.

The equilibrium partition coefficients were then measured for 37 kDa Ficoll (r_s = 3.5 nm) for PBS ionic strengths of 0.011 M to 0.1 M (Figure 4.3). While there was no statistical difference between the partition coefficients for the blank membranes, the partition coefficients for GAG-containing membranes were statistically lower at 0.01 and 0.02 M. Since the Ficoll molecules had previously been shown to have negligible charge from the fluorescein tag, there should not be charge interactions between the Ficoll solute and the GAG fibers.

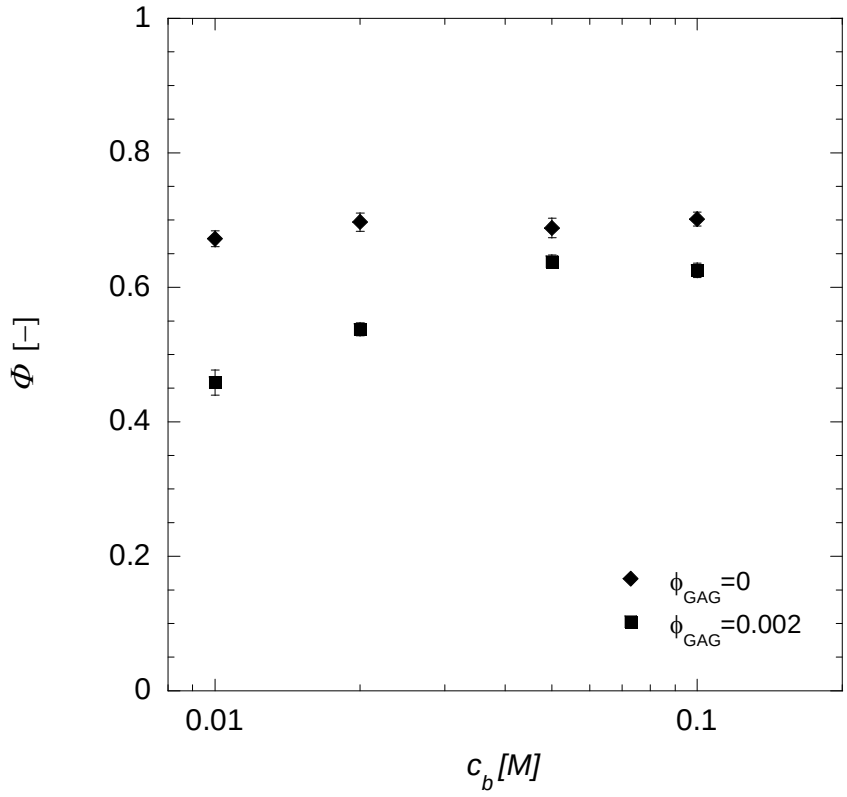

Figure 4.3 Partition coefficients (Φ) of 3.5 nm Ficoll over a range of solution ionic strengths in 4 v% agarose membranes with 0 v% and 0.2 v% GAG. Error bars are one standard error with n = 10-11 samples.

It is possible that the 27% decrease was due to changes in the GAG structure, with interchain repulsion at low ionic strengths resulting in a more rod-like conformation. However, we are unable to evaluate such a hypothesis without developing a technique to freeze and visualize individual GAG molecules at a given ionic strength. Using partitioning theories for hard spheres, rods, and coils (Lazzara et al. 2000, White and

Deen 2000), the partition coefficients were compared for a hard sphere partitioning into GAG fibers versus GAG coils; the derivations of sphere-coil interactions in partitioning are detailed in Appendix D. Assuming a GAG radius of gyration of r_g = 7.5 nm (Bertini et al. 2005) and a GAG fiber volume fraction of ϕ_{GAG} = 0.002, the partition coefficient for a 3.5 nm Ficoll was 3% lower if the GAG were a rod versus a coil. While this result is consistent with the hypothesis that the GAG fibers may be coiled at high ionic strengths and elongated at low ionic strengths, the difference is much less than was experimentally observed. In addition, hydraulic permeability models that assumed GAG was a fiber provided good agreement with the data at all ionic strengths. It remains unclear what caused the decrease in Ficoll partitioning in agarose-GAG membranes at 0.011 M.

The equilibrium partition coefficients were then measured in the same membranes for BSA in 0.011 M to 0.5 M ionic strength buffer solutions (Figure 4.4). The partition coefficient in the 0.2 v% GAG gels was constant at 0.54 at high ionic strengths, but decreased by 45% at 0.011 M, suggesting significant charge interactions between the anionic BSA and GAG. In contrast with the current findings, it was previously observed that there may be some charge interactions between proteins and agarose at very low ionic strengths (Crone 1974, Edwards and Dubin 1993), though those studies were performed with Sepharose and Superose chromatography beads composed of cross-linked agarose. Based on the agarose charge density in the Superose studies (-0.011 C/m^2) (Johnson and Deen 1996a), the agarose could contribute nearly as much charge as the 0.2 v% GAG (-5x10^5 C/m^2 versus -9x10^5 C/m^2). However, from the manufacturer's literature, Superose appears to be agarose which has been functionalized to increase hydrophobic interactions; these groups may impart additional charge to agarose. In contrast, the slope of the partition coefficients in blank membranes versus ionic strength was statistically indistinguishable from 0, supporting that the agarose in the current study can be treated as neutral and that charge interactions do not play a role between neutral agarose fibers and charged solutes.

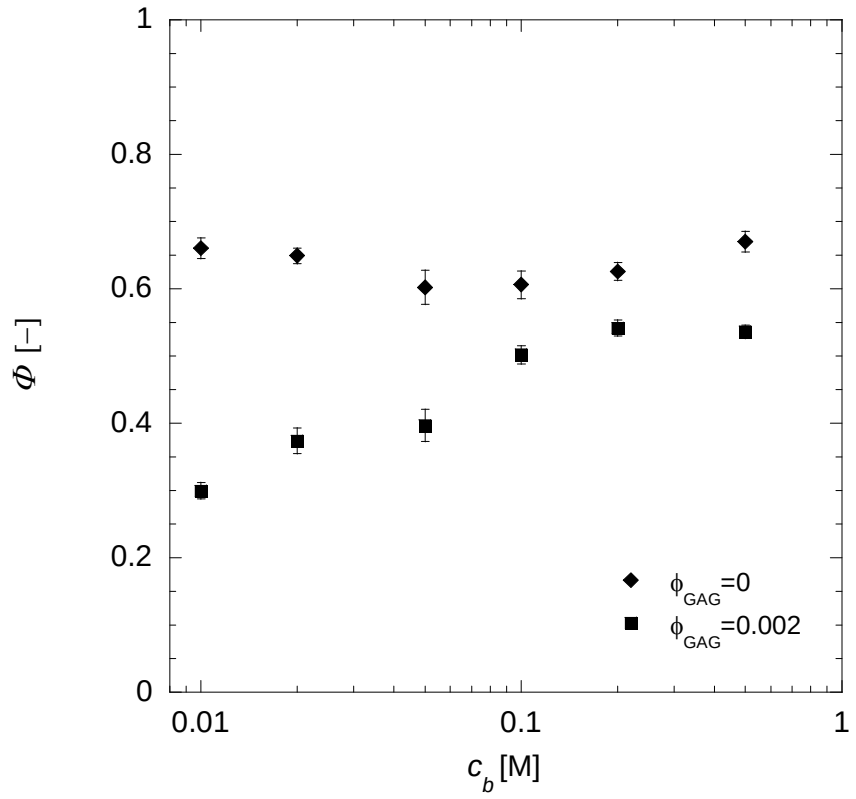

Figure 4.4 Partition coefficients (Φ) of bovine serum albumin (BSA) over a range of solution ionic strengths in 4 v% agarose membranes with 0 v% and 0.2 v% GAG. Error bars are one standard error with n = 10-11 samples.

The 37 kDa Ficolls have a similar hydrodynamic radius to BSA (r_s = 3.5 nm and 3.6 nm, respectively). At neutral conditions (highest ionic strength) the partition coefficients in the blanks gels were $\Phi_{BSA} = 0.67 \pm 0.02$ and $\Phi_{Ficoll} = 0.70 \pm 0.01$ (standard error with n = 10); in the 0.2 v% GAG gels, $\Phi_{BSA} = 0.54 \pm 0.01$ and $\Phi_{Ficoll} = 0.63 \pm 0.01$ (n = 11). While the values are similar between BSA and Ficoll, there is a statistical difference between the partition coefficients (in the t-test, $p = 0.0012$ for blanks and $p = 0.0001$ for GAG). This difference is larger than the ~2% difference predicted by partitioning models based on the small difference in solute size. There are numerous potential causes for the difference: there is some uncertainty in the radius of the Ficoll, as shown in Table 4.2; BSA is actually a prolate spheroid instead of a sphere, which would reduce the partition coefficient by up to 10% in 4 v% agarose (Lazzara et al. 2000); there could be a systematic error in experiments with Ficolls or BSA; Ficolls may be more deformable than proteins; or there may be weak long-range intermolecular forces acting on BSA.

4.4.2. Modeling

The previously described models were used to predict the partition coefficients for agarose-GAG gels. Identical to the hydraulic permeability model described in Chapter 3, the heterogeneity of the gels was captured by arbitrarily selecting a value of ε_2 and fitting ϕ_2/ϕ to the hydraulic permeability of the blank gels. It was assumed that agarose and GAG were in equal proportions in both the dense and sparse regions, so that ϕ_2/ϕ could be used for both fibers to determine the volume fraction in each region. The partition coefficient for a mixture of the two fibers was found for each region from Equation (4.4), and the effective partition coefficient from both regions was calculated from Equation (4.14). The properties of agarose and GAG are the same as those used for hydraulic permeability models, summarized in Table 4.5. BSA was modeled as a spherical solute with r_s = 3.6 nm and a net charge of -21 (corresponding to $\sigma_{s,BSA}$ = -0.021 C/m^2). In the Donnan model, the volumetric charge density (c_m) is calculated from the GAG fiber volume fraction by

$$c_m = \frac{2\left|\sigma_{s,GAG}\right|}{r_{f,GAG}F}\phi_{GAG} \ . \tag{4.19}$$

Table 4.5 Parameter values used in the Donnan and microstructural partitioning models, assuming an aqueous pH 7.4 0.1 M solution at room temperature.

Property	Value	Property	Value
Constants		BSA	
RT	2480 J/mol	r_s	3.6 nm
F	96500 C/mol	$\sigma_{s,BSA}$	-0.021 C/m^2
Agarose		Ficoll	
$r_{f,a}$	1.6 nm	r_s	2.7, 3.5, 4.5, or 5.9 nm
$\sigma_{s,a}$	0 C/m^2	$\sigma_{s,BSA}$	0 C/m^2
GAG			
$r_{f,GAG}$	0.5 nm		
$\sigma_{s,GAG}$	-0.10 C/m^2		

Unlike hydraulic permeability (Figure 3.24), the clump volume fraction (ε_2) affected the predicted partition coefficient for the blank and GAG-containing gels. Figure 4.5 shows the predicted neutral partition coefficient for agarose and agarose-GAG gels over a range of ε_2. For each ε_2, the corresponding value of ϕ_2/ϕ was fit to the hydraulic permeability model and the experimental blank permeability of 262 nm^2. The partition coefficient for a homogeneous system is reached in the limit of $\varepsilon_2 \to 1$. The Figure shows that the neutral partition coefficient for the 4 v% agarose gels with 0.2 v% GAG could be up to 58% higher than the homogeneous value, depending on the choice of ε_2. Comparison with Figure 4.4 shows that the experimental data are more consistent with the model at higher values of ε_2, where the clumps are only slightly more dense than the surrounding matrix. For that reason, the following partitioning models all use $\varepsilon_2 = 0.5$, instead of $\varepsilon_2 = 0.1$ previously assumed for hydraulic permeability models. For the 4 v% agarose blank permeability of $\kappa = 262$ nm^2, $\varepsilon_2 = 0.5$ corresponded to $\phi_2/\phi = 1.95$.

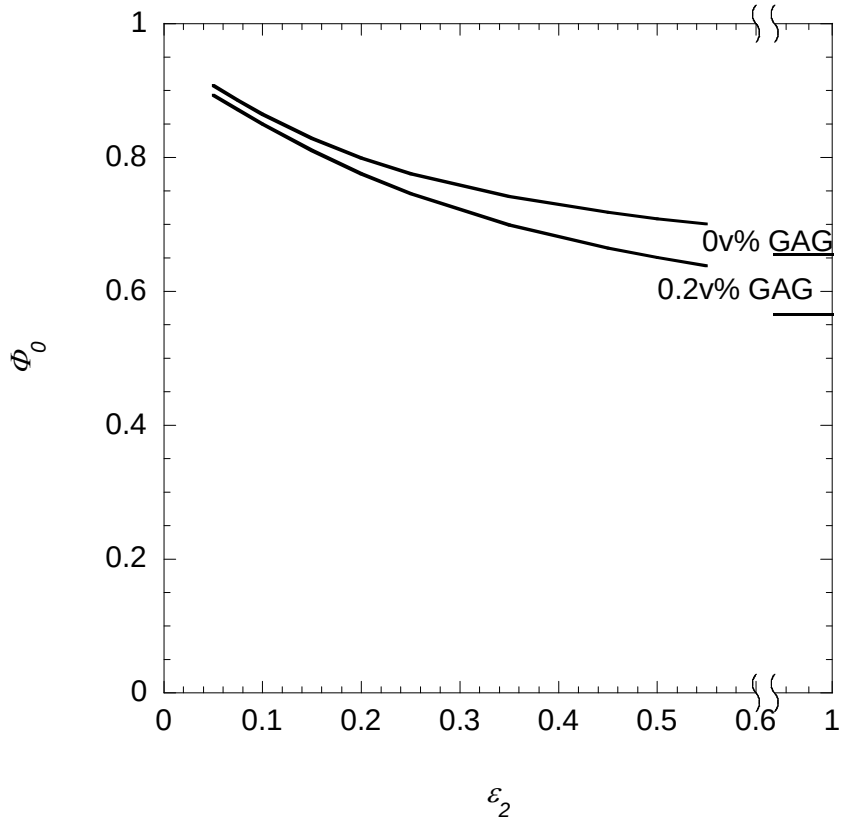

Figure 4.5 Predicted neutral partition coefficient (Φ_0) for BSA into agarose-GAG membranes for a range of clump volume fractions, ε_2. The model used the value of ϕ_2/ϕ that fit the blank hydraulic permeability of 262 nm^2, as described in the previous chapter.

The model was first applied to the partitioning of narrow-fraction Ficolls of different Stokes radii (Figure 4.6). Only neutral solute-fiber models were used. The model was able to capture the relative decrease in the partition coefficient with increasing solute size, as well as the decrease due to the addition of 0.2 v% of GAG fibers. These observations are consistent with previous applications of the homogeneous form of the model to agarose-dextran gels (Kosto et al. 2004).

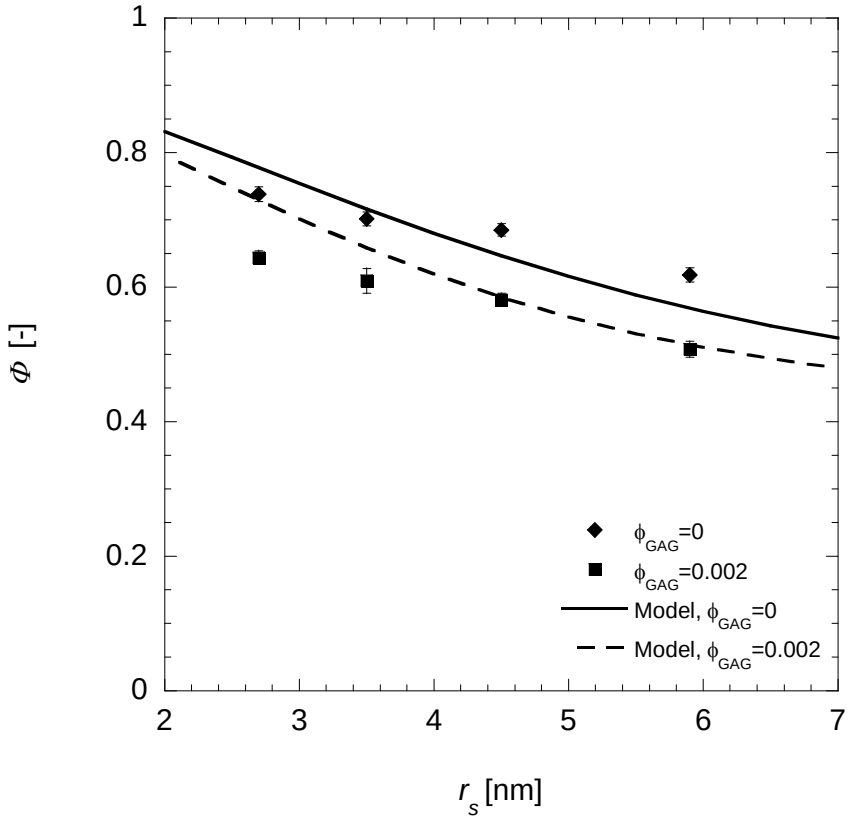

Figure 4.6 Partition coefficients (Φ) of Ficoll of various Stokes-Einstein radii in 4 v% agarose membranes. Data are from Figure 4.2, measured in 0.1 M PBS with error bars equal to 1 standard error (n = 10-11). The model curves used neutral fiber models with heterogeneity parameters $\varepsilon_2 = 0.5$ and $\phi_2/\phi = 1.95$. The values of model parameters are given in Table 4.5.

The model was applied to BSA partitioning data to see how well it captured the decrease in partitioning due to solute-GAG charge interactions. The charge effects were modeled by either the structural model (Equations (4.9)-(4.13)) or the Donnan model (Equation (4.6) and (4.8)). The charge effects depended on the GAG volume fraction within each heterogeneous region, with Donnan model using $c_{m,1} = 0.46$ mM and

$c_{m,2}$ = 18 mM. As seen from the curves in Figure 4.7, there is relatively little difference in the partition coefficient predicted from the structural and Donnan models. The neutral partition coefficient is identical for both models, and the decrease at low ionic strengths is similar (27% decrease at 0.01 M for the structural model and 41% for the Donnan model). The stronger charge effect in the Donnan model is likely a result of assuming continuous charge in a system where the distance between fiber surfaces is much larger than the fiber diameter (assuming a square array, the distance is 30 r_f). This result is similar to the comparison of structural and Donnan models for Darcy permeability (Figure 3.9), where the charge effect of the Donnan model was similar but slightly stronger than the corresponding structural model for 0.37 v% GAG. However, unlike the Darcy permeability model, the charge effect in the partitioning model is not reduced by the presence of agarose fibers.

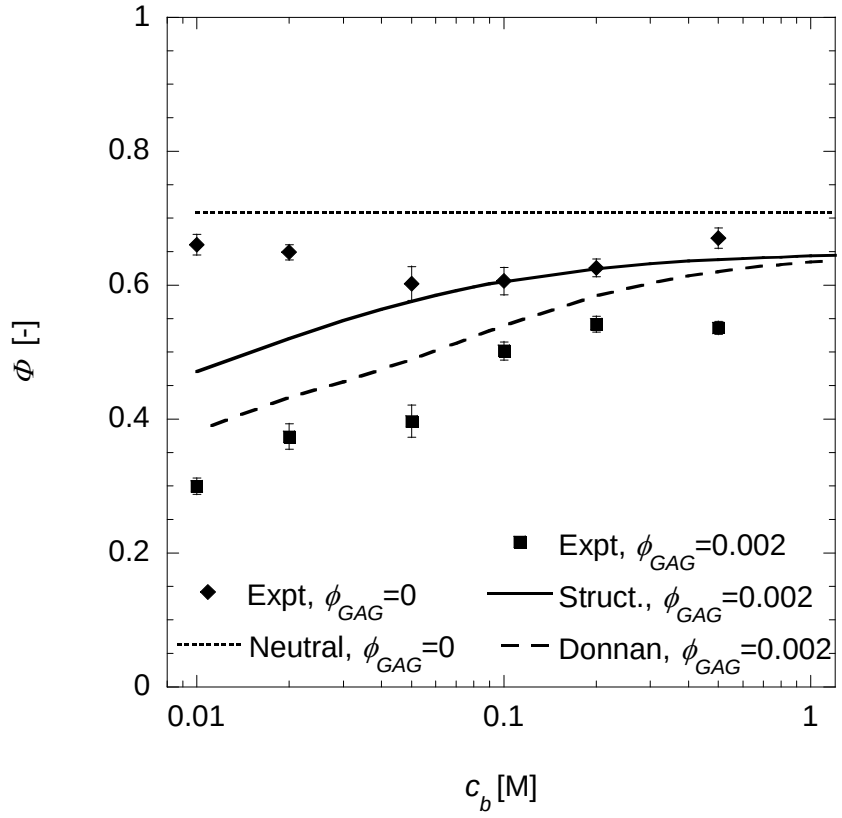

Figure 4.7 Partition coefficients (Φ) of bovine serum albumin (BSA) over a range of solution ionic strengths in 4 v% agarose membranes with 0 v% and 0.2 v% GAG contents. Data are from Figure 4.4. The GAG contribution to the partition coefficient was calculated with either the Johnson structural model (solid; Equations (4.9)-(4.13)) or the Donnan equilibrium model (dashed curve; Equation (4.6) and (4.8)). The agarose contribution used the neutral model in Equation (4.3). The models used heterogeneity parameters ε_2 = 0.5 and ϕ_2/ϕ = 1.95; the values of other model parameters are given in Table 4.5.

The fit between the structural model and the data in Figure 4.7 could be improved if the neutral partition coefficients were decreased by 10~15% and the ionic strength effect were slightly stronger. Several factors could improve this fit. A slightly smaller agarose fiber radius would decrease the partition coefficient; however, the current estimate of $r_{f,a}$ ~ 1.6 nm is already at the lower end of reported values (Lazzara and Deen 2004). The charge of BSA is affected by the chloride ion concentration, with a charge of -29 at 1 M KCl, -21 at 0.15 M, and -14 at 0.01 M (all at pH 7.4) (Vilker 1976, Vilker et al. 1981). However, accounting for this change in BSA charge increased the partition coefficient predicted by the model by less than 3%.

In the hydraulic permeability results in Chapter 3, the reduction in permeability at low ionic strengths was best captured by the Donnan model with a charge density between that predicted by the heterogeneous GAG density and that from a macroscopically homogeneous charge density (Figure 3.45). It was hypothesized that gradients in the electrical potential due to the highly charged clumps extended well into the matrix. To evaluated if the macroscopic charge density applied to both hydraulic permeability and partitioning, Figure 4.8 compares Donnan model predictions using the macroscopic charge density and the local charge density. Macroscopically, the membrane contains 0.2 v% GAG, which corresponds to 9.0 mM fixed charge. This charged was used in Equations (4.6)-(4.8) with the neutral, heterogeneous permeability from Equations (4.3) and (4.14). In the heterogeneous model with $\varepsilon_2 = 0.5$ and $\phi_2/\phi = 1.95$, the matrix contained 0.011 v% GAG ($c_{m,1} = 0.46$ mM) and the clumps contained 0.43 v% GAG ($c_{m,2} = 18$ mM). The Donnan model (Equations (4.8)) was applied to the neutral partition coefficient in each region before using Equation (4.14) to account for the heterogeneity. Unlike the hydraulic permeability in Chapter 3, the charge effects in partitioning in Figure 4.8 are much more consistent with using the local charge density. Using a homogeneous charge density based on the macroscopic GAG concentration predicted a much greater decrease in the partition coefficient at low ionic strength than was observed experimentally.

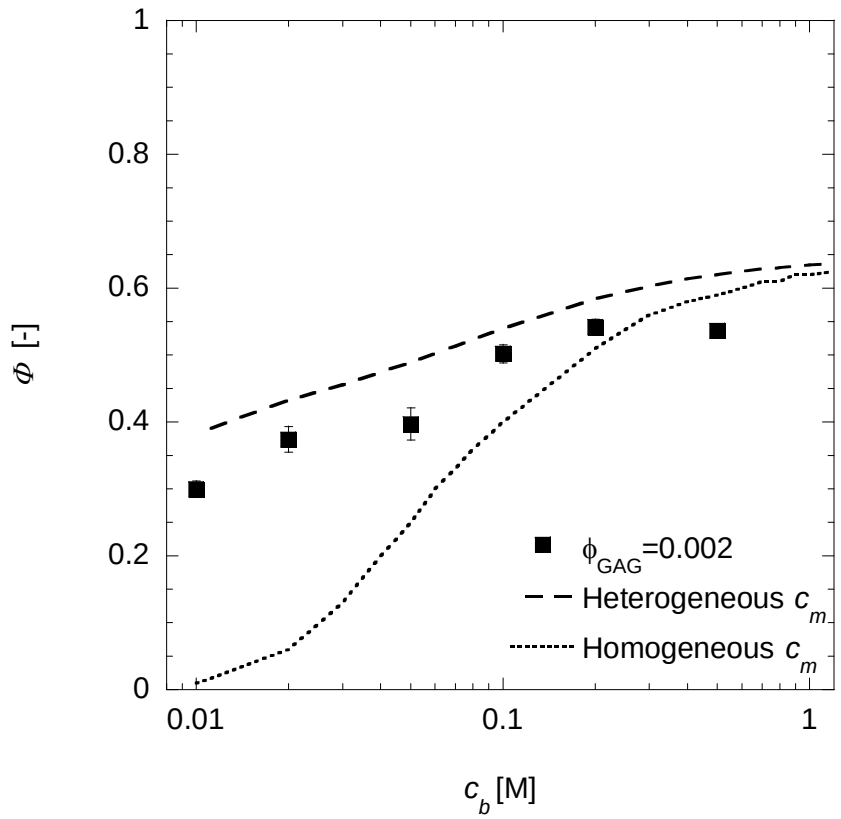

Figure 4.8 Partition coefficient of BSA in agarose-GAG gels with Donnan model predictions using different fixed charge densities, c_m. The dashed curve ("Heterogeneous") assumes a fixed charge density based on the local GAG fiber density ($c_{m,1}$ = 0.46 mM, $c_{m,2}$ = 18 mM). The dotted curve ("Homogeneous") assumes a uniform fixed charge density based on the membrane's total GAG fiber content (c_m = 9.0 mM). Both curves use the heterogeneous model for neutral fibers with ε_2 = 0.5 and ϕ_2/ϕ = 1.95; the values of other model parameters are given in Table 4.5. The experimental data is identical to Figure 4.4

The heterogeneities in the agarose were assumed to be characterized by spherical clumps surrounded by a lower-density matrix. Realistically, there are not simply two distinct regions with high and low fiber densities; there is a distribution of fiber densities throughout the gel volume. The structural model (Equations (4.9)-(4.13)) was compared for the 2-region model of heterogeneity (ε_2 = 0.5 and ϕ_2/ϕ = 1.95) versus a homogeneous material (ϕ_2/ϕ = 1), shown in Figure 4.9. The partitioning predicted by the homogeneous model was lower than predicted by the heterogeneous model, and had a larger decrease at low ionic strengths. This is because in the heterogeneous system, more solute was excluded from the denser clumps than was able to enter the less-dense matrix. Comparing the experimental values of the partition coefficients to the two models suggests that the experimental membranes are most similar to the homogeneous fiber density. While the hydraulic permeability model is dominated by the properties of a

continuous phase with lower fiber density, the partition coefficient model is a function of both regions. It may not be possible to accurately capture both these effects in a simple two-region model.

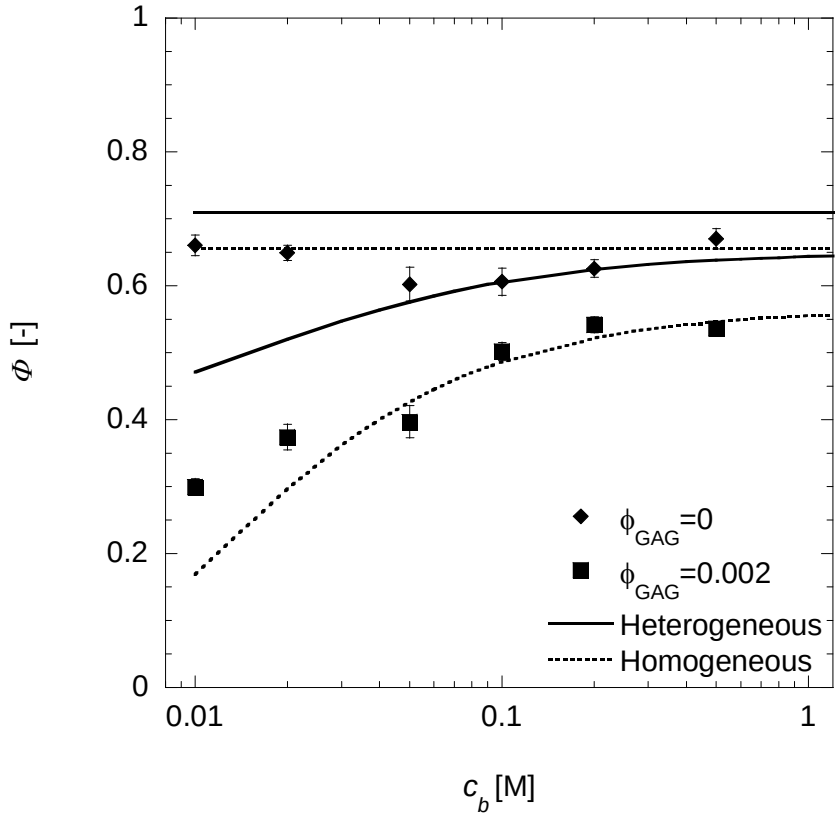

Figure 4.9 Partition coefficients (Φ) of bovine serum albumin (BSA) over a range of solution ionic strengths in 4 v% agarose membranes with 0 v% and 0.2 v% GAG contents. The structural model was used with either heterogeneous regions (ε_2 = 0.5 and ϕ_2/ϕ = 1.95; solid curve) or a single homogeneous region (ϕ_2/ϕ = 1; dotted curve); the values of other model parameters are given in Table 4.5. Data are from Figure 4.4.

It was also assumed that the GAG was distributed in proportional to the agarose (that bound concentration was in proportion to the concentration of binding sites). Since GAG diffuses into the agarose after the gel heterogeneities formed, it is possible that the GAG partitioned and bound in higher concentrations in regions with lower agarose density. As seen in Figure 2.13, the product of the GAG partition coefficient and GAG concentration in bulk solution ($\Phi_G \times c_{G,0}$) would have to be reduced several-fold to have a measurable reduction on the bound GAG content. The partition coefficient of CS in blank 4 v% agarose gels was measured to be Φ_G = 0.57 ± 0.04. Using the model for GAG partitioning into heterogeneous agarose with ε_2 = 0.5 and ϕ_2/ϕ = 1.95 predicts a five-fold

difference in GAG concentrations between the 2 regions when $\Phi_G = 0.57$ (assuming that GAG acts as a solid sphere ($r_s = 5.9$ nm), which is a very crude approximation). From Figure 2.13, this corresponds to a 50% lower bound GAG content (μg GAG/mg agarose) in the denser regions.

Using the structural partitioning model with $(\phi_{GAG}/\phi_a)_1/(\phi_{GAG}/\phi_a)_2 = 3/2$ (50% less GAG in clumps) is shown in Figure 4.10, in comparison with previously assumed proportional GAG distribution where $(\phi_{GAG}/\phi_a)_1/(\phi_{GAG}/\phi_a)_2 = 1$. The disproportionate GAG model predicts at most a 4% decrease in the partition coefficient relative to the proportional GAG distribution. For comparison, the model is also compared to the case where the GAG is uniformly distributed in both regions at 0.2 v% ($(\phi_{GAG}/\phi_a)_1/(\phi_{GAG}/\phi_a)_2 \sim 38$). This distribution of GAG decreases the neutral partition coefficient, but also increases the charge effect at low ionic strengths.

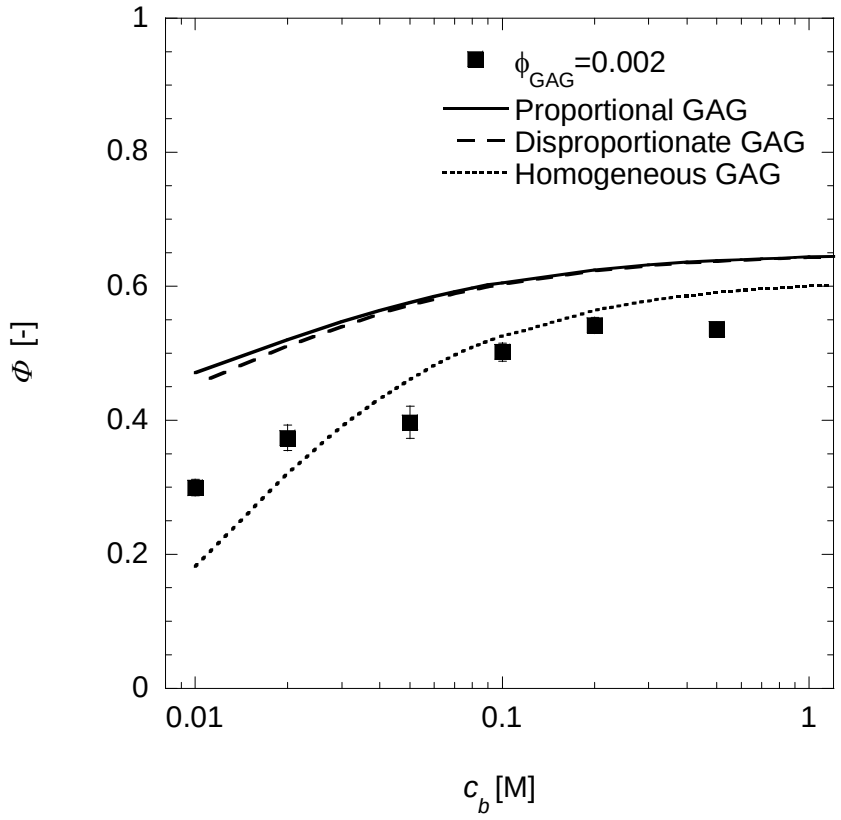

Figure 4.10 Partition coefficients (Φ) of bovine serum albumin (BSA) over a range of solution ionic strengths in 4 v% agarose membranes with 0 v% and 0.2 v% GAG contents. Data are from Figure 4.4. The structural model was used with either GAG in proportion to the agarose fiber density (solid curve), GAG based on partitioning estimates and the binding model (dashed curve), or GAG uniformly distributed everywhere at 0.2 v% (dotted curve). For all models, agarose heterogeneities used $\varepsilon_2 = 0.5$ and $\phi_2/\phi = 1.95$; the values of other model parameters are given in Table 4.5.

4.5. Conclusions

Partition coefficients were measured in 4 v% agarose with 0 or 0.2 v% GAG. The partition coefficients were measured for several narrow Ficoll fractions as a function of solute size and for BSA as a function of ionic strength. The decrease in partition coefficient with larger Ficolls was consistent with previous observations in agarose-dextran. The charge interactions between anionic BSA and anionic GAG were shielded at high ionic strengths ($\geq$ 0.2 M), but caused a 45% decrease in partitioning at 0.011 M. There were no charge effects in the partitioning of BSA in blank agarose, indicated by a partition coefficient that was invariant with ionic strength. The partition coefficients of BSA at neutral conditions and of Ficoll were similar in blank agarose gels, but 15% different in agarose-GAG gels.

Several variations of a model for partitioning were evaluated. The model used existing excluded volume theories for neutral partitioning, Donnan or microstructural models for charged partitioning, and a 2-region model for heterogeneity. Using the model for agarose heterogeneity previously developed for Darcy permeability, it was found that experimental partition coefficients were most consistent with a nearly homogeneous distribution of fibers (ϕ_2/ϕ ~1-2). The excluded volume model provided good agreement for Ficoll partitioning in gels with one or two fiber types with a range of solute radii. The model assumption that the steric excluded volume of agarose was independent from the steric and electrostatic exclusions of GAG provided reasonable agreement with the experimental data. Unlike previously observations for hydraulic permeability, the Donnan and microstructural models both gave partitioning results that were in good agreement with the experimental data. The charge interactions between the solute and fibers were well modeled by a heterogeneous charge density in both models, though the structural model also provided good agreement with a homogeneous distribution of gibers. Unlike Darcy permeability (Figure 3.46), the Donnan model over-predicted charge effects if it used the macroscopic charge density.

In summary, experimental partition coefficients in charged and neutral fibrous systems were well modeled by existing microstructural models with a two-region model to account for heterogeneities in fiber density.

Chapter 5. MACROMOLECULE SIEVING

5.1. Introduction

Of particular interest in understanding the role of GAGs and the endothelial glycocalyx is the way in which they hinder the passage of solutes. This chapter studies the convective transport of macromolecules through agarose-GAG membranes. The effects of solute size and charge, as well as membrane composition were investigated in the membrane sieving coefficients (Θ).

5.1.1. Overview of Hindered Transport

When a solute passes through a medium with a pore radius or interfiber spacing comparable to the solute dimension, the rates of diffusion and convection tend to be lower than in bulk solution. This phenomena of "hindered transport" is the result of steric, hydrodynamic, and electrostatic interactions between the solute and the medium (Deen 1987). The flux of the solute (**n**) through an isotropic medium can be expressed as

$$\mathbf{n} = -K_d D_\infty \nabla c' + K_c \mathbf{v} c' \tag{5.1}$$

where c' is the solute concentration within the medium, D_∞ is the free-solution diffusivity, and **v** is the superficial fluid velocity. (For simplicity, the solute subscript i is

left off in this chapter.) The interactions between the solute and the medium are captured by the diffusive (K_d) and convective (K_c) hindrance coefficients. The diffusive hindrance coefficient is the ratio of the apparent diffusivity within the medium (D) to that in free solution. The convective hindrance coefficient is the ratio of the solute velocity (in the absence of diffusion) to the fluid velocity.

For unidirectional transport across a membrane, Equation (5.1) can be integrated across the membrane thickness (δ), subject to the partition coefficient at the surfaces to relate c' to the external solution concentrations. The concentration profile can be expressed as a sieving coefficient (Θ), which is the ratio of the downstream filtrate concentration (c_F) to the upstream retentate concentration (c_R):

$$\Theta = \frac{c_F}{c_R} = \frac{\Phi K_c}{1-\left(1-\Phi K_c\right)e^{-\mathrm{Pe}}} \tag{5.2}$$

where the Péclet number in the membrane is

$$\mathrm{Pe} = \frac{\left(\Phi K_c\right)\mathrm{v}\,\delta}{\left(\Phi K_d\right)D_\infty} \quad . \tag{5.3}$$

Alternatively, the hindrance coefficients are sometimes expressed as $H = \Phi K_d$ and $W = \Phi K_c$ (Deen 1987). The diffusive hindrance coefficient can also be expressed as the "solute permeability", which equals HD_∞/δ. In the limit of high Péclet number, the sieving coefficient can be related to the filtration reflection coefficient (σ_f):

$$\lim_{Pe\to\infty}\left(\Theta\right) = \Phi K_c = 1-\sigma_f \quad . \tag{5.4}$$

Equation (5.4) shows that it is possible to determine K_c without knowledge of K_d if sieving is performed at high Pe and Φ can be measured independently.

5.1.2. Experimental Literature

While numerous studies have looked at the equilibrium partitioning or hindered diffusion of macromolecules in fibrous membranes, a limited number have looked at hindered convection in a quantitative manner. Several studies have investigated the role of fiber volume fraction and solute size in neutral fibrous systems. The hindered diffusion and reflection coefficient of two proteins (ribonuclease A and BSA) were measured in poly(vinylidine fluoride) membranes with polyacrylamide-filled pores (Kapur et al. 1997). Our lab has previously studied the hindered diffusion, partitioning,

and sieving of several globular proteins and Ficoll fractions in 4-8 v% agarose (Johnston and Deen 2002, 1999). The sieving of four Ficoll fractions was studied in agarose-dextran gels of varying composition (Kosto and Deen 2005), which appears to be the only data for a well-characterized fiber mixture.

Some work has been done to investigate the role of charge in filtration, though results are mostly available for porous (not fibrous) membranes. It was shown that the sieving coefficient of BSA through polyethersulfone membranes was reduced by nearly two orders of magnitude when the ionic strength was decreased from 0.15 M to 0.0015 M (Pujar and Zydney 1994). The transmission of cytochrome c through charge-modified cellulose membranes was also decreased at lower ionic strengths or with greater membrane charge (Mehta and Zydney 2006). Numerous additional studies in porous membranes reported similar results, with protein transmission being affected by the solution pH and membrane charge (Balakrishnan and Agarwal 1996, Burns and Zydney 1999, Millesime et al. 1994, Miyama et al. 1988, Nakao et al. 1988, van Reis et al. 1999). However, no systematic study of charge effects in sieving through *fibrous* membranes was found in the literature. Sieving was studied in isolated renal capillary GBM, a fibrous mixture of collagen and GAG, though the composition of those membranes was not fully characterized (Bolton et al. 1998).

5.1.3. Theory

While hindered transport theory is fairly well developed for cylindrical pores (Deen 1987), such theories provide little insight for structure-function relationships in fibrous membranes. The corresponding theories for fibrous systems are much less developed. Several theories have been developed for the interactions of solutes and rigid fibers during diffusion (Johnson et al. 1996, Phillips 2000). Of these, only the effective medium model, which correlates the Darcy permeability to the diffusive hindrance, is readily applied to systems with two or more types of fibers (Kosto and Deen 2004). Only one theory has been developed for K_c in a fibrous system, which is limited to neutral, spherical solutes passing through a parallel array of fibers (Phillips et al. 1990, Phillips et al. 1989). Phillips et al. performed simulations for the convection of a spherical solute perpendicular to a periodic square array of fibers. The results were expressed as

$$K_c = 1 + B\hat{\phi} + \Gamma\hat{\phi}^2 \tag{5.5}$$

where $\hat{\phi}$ is the volume fraction of the fibers and the parameters B and Γ are functions of $\lambda = r_s/r_f$. Fit to data over the range $0 \le \lambda \le 5$, the parameters are evaluated from

$$B = 5.1712 - 0.9727\left(\frac{1}{\lambda}\right) - 1.1355\left(\frac{1}{\lambda}\right)^2 + 0.2511\left(\frac{1}{\lambda}\right)^3 \tag{5.6}$$

$$\Gamma = -9.97883 + 8.9787\,\lambda - 31.6717\,\lambda^2 - 2.9586\,\lambda^3 \quad . \tag{5.7}$$

The fibers in the simulation were represented by a bead-and-string arrangement, with a bead radius of r_f and a distance between the beads of $0.05r_f$. As noted by Phillips et al., the Darcy permeability of the bead-and-string fibers correlates reasonably with both fibers of the same volume fraction or total length when $\lambda = 1$ (Phillips et al. 1989). Since fiber length was shown in Chapter 3 to be the primary determinant of hydraulic permeability in slender body theory, the volume fraction of bead-and-string fibers was equated with the volume fraction for a cylindrical fiber such that both fibers had the same total length and the same radius r_f:

$$\hat{\phi} = \frac{(2 + 0.05)r_s}{(4/3)r_s}\phi = 0.65\phi \quad . \tag{5.8}$$

Charged Membranes

When the solute is charged, there is an additional term in Equation (5.1) that accounts for electrophoretic motion in response to a potential gradient ($\nabla\psi$) within the membrane:

$$\mathbf{n} = -K_d D_\infty\left(\nabla c' + zc'\frac{F}{RT}\nabla\psi\right) + K_c\mathbf{v}c' \quad . \tag{5.9}$$

where z is the charge of the solute. As was discussed in Chapter 3, the flow of an ionic solution through a charged membrane causes a streaming potential and a decrease in the hydraulic permeability relative to a neutral system. For no net current across the membrane, the induced streaming potential is proportional to the bulk fluid velocity,

$$\mathbf{v} = \left(k_{21} - \frac{k_{11}k_{22}}{k_{12}}\right)\nabla\psi \tag{5.10}$$

where the electrokinetic coupling coefficients, k_{ij}, are the same as those defined in

Equation (3.4). Since the streaming potential and velocity are proportional, it is possible to group them into a single convective term in the flux expression in Equation (5.9)

$$\mathbf{n} = -K_d D_\infty \nabla c' + K_c \left(1+\omega\right) \mathbf{v} c' \tag{5.11}$$

where ω is the electrophoretic contribution from Equation (5.9) (Pujar and Zydney 1997):

$$\omega = \frac{K_d}{K_c} D_\infty z_i \frac{F}{RT} \Bigg/ \left(\frac{k_{11}k_{22}}{k_{12}} - k_{21} \right) \quad . \tag{5.12}$$

Using calculations of k_{ij} from Chapter 3, the coupling coefficients for the agarose-GAG-like membrane in Figure 3.18 are summarized in Table 5.1. Using those values, a BSA diffusivity of $6\text{x}10^{-11}$ m^2/s (Johnson et al. 1995), and assuming $K_d/K_c \sim 1$ in Equation (5.12), the electrophoretic contribution is negligible in the current experiments with $\omega \sim 10^{-2}$-10^{-4}.

Table 5.1 Electrokinetic coupling coefficients (k_{ij}) in a square fiber array similar to agarose-GAG membranes. Values are from the simulations in Figure 3.18, where fiber population 1 ("GAG") has $r_{f,1}$=0.5 nm, ϕ_1=0.004 and $\sigma_{s,1}$=-120 mC/m^2; fiber population *2* ("agarose") has $r_{f,2}$=1.6 nm, ϕ_2=0.041 and σ_{s2}=0 mC/m^2.

c_b [M]	k_{11} [x10^{-14} m^4/N-s]	k_{12}=k_{21} [x10^{-8} m^2/V-s]	k_{22} [N/V^2-s]
Axial flow			
1 M	1.50	-0.90	12.10
0.1 M	1.50	-1.72	1.28
0.01 M	1.50	-2.23	0.21
Transverse flow			
1 M	0.75	-0.48	11.55
0.1 M	0.74	-0.71	1.16
0.01 M	0.73	-0.83	0.13

When the solute and membrane fibers are both charged, there is also an electrostatic interaction between them that affects the solute concentration distribution (Deen 1987), in much the same way the Boltzman factor was included in charged partitioning theory in the previous chapter. While this effect has been investigated for cylindrical pores, no structural model is currently available for sieving in charged fibrous systems.

While a complete microstructural model is not available for charged fibers, several researchers have made use of models which separate the charge effects in the sieving coefficient. These models assume that the charge effects in sieving are predominantly contained within the partition coefficient, allowing the convective hindrance coefficient to be determined from neutral models ($K_{c,0}$) (Deen et al. 1980, Sörensson et al. 2001):

$$\Theta(c_b) \approx \Phi(c_b) K_{c,0} \quad . \tag{5.13}$$

While this form has not been rigorously derived, it is similar to assumptions made in pore theory. In pores, it has long been assumed that the local hindrance factors (denoted K and G in (Deen 1987)) are not a function of charge; averaging K and G across the pore cross section gives values of K_c and K_d which have a extremely weak dependence on charge. It should be noted that this assumption in pore theory has also not yet been fully tested.

Heterogeneity

The only model in the literature for the flux of solutes through a heterogeneous membrane was a simple parallel region model used for agarose-dextran gels (Kosto and Deen 2005). In this model, two regions of different fiber density are arranged in parallel, each with a fractional cross-sectional area ε_j (j = 1 or 2). It was shown that the appropriate weighting factor for sieving at a high Péclet number is

$$\Theta = \Phi K_c = \frac{\sum_{j=1}^{2} \varepsilon_j \kappa_j \Phi_j K_{c,j}}{\sum_{j=1}^{2} \varepsilon_j \kappa_j} \tag{5.14}$$

where the subscript j refers the properties of a region with fiber density ϕ_j.

The hydraulic permeability weighting factor in Equation (5.14) has the effect that the flux of solute through regions of high hydraulic permeability (high water flux) contribute more to the overall sieving coefficient. In the region with a lower fiber density, the partition coefficient, convective hindrance factor, and the hydraulic permeability will all be increased. Since this region will be more heavily weighted in the overall sieving coefficient, the effect is a higher sieving coefficient than would be predicted from a homogeneous material. While the homogeneous model for K_c predicts values that have a

maximum only slightly above one, the hydraulic weighting factor in Equation (5.14) can result in a heterogeneous K_c that can exceed two (Kosto and Deen 2005).

It was considered whether the model for spherical heterogeneous regions used for hydraulic permeability could be applied to the convective flux of a solute. However, because the convective flux is the product of two spatially variant properties (**v** and c_i), it was not possible to simply extend the Maxwell solution to sieving or convective hindrance coefficients. An additional complication is the possibility for the overall Péclet number for the membrane to be large while the local Péclet number within the spherical clumps is small, which would require the heterogeneity model to include both convection and diffusion.

5.1.4. Concentration Polarization

The sieving coefficient is the ratio of the solute concentrations immediately downstream and upstream of the membrane. However, in an experimental ultrafiltration system where the retained solution is not perfectly mixed, the well-known phenomena of *concentration polarization* occurs. This is the tendency of retained solutes to accumulate at the upstream surface of the membrane. The increased concentration at the upstream surface increases the flux of solutes through the membrane and causes the apparent sieving coefficient (Θ') based on the bulk retentate concentration (c_R) to be greater than the true membrane sieving coefficient (Θ):

$$\Theta' = \frac{c_F}{c_R} \geq \Theta = \frac{c_F}{c_M} \tag{5.15}$$

where c_M is the concentration at the upstream membrane surface ($c_M \geq c_R$).

Concentration polarization in the ultrafiltration cell used in this work was previously analyzed (Johnston et al. 2001). They used laminar boundary-layer theory with rigid body rotation above a stationary surface (Bödewadt flow) to model the flow in the ultrafiltration cell. The results were then compared with an uniform stagnant film model and a hybrid model, as well as against experimental data for BSA solutions. Using their local stagnant film model (hybrid model), the corrections to the apparent sieving coefficients in the following work were evaluated from

$$\frac{\Theta'}{\Theta} = 2\int_0^1 \frac{B(Y)(1-Y)}{1-\Theta[1-B(Y)]}dY \tag{5.16}$$

where the dimensionless position variable Y is related to the radial coordinate, r, and the radius of the membrane, R, by

$$Y = 1 - \frac{r}{R} \tag{5.17}$$

and the function B is defined as

$$B(Y) \equiv \frac{c_M(Y) - c_F(Y)}{c_R - c_F(Y)} = \exp\left[\frac{\alpha}{0.6381\,Y^{-1/3} - 0.410\,Y}\right] . \tag{5.18}$$

The dimensionless filtrate velocity, α, is defined as

$$\alpha = \frac{\mathrm{v}}{\sqrt{\mu\omega/\rho}} Sc^{2/3} = \frac{\mathrm{v}}{\sqrt{\mu\omega/\rho}} \left(\frac{\mu}{\rho D_\infty}\right)^{2/3} \tag{5.19}$$

with the fluid viscosity, μ; fluid density, ρ; the average filtrate velocity through the membrane, v; the angular velocity of the bulk fluid, ω; and the Schmidt number, Sc. In the 10 mL ultrafiltration cell used in the current study, it was found that the fluid angular velocity was related to the stir bar speed (ω_{sb}) by $\omega = 0.36\ \omega_{sb}$.

The results of this hybrid model differed from the full boundary layer theory by a maximum of 15% for $0 \le \alpha \le 1$; the models were most similar at smaller values of α. The model requires that Re >> 1, Sc >> 1, and $\alpha/Sc^{2/3} << 1$; the conditions were all readily satisfied for the sieving conditions in the present work (Re~10^2, Sc~10^4, $\alpha/Sc^{2/3}$~10^{-3}). The model also required that the osmotic pressure be much less than the applied pressure, such that the filtration velocity does not vary with radial position. Using the expression for BSA osmotic pressure given in Equation (2.15), the maximum osmotic pressure for 1 g/L BSA (0.10 kPa at 0.011 M) was an order of magnitude less than the lowest applied pressure for the blank gels (1.1 kPa). For the majority of sieving conditions, the difference between osmotic and applied pressures was much greater.

For results in the following sections, Equation (5.16) was numerically integrated to find a value of Θ that satisfied the equality for the experimental values of Θ' and α.

5.2. Experimental Materials & Methods

5.2.1. Flow Rate Compromise

As was noted in Chapter 4, the membrane properties were changed from 3 v% agarose (used for most of the Darcy permeability measurements in Chapter 3) to 4 v% agarose for the partitioning and sieving measurements in Chapters 4 and 5. One motivation for this change was to create membranes that were more selective to BSA (lower Θ and Φ). The other motivation for this change was the desire to measure sieving coefficients at a high Péclet number such that Equation (5.4) could be used, but at a low enough flow rate such that the concentration polarization correction was valid. The polarization model is most accurate for small values of α; the model was previously validated using experiments in the range $0.1 \leq \alpha \leq 0.5$ (Johnston et al. 2001). Since both the Péclet number and α are linearly related to the fluid velocity through the membrane, it was necessary to perform sieving experiments in a narrow pressure range that satisfied both conditions. Since K_d and K_c were not known *a priori*, all calculations were performed with the minimum Péclet number, $\mathrm{Pe}_{\min} = \delta \mathrm{v}/D_\infty$. The ratio K_c/K_d was greater than one in prior experiments with agarose and agarose-dextran (Kosto and Deen 2004, 2005), so $\mathrm{Pe}_{\min}$ should provide an upper bound for the deviation from ΦK_c. Pore theory (Deen 1987) and fiber theory (Phillips et al. 1990) also predict that the ratio K_c/K_d is greater than unity.

The effect of $\mathrm{Pe}_{\min}$ on the true and apparent sieving coefficients is illustrated in Figure 5.1. The figure assumes BSA passing through a 95 μm membrane with $\Phi K_c = 0.75$. As expected from Equation (5.2), the true sieving coefficient decreases from one to a constant value of ΦK_c as the Péclet number increases. At low flow rates (small $\mathrm{Pe}_{\min}$), Θ and Θ' are similar; higher flow rates increase concentration polarization and cause a larger difference between Θ and Θ'. Figure 5.1 illustrates the difficulty in selecting a flow rate that minimizes both the deviation of Θ from ΦK_c, as well as the difference between Θ and Θ'.

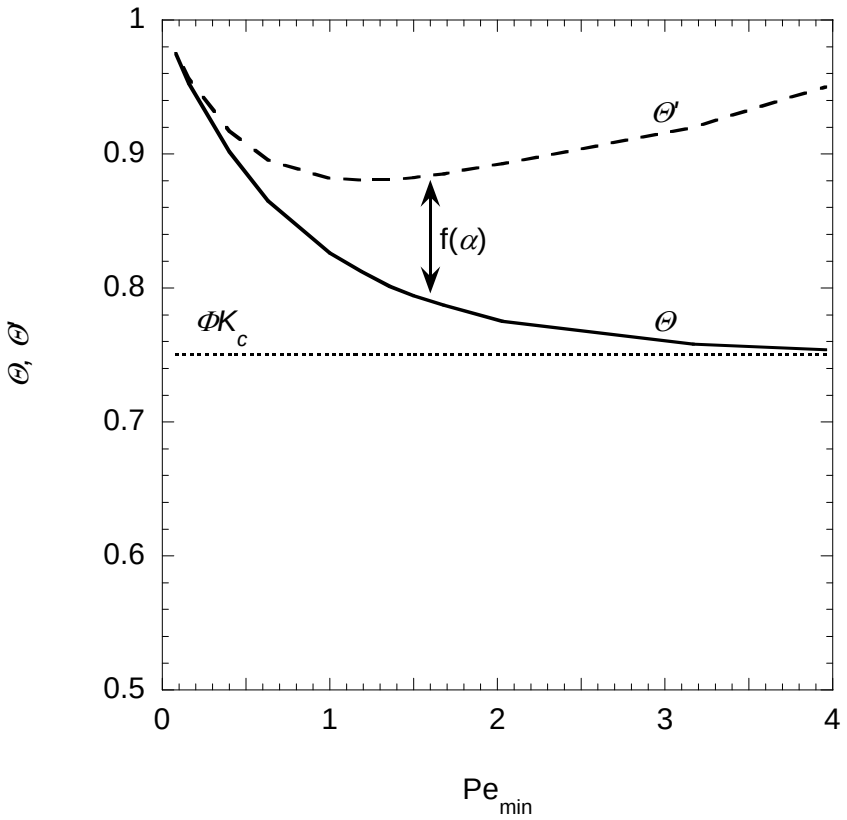

Figure 5.1 Membrane (Θ) and apparent (Θ') sieving coefficients over a range of flow rates. The calculations assume BSA (D_∞ = 6x10^{-11} m^2/s) passing through a δ = 95 μm membrane with ΦK_c = 0.75. The minimum Péclet number was defined as $Pe_{min} = \delta v/D_\infty$.

To stay near the bounds in which the polarization model had previously been validated, it was desired to perform experiments such that $\alpha \leq 0.6$. When sieving experiments were performed at $\alpha = 0.6$, the correction to the apparent sieving coefficient was at most ~25% (when Θ ~0.5 for BSA at low ionic strengths). A majority of experiments had sieving coefficients of $\Theta \geq 0.8$, such that the correction from Equation (5.16) with $\alpha = 0.6$ was less than 10%.

For a 70 μm membrane, a flow rate which gave $\alpha = 0.6$ corresponded to $Pe_{min} = 1.2$. It was difficult to neglect diffusive transport at this small minimum Péclet number. However, by increasing the membrane thickness to 95 μm, then $\alpha = 0.6$ corresponded to $Pe_{min} = 1.7$. Using $Pe_{min} = 1.7$ in Equation (5.2) and assuming $\Phi K_c = 0.75$, the sieving coefficient deviated by less than 5% from the high Péclet limit.

5.2.2. Sieving

The sieving measurements were performed in two steps. First, the hydraulic permeability was measured for the gel in the absence of a test solute. This both provided a check that the membrane was intact and washed any residual solute from the membrane. Following that, a solution of the test solute was filtered across the membrane to find the sieving coefficient. The solutes and buffer solutions used were identical to those used for partitioning in Chapter 4 (BSA and four Ficoll fractions in pH 7.4 PBS).

Hydraulic Permeability

The hydraulic permeability was measured in the same fashion described in Chapter 3. Briefly, the membrane was first equilibrated for several minutes in 5-10 mL of buffer of the ionic strength of interest if it was different than the previous experiment. This was done to wash out any excess salt that may increase the ionic strength. The membrane was then placed in a 10 mL ultrafiltration cell (Amicon 8010; Millipore, Bedford, MA) and covered with ~10 mL of buffer. The ultrafiltration cell was then pressurized (1-5 kPa) with nitrogen to achieve the same flow rate that would be used in sieving. After the flow equilibrated, samples of filtrate collected over timed intervals were used to determine the flow rate. The flow rate, the applied pressure drop, the membrane thickness, the membrane area, and a mesh correction factor were used to calculate the Darcy permeability.

Sieving Coefficient

Following the Darcy permeability measurement, the apparent sieving coefficient was measured. The ultrafiltration cell was emptied and refilled with approximately 10 mL of the macromolecule solution. The stir bar was inserted and the solution mixed for several minutes before a sample of the retentate solution was removed from the reservoir. The ultrafiltration cell was then repressurized with nitrogen and the stirring speed was set to 220 ± 5 rpm, as measured by an optical tachometer. The filtrate was collected while the system equilibrated, such that at least 1-2 mL (1.5~3 times the retention volume of the cell) was collected. The solute concentration in this sample is denoted as c_{eq}. The collection vessel was then switched and a filtrate sample was collected over a timed

interval. The solute concentration in this sample is denoted as c_F. At the end of filtrate collection, a second sample was taken of the retentate in the reservoir. The initial and final retentate concentrations are denoted as c_{Ri} and c_{Rf}, respectively. Each of these concentrations was measured by the assays described in the Chapter 4.

The apparent sieving coefficient was calculated from the average bulk retentate and filtrate concentrations:

$$\Theta' = \frac{c_F}{0.5\left(c_{Ri} + c_{Rf}\right)} \quad . \tag{5.20}$$

The maximum difference between the retentate concentrations was 14%, with an average of 4%. The mass conservation of the solute was evaluated from

$$\%\ \text{recovery} = \frac{c_{Rf}V_{Rf} + c_F V_F + c_{eq}V_{eq}}{c_{Ri}\left(V_{Rf} + V_f + V_{eq}\right)} \tag{5.21}$$

where V_f and V_{eq} are the total volume collected of the sample filtrate and the equilibration filtrate, respectively, and V_{Rf} is the final volume of the retentate as determined from the height of fluid in the reservoir at the end of sieving. Because of the intrinsic variability in the solute assays, it was possible for the apparent sieving coefficient to slightly exceed 1.00. If the mass balance closed within ± 10% and $\Theta' < 1.10$, then the corresponding true sieving coefficient was assumed to be 1.00.; if $\Theta' > 1.10$, then the data point was thrown away. Any experiment where the solute was not conserved to within ± 10% was immediately rejected. If the Darcy permeability varied by more than 15% between the initial measurement and the measurement during sieving, the data point was thrown away. The Darcy permeability generally agreed much better than this, differing on average by only 4%.

5.3. Results and Discussion

Method Verification

One of the main questions to be answered about the sieving method was whether the macromolecule solutes adsorbed to the agarose-GAG membranes (or other parts of the experimental apparatus). This was first confirmed on a large scale by checking the overall mass balance as given in Equation (5.21). For BSA, the recovery was 99.6% ± 0.2% standard error (SE) (n = 107); for Ficolls, recovery was 100.0% ± 0.7% (n = 85).

To verify that the membranes were not being fouled by solute adsorption or other contaminants, the Darcy permeability measured with solute-free buffer prior to sieving was compared to the permeability measured during sieving (shown in Figure 5.2). As seen in Chapter 3, even 0.2 v% of GAG can reduce the hydraulic permeability of 4 v% agarose gels by nearly half; the Darcy permeability should therefore be a very sensitive measure for even a small amount of solute binding. The ratio of the Darcy permeability with the solute to without was 98.8% ± 0.4% (SE) for BSA and 98.1% ± 0.8% for Ficolls. Statistically, the permeability before and during sieving was indistinguishable (p = 0.85 and 0.73 for BSA and Ficolls, respectively, with a Students t-test with alpha=0.05). This supports that solute binding to the membranes was negligible.

To verify that experiments were performed at a high enough Péclet number that the limit in Equation (5.4) could be assumed, BSA sieving experiments were performed over a range of applied pressures for 4 v% agarose gels with 0.19 v% GAG. The protein solution was 1 g/L BSA in 0.011 M PBS; the mean thickness of the membranes was 100 μm. The apparent sieving coefficients are show in Figure 5.3, as well as the actual sieving coefficients calculated from the concentration polarization model. The apparent sieving coefficient remained nearly constant, with a slight increase at the highest Péclet number. The corrected sieving coefficient monotonically decreased with increasing Péclet number.

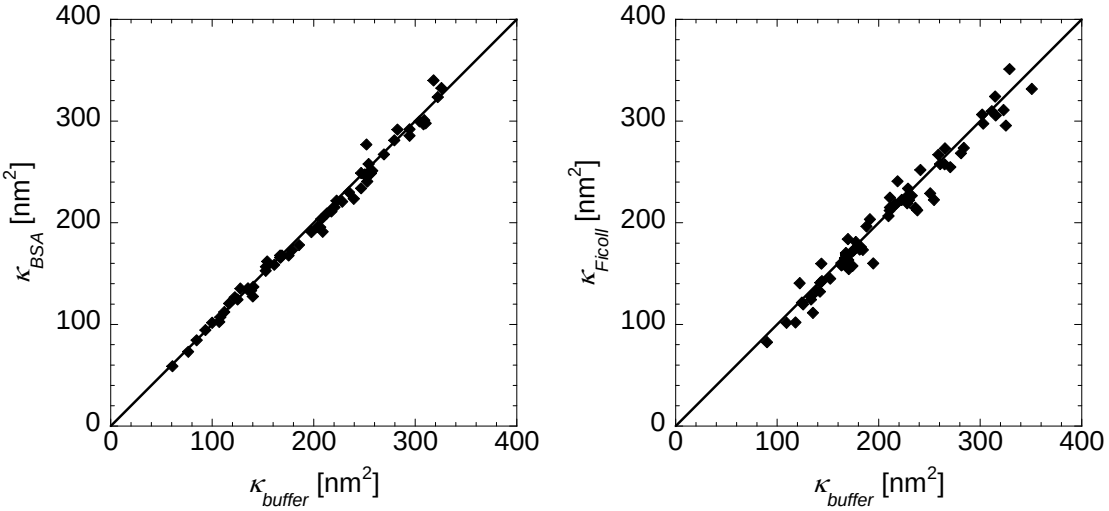

Figure 5.2 Darcy permeability of the 4 v% agarose membranes as measured before and during sieving, shown for both BSA and Ficolls. Permeability before sieving was measured in solute-free buffer. Data include both blank and 0.2 v% GAG membranes.

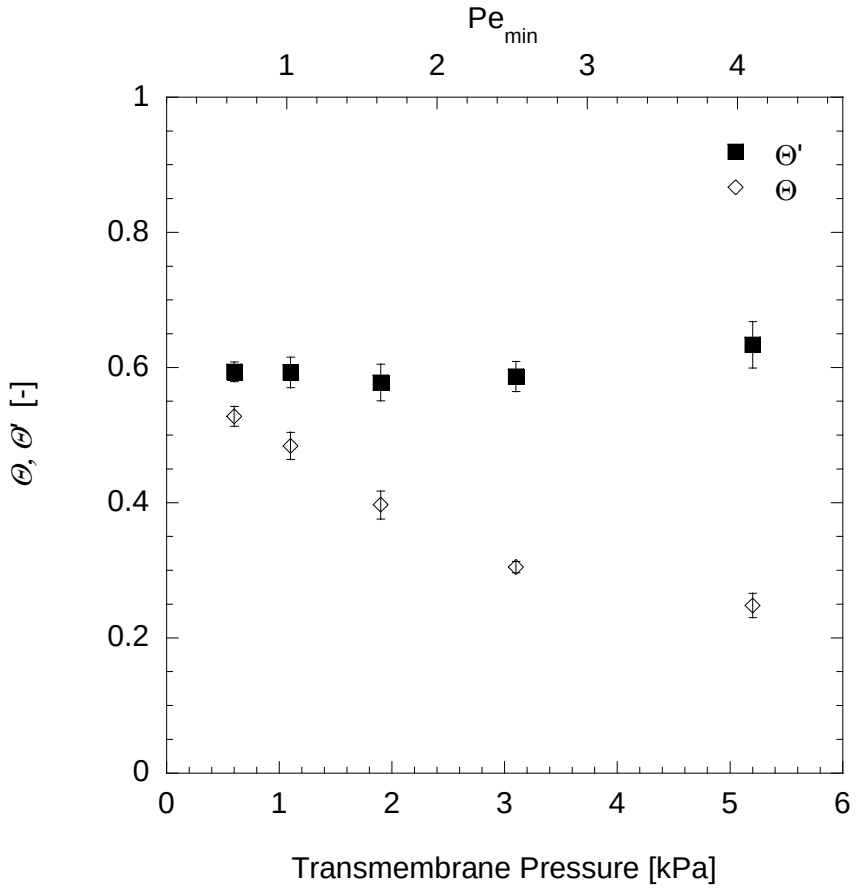

Figure 5.3 Corrected and apparent sieving coefficients (Θ and Θ', respectively) measured for several applied pressures. Also shown is the corresponding minimum Péclet number, $Pe_{min} = v\delta/D$, based on the mean flow rate through the gels and the mean thickness of 100 μm. All measurements are for BSA in 0.011 M PBS being sieved through 4 v% agarose gels with 0.19v% GAG. Error bars are one standard error for $n = 3$.

The experimental data in Figure 5.3 can be compared to the theoretical behavior in Figure 5.1. Sieving at lower applied pressures was infeasible with the current apparatus, so the increase in apparent sieving coefficients at Pe << 1 was not captured in Figure 5.3. However, there was a slight increase in the apparent sieving at the highest flow rate, consistent with theoretical predictions. Unfortunately, the actual membrane sieving coefficients did not plateau at a constant value as predicted in Figure 5.3. Given that the minimum Péclet numbers spanned 0.6-4, the actual sieving coefficients should have been nearly equal at the two highest flow rates. However, the value of the concentration polarization parameter, α, spanned the range of 0.20-1.37, which extends far beyond the validated range of the model $\alpha = 0$-0.5. This suggests that the lack of a plateau in the

actual sieving coefficient in Figure 5.3 might be due to shortcomings in using the concentration polarization model outside of its range. Since it was not possible to experimentally determine the flow rate at which the high Péclet limit in Equation (5.4) applies, the minimum Péclet number was used to provide a worst-case estimate of the deviation of the sieving coefficient from the high Péclet number limit.

Experimental Results - Sieving

Sieving coefficients were measured in 4 v% agarose gels without GAG and with 0.2 v% GAG. The true sieving coefficients (Θ), corrected for concentration polarization, are shown in Figure 5.4 for Ficolls of four different Stokes-Einstein radii (r_s). The smallest Ficoll fraction freely filtered through the membranes, with a sieving coefficient of approximately unity. The sieving coefficients for larger Ficoll fractions decreased with increasing solute radius. The sieving coefficients were also lower for membranes containing 0.2 v% GAG versus those without GAG. These observations are consistent with similar sieving coefficients previously measured for the same Ficoll fractions in 4 v% agarose-dextran gels, as shown in Figure 5.5 (Kosto and Deen 2005). It is expected that dextran and GAG should act similarly under neutral conditions, since both are high molecular weight polysaccharide fibers with $r_s \sim 0.5$ nm. The smaller Ficoll fractions freely filtered through the agarose-dextran gels, with decreasing sieving coefficients for larger Ficoll fractions. The sieving coefficient was decreased by up to 10% by the addition of only 0.08 v% dextran. The sieving coefficients of Ficolls through the blank agarose gels differed by as much as 10% between the two studies. However, as was noted in the previous chapter on partitioning, the blank gels were treated differently between the GAG and dextran studies, so it is not surprising that there were slight variations between sieving coefficients in the blank gels.

The sieving coefficients for 37 kDa Ficoll (r_s = 3.5 nm) were measured for solution ionic strengths of 0.011, 0.05, and 0.1 M, as shown in Figure 5.6. Similar to the partition coefficients measured under the same conditions (Figure 4.2), the sieving coefficients were nearly constant at high ionic strengths, but decreased at lower ionic strengths. Unlike the partition coefficients, the decrease in sieving coefficients occurred for both GAG-containing and GAG-free membranes.

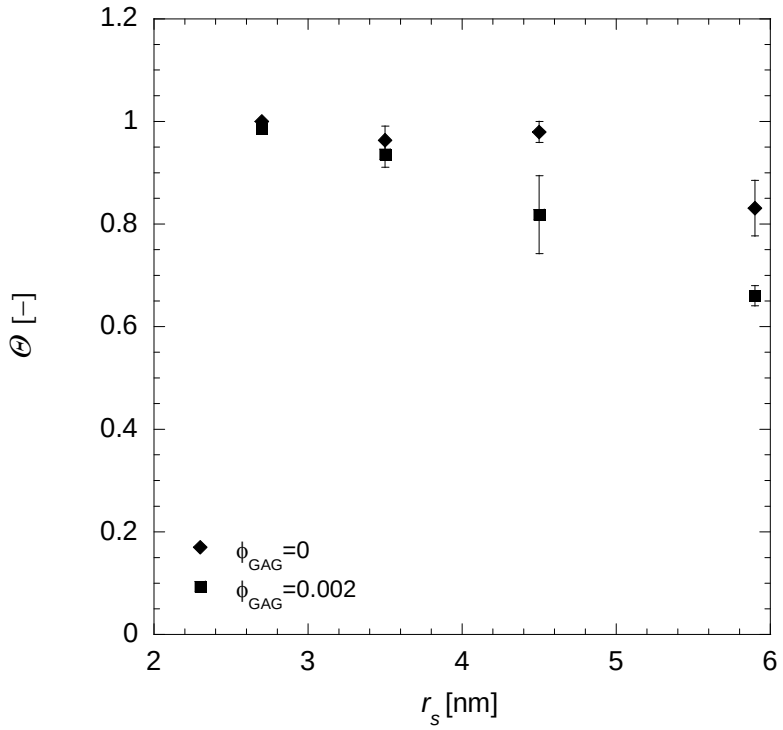

Figure 5.4 True sieving coefficient (Θ) of Ficolls, as a function of Stokes-Einstein radius (r_s), in 4 v% agarose gels with 0 or 0.2 v% of GAG. All experiments were performed in 0.1 M PBS. Error bars are one standard error with n = 5-6.

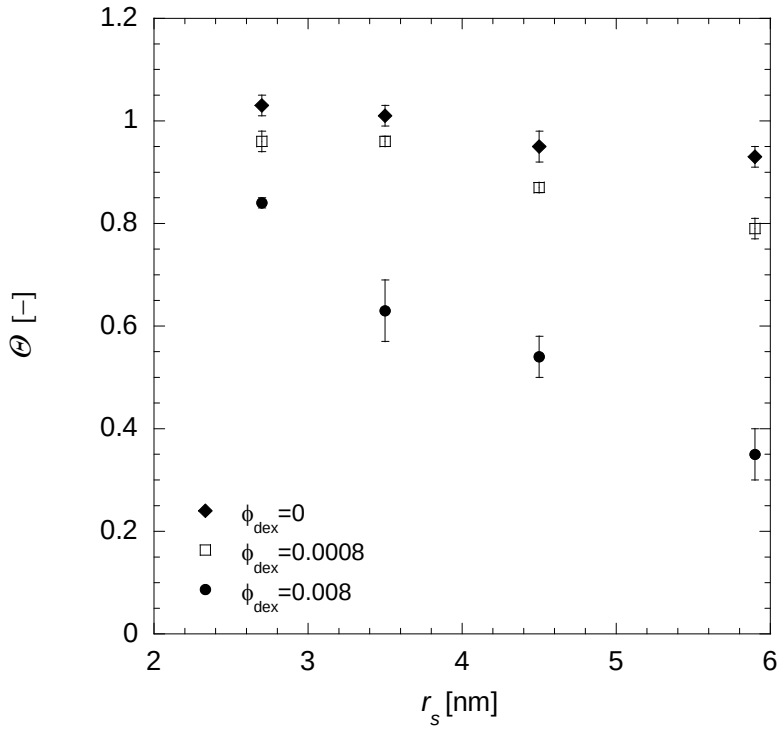

Figure 5.5 True sieving coefficient (Θ) of Ficolls, as a function of Stokes-Einstein radius (r_s), from a previous study with 4 v% agarose and various dextran contents (Kosto and Deen 2005). All experiments were performed in 0.1 M PBS. Error bars are one standard error with n = 3.

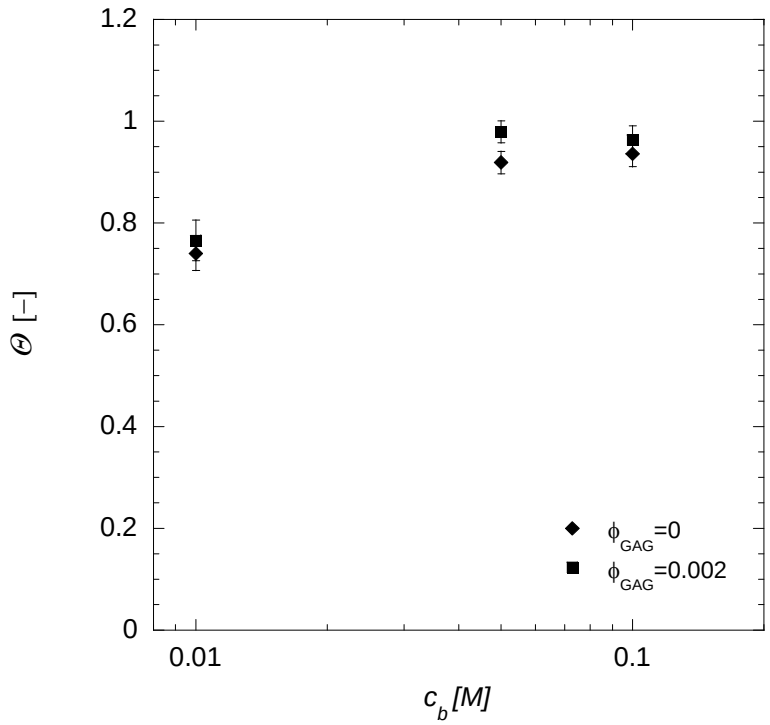

Figure 5.6 True sieving coefficient (Θ) of 3.5 nm Ficoll, over a range of solution ionic strengths (c_b), in 4 v% agarose gels with 0 or 0.2 v% of GAG. Error bars are one standard error with n = 5-6.

It is difficult to explain the decrease in Ficoll sieving in the uncharged blank agarose membranes, where there are no charge interactions which would be affected by ionic strength. One possible cause is the difference in applied pressures between the samples, with a mean of 1.1 kPa for 0.05 and 0.1 M versus a mean of 1.6 kPa for 0.01 M. The change in pressure was needed to maintain a constant flow rate in response to a decrease in Darcy permeability (blank gels had a mean permeability of $\kappa = 279 \pm 44$ nm^2 at 0.1 M versus 187 ± 88 at 0.011 M); as seen in Table 5.2, Pe_{min} (and therefore flow rate) was nearly constant for the three ionic strengths. The higher Darcy permeability at lower pressure is consistent with observations in 3 v% agarose, where the permeability was elevated at pressures <5 kPa (Figure 3.40). This change in hydraulic permeability could suggest a change in agarose structure, which would also affect the sieving. However, this hypothesis would not explain the changes observed in partitioning, in which there is no applied pressure. Additionally, a decrease in sieving through blank agarose was not observed with BSA (as will be shown shortly), indicating that the decrease observed with Ficoll may be anomalous.

Table 5.2 Sieving coefficients, sieving conditions, and partition coefficients for 37 kDa Ficoll (r_s = 3.5 nm) in 4 v% agarose membranes over a range of ionic strengths. Results are presented as mean ± one standard error, with n = 5-6 except Φ where n = 9-11.

	Θ'	Θ	Pe_{min}	κ	Φ
Blank (0v% GAG)					
0.011 M	0.88 ± 0.03	0.77 ± 0.04	2.0 ± 0.2	187 ± 36	0.67 ± 0.01
0.05 M	1.01 ± 0.01	0.98 ± 0.02	2.0 ± 0.1	256 ± 14	0.69 ± 0.01
0.1 M	1.00 ± 0.01	0.96 ± 0.03	2.2 ± 0.2	279 ± 19	0.70 ± 0.01
0.2 v% GAG					
0.011 M	0.85 ± 0.03	0.74 ± 0.03	1.6 ± 0.1	113 ± 18	0.46 ± 0.02
0.05 M	0.96 ± 0.02	0.92 ± 0.02	1.8 ± 0.1	161 ± 14	0.64 ± 0.01
0.1 M	0.96 ± 0.02	0.94 ± 0.02	1.5 ± 0.1	159 ± 16	0.63 ± 0.01

Sieving coefficients for BSA were measured in the same membranes for solution ionic strengths of 0.011, 0.02, 0.05, and 0.1 M, as shown in Figure 5.7. As expected, the sieving of BSA through the neutral agarose membranes without GAG was constant with ionic strength. The sieving coefficient for BSA through membranes with 0.2 v% GAG decreased by over 50% from 0.1 M to 0.011 M. Statistically, there was no difference between the sieving coefficient of BSA (r_s = 3.6 nm) and 3.5 nm Ficoll in the blank gels at the highest ionic strength (Students t-test p=0.12 for alpha=0.05). There was a statistical difference between BSA and Ficoll in the 0.2 v% GAG gels at 0.1 M (p=0.002); however, this difference is likely to have been because the BSA sieving at 0.1 M was not equivalent to neutral conditions. As shown in Figure 5.7, there was still a significant increase in the sieving coefficient between 0.05 and 0.1 M, indicating that charge effects were not fully screened at 0.1 M.

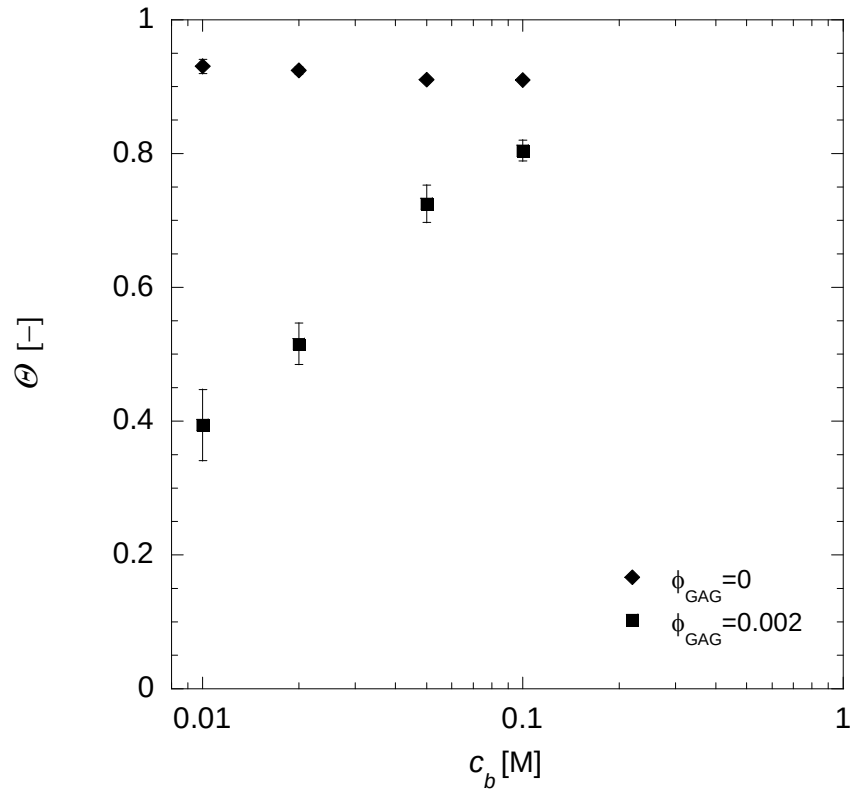

Figure 5.7 True sieving coefficient (Θ) of bovine serum albumin (BSA), over a range of solution ionic strengths (c_b), in 4 v% agarose gels with 0 or 0.2 v% of GAG. Error bars are one standard error with $n = 6$.

The sieving coefficients for BSA were also measured in 3 v% agarose gels, shown in Figure 5.8 for a range of ionic strengths. These gels were the same as those used for Darcy permeability in Chapter 3, with a mean thickness of 73 ± 1 μm and GAG contents of 0 or 0.4 v%. The charge effects in these gels are comparable to those shown in Figure 5.7 with 4 v% agarose. However, the results for the 3 v% agarose gels should be treated cautiously. As previously discussed, it was difficult to maintain both a high Péclet number and low concentration polarization correction. Sieving coefficients for 3 v% gels were performed at similar Péclet numbers to the 4 v% gels (Pe_{min} = 1.3-2.1). This caused the concentration polarization factor, α, to be higher for the 3 v% membranes, with average values of α = 0.96 for blank gels and α = 0.71 for 0.4 v% GAG gels. The correction for concentration polarization was minimal for the blank gels (<8%), where Θ was large; however, corrections for the 0.4 v% GAG gels were as much as 26% and were subject to errors since α was outside the validated range.

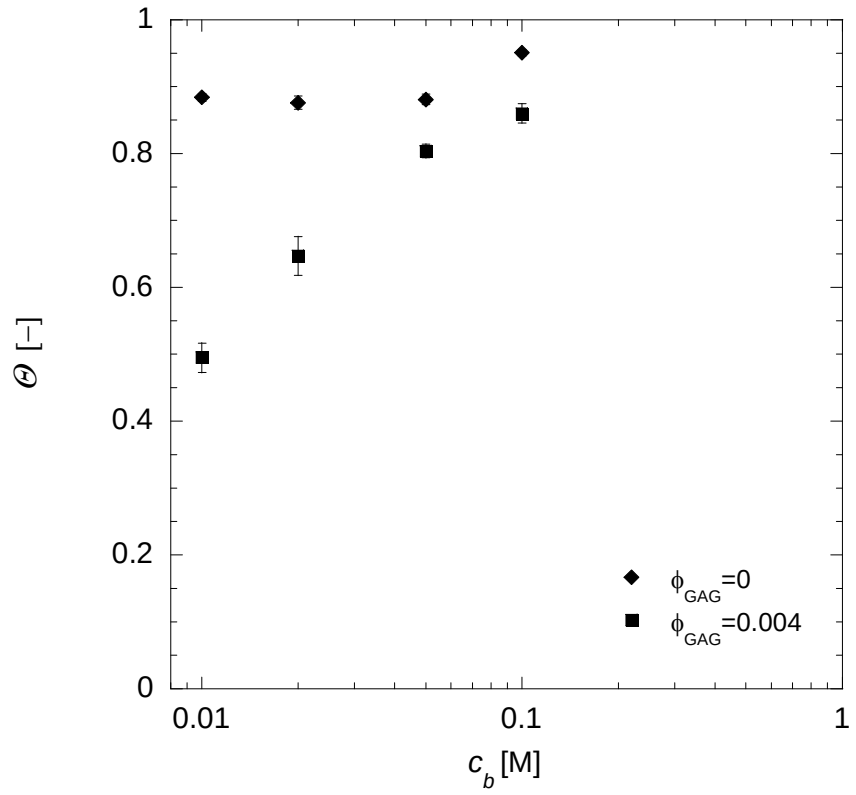

Figure 5.8 True sieving coefficient (Θ) of bovine serum albumin (BSA), over a range of solution ionic strengths (c_b), in 3 v% agarose gels with 0 or 0.4 v% of GAG. Error bars are one standard error with $n = 6$.

Convective Hindrance Factor

Remember from Equation (5.4) that the sieving coefficient at high Péclet number is equal to the product of Φ and K_c. It had been proposed that the charge effects observed in the sieving coefficient are primarily contained within the partition coefficient, Φ, and that K_c can be determined solely from neutral hydrodynamic models. To investigate this hypothesis, the independently measured values of Φ and Θ for BSA in 4 v% agarose+0.2 v% GAG membranes are plotted against each other in Figure 5.9. A linear function was fit to the mean values for BSA, assuming the form $\Theta = K_c\Phi$. The best-fit slope of this line was $K_c = 1.57$ with a correlation coefficient $R = 0.89$. Previous researchers have discussed how heterogeneities in the agarose fiber density can result in values of K_c significantly greater than unity due to the solvent flux weighting factor for Θ given in Equation (5.14)(Kosto and Deen 2005); a summary of their discussion was presented in Section 5.1.3.

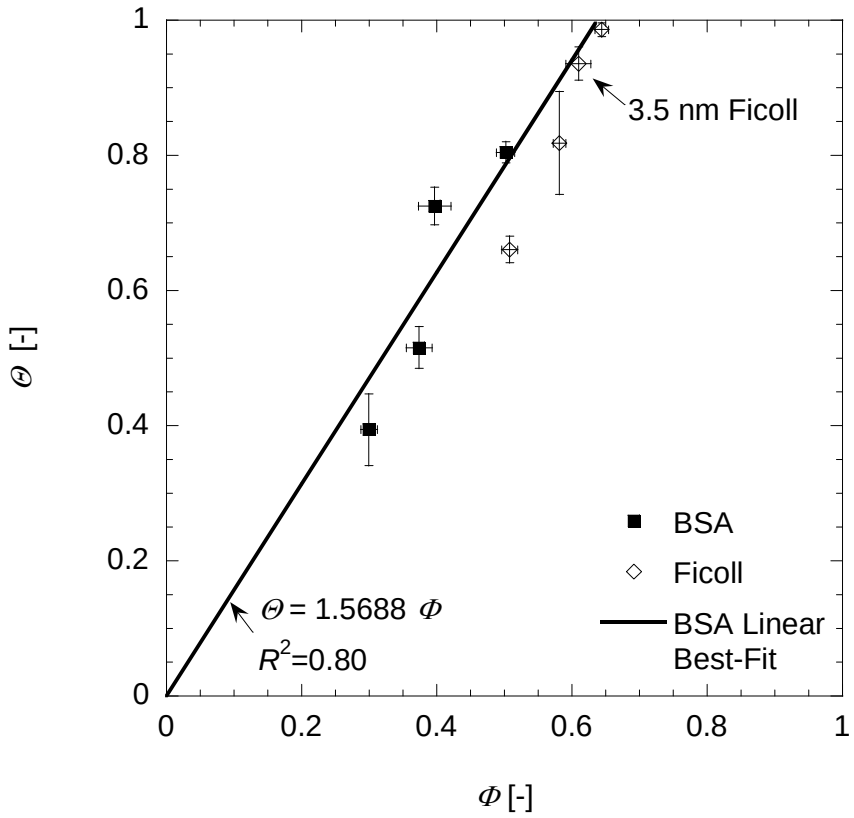

Figure 5.9 True sieving coefficients (Θ) of bovine serum albumin (BSA) and Ficolls as a function of the corresponding partition coefficients (Φ). BSA values were measured over a range of solution ionic strengths (c_b = 0.011-0.1 M) and Ficoll values were measured at c_b = 0.1 M. All measurements were performed in 4 v% agarose gels with 0.2 v% of GAG. Error bars are one standard error with n = 6 for Θ and n = 10-11 for Φ. The line is the least-squares linear equation to the BSA data with a forced intercept of 0.

The values of Φ and Θ for the four Ficoll fraction in 0.1 M PBS are also plotted against each other in Figure 5.9. Measurements were made in the same 4 v% agarose+0.2 v% GAG membranes used for the BSA measurements. Based on the model (Equation (5.5)), the value of K_c varies for different Ficoll r_s. This means that a single line will not fit through the Ficoll points in Figure 5.9, since the slope (K_c) will be smaller for larger solutes. However, the 3.5 nm Ficoll does fall near the best-fit line for the similarly-sized BSA (3.6 nm), as expected from the K_c model.

To further investigate the role of charge in K_c, the ratio Θ/Φ ($\sim K_c$) is plotted in Figure 5.10 as a function of ionic strength. The data shown are for BSA in 4 v% agarose with 0 and 0.2 v% GAG. A line was fit through each type of membrane, weighting each point by the inverse variance (to account for difference uncertainties at each ionic strength).

The slope of Θ/Φ versus $\log(c_b)$ was 0.104 ± 0.170 (SD) for blank gels and 0.276 ± 0.376 for 0.2 v% GAG. Since the slopes of these lines were not statistically different from zero, this data does not disprove the hypothesis than K_c is independent of charge interactions. However, additional tests of charged membranes with smaller errors in Θ and Φ are needed to more accurately predict if K_c is truly independent of the solution ionic strength. The weighted mean values of Θ/Φ were 1.44 ± 0.01 for the blank gels and 1.56 ± 0.02 for the 0.2 v% GAG gels. This mean value of $K_c \sim \Theta/\Phi$ in 0.2 v% gels agrees well with the estimate of K_c from Figure 5.9 (K_c = 1.57). The methods for calculating weighted means and weighted-least-squares fits are summarized in Appendix E.

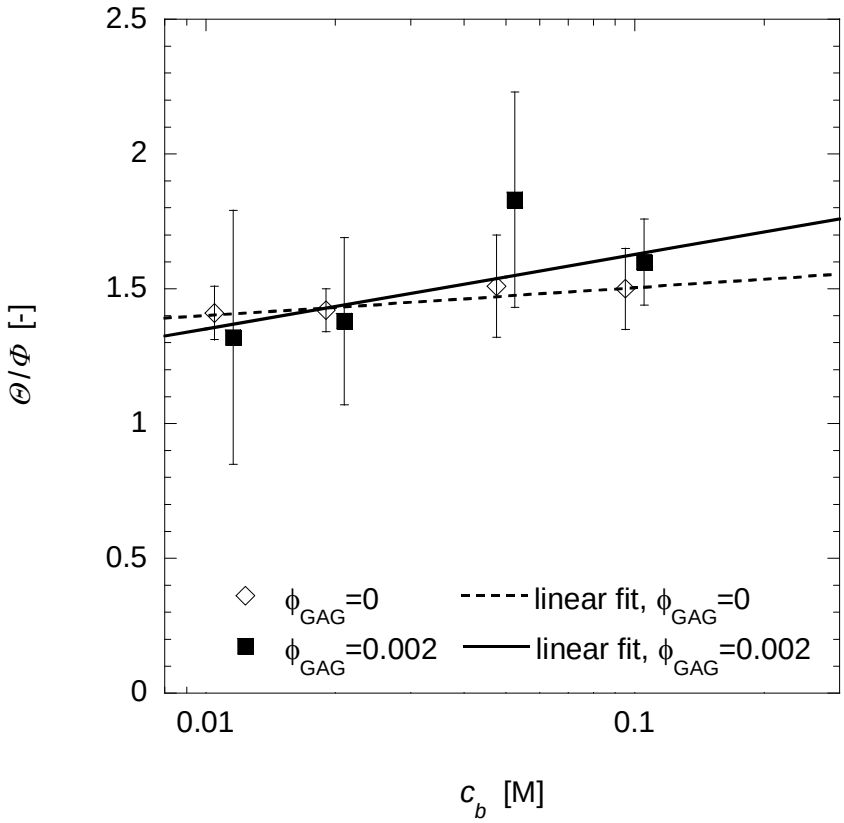

Figure 5.10 Ratio of true sieving coefficient (Θ) to partition coefficient (Φ) for bovine serum albumin (BSA) as a function of solution ionic strengths (c_b) in 4 v% agarose gels with 0 or 0.2 v% of GAG. Lines are a weighted least-squares fit to the data (weighting by inverse variance). Error bars are one standard deviation. The points are offset by ±5% in c_b for clarity.

The ratio Θ/Φ ($\sim K_c$) is plotted for Ficolls in Figure 5.11 as a function of solute radius. The apparent K_c tends to decrease with larger values of r_s, where the larger solutes experience more steric hindrance from the membrane fibers; however, this decrease was statistically significant only for the 0.2 v% GAG gels over the range of solute radii investigated. This trend differs from the results found in agarose-dextran gels, where there was an apparent maximum in K_c for the 4.6 nm Ficolls (Kosto and Deen 2005). Theoretical values of K_c were generated from Equations (5.5)-(5.8), as a function of dimensionless solute radius, $\lambda = r_s/r_f$. The values of K_c are shown in Figure 5.12 for several fiber volume fractions. As shown in the figure, the model for K_c *does* predict a maximum value. However, for the fiber size and volume fractions in the current agarose gels ($r_f = 1.6$ nm, $\phi = 0.04$), the maximum generally occurs at smaller solute radii ($\lambda \sim 1.2$, or $r_s \sim 1.9$ nm) than the reported maximum in agarose-dextran. The experimental data in agarose-GAG gels are qualitatively consistent with the model's decrease in K_c for solute radii larger than 2 nm.

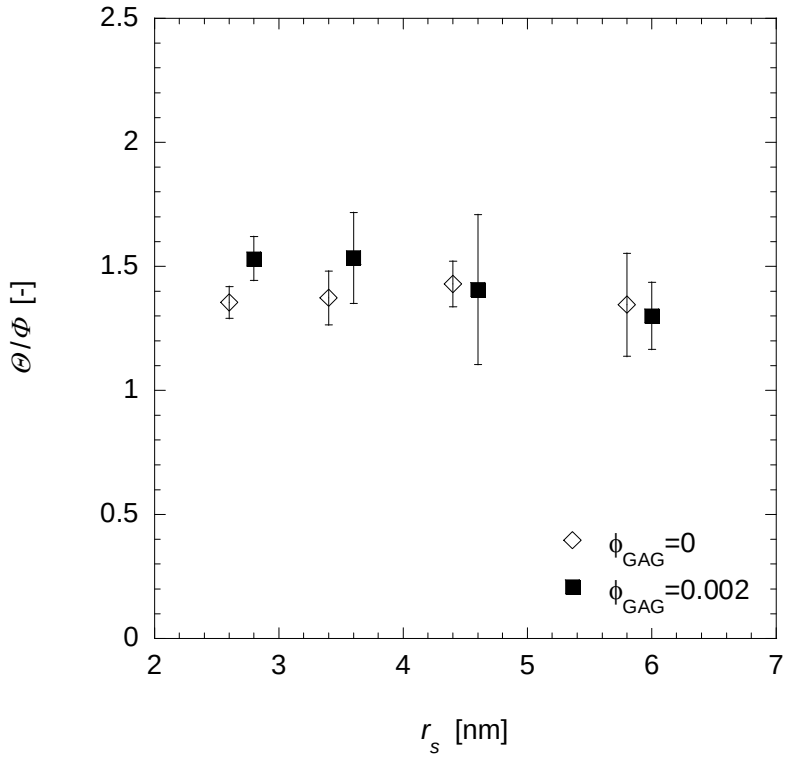

Figure 5.11 Ratio of corrected sieving coefficient (Θ) to partition coefficient (Φ) for Ficolls as a function of Stokes-Einstein radius (r_s) in 4 v% agarose gels with 0 or 0.2 v% of GAG. Error bars are one standard deviation. The points are offset by ±0.1 nm in r_s for clarity.

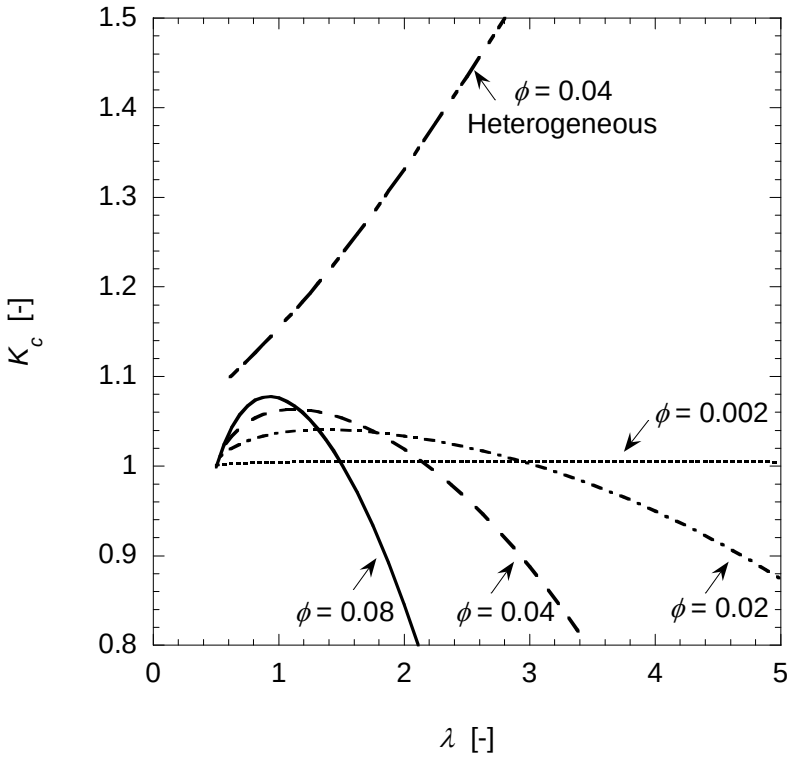

Figure 5.12 Theoretical predictions for the convective hindrance coefficient, K_c, as a function of $\lambda = r_s/r_f$. Curves were generated from Equations (5.5)-(5.8). All curves assumed a homogeneous ϕ unless noted otherwise. The heterogeneous curve is based on Equation (5.14) with Equations (3.3) and (4.2) used to model κ and Φ. The heterogeneity was characterized by $\varepsilon_2 = 0.5$ and $\phi_2/\phi = 1.95$, similar to values used in partitioning models.

Figure 5.12 also includes predictions of K_c for a heterogeneous gel using Equation (5.14). The theoretical values of the hydraulic permeability were found with Equation 3.3 for flow perpendicular to a square array of fibers, similar to that assumed in the K_c model; Equation 4.2 was used to predict the partition coefficient. The value of the fiber radius used in the hydraulic permeability model was unimportant, since it cancels between the numerator and denominator in Equation (5.14). Heterogeneity parameters were the same as used in partitioning models in Chapter 4: $\varepsilon_2 = 0.5$ and $\phi_2/\phi = 1.95$. The experiments performed with Ficoll in agarose ($r_f = 1.6$ nm, $\phi = 0.04$) in Figure 5.11 correspond to values of $\lambda = 1.7$-3.7. The heterogeneous model predicts values of K_c in the range of 1.3-1.7 for solutes of this size, which is in excellent agreement with the experimental data. The trend with size dependence appears to differ between experiments (K_c decreases with λ) and model (K_c increases with λ). However, the trend in the experimental data was only statistically significant for the GAG-containing

membranes. Additionally, there are many idealizations in the model (ordered fibers, parallel heterogeneous regions) that makes its predictions inexact.

5.4. Conclusions

The experimental results for the sieving coefficients in agarose-GAG gels provided new information about the role of charge in sieving through fibrous membranes. Ionic strength had little effect on the sieving of anionic BSA through neutral agarose. However, the sieving coefficient of BSA through agarose-GAG membranes decreased by over 50% from 0.1 M to 0.011 M. The decrease in sieving at lower ionic strength was highly correlated with the decrease in the corresponding partition coefficient. At the flow rates used in the experiments, the sieving coefficient could be well approximated as $K_c\Phi$. The BSA sieving data are consistent with the hypothesis that charge interactions in sieving are primarily described by the partition coefficient, and that the convective hindrance coefficient, K_c, is relatively insensitive to charge interactions between the solute and fibers.

The sieving results with Ficoll confirmed several previously reported observations, such that sieving decreases for larger solutes and with the addition of small volume fractions of fine fibers. The apparent value of K_c was nearly 50% higher than that predicted by a fibrous model, but this discrepancy may be accounted for if the membrane has a heterogeneous regions with different fiber densities. Current models for sieving and convective hindrance are limited to ordered arrays of fibers and membranes with a single type of fiber, so predictive models for sieving through agarose-GAG membranes were not possible at this time.

Chapter 6. CONCLUDING REMARKS

6.1. Implications for Glomerular Filtration

As discussed in Chapter 1, this thesis research was inspired by hindered transport across the glomerular capillary wall. In particular, it was hoped to provide some insight into the role that the GAG-rich endothelial glycocalyx plays in glomerular ultrafiltration of blood plasma. Unfortunately, information about the structure of the glomerular endothelial glycocalyx is limited. As discussed in Chapter 1, the glycocalyx is primarily composed of proteins, proteoglycans, and glycoproteins. The estimated thickness of the glycocalyx has increased as fixation techniques have improved. Estimates of the thickness range from 100 to 1000 nm, with a thickness of approximately 300 nm being most consistent with recent observations (Rostgaard and Qvortrup 2002, Squire et al. 2001, Vink and Duling 2000, Weinbaum et al. 2007). The density of fibers within the glycocalyx is even less known. The only current estimates come from observations of a periodic structure in the glycocalyx of a mesenteric capillary, where 10-12 nm diameter structures (believed to be core proteins with assemblages of glycoproteins or proteins) were located at 20 nm spacings (Squire et al. 2001).

Since knowledge about the structure of the glycocalyx is currently incomplete, a simplified model was developed to evaluate if endothelium could have a low hydraulic resistance while providing some selectivity in sieving BSA. The composition of the glycocalyx was assumed to be only GAG, neglecting proteins and glycoproteins. The fiber volume fraction (ϕ) and thickness of the glycocalyx (δ_g) were treated as variables. The potential thickness was bounded by 100 and 1000 nm; the fiber volume fraction was bounded by 0 and 0.28 (assuming the 12 nm periodic structures were solid). It was assumed that the GAG fibers were randomly oriented with a uniform fiber density throughout the glycocalyx and within the fenestra. The GAG properties were assumed to be the same as used for chondroitin sulfate in Chapters 2-5: a fiber radius, $r_f = 0.5$ nm, and a surface charge density, $\sigma_s = -0.1$ C/m^2.

A structure for the glomerular endothelium has been proposed based on microscopy observations (Drumond and Deen 1994, Lea et al. 1989). A schematic representation of a unit cell based on a single fenestra is shown in Figure 6.1. The fenestra has a circular opening with an hourglass-shaped cross-section, with a radius at the narrowest point (R_f) equal to half the endothelial cell thickness. The fenestra radius was assumed to be $R_f = 30$ nm; the unit cell half-width, b, was 60 nm based on a fenestra fractional area $\varepsilon_f = \pi R_f^2/4b^2 = 0.2$ (Drumond and Deen 1994).

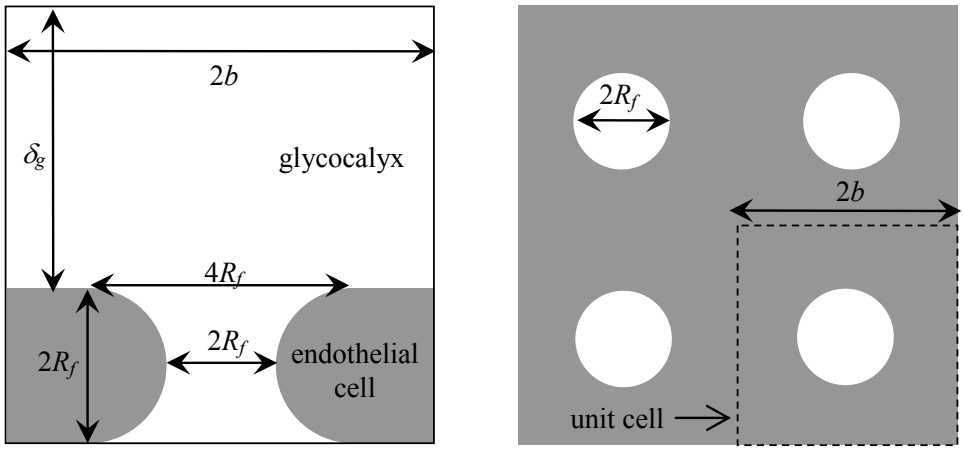

(a) Side View (b) Bottom View

Figure 6.1 Schematic representation of a unit cell based on a single fenestra, (a) as viewed from the side and (b) as viewed from the bottom, with the boundaries of the single unit cell shown by the dashed line.

While the structure of the endothelial glycocalyx is not fully known, some limits can be placed on its properties. As discussed in Chapter 1, the endothelium is the first of three layers in series through which blood plasma passes during ultrafiltration. The hydraulic resistances of each of these layers ($1/k_i$) are summed in series to give the hydraulic resistance of the entire glomerular capillary wall ($1/k$):

$$\frac{1}{k} = \frac{1}{k_{endo}} + \frac{1}{k_{GBM}} + \frac{1}{k_{epi}} \tag{6.1}$$

where the subscripts refer to the endothelim (*endo*), basement membrane (*GBM*), and epithelim (*epi*). Based on micropuncture experiments in rats, the permeability of the glomerular capillary wall is $k = 3\text{-}5\text{x}10^{-9}$ m/s-Pa. Experiments on isolated basement membranes combined with models for the membrane surfaces blocked by endothelial and epithelial cells predicted a basement membrane hydraulic permeability of $k_{GBM} = 4\text{-}8\text{x}10^{-9}$ m/s-Pa. A model of the resistance from the epithelium predicted a hydraulic permeability of $k_{epi} = 8.6\text{x}10^{-9}$ m/s-Pa (Deen 1987, Deen and Lazzara 2004), though the permeability could be much higher than this. From these numbers, we expect that the endothelium (and its glycocalyx) contributes 0-63% of the total hydraulic resistance across the glomerular capillary wall, or $k_{endo} \geq 4.8\text{x}10^{-9}$ m/s-Pa. Using the microstructural models for hydraulic permeability in Chapter 3, the lower limit on k_{endo} should provide some limits on the thickness and fiber density of the glycocalyx.

Sieving through the capillary wall (Θ) can be represented as the product of the sieving coefficients of each layer,

$$\Theta = \Theta_{endo}\Theta_{GBM}\Theta_{epi} \tag{6.2}$$

though it should be noted that each layer's sieving coefficient is dependent on the properties of the other layers. The following discussions will refer to the sieving of albumin, an abundant plasma protein which is the focus of many renal studies. The sieving coefficient of albumin across the capillary wall has been estimated as $\Theta = 4\text{-}6\text{x}10^{-4}$ in rats (Deen 2004). (In contrast, the sieving coefficient for neutral 3.6 nm Ficoll was reported to be $\Theta = 0.03$ (Ohlson et al. 2000).) Studies and models of the basement membrane indicate that, while it provides some selectivity in isolation, the *in situ* sieving coefficient of albumin is $\Theta \sim 1$ (Deen 2004). It has been observed that disruption of either the epithelial or endothelial layer can result in proteinurea, which implies that Θ_{epi}

and Θ_{endo} are likely both ≤ 0.1 (Deen 2004). From these observations, we estimate that $10^{-3} \le \Theta_{endo} \le 10^{-1}$. Using the microstructural models developed in Chapters 4 and 5 for partitioning and sieving, we would like to predict which endothelial properties could result in a sieving coefficient in this range and if charge interactions between GAG and BSA play a role in the sieving selectivity.

6.1.1. Hydraulic Resistance

Model Development

For assumed values of ϕ and δ_g, the Darcy permeability was calculated with the neutral hydraulic permeability given in Section 3.1.3 (Clague et al. 2000):

$$\frac{\kappa}{r_f^2} = \left[\frac{1}{2}\sqrt{\frac{\pi}{\phi}} - 1\right]^2 \left[0.71407 \exp\left(-0.51854\phi\right)\right] \tag{6.3}$$

and electrokinetic reduction given by the Donnan model in Section 3.1.2:

$$\kappa = \kappa_n \left[1 + \frac{\left(\kappa_n / \mu\right) RTc_b \left(c_b \left(D_+ - D_-\right) - c_+^{'} \left(D_+ - D_-\right) + c_m D_+\right)}{D_+ D_- \left(2c_+^{'} - c_m\right)}\right]^{-1} \tag{6.4}$$

$$c_+^{'} = \frac{c_m}{2} + \sqrt{\frac{c_m^2}{4} + c_b^2} \tag{6.5}$$

The diffuse double layer microstructural model for hydraulic permeability in charged fibers could also have been used, but would have required a large computational effort for the range of parameters being considered in the current analysis. As was shown in Figure 3.9, there was relatively little difference between the two models at a low volume fraction (ϕ = 0.00375); the difference was expected to be even smaller at larger volume fractions when the assumptions in the Donnan model are more closely met. Blood plasma is approximately 0.15 M NaCl; the properties of an aqueous sodium chloride solution were given in Table 3.2.

The flow through the glycocalyx is affected by the presence of impermeable endothelial cells. The fiber-filled fenestra in Figure 6.1 is very similar to the gel-filled polyester support mesh modeled in Section 3.3.3. A correction factor, β_f, was inserted into Darcy's law to account for the decreased hydraulic permeability due to the presence of the endothelial cells:

$$q_v = k_{endo}\Delta P = \frac{\kappa\beta_f}{\mu\delta}\Delta P \tag{6.6}$$

where the volumetric flux (q_v) is related to the pressure drop (ΔP) across the endothelial thickness $\delta = 2R_f + \delta_g$. The correction factor, β_f, could have been found by an analytical solution for a pore with a constant radius (Keller and Stein 1967), or solved for the hourglass geometry by finite element software using Equations (3.77)-(3.79). The results for the latter approach, solved with Comsol Multiphysics™, are shown in Figure 6.2 for a range of glycocalyx thicknesses, δ_g, assuming the geometry in Figure 6.1 with $R_f = 30$ nm and $b = 60$ nm. The data were least-squares fit to the expression

$$\beta_f = 0.3462 + 0.4033\log(\delta_g / b) \tag{6.7}$$

with $R^2 = 0.998$. The simulation results and Equation (6.7) differed by at most 1.5% over the range shown in Figure 6.2.

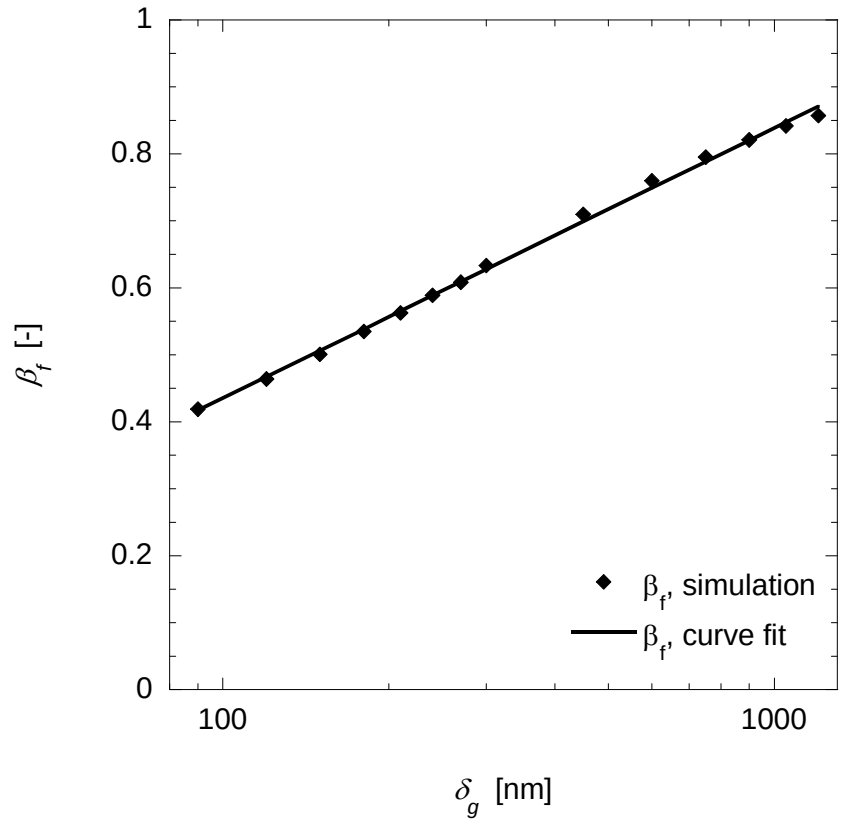

Figure 6.2 Correction factor, β_f, for reduced flow through the endothelium due to the presence of the fenestra, as a function of the glycocalyx thickness δ_g. Solid symbols are results of a finite element simulation using the hour-glass geometry in Figure 6.1 with $R_f = 30$ nm and $b = 60$ nm. The solid line is the least-squares fit to the data given by Equation (6.7).

Model Results

The endothelial model was used with the ranges of glycocalyx thickness and fiber density described above: $0 \le \phi \le 0.28$ and $100\text{ nm} \le \delta_g \le 1000\text{ nm}$. First, the hydraulic resistance of the endothelium was analyzed to determined if the ranges of glycocalyx thickness or fiber density could be narrowed. The hydraulic permeability of the endothelium is shown in Figure 6.3 for several thicknesses over a range of fiber densities. The hydraulic permeability goes below the minimum estimated value of $4.8\text{x}10^{-9}$ m/s-Pa for several of the conditions. For the range of glycocalyx thicknesses considered, fiber volume fractions $\phi \ge 0.04$ gave hydraulic resistances that were too high. For an extremely thick glycocalyx ($\delta_g = 1000$ nm), a low fiber density ($\phi < 0.013$) was needed to not exceed the estimated permeability. From the results in Figure 6.3, the viable range of fiber densities in the glycocalyx can be narrowed to $\phi \le 0.04$.

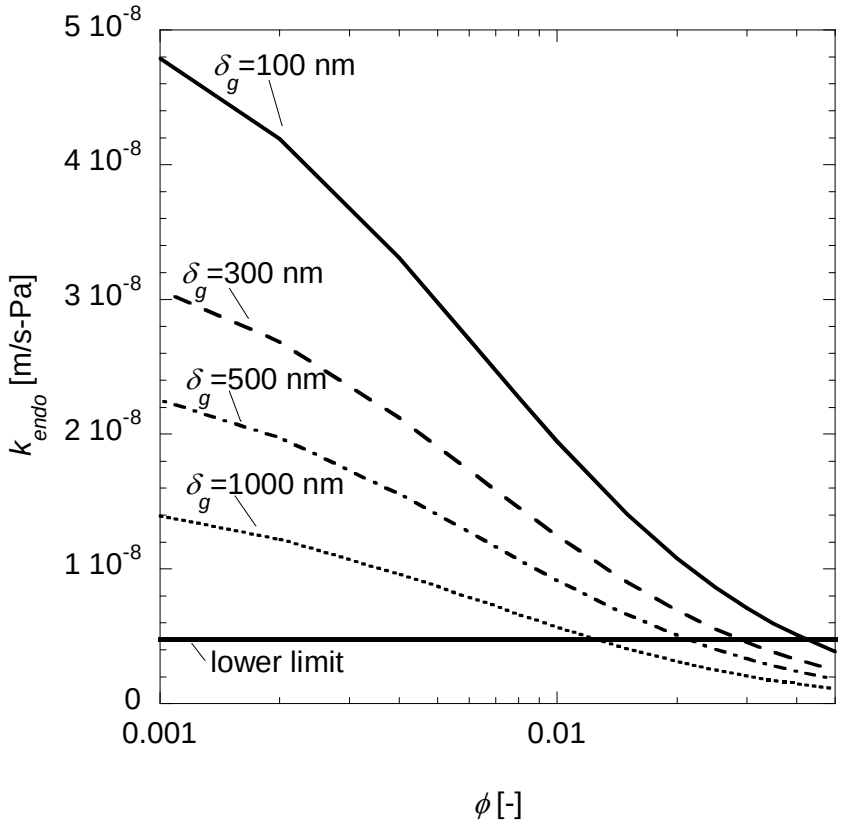

Figure 6.3 Hydraulic permeability of the endothelium (k_{endo}) for several combinations of glycocalyx thickness (δ_g) and fiber volume fraction (ϕ). The thick line represents the lower limit of hydraulic permeability, based on physiological observations and models of the other capillary layers. The model assume the endothelial geometry shown in Figure 6.1; model parameters are given in the text.

6.1.2. Sieving

Model Development

For an assumed value of ϕ, the partition coefficient of a charged solute was calculated from the microstructural model given by Equations (4.9)-(4.13). The partition coefficient for an equivalent neutral solute was calculated from Equation (4.3). The convective hindrance factor, K_c, was assumed to be independent of charge, as was supported by the results in Chapter 5. It was evaluated by equations given in Section 5.1.3 (Phillips et al. 1990):

$$K_c = 1 + B(0.65\phi) + \Gamma(0.65\phi)^2 \tag{6.8}$$

$$B = 5.1712 - 0.9727\left(\frac{1}{\lambda}\right) - 1.1355\left(\frac{1}{\lambda}\right)^2 + 0.2511\left(\frac{1}{\lambda}\right)^3 \tag{6.9}$$

$$\Gamma = -9.97883 + 8.9787\,\lambda - 31.6717\,\lambda^2 - 2.9586\,\lambda^3 \tag{6.10}$$

where $\lambda = r_s/r_f$. Care must be taken, since the model was only developed for λ = 0-5 and for ϕ that resulted in $K_c \geq 0.8$.

Given that sieving through the glycocalyx may not occur at a high Péclet number (Deen 2006), an estimate of the diffusive hindrance factor, K_d, was needed to estimate the Péclet number. Assuming that a neutral model can be used for estimating K_d, one such model was (Kosto and Deen 2004, Phillips 2000)

$$K_d = \exp\left[-0.84\,(1+\lambda)^{2.18}\phi^{1.09}\right]\exp\left[-a\,\phi^b\right] \tag{6.11}$$

where $\lambda = r_s/r_f$ and the parameters a and b are given by

$$a = 3.727 - 2.460(1/\lambda) + 0.822(1/\lambda)^2 \tag{6.12}$$

$$b = 0.358 + 0.366(1/\lambda) - 0.0939(1/\lambda)^2 \quad . \tag{6.13}$$

An average volume flux of 4 μm/s was reported for the basement membrane (Deen 1987). Since the layers of the capillary wall are in series, the volume flux is constant between the three layers and the area-averaged velocity through the glycocalyx will also be v = 4 μm/s (based on the cross-sectional area of the unit cell). The Péclet number was calculated with a correction factor (β_f) that accounts for the reduced flow from the endothelial cells blocking part of the down-stream surface:

$$\mathrm{Pe} = \frac{K_c v \delta}{K_d D_\infty \beta_f} \quad . \tag{6.14}$$

with a total endothelial thickness $\delta = \delta_g + 2R_f$. This approach of including a correction factor in Pe had been verified for sieving in the basement membrane, where the surfaces were also partially blocked by cells (Deen 1987, Edwards et al. 1999). A justification for using this approach for the entire endothelial layer, and not just the glycocalyx, is presented in Appendix VI.

The sieving coefficient through a single layer was given by Section 5.1.1:

$$\Theta = \frac{c_F}{c_R} = \frac{\Phi K_c}{1-\left(1-\Phi K_c\right)e^{-\mathrm{Pe}}} \quad . \tag{6.15}$$

The sieving coefficients for layers in series are dependent on the sieving of the downstream layers. For a layer i in a series ($i = 1$ being farthest upstream and $i = n$ being farthest downstream), the sieving coefficient of layer i is (Deen 2006, Haraldsson et al. 2008)

$$\Theta_i = \frac{\Phi_i K_{c,i}}{\Theta_{i+1}\Theta_{i+2}\ldots\Theta_n\left(1-e^{-Pe_i}\right)+\Phi_i K_{c,i} e^{-Pe_i}} \quad . \tag{6.16}$$

While the sieving coefficient of the epithelium is unknown, Equation (6.16) can be rearranged and combined with Equation (6.2) to give

$$\Theta_{endo} = \frac{1-\dfrac{\Theta}{\Phi_{endo} K_{c,endo}}\left(1-e^{-Pe_{endo}}\right)}{e^{-Pe_{endo}}} \tag{6.17}$$

where Θ is the sieving coefficient through the entire capillary wall.

Model Results

The product of the partition coefficient and convective hindrance factor (ΦK_c) was calculated for albumin and an equivalent neutral sphere. The model for K_c in Equations (5.5)-(5.7) was only developed for $r_s/r_f \leq 5$ and fiber volume fractions that resulted in $K_c \geq 0.8$. The ratio of albumin radius to GAG radius (3.6 nm/ 0.5 nm ~ 7) slightly exceeded the range of the model. Fiber densities $\phi > 0.012$ also exceeded the range of K_c for which computational results were available. The results for ΦK_c are shown in Figure 6.4 for a range of fiber volume fractions. The decrease in ΦK_c is due almost exclusively

to the partition coefficient; for the range of volume fractions in Figure 6.4 ($\phi \leq 0.012$), K_c had a minimum value of 0.88. The partition coefficients for anionic albumin were up to a third less than those of an equivalent neutral sphere. Therefore, any resistance towards albumin in the glycocalyx would have a significant contribution from charge interactions.

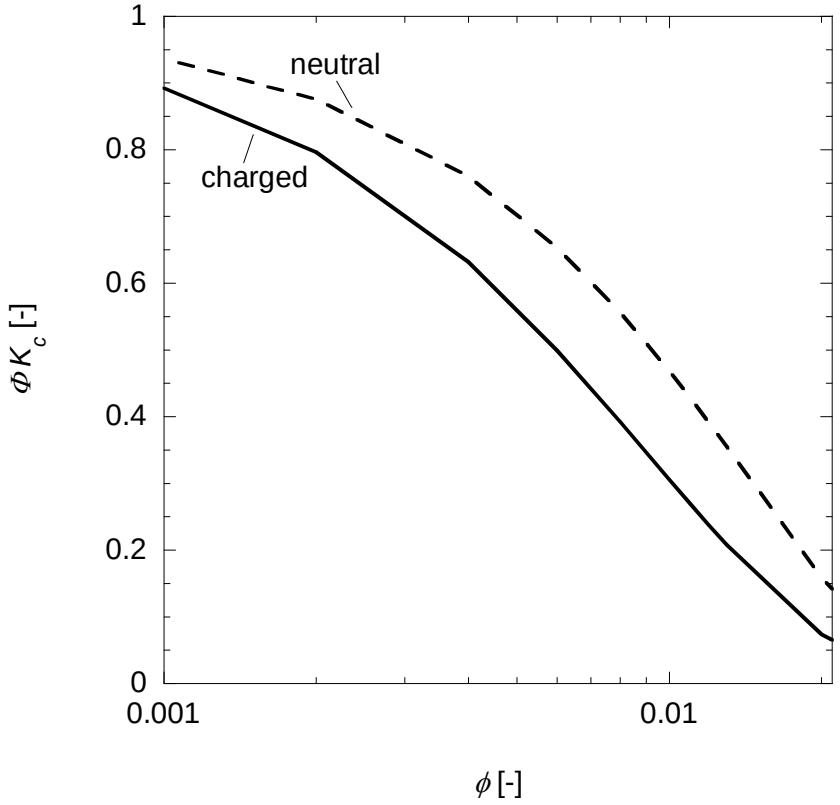

Figure 6.4 Product of the convective hindrance factor (K_c) and partition coefficient (Φ) in the glycocalyx for different fiber densities. Results are shown for albumin (charged; solid line) and a neutral molecule of the same size (dashed line). Model parameters for the solute (albumin) and glycocalyx fibers (GAG) are given in the text.

Sieving coefficients for an isolated endothelium were calculated from Equation (5.2) for a range of Péclet numbers. These sieving coefficients are shown in Figure 6.5 for BSA and an equivalent neutral sphere in matrices of 0.2 and 2 v% GAG, with the corresponding ΦK_c given in Figure 6.4. As expected, the sieving coefficient approaches unity at very small Pe, then decreases to a constant value of ΦK_c at high Pe (Pe $\geq$ 1). The sieving coefficient and ΦK_c are smaller for higher fiber densities and when there is charge repulsion between the solute and fibers.

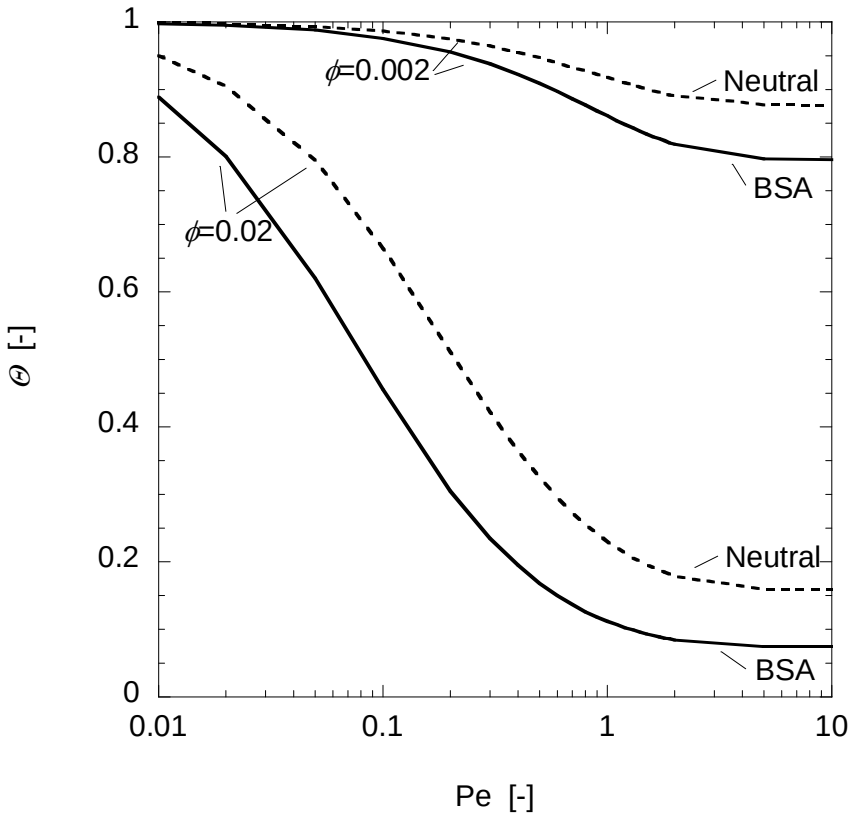

Figure 6.5 Sieving coefficient (Θ) for a single-layer membrane. Curves are shown for fiber densities of $\phi = 0.02$ and 0.002, using Equation (5.2). The values of ΦK_c were calculated from the equations given in the text for BSA at 0.15 M and a neutral sphere of the same radius ($r_s = 3.6$ nm). Model parameters for the solute and fibers (GAG) are given in the text.

The endothelium was then considered as the first layer in a series, where the combined downstream layers have a sieving coefficient Θ_n. Using Equation (6.16), the sieving coefficient was calculated for BSA in 2 v% GAG ($\Phi_1 K_{c,1} = 0.074$). Sieving coefficients are shown in Figure 6.6 for several downstream sieving coefficients. In the case that there is no downstream resistance to sieving ($\Theta_n = 1$), the endothelium behaves as if it were in isolation, identically to Figure 6.5. As the downstream sieving coefficient decreases, there is internal concentration polarization that increases Θ for the upstream layer. When the downstream sieving coefficient is equal to ΦK_c of the endothelium, the selective sieving in the endothelium is balanced to the downstream concentration polarization, such that $\Theta_1 = 1$. When the downstream sieving coefficients is less than ΦK_c of the endothelium, concentration polarization dominates and the sieving coefficient across the endothelium is greater than one. Similar to sieving across a single-layer

membrane, the sieving coefficient of the endothelium has the limits $\Theta_1 \rightarrow 1$ at low Péclet number and $\Theta_1 \rightarrow \Phi_1 K_{c,1}/\Theta_n$ at high Péclet number.

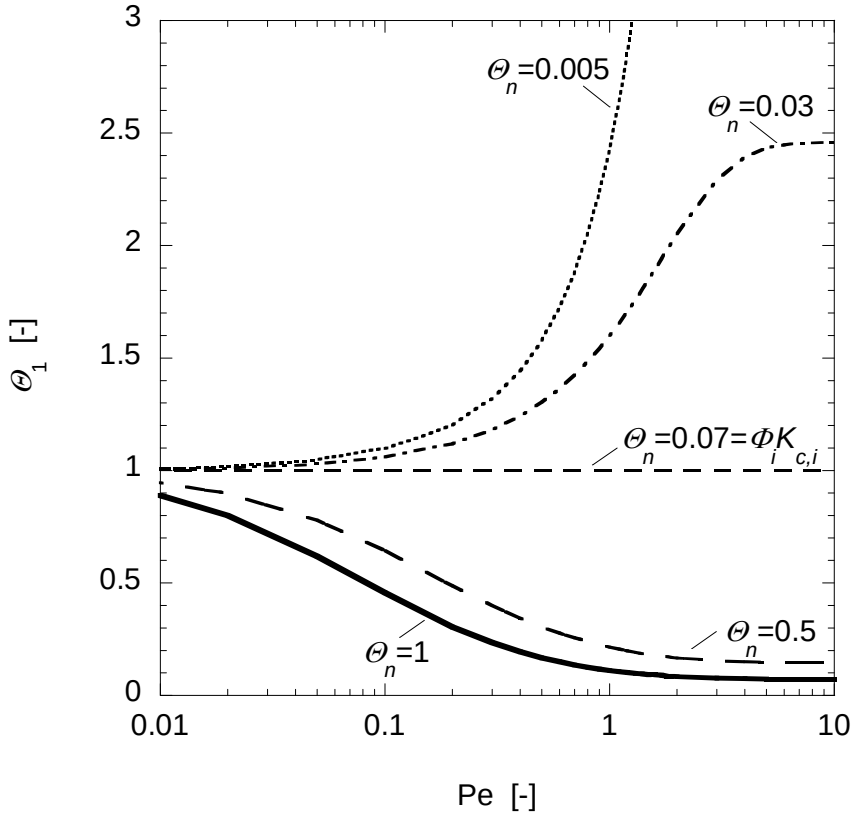

Figure 6.6 Sieving coefficient of layer 1 (Θ_1) for a two-layer membrane with variable downstream sieving coefficient (Θ_n). Curves were calculated from Equation (6.16). The curves are based on BSA in $\phi = 0.02$ GAG at 0.15 M, which gave $\Phi_1 K_{c,1} = 0.074$.

The remaining question is whether the endothelium provides any significant resistance to BSA. As seen in the previous figures, in order for the endothelium to be a selective barrier ($\Theta < 1$), it must have a moderate or high Péclet number and ΦK_c less than the downstream sieving coefficients. Figure 6.7 shows the value of ΦK_c needed for a given Péclet number in order to achieve the specified values of endothelial and capillary wall sieving coefficients. Sieving coefficients were considered across the range of expected values discussed earlier: $\Theta = 10^{-3}$-10^{-4} and $\Theta_{endo} \leq 0.1$. As seen in Figure 6.7, the value of ΦK_c increases with increasing Péclet number until Pe > 1. The value of ΦK_c is relatively insensitive to the sieving coefficient of the endothelium, but is strongly dependent on the overall sieving coefficient. Only when Θ_{endo} becomes large (>0.5) does

ΦK_c begin to increase with increasing Θ_{endo}; however, this is outside the expected range based on physiological observations.

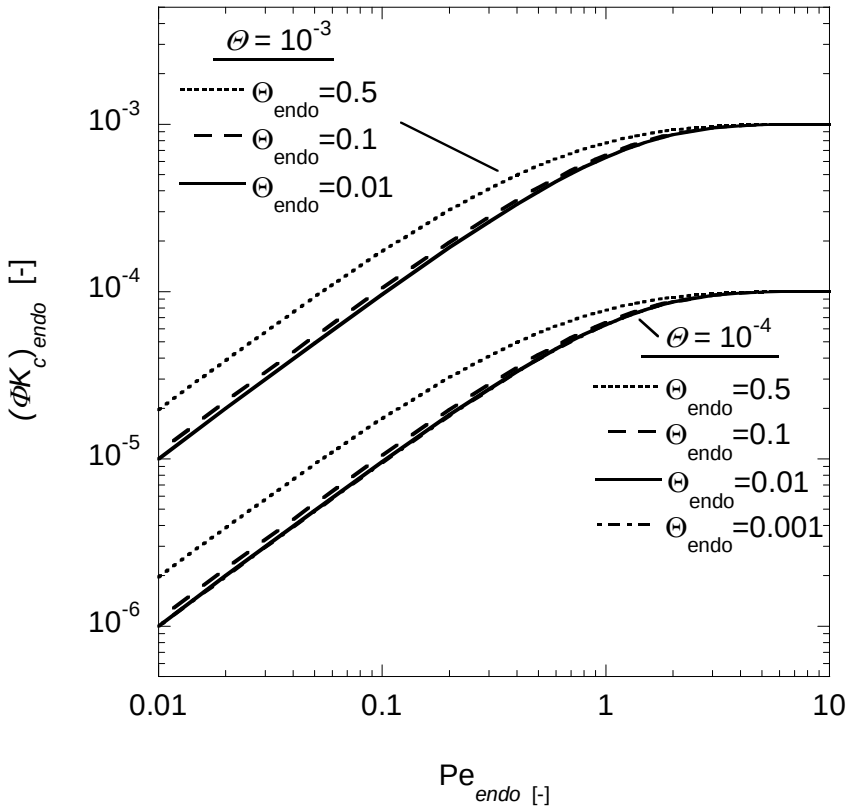

Figure 6.7 Product of the partition coefficient and convective hindrance factor (ΦK_c) in the endothelium that is required to achieve the given sieving coefficients for the endothelium (Θ_{endo}) and capillary wall (Θ) as a function of Péclet number. Calculations are from Equation (6.17). The curves for $\Theta_{endo} = 0.01$ and 0.001 for $\Theta = 10^{-4}$ are nearly identical.

For the combinations of glycocalyx thickness and fiber density that exceeded the hydraulic permeability lower limit in Figure 6.4, the Péclet numbers were 0.03-0.22. These fiber densities corresponded to $\Phi K_c = 0.89$-0.003 for BSA. These values of Pe and ΦK_c fall well above the curves in Figure 6.7, implying that the endothelium does not contribute to the overall sieving coefficient. However, a significant limitation in these estimates is the calculation of the hindrance coefficients K_c and K_d. Both the Péclet number and the sieving coefficient are functions of these hindrace coefficients. However, fiber models for hindrance coefficients are currently limited to low fiber volume fractions where $K_c \geq 0.8$-0.9 ($\phi \leq 0.012$ for BSA in agarose). Many of the possible fiber densities from Figure 6.3 fall beyond this range (up to $\phi = 0.04$). For a periodic square array of

GAG fibers, these fibers would have center-to-center spacing as small at 4.4 nm, which would be very restrictive to BSA with a 3.6 nm radius. In pore theory, it is under these tightly fitting conditions that the ratio K_c/K_d is highest, exceeding 10 under some conditions (Deen 1987). High values of K_c/K_d result in a high Péclet number. Higher fiber densities also result in a small value of ΦK_c. For this reason, it is very possible that the fiber densities predicted by the hydraulic permeability model in Figure 6.3 could result in a selective endothelium. However, without fiber models that are able to predict hindrance factors for tightly-fitting solutes, we are unable to determined the role of the endothelium in the sieving across the glomerular capillary wall.

6.2. Summary and Future Work

6.2.1. Research Summary

This research investigated hindered transport in biologically-relevant fibrous membranes, focusing on the role of fiber and solute charges. Experiments were performed in agarose-GAG hydrogels. Agarose is a nearly neutral fiber that provided structural integrity to the hydrogel membranes. Chondroitin sulfate, a 50 kDa anionic GAG representative of GAGs and proteoglycans in a variety of biological materials, was covalently bound to agarose. A systematic investigation of the CDAP reaction used to attach GAG increased the bound GAG content within the membranes, as well as verified that the bound GAG was spatially uniform.

Darcy (hydraulic) permeability measurements through the agarose-GAG membranes investigated the effects of solution ionic strength and membrane GAG content. Electrokinetic coupling within charged membranes induced a streaming potential which reduced the open-circuit hydraulic permeability of the membranes. This reduction was greatest at low ionic strength and in gels with high GAG contents, where charge effects were greatest. No reduction in Darcy permeability was observed in gels that only contained neutral agarose.

The permeability of several macromolecules (anionic BSA and neutral Ficoll) were measured in the agarose-GAG membranes. Specifically, equilibrium partition coefficients and convective sieving coefficients were measured as a function of ionic strength and Ficoll Stokes-Einstein radius. At high ionic strengths, there was a slight

decrease in permeability by the addition of small fractions of GAG (0.2 v% GAG, versus 4 v% agarose). Both the partition coefficient and sieving coefficient in agarose-GAG membranes decreased by nearly half for BSA in 0.011 M versus 0.1 M buffer. However, sieving and partitioning in systems that did not have charge interactions (agarose / BSA, agarose-GAG / Ficoll, agarose / Ficoll) generally did not vary with ionic strength. There was a strong correlation between the decreases in the partition coefficient and the sieving coefficient for BSA in agarose-GAG gels, supporting the hypothesis that charge interactions can be neglected in the convective hindrance coefficient (ratio of the sieving coefficient to partition coefficient at high Péclet number).

Microstructural models for fibrous materials correlated the physical properties of the solutes and membranes to the measured properties (hydraulic permeability, partition coefficient, and sieving coefficient). The literature provided several microstructural models for hydraulic permeability, which were adapted to the agarose-GAG membranes used in this research. The main complication encountered was the lack of a rigorous model for the permeability of a mixture of fibers. Several "mixing rules" were evaluated to compare the hydraulic permeabilities predicted by monodisperse fiber models to simulations of polydisperse systems. A simulation of flow past ordered arrays of two types of charged fibers was developed to provide data for evaluating the mixing rules in charged systems. Weighting the hydraulic resistivities by the fiber volume fractions was found to provide the most reliable estimates for multi-fiber systems with different fiber diameters and charges.

Microstructural models provided good agreement with hydraulic permeability measurements at high ionic strengths (neutral conditions). However, a macroscopic model of electrokinetic coupling provided much better agreement with the experimental Darcy permeability than the microstructural model, suggesting that improvements are needed in the way charge was treated in my agarose-GAG model. Microstructural models were in good agreement with partition coefficients in both neutral systems and charged systems over a range of ionic strengths. A microstructural model for convective sieving in a mixture of fibers is currently not available.

6.2.2. Future Work

While it has been common to perform transport studies in porous membranes, fibrous membranes tend to be more relevant to biological systems. A limited number of experiments have been performed in *well-characterized*, *charged* fibrous materials. Additional studies in such materials (with mono- or polydisperse fibers) would provide useful information to validate existing microstructural models. The agarose-GAG hydrogels used in this study had heterogeneities in fiber density due to the gelation mechanism of agarose. Identification of a structurally stable fibrous material with a homogeneous fiber density would be beneficial, as it would simplify comparisons between experimental results and the models. One potential material that might meet this criteria is polyacrylamide gel (Kapur et al. 1997); additional chemistry may be available to functionalize the polyacrylamide fibers with charged groups.

The microstructural model for hydraulic permeability in agarose-GAG gels under-predicted the reduction in permeability from electrokinetic coupling. It was speculated that this was due to the handling of charge in a heterogeneous material with two regions of different charge density (eg - imposing no-current conditions in each sub-region and assuming that electrical potentials were non-interacting between regions). Further investigations into this problem may be beneficial.

Macromolecule permeability was studied in this thesis research with BSA (an anionic globular protein) and with Ficolls (neutral, spherical sugars). Additional permeability studies with other solutes would provide useful information on the effects of solute size and charge. Permeability studies in denser fibrous systems would allow for the use of other well-characterized anionic globular proteins (eg – lactalbumin, ovalbumin) and neutral and anionic forms of horseradish peroxidase (HRP). HRP is a particularly appealing solute, since the ability to add negatively charged groups allows the solute surface charge density to be varied independently of solute radius.

The current microstructural models for partitioning seem adequate for systems that have charged solute interactions with a single type of charged fiber. The model would have to be extended for a mixture of multiple types of charged fibers. Microstructural models for convective hindrance are currently very limited. Simulations of sieving in arrays of charged fibers will help show more rigorously if and when charge interactions

can be neglected in the convective hindrance factor. Models for the convective hindrance factor that allow for multiple types of fibers would also be useful for understanding sieving in a variety of biological materials. Convective hindrance models for fibers would benefit from being extended to high fiber volume fractions where there is significant hindrance between the fibers and the solute; such a model would be beneficial for both periodic and random fiber arrays.

Appendix A. AGAROSE-GAG MEMBRANE SYNTHESIS DATA

The following tables report the values of experimental data used in the figures in Chapter 1.

Table A.1 Active cyanate ester site degradation during protonation, aqueous wash and attachment process steps, shown in Figure 2.9.

Sample Description	**Sites/Gel** *(nmol/gel)*	**Gel Width** *(μm)*	**Sites/Fiber** *(nmol/mg)*
5 min HCl	1,414	75	2,406
	1,362	76	2,260
30 min HCl	1,270	73	2,278
	1,246	77	2,017
30 min HCl + 5 min H_2O	1,267	73	2,272
	1,205	69	2,423
30 min HCl + 25 min H_2O	1,002	70	1,957
	1,166	72	2,149
30 min HCl + 45 min H_2O	817	70	1,595
	747	71	1,417
30 min HCl + 45 min H_2O	473	72	872
+ 1 hr blank attachment	389	73	698

Table A.2 Agarose-GAG gel synthesis conditions and bound GAG content for variable CDAP activation conditions, as shown in Figure 2.7.

Description		Activation Conditions									Attachment Conditions												Assay Results	
Variable	Values*	batch date	agarose type	agarose v%	gel thickness	CDAP/gel	TEA time	HCl/H2O temp	HCl conc.	HCl/H2O time	air exp. time	GAG type	GAG conc.	soln. type	soln. conc.	ionic conc.	pH	GAG time	mixing speed	temp.	support	misc.	Rel. GAG Content	std. dev.
(-)	(-)	(-)	(-)	(%)	(μm)	(g)	(min)	(C)	(N)	(min)/(min)	(min)	(-)	(g/L)	(-)	(M)	(M)	(-)	(hr)	(rpm)	(C)	(-)	(-)	(μg/mg)	(μg/mg)
"Baseline"			VI	3	70-80	0.1	5	4	0.05	~30/45	0	CS-A	1	NaHCO3	0.1	0.1	8.4	40	200	4	rnd. Cassette			
baseline																								
	14-Feb	14-Feb-05	VI	3	70-80	0.1	5	4	0.05	40/45	0	CS-A	1	NaHCO3	0.1	0.1	8.4	40	200	4	rnd. Cassette	"baseline"	65.9	3.3
	14-Mar	14-Mar-05	VI	3	70-80	0.1	5	>4	0.05	40/45	0	CS-A	1	NaHCO3	0.1	0.1	8.4	40	200	4	rnd. Cassette	"baseline"	47.8	1.8
	8-Apr	8-Apr-05	VI	3	70-80	0.1	5	4	0.05	35/45	0	CS-A	1	NaHCO3	0.1	0.1	8.4	40	200	4	rnd. Cassette	"baseline"	63.5	5.6
	3-May	3-May-05	VI	3	70-80	0.1	5	4	0.05	35/45	0	CS-A	1	NaHCO3	0.1	0.1	8.4	40	200	4	rnd. Cassette	"baseline"	72.2	6.4
	11-May	11-May-05	VI	3	70-80	0.1	5	4	0.05	35/45	0	CS-A	1	NaHCO3	0.1	0.1	8.4	40	200	4	rnd. Cassette	"baseline"	72.6	2.0
	18-May	18-May-05	VI	3	70-80	0.1	5	4	0.05	35/45	0	CS-A	1	NaHCO3	0.1	0.1	8.4	**24**	200	4	rnd. Cassette	"baseline"	59.0	9.0
	2-Jun	2-Jun-05	VI	3	70-80	0.1	5	>4	0.05	35/45	0	CS-A	1	NaHCO3	0.1	0.1	8.4	40	200	4	rnd. Cassette	"baseline"	51.8	6.3
	24-Jun	24-Jun-05	VI	3	70-80	0.1	5	4	0.05	35/45	0	CS-A	1	NaHCO3	0.1	0.1	8.4	40	200	4	rnd. Cassette	"baseline"	72.4	1.3
	1-Jul	1-Jul-05	VI	3	70-80	0.1	5	4	0.05	35/45	0	CS-A	1	NaHCO3	0.1	0.1	8.4	40	200	4	rnd. Cassette	"baseline"	70.0	4.4
	15-Jul	15-Jul-05	VI	3	70-80	0.1	5	4	0.05	35/45	0	CS-A	1	NaHCO3	0.1	0.1	8.4	40	200	4	rnd. Cassette	"baseline"	51.3	15.4
	5-Aug	5-Aug-05	VI	3	70-80	0.1	5	4	0.05	35/45	0	CS-A	1	NaHCO3	0.1	0.1	8.4	40	200	4	rnd. Cassette	"baseline"	69.9	4.8
agarose type																								
	I-B	14-Mar-05	**I-B**	3	70-80	0.1	5	>4	0.05	40/45	0	CS-A	1	NaHCO3	0.1	0.1	8.4	40	200	4	rnd. Cassette		50.4	4.7
	VI	14-Mar-05	VI	3	70-80	0.1	5	>4	0.05	40/45	0	CS-A	1	NaHCO3	0.1	0.1	8.4	40	200	4	rnd. Cassette	"baseline"	47.8	1.8
mesh type																								
	polyester	24-Jun-05	VI	3	70-80	0.1	5	4	0.05	35/45	0	CS-A	1	NaHCO3	0.1	0.1	8.4	40	200	4	rnd. Cassette	"baseline"	72.4	1.3
	nylon	24-Jun-05	VI	3	70-80	0.1	5	4	0.05	35/45	0	CS-A	1	NaHCO3	0.1	0.1	8.4	40	200	4	rnd. Cassette	**nylon mesh**	57.2	13.5
CDAP conc.																								
	0.05 g/gel	7-Jul-05	VI	3	70-80	**0.05**	5	4	0.05	35/45	0	CS-A	1	NaHCO3	0.1	0.1	8.4	40	200	4	rnd. Cassette		56.7	2.2
	0.1 g/gel	14-Feb-05	VI	3	70-80	0.1	5	4	0.05	40/45	0	CS-A	1	NaHCO3	0.1	0.1	8.4	40	200	4	rnd. Cassette	"baseline"	65.9	3.3
	0.1 g/gel	8-Apr-05	VI	3	70-80	0.1	5	4	0.05	35/45	0	CS-A	1	NaHCO3	0.1	0.1	8.4	40	200	4	rnd. Cassette	"baseline"	63.5	5.6
	0.1 g/gel	24-Jun-05	VI	3	70-80	0.1	5	4	0.05	35/45	0	CS-A	1	NaHCO3	0.1	0.1	8.4	40	200	4	rnd. Cassette	"baseline"	72.4	1.3
	0.2 g/gel	9-Mar-05	VI	3	70-80	**0.2**	5	4	0.05	35/45	0	CS-A	1	NaHCO3	0.1	0.1	8.4	40	200	4	rnd. Cassette		77.0	7.6
activation time																								
	2 min	1-Oct-04	VI	**4**	70-80	0.1	**2**	4	0.05	40/45	0	CS-A	1	NaHCO3	0.1	0.1	8.4	**16**	**0**	4	rnd. Cassette		60.2	5.1
	2 min	1-Oct-04	VI	**4**	70-80	0.1	**2**	4	0.05	40/45	0	CS-A	1	NaHCO3	0.1	0.1	8.4	**16**	**0**	4	rnd. Cassette	after 1hr perm.	61.6	9.5
	5 min	14-Feb-05	VI	**4**	70-80	0.1	5	4	0.05	40/45	0	CS-A	1	NaHCO3	0.1	0.1	8.4	**16**	200	4	rnd. Cassette		51.7	3.2

Table A.3 Agarose-GAG gel synthesis conditions and bound GAG content for variable cyanate protonation and aqueous wash conditions, as shown in Figure 2.8.

Description		Activation Conditions										Attachment Conditions										Assay Results	
Variable	Values*	batch date	agarose type	agarose v%	gel thickness	CDAP/gel	TEA time	HCl/H2O temp	HCl conc.	HCl/H2O time	air exp. time	GAG type	GAG conc.	soln. type	soln. conc.	ionic conc.	pH	GAG time	mixing speed	temp.	support	misc.	Rel. GAG Content	std. dev.
(-)	(-)	(-)	(-)	(%)	(μm)	(g)	(min)	(°C)	(N)	(min)/(min)	(min)	(-)	(g/L)	(-)	(M)	(M)	(-)	(hr)	(rpm)	(°C)	(-)	(-)	(μg/mg)	(μg/mg)
"Baseline"			VI	3	70-80	0.1	5	4	0.05	~30/45	0	CS-A	1	NaHCO3	0.1	0.1	8.4	40	200	4	rnd. Cassette			
acid wash																								
	0.05 N	3-May-05	VI	3	70-80	0.1	5	4	0.05	35/45	0	CS-A	1	NaHCO3	0.1	0.1	8.4	40	200	4	rnd. Cassette	"baseline"	72.2	6.4
	0.2 N	3-May-05	VI	3	70-80	0.1	5	4	**0.2**	35/45	0	CS-A	1	NaHCO3	0.1	0.1	8.4	40	200	4	rnd. Cassette		48.6	0.4
acid wash time																								
	10 min	18-May-05	VI	3	70-80	0.1	5	4	0.05	**10/5**	0	CS-A	1	NaHCO3	0.1	0.1	8.4	24	200	4	rnd. Cassette		86.9	9.3
	30 min	18-May-05	VI	3	70-80	0.1	5	4	0.05	**30/5**	0	CS-A	1	NaHCO3	0.1	0.1	8.4	24	200	4	rnd. Cassette		107.6	6.2
water wash																								
	14 min	3-May-05	VI	3	70-80	0.1	5	4	0.05	**35/14**	0	CS-A	1	NaHCO3	0.1	0.1	8.4	40	200	4	rnd. Cassette		109.7	0.3
	45 min	3-May-05	VI	3	70-80	0.1	5	4	0.05	35/45	0	CS-A	1	NaHCO3	0.1	0.1	8.4	40	200	4	rnd. Cassette	"baseline"	72.2	6.4
	5 min	18-May-05	VI	3	70-80	0.1	5	4	0.05	**30/5**	0	CS-A	1	NaHCO3	0.1	0.1	8.4	24	200	4	rnd. Cassette		107.6	6.2
	45 min	18-May-05	VI	3	70-80	0.1	5	4	0.05	35/45	0	CS-A	1	NaHCO3	0.1	0.1	8.4	24	200	4	rnd. Cassette	"baseline"	59.0	9.0
wash temp																								
	0°C (ice)	18-May-05	VI	3	70-80	0.1	5	**0**	0.05	35/45	0	CS-A	1	NaHCO3	0.1	0.1	8.4	24	200	4	rnd. Cassette		104.7	5.9
	4°C (fridge)	18-May-05	VI	3	70-80	0.1	5	4	0.05	35/45	0	CS-A	1	NaHCO3	0.1	0.1	8.4	24	200	4	rnd. Cassette	"baseline"	59.0	9.0
wash temp + time																								
	4°C / 30+45 min	2-Jun-05	VI	3	70-80	0.1	5	>4	0.05	35/45	0	CS-A	1	NaHCO3	0.1	0.1	8.4	40	200	4	rnd. Cassette	"baseline"	51.8	6.3
	0°C / 10+5 min	2-Jun-05	VI	3	70-80	0.1	5	**0**	0.05	**10/5**	0	CS-A	1	NaHCO3	0.1	0.1	8.4	40	200	4	rnd. Cassette		114.6	6.8
	4°C / 30+45 min	5-Aug-05	VI	3	70-80	0.1	5	4	0.05	35/45	0	CS-A	1	NaHCO3	0.1	0.1	8.4	40	200	4	rnd. Cassette	"baseline"	69.9	4.8
	0°C / 10+15 min	5-Aug-05	VI	3	70-80	0.1	5	**0**	0.05	**10/15**	0	CS-A	1	NaHCO3	0.1	0.1	8.4	40	200	4	rnd. Cassette		101.9	1.6
air exposure																								
	0 min	2-Jun-05	VI	3	70-80	0.1	5	>4	0.05	35/45	0	CS-A	1	NaHCO3	0.1	0.1	8.4	40	200	4	rnd. Cassette	"baseline"	51.8	6.3
	10 min	2-Jun-05	VI	3	70-80	0.1	5	>4	0.05	35/45	**10**	CS-A	1	NaHCO3	0.1	0.1	8.4	40	200	4	rnd. Cassette		61.7	3.4

Table A.4 Agarose-GAG gel synthesis conditions and bound GAG content for variable GAG attachment conditions affecting binding kinetics, as shown in Figure 2.5.

Description		Activation Conditions									Attachment Conditions											Assay Results	
Variable	Values*	batch date	agarose type	agarose v/v%	gel thickness	CDAP/gel	TEA time	HCl/H2O temp	HCl conc.	HCl/H2O time	air exp. time	GAG type	GAG conc.	soln. type	soln. conc.	ionic conc.	pH	GAG time	mixing speed	temp.	support	misc.	Rel. GAG Content	std. dev.
(-)	(-)	(-)	(-)	(%)	(μm)	(g)	(min)	(°C)	(N)	(min/min)	(min)	(-)	(g/L)	(-)	(M)	(M)	(-)	(hr)	(rpm)	(°C)	(-)	(-)	(μg/mg)	(μg/mg)
"Baseline"		VI	3	70-80	0.1	5	4	0.05	-30/45	0	CS-A	1	NaHCO3	0.1	0.1	8.4	40	200	4	rnd. Cassette			
within-Rx variance																							
	Jar #1	3-May-05	VI	3	70-80	0.1	5	4	0.05	35/45	0	CS-A	1	NaHCO3	0.1	0.1	8.4	40	200	4	rnd. Cassette	"baseline"	72.2	6.4
	Jar #2	3-May-05	VI	3	70-80	0.1	5	4	0.05	35/45	0	CS-A	1	NaHCO3	0.1	0.1	8.4	40	200	4	rnd. Cassette	"baseline"	70.0	0.9
	Jar #3	3-May-05	VI	3	70-80	0.1	5	4	0.05	35/45	0	CS-A	1	NaHCO3	0.1	0.1	8.4	40	200	4	rnd. Cassette	"baseline"	76.7	4.1
GAG conc.																								
	1 g/L	14-Mar-05	VI	3	70-80	0.1	5	>4	0.05	40/45	0	CS-A	1	NaHCO3	0.1	0.1	8.4	40	200	4	rnd. Cassette	"baseline"	47.8	1.8
	5 g/L	14-Mar-05	VI	3	70-80	0.1	5	>4	0.05	40/45	0	CS-A	**5**	NaHCO3	0.1	0.1	8.4	40	200	4	rnd. Cassette		42.8	3.1
	0.2 g/L	8-Apr-05	VI	3	70-80	0.1	5	4	0.05	35/45	0	CS-A	**0.2**	NaHCO3	0.1	0.1	8.4	40	200	4	rnd. Cassette	"baseline"	39.5	10.4
	1 g/L	8-Apr-05	VI	3	70-80	0.1	5	4	0.05	35/45	0	CS-A	1	NaHCO3	0.1	0.1	8.4	40	200	4	rnd. Cassette		63.5	5.6
	0.2 g/L	2-Jun-05	VI	3	70-80	0.1	5	>4	0.05	35/45	0	CS-A	**0.2**	NaHCO3	0.1	0.1	8.4	40	200	4	rnd. Cassette		16.7	5.3
	1 g/L	2-Jun-05	VI	3	70-80	0.1	5	>4	0.05	35/45	0	CS-A	1	NaHCO3	0.1	0.1	8.4	40	200	4	rnd. Cassette	"baseline"	51.8	6.3
	0.2 g/L	1-Jul-05	VI	3	70-80	0.1	5	4	0.05	35/45	0	CS-A	**0.2**	NaHCO3	0.1	0.1	8.4	40	200	4	rnd. Cassette		48.0	3.4
	0.5 g/L	1-Jul-05	VI	3	70-80	0.1	5	4	0.05	35/45	0	CS-A	**0.5**	NaHCO3	0.1	0.1	8.4	40	200	4	rnd. Cassette		70.2	4.9
	1 g/L	1-Jul-05	VI	3	70-80	0.1	5	4	0.05	35/45	0	CS-A	**1**	NaHCO3	0.1	0.1	8.4	40	200	4	rnd. Cassette	"baseline"	70.0	4.4
	2 g/L	1-Jul-05	VI	3	70-80	0.1	5	4	0.05	35/45	0	CS-A	**2**	NaHCO3	0.1	0.1	8.4	40	200	4	rnd. Cassette		76.0	1.5
	5 g/L	1-Jul-05	VI	3	70-80	0.1	5	4	0.05	35/45	0	CS-A	**5**	NaHCO3	0.1	0.1	8.4	40	200	4	rnd. Cassette		93.2	29.1
attachment soln. type																								
	$NaHCO_3$	14-Mar-05	VI	3	70-80	0.1	5	>4	0.05	40/45	0	CS-A	1	NaHCO3	0.1	0.1	8.4	40	200	4	rnd. Cassette	"baseline"	47.8	1.8
	bicine	14-Mar-05	VI	3	70-80	0.1	5	>4	0.05	40/45	0	CS-A	1	**bicine**	0.1	0.1	8.4	40	200	4	rnd. Cassette		16.9	2.7
	$NaHCO_3$ (pH 9)	14-Mar-05	VI	3	70-80	0.1	5	>4	0.05	40/45	0	CS-A	1	NaHCO3	0.1	0.1	**9.0**	40	200	4	rnd. Cassette		36.0	13.5
	bicine (pH 9)	14-Mar-05	VI	3	70-80	0.1	5	>4	0.05	40/45	0	CS-A	1	**bicine**	0.1	0.1	**9.0**	40	200	4	rnd. Cassette		14.6	9.3
	$NaHCO_3$	8-Apr-05	VI	3	70-80	0.1	5	4	0.05	35/45	0	CS-A	1	NaHCO3	0.1	0.1	8.4	40	200	4	rnd. Cassette	"baseline"	63.5	5.6
	phosphate	8-Apr-05	VI	3	70-80	0.1	5	4	0.05	35/45	0	CS-A	1	**phosphate**	0.1	0.1	8.4	40	200	4	rnd. Cassette		23.1	0.9
attachment pH																								
	8.4	14-Mar-05	VI	3	70-80	0.1	5	>4	0.05	40/45	0	CS-A	1	NaHCO3	0.1	0.1	8.4	40	200	4	rnd. Cassette	"baseline"	47.8	1.8
	9.0	14-Mar-05	VI	3	70-80	0.1	5	>4	0.05	40/45	0	CS-A	1	NaHCO3	0.1	0.1	**9.0**	40	200	4	rnd. Cassette		36.0	13.5
	8.4 (bicine)	14-Mar-05	VI	3	70-80	0.1	5	>4	0.05	40/45	0	CS-A	1	**bicine**	0.1	0.1	8.4	40	200	4	rnd. Cassette		16.9	2.7
	9 (bicine)	14-Mar-05	VI	3	70-80	0.1	5	>4	0.05	40/45	0	CS-A	1	**bicine**	0.1	0.1	**9.0**	40	200	4	rnd. Cassette		14.6	9.3
	7.0	8-Apr-05	VI	3	70-80	0.1	5	4	0.05	35/45	0	CS-A	1	NaHCO3	0.1	0.1	**7.0**	40	200	4	rnd. Cassette	"baseline"	69.0	0.2
	8.4	8-Apr-05	VI	3	70-80	0.1	5	4	0.05	35/45	0	CS-A	1	NaHCO3	0.1	0.1	8.4	40	200	4	rnd. Cassette		63.5	5.6
attach. time																								
	16 hr	14-Feb-05	VI	3	70-80	0.1	5	4	0.05	40/45	0	CS-A	1	NaHCO3	0.1	0.1	8.4	**16**	200	4	rnd. Cassette	"baseline"	58.4	4.6
	40 hr	14-Feb-05	VI	3	70-80	0.1	5	4	0.05	40/45	0	CS-A	1	NaHCO3	0.1	0.1	8.4	40	200	4	rnd. Cassette		65.9	3.3
	1 hr	11-May-05	VI	3	70-80	0.1	5	4	0.05	35/45	0	CS-A	1	NaHCO3	0.1	0.1	8.4	1	200	4	rnd. Cassette		57.8	8.7
	40 hr	11-May-05	VI	3	70-80	0.1	5	4	0.05	35/45	0	CS-A	1	NaHCO3	0.1	0.1	8.4	40	200	4	rnd. Cassette	"baseline"	72.6	2.0
	0.5 hr	13-Jun-05	VI	3	70-80	0.1	5	4	0.05	**35/0**	0	CS-A	1	NaHCO3	0.1	0.1	8.4	**0.5**	200	4	rnd. Cassette		81.8	8.7
	1 hr	13-Jun-05	VI	3	70-80	0.1	5	4	0.05	**35/0**	0	CS-A	1	NaHCO3	0.1	0.1	8.4	**1**	200	4	rnd. Cassette		81.5	9.9
	6 hr	13-Jun-05	VI	3	70-80	0.1	5	4	0.05	**35/0**	0	CS-A	1	NaHCO3	0.1	0.1	8.4	**6**	200	4	rnd. Cassette		102.2	9.0
	40 hr	13-Jun-05	VI	3	70-80	0.1	5	4	0.05	**35/0**	0	CS-A	1	NaHCO3	0.1	0.1	8.4	**40**	200	4	rnd. Cassette		96.1	1.0
	6 min	15-Jul-05	VI	3	70-80	0.1	5	4	0.05	35/45	0	CS-A	1	NaHCO3	0.1	0.1	8.4	**0.1**	200	4	rnd. Cassette		16.3	0.8
	10 min	15-Jul-05	VI	3	70-80	0.1	5	4	0.05	35/45	0	CS-A	1	NaHCO3	0.1	0.1	8.4	**0.17**	200	4	rnd. Cassette		21.2	1.2
	30 min	15-Jul-05	VI	3	70-80	0.1	5	4	0.05	35/45	0	CS-A	1	NaHCO3	0.1	0.1	8.4	**0.5**	200	4	rnd. Cassette		34.7	4.8
	40 hr	15-Jul-05	VI	3	70-80	0.1	5	4	0.05	35/45	0	CS-A	1	NaHCO3	0.1	0.1	8.4	40	200	4	rnd. Cassette	"baseline"	51.3	15.4
attach. temp																								
	0°C -> 4°C	2-Jun-05	VI	3	70-80	0.1	5	>4	0.05	35/45	0	CS-A	1	NaHCO3	0.1	0.1	8.4	40	200	**0->4**	rnd. Cassette		57.2	25.8
	4°C	2-Jun-05	VI	3	70-80	0.1	5	>4	0.05	35/45	0	CS-A	1	NaHCO3	0.1	0.1	8.4	40	200	4	rnd. Cassette	"baseline"	51.8	6.3
	0°C (30 min)	15-Jul-05	VI	3	70-80	0.1	5	4	0.05	35/45	0	CS-A	1	NaHCO3	0.1	0.1	8.4	**0.5**	200	**0**	rnd. Cassette		48.1	6.7
	4°C (30 min)	15-Jul-05	VI	3	70-80	0.1	5	4	0.05	35/45	0	CS-A	1	NaHCO3	0.1	0.1	8.4	**0.5**	200	**0**	rnd. Cassette		34.7	4.8
	0°C	15-Jul-05	VI	3	70-80	0.1	5	4	0.05	35/45	0	CS-A	1	NaHCO3	0.1	0.1	8.4	40	200	**0**	rnd. Cassette		43.0	1.3
	4°C	15-Jul-05	VI	3	70-80	0.1	5	4	0.05	35/45	0	CS-A	1	NaHCO3	0.1	0.1	8.4	40	200	4	rnd. Cassette	"baseline"	51.3	15.4

Table A.5 Agarose-GAG gel synthesis conditions and bound GAG content for variable GAG attachments conditions affecting GAG transport, as shown in Figure 2.6.

Description		Activation Conditions								Attachment Conditions												Assay Results	
Variable	Values*	batch date	agarose type	agarose v%	gel thickness	CDAP/gel	TEA time	HCl/H_2O temp	HCl conc.	HCl/H_2O time	air exp. time	GAG type	GAG conc.	soln. type	soln. conc.	ionic conc.	pH	GAG time	mixing speed	temp.	support	misc.	Rel. GAG Content	std. dev.
(-)	(-)	(-)	(-)	(%)	(μm)	(g)	(min)	(°C)	(N)	(mm)/(min)	(min)	(-)	(g/L)	(-)	(M)	(M)	(-)	(hr)	(rpm)	(°C)	(-)	(-)	(μg/mg)	(μg/mg)
"Baseline"			VI	3	70-80	0.1	5	4	0.05	~30/45	0	CS-A	1	NaHCO3	0.1	0.1	8.4	40	200	4	rnd. Cassette			
agarose content																								
	2v%	14-Feb-05	VI	**2**	70-80	0.1	5	4	0.05	40/45	0	CS-A	1	NaHCO3	0.1	0.1	8.4	**16**	200	4	rnd. Cassette	no blank avail.	75.7	9.8
	3v%	14-Feb-05	VI	3	70-80	0.1	5	4	0.05	40/45	0	CS-A	1	NaHCO3	0.1	0.1	8.4	**16**	200	4	rnd. Cassette		58.4	4.6
	4v%	14-Feb-05	VI	**4**	70-80	0.1	5	4	0.05	40/45	0	CS-A	1	NaHCO3	0.1	0.1	8.4	**16**	200	4	rnd. Cassette	no blank avail.	51.7	3.2
	4v%*	1-Oct-04	VI	**4**	70-80	0.1	**2**	4	0.05	40/45	0	CS-A	1	NaHCO3	0.1	0.1	8.4	**16**	**0**	4	rnd. Cassette		60.2	5.1
	4v%*	1-Oct-04	VI	**4**	70-80	0.1	**2**	4	0.05	40/45	0	CS-A	1	NaHCO3	0.1	0.1	8.4	**16**	**0**	4	rnd. Cassette	after 1hr perm.	61.6	9.5
	2v%	8-Apr-05	VI	**2**	70-80	0.1	5	4	0.05	35/45	0	CS-A	1	NaHCO3	0.1	0.1	8.4	40	200	4	rnd. Cassette		73.0	6.7
	3v%	8-Apr-05	VI	3	70-80	0.1	5	4	0.05	35/45	0	CS-A	1	NaHCO3	0.1	0.1	8.4	40	200	4	rnd. Cassette	"baseline"	63.5	5.6
	2v%	2-Jun-05	VI	**2**	70-80	0.1	5	>4	0.05	35/45	0	CS-A	1	NaHCO3	0.1	0.1	8.4	40	200	4	rnd. Cassette		42.2	12.6
	3v%	2-Jun-05	VI	3	70-80	0.1	5	>4	0.05	35/45	0	CS-A	1	NaHCO3	0.1	0.1	8.4	40	200	4	rnd. Cassette	"baseline"	51.8	6.3
gel thickness																								
	70-80 .	24-Jun-05	VI	3	70-80	0.1	5	4	0.05	35/45	0	CS-A	1	NaHCO3	0.1	0.1	8.4	40	200	4	rnd. Cassette	"baseline"	72.4	1.3
	110-160 .	24-Jun-05	VI	3	**114-161**	0.1	5	4	0.05	35/45	0	CS-A	1	NaHCO3	0.1	0.1	8.4	40	200	4	rnd. Cassette		38.0	9.9
	310-350 .	24-Jun-05	VI	3	**314-353**	0.1	5	4	0.05	35/45	0	CS-A	1	NaHCO3	0.1	0.1	8.4	40	200	4	rnd. Cassette		13.9	2.4
	50-55 .	5-Aug-05	VI	3	**50-55**	0.1	5	4	0.05	35/45	0	CS-A	1	NaHCO3	0.1	0.1	8.4	40	200	4	rnd. Cassette		59.5	5.0
	70-80 .	5-Aug-05	VI	3	70-80	0.1	5	4	0.05	35/45	0	CS-A	1	NaHCO3	0.1	0.1	8.4	40	200	4	rnd. Cassette	"baseline"	69.9	4.8
GAG type																								
	50 kDa CS-A	1-Jul-05	VI	3	70-80	0.1	5	4	0.05	35/45	0	CS-A	1	NaHCO3	0.1	0.1	8.4	40	200	4	rnd. Cassette	"baseline"	70.0	4.4
	15 kDa Heparin	1-Jul-05	VI	3	70-80	0.1	5	4	0.05	35/45	0	**Heparin**	1	NaHCO3	0.1	0.1	8.4	40	200	4	rnd. Cassette		78.2	11.6
attach. mix spd.																								
	0 rpm	18-May-05	VI	3	70-80	0.1	5	4	0.05	35/45	0	CS-A	1	NaHCO3	0.1	0.1	8.4	24	**0**	4	rnd. Cassette		66.2	8.7
	200 rpm	18-May-05	VI	3	70-80	0.1	5	4	0.05	35/45	0	CS-A	1	NaHCO3	0.1	0.1	8.4	24	200	4	rnd. Cassette	"baseline"	59.0	9.0
attach. temp/ mix																								
	4°C / 200 rpm	3-May-05	VI	3	70-80	0.1	5	4	0.05	35/45	0	CS-A	1	NaHCO3	0.1	0.1	8.4	40	200	4	rnd. Cassette	"baseline"	72.2	6.4
	22°C / 0rpm	3-May-05	VI	3	70-80	0.1	5	4	0.05	35/45	0	CS-A	1	NaHCO3	0.1	0.1	8.4	40	**0**	**22**	rnd. Cassette		54.0	5.3
attachment ionic conc.																								
	0.1 M	14-Feb-05	VI	3	70-80	0.1	5	4	0.05	40/45	0	CS-A	1	NaHCO3	0.1	0.1	8.4	40	200	4	rnd. Cassette	"baseline"	65.9	3.3
	2.0 M (+NaCl)	14-Feb-05	VI	3	70-80	0.1	5	4	0.05	40/45	0	CS-A	1	NaHCO3	0.1	**2**	**8.0**	16	200	4	rnd. Cassette		18.5	2.7
	0.1 M	8-Apr-05	VI	3	70-80	0.1	5	4	0.05	35/45	0	CS-A	1	NaHCO3	0.1	0.1	8.4	40	200	4	rnd. Cassette	"baseline"	63.5	5.6
	0.5 M	8-Apr-05	VI	3	70-80	0.1	5	4	0.05	35/45	0	CS-A	1	NaHCO3	**0.5**	**0.5**	8.4	40	200	4	rnd. Cassette	no NaCl	17.7	3.5
	2.0 M (+NaCl)	8-Apr-05	VI	3	70-80	0.1	5	4	0.05	35/45	0	CS-A	1	NaHCO3	0.1	**2**	8.4	40	200	4	rnd. Cassette		63.8	0.2
	0.05 M	1-Jul-05	VI	3	70-80	0.1	5	4	0.05	35/45	0	CS-A	1	NaHCO3	**0.05**	**0.05**	8.4	40	200	4	rnd. Cassette		61.7	11.0
	0.1 M	1-Jul-05	VI	3	70-80	0.1	5	4	0.05	35/45	0	CS-A	1	NaHCO3	0.1	0.1	8.4	40	200	4	rnd. Cassette	"baseline"	70.0	4.4
	0.5 M	1-Jul-05	VI	3	70-80	0.1	5	4	0.05	35/45	0	CS-A	1	NaHCO3	**0.5**	**0.5**	8.4	40	200	4	rnd. Cassette		21.0	7.8
attach. support																								
	rnd. cassette	18-May-05	VI	3	70-80	0.1	5	4	0.05	35/45	0	CS-A	1	NaHCO3	0.1	0.1	8.4	24	200	4	rnd. Cassette	"baseline"	59.0	9.0
	no cassette	18-May-05	VI	3	70-80	0.1	5	4	0.05	35/45	0	CS-A	1	NaHCO3	0.1	0.1	8.4	24	200	4	**indiv. dish**		63.2	11.2

Table A.6 Parameter estimates for diffusion-reaction model of GAG binding from Table 2.6, with additional comments about the source of parameter values.

Parameter	Value / Range	Comments
$c_{G,0}$	$2\text{x}10^{-8}$ mol/mL *($0.4\text{-}10\text{x}10^{-8}$ mol/mL)*	Determined directly for experiments, using the reported molecular weight of 50 kDa for CS-A. Concentrations used were 0.2-5 g/L.
$c_{A,init}$	$4\text{x}10^{-5}$ mol/mL *($3.2\text{-}4.6\text{x}10^{-5}$ mol/mL)*	Assays of active sites at the beginning of GAG attachment from 4 characteristic batches: 1040±120, 1390±140, 1510±130, 1420±120 μmol active sites/g agarose. 3v% agarose gels are 30.75 mg agarose per mL gel.
δ	$7\text{x}10^{-3}$ cm *($5\text{x}10^{-3}$-10^{-1} m)*	Measured directly in experiments. Average mesh thickness is 70-75 μm. Thickness can be adjusted with a thinner mesh or using spacers during gel casting.
$D_G(0)$	10^{-7} cm^2/s *(10^{-7}–10^{-9} cm^2/s)*	Based on hindered diffusivity experiments in 4% agarose with globular proteins [14-68 kDa; D=3.2-6.4x10^{-7} cm^2/s; D/D_∞=0.53-0.63], spherical Ficolls [21-105 kDa; D=4.4-1.2x10^{-7} cm^2/s; D/D_∞=0.35-0.62](Johnson et al. 1996) [21-105 kDa; D=4.5-1.9x10^{-7} cm^2/s; D/D_∞=0.41-0.56](Kosto and Deen 2004) and dextrans 500-3800 kDa; D=0.4-0.8x10^{-7} cm^2/s; D/D_∞=0.1-0.8](Key and Sellen 1982). Also 2% agarose with proteins [14-68 kDa; D~3-5x10^{-7} cm^2/s; D/D_∞~0.5] and dextran [4.4-2000 kDa; D~0.5-6x10^{-7} cm^2/s; D/D_∞~0.5] (Pluen et al. 1999). Using the Stokes-Einstein relation for the temperature dependence of diffusivity, $D_{\infty,0°C}$=0.465$D_{\infty,25°C}$.
Φ_G	1 *(0.86-1.08)*	Partitioning experiments for GAG and 3 v% unactivated agarose with CS-A concentrations of 0.2-5 g/L in 0.1 $NaHCO_3$. Note that later improvements to the partitioning method, described in Chapter 4, resulted in a lower value in 4 v% agarose.
ϕ_A	$1.2\text{x}10^{-3}$	Molar ratio of assay of bound GAG at end of attachment to actives sites at the beginning of GAG attachment from 4 characteristic batches: 0.9, 1.0, 1.3, 1.4x10^{-3}
$k_1(0)$	$4\text{x}10^4$ mL/mol/s *(10^4-10^5 mL/mol/s)*	Based on amount of bound GAG as short times, assuming constant initial concentration of active sites and unbound GAG concentrations of approximately $c_{A,0}$. From three sets of experiments with attachment times 30-60 minutes, k_1 = 1.1-2.4x10^4 mL/mol/s. From one experiment with attachment times of 6-10 minutes, k_1=3.4-4.4x10^4 mL/mol/s.
k_2	$5\text{x}10^{-5}$ s^{-1} *($2\text{-}7\text{x}10^{-5}$ s^{-1})*	Based on rates of active site degradation in buffer at 0-4°C. Most attachment studies were performed at 4°C.
Group	**Value**	
Da_1	0.2	Damköhler number for binding
Da_2	0.006	Damköhler number for active site degradation
γ_G	0.4	Concentration ratio of maximum free GAG to maximum active sites
$\tau_D = \frac{(\delta/2)^2}{D_G(0)}$	2 minutes	Characteristic diffusion time

Appendix B. HYDRAULIC PERMEABILITY DATA

The following tables summarize the experimental data reported in Chapter 3 for hydraulic permeability.

Table B.1 Darcy permeability (κ) and composition of agarose-dextran gels used in Figure 3.33. Data from [1] has been reinterpreted with the dextran immobilization efficiency reported in reference [2]. Gels were prepared with a dextran equilibration solution of concentration $c_{o,dex}$ and dextran partition coefficient in agarose of Φ_{dex}. Errors reported are one standard deviation.

ϕ_a	ϕ_{dex}	$c_{o,dex}$ [mg/mL]	Φ_{dex}	κ [nm^2]
0.04[1]	0	0	0	255.1(±5.4)
	$2.4(\pm0.1)\times10^{-5}$	10	0.23	241.3(±44.1)
	$2.3(\pm0.2)\times10^{-4}$	30	0.3	157.5(±12.1)
	$7.6(\pm0.4)\times10^{-4}$	50	0.37	77.6(±13.8)
0.04[2]	0	0	0	264.1(±9.5)
	$8.0(\pm0.0)\times10^{-4}$	50	0.39	110.2(±4.2)
	$7.6(\pm0.9)\times10^{-3}$	150	0.43	19.5(±1.4)
0.08[1]	0	0	0	41.1(±1.0)
	$4.4(\pm0.2)\times10^{-6}$	10	0.027	46.7(±0.0)
	$1.6(\pm0.1)\times10^{-4}$	30	0.125	22.9(±0.4)
	$4.7(\pm0.3)\times10^{-4}$	50	0.14	19.0(±2.4)
0.08[2]	0	0	0	34.1(±1.9)
	$8.0(\pm4.0)\times10^{-4}$	50	0.24	16.1(±0.5)
	$1.1(\pm0.1)\times10^{-2}$	150	0.38	2.9(±0.1)

[1] Data from White and Deen (White and Deen 2002), adjusted for immobilization efficiency from Kosto and Deen (Kosto and Deen 2005)

[2] Data from Kosto and Deen (Kosto and Deen 2005)

Table B.2 Composition of phosphate buffered saline (PBS) solutions with pH=7.4 at 25°C. Buffer recipes were calculated by *http://researchlink.labvelocity.com/tools/bufferCalculator.jhtml*. Note that values of moles and grams in the table may not convert exactly due to rounding.

Ionic Strength	***(M)***	**1**	**0.5**	**0.2**	**0.1**	**0.05**	**0.02**	**0.011**
log([I])	*(- -)*	*0.0*	*-0.3*	*-0.7*	*-1.0*	*-1.3*	*-1.7*	*-2.0*
Buffer Strength	*(M)*	0.01	0.01	0.01	0.01	0.005	0.005	0.005
Ionic Strength due to Buffer	*(M)*	0.026	0.026	0.026	0.025	0.012	0.012	0.011
Acid Component	*(mol)*	*0.0017*	*0.0017*	*0.0019*	*0.0022*	*0.0012*	*0.0014*	*0.0015*
NaH_2PO_4-H_2O	*(g)*	0.235	0.235	0.262	0.304	0.166	0.193	0.207
Base Component	*(mol)*	*0.0082*	*0.0082*	*0.0080*	*0.0077*	*0.0037*	*0.0035*	*0.0034*
Na_2HPO_4-$7H_2O$	*(g)*	2.198	2.198	2.145	2.064	0.992	0.938	0.912
Salt	*(mol)*	*0.974*	*0.474*	*0.174*	*0.075*	*0.038*	*0.008*	*0*
KCl	*(g)*	72.59	35.30	12.97	5.553	2.799	0.590	0
Volume H2O	*(mL)*	1000	1000	1000	1000	1000	1000	1000

Table B.3 Transmembrane pressure-dependence of the Darcy permeability of agarose-GAG gels, as shown in Figure 3.39 and Figure 3.40. High GAG gels are 3 v% agarose and 129 mg GAG/g agarose (0.37 v% GAG); agarose gels are 4 v% agarose and no GAG.

Agarose (No GAG); 0.1 M PBS					
	1.5 kPa	5 kPa	10 kPa	15 kPa	20 kPa
Mean [nm^2]	191	162	158	151	159
Std. Dev. [nm^2]	33	26	23	23	14
# Samples	6	7	7	7	4
Minimum [nm^2]	132	122	117	109	141
Maximum [nm^2]	222	187	181	177	173
High GAG; 0.011 M PBS					
	1.5 kPa	5 kPa	10 kPa	15 kPa	20 kPa
Mean [nm^2]	164	142	136	-*	131
Std. Dev. [nm^2]	15	19	29	-*	15
# Samples	4	4	4	-*	4
Minimum [nm^2]	147	124	114	-*	117
Maximum [nm^2]	182	165	176	-*	149
High GAG; 0.1 M PBS					
	1.5 kPa	5 kPa	10 kPa	15 kPa	20 kPa
Mean [nm^2]	279	250	226	-*	223
Std. Dev. [nm^2]	27	23	32	-*	21
# Samples	4	4	4	-*	4
Minimum [nm^2]	251	231	199	-*	205
Maximum [nm^2]	311	280	263	-*	249
High GAG; 1 M PBS					
	1.5 kPa	5 kPa	10 kPa	15 kPa	20 kPa
Mean [nm^2]	357	309	285	-*	269
Std. Dev. [nm^2]	33	21	17	-*	29
# Samples	4	4	4	-*	4
Minimum [nm^2]	325	291	271	-*	244
Maximum [nm^2]	400	338	310	-*	304

*- Permeability not measured.

Table B.4 Darcy permeability (κ) of 3v% agarose-GAG gels over a range of ionic strengths of phosphate buffered saline solution, as shown in Figure 3.43.

Blank (0 mg GAG / g agarose)							
	2 M	1 M	0.2 M	0.1 M	0.05 M	0.02 M	0.011 M
Mean [nm^2]	481	466	452	442	450	455	453
Std. Dev. [nm^2]	26	28	23	22	37	30	24
# Samples	6	6	6	6	6	6	6
Minimum [nm^2]	440	428	412	400	390	412	426
Maximum [nm^2]	508	495	472	459	490	490	481
Medium GAG (54.4±0.3 mg GAG / g agarose)							
	2 M	1 M	0.2 M	0.1 M	0.05 M	0.02 M	0.011 M
Mean [nm^2]	-*	330	300	292	283	256	226
Std. Dev. [nm^2]	-*	49	44	43	42	48	34
# Samples		6	6	6	6	6	6
Minimum [nm^2]		257	236	228	220	199	173
Maximum [nm^2]		386	349	338	326	297	260
High GAG (128.6±13.6 mg GAG / g agarose)							
	2 M	1 M	0.2 M	0.1 M	0.05 M	0.02 M	0.011 M
Mean [nm^2]	285	272	239	217	196	160	138
Std. Dev. [nm^2]	29	30	28	25	21	16	15
# Samples	6	6	6	6	6	6	6
Minimum [nm^2]	252	237	207	191	168	138	115
Maximum [nm^2]	322	311	278	251	222	180	145

* - Permeability not measured.

Appendix C. MACROMOLECULE PARTITIONING AND SIEVING DATA

The following tables summarize the experimental data reported in Chapters 4 and 5.

Table C.1 Transport properties (Θ, Φ, κ) for Ficoll in 4v% agarose – 0.2 v% GAG gels, as a function of Ficoll Stoke's radius. The standard error of a sample is the standard deviation divided by $\sqrt{n}$.

Θ	2.7 nm	3.5 nm	4.5 nm	5.9 nm
Mean	***0.99***	***0.94***	***0.82***	***0.66***
St. Dev.	0.02	0.06	0.17	0.05
n	6	6	5	6
Min	0.94	0.85	0.66	0.62
Max	1.00	1.00	1.00	0.75

Θ'	2.7 nm	3.5 nm	4.5 nm	5.9 nm
Mean	***1.01***	***0.96***	***0.91***	***0.81***
St. Dev.	0.04	0.04	0.12	0.04
n	6	6	5	6
Min	0.97	0.91	0.80	0.77
Max	1.07	1.00	1.08	0.88

κ	2.7 nm	3.5 nm	4.5 nm	5.9 nm
Mean (nm^2)	***164***	***159***	***170***	***168***
St. Dev.	27	16	26	17
n	6	6	5	6
Min	132	133	141	143
Max	215	174	212	196

Pe_{min}	2.7 nm	3.5 nm	4.5 nm	5.9 nm
Mean	***1.7***	***1.5***	***1.7***	***1.7***
St. Dev.	0.2	0.1	0.2	0.2
n	6	6	5	6
Min	1.5	1.3	1.5	1.4
Max	2.2	1.7	2.1	2.0

Φ	2.7 nm	3.5 nm	4.5 nm	5.9 nm
Mean	***0.64***	***0.61***	***0.58***	***0.51***
St. Dev.	0.03	0.06	0.03	0.04
n	11	11	11	10
Min	0.58	0.45	0.54	0.43
Max	0.70	0.67	0.63	0.55

$\Theta/\Phi \sim K_c$	2.7 nm	3.5 nm	4.5 nm	5.9 nm
Mean	***1.53***	***1.53***	***1.41***	***1.30***
St. Dev.	0.09	0.18	0.30	0.14

Table C.2 Transport properties (Θ, Φ, κ) for Ficoll in blank 4v% agarose, as a function of Ficoll Stoke's radius.

Θ	2.7 nm	3.5 nm	4.5 nm	5.9 nm
Mean	***1.00***	***0.96***	***0.98***	***0.83***
St. Dev.	0.00	0.06	0.05	0.12
n	4	5	5	5
Min	1.00	0.86	0.90	0.66
Max	1.00	1.00	1.00	0.96

Θ'	2.7 nm	3.5 nm	4.5 nm	5.9 nm
Mean	***1.06***	***1.00***	***1.00***	***0.91***
St. Dev.	0.02	0.04	0.05	0.08
n	4	5	5	5
Min	1.03	0.95	0.92	0.80
Max	1.07	1.04	1.05	0.98

κ	2.7 nm	3.5 nm	4.5 nm	5.9 nm
Mean (nm^2)	***232***	***279***	***265***	***274***
St. Dev.	28	44	39	57
n	4	5	5	5
Min	212	222	223	215
Max	274	332	306	351

Pe_{min}	2.7 nm	3.5 nm	4.5 nm	5.9 nm
Mean	***1.5***	***2.2***	***1.7***	***1.8***
St. Dev.	0.2	0.5	0.3	0.4
n	4	5	5	5
Min	1.2	1.5	1.4	1.4
Max	1.8	2.9	2.0	2.4

Φ	2.7 nm	3.5 nm	4.5 nm	5.9 nm
Mean	***0.74***	***0.70***	***0.69***	***0.62***
St. Dev.	0.03	0.03	0.03	0.03
n	10	10	10	10
Min	0.66	0.65	0.65	0.56
Max	0.78	0.75	0.74	0.69

$\Theta/\Phi \sim K_c$	2.7 nm	3.5 nm	4.5 nm	5.9 nm
Mean	***1.35***	***1.37***	***1.43***	***1.34***
St. Dev.	0.06	0.11	0.09	0.21

Table C.3 Transport properties (Θ, Φ, κ) for 3.5 nm Ficoll in 4v% agarose – 0.2 v% GAG gels, as a function of ionic strength.

Θ	0.01 M	0.05 M	0.1 M
Mean	***0.74***	***0.92***	***0.94***
St. Dev.	0.07	0.06	0.06
n	5	6	6
Min	0.64	0.81	0.85
Max	0.81	0.96	1.00

Θ'	0.01 M	0.05 M	0.1 M
Mean	***0.85***	***0.96***	***0.96***
St. Dev.	0.06	0.03	0.04
n	5	6	6
Min	0.75	0.91	0.91
Max	0.89	0.98	1.00

κ	0.01 M	0.05 M	0.1 M
Mean (nm^2)	***113***	***161***	***159***
St. Dev.	18	14	16
n	5	6	6
Min	83	141	133
Max	128	184	174

Pe_{min}	0.01 M	0.05 M	0.1 M
Mean	***1.6***	***1.8***	***1.5***
St. Dev.	0.2	0.2	0.1
n	5	6	6
Min	1.2	1.7	1.3
Max	1.8	2.1	1.7

Φ	0.01 M	0.02 M	0.05 M	0.1 M
Mean	***0.46***	***0.54***	***0.64***	***0.63***
St. Dev.	0.06	0.03	0.03	0.03
n	11	11	10	10
Min	0.38	0.47	0.61	0.57
Max	0.60	0.59	0.69	0.67

$\Theta/\Phi \sim K_c$	0.01 M	0.05 M	0.1 M
Mean	***1.62***	***1.44***	***1.50***
St. Dev.	0.27	0.11	0.13

Table C.4 Transport properties (Θ, Φ, κ) for 3.5 nm Ficoll in blank 4v% agarose gels, as a function of ionic strength.

Θ	0.01 M	0.05 M	0.1 M
Mean	***0.77***	***0.98***	***0.96***
St. Dev.	0.10	0.05	0.06
n	6	5	5
Min	0.68	0.89	0.86
Max	0.89	1.00	1.00

Θ'	0.01 M	0.05 M	0.1 M
Mean	***0.88***	***1.01***	***1.00***
St. Dev.	0.07	0.04	0.04
n	6	5	5
Min	0.81	0.95	0.95
Max	0.95	1.05	1.04

κ	0.01 M	0.05 M	0.1 M
Mean (nm^2)	***187***	***256***	***279***
St. Dev.	88	32	44
n	6	5	5
Min	102	219	222
Max	306	306	332

Pe_{min}	0.01 M	0.05 M	0.1 M
Mean	***2.0***	***2.0***	***2.2***
St. Dev.	0.4	0.3	0.5
n	6	5	5
Min	1.5	1.6	1.5
Max	2.6	2.3	2.9

Φ	0.01 M	0.02 M	0.05 M	0.1 M
Mean	***0.67***	***0.70***	***0.69***	***0.70***
St. Dev.	0.04	0.04	0.05	0.03
n	9	10	10	10
Min	0.59	0.63	0.63	0.65
Max	0.71	0.76	0.75	0.75

$\Theta/\Phi \sim K_c$	0.01 M	0.05 M	0.1 M
Mean	***1.14***	***1.49***	***1.43***
St. Dev.	0.16	0.17	0.15

Table C.5 Transport properties (Θ, Φ, κ) for BSA in 4v% agarose – 0.2 v% GAG gels, as a function of ionic strength.

Θ	0.01 M	0.02 M	0.05 M	0.1 M	1.0 M
Mean	*0.39*	*0.52*	*0.72*	*0.80*	*0.88*
St. Dev.	0.13	0.08	0.07	0.04	0.02
n	6	6	6	6	6
Min	0.22	0.42	0.63	0.75	0.84
Max	0.60	0.64	0.83	0.87	0.91

Θ'	0.01 M	0.02 M	0.05 M	0.1 M	1.0 M
Mean	*0.56*	*0.68*	*0.84*	*0.89*	*0.94*
St. Dev.	0.16	0.09	0.06	0.03	0.02
n	6	6	6	6	6
Min	0.31	0.53	0.73	0.83	0.90
Max	0.78	0.80	0.91	0.93	0.95

κ	0.01 M	0.02 M	0.05 M	0.1 M	1.0 M
Mean (nm^2)	*103*	*118*	*145*	*152*	*177*
St. Dev.	27	25	29	29	33
n	6	6	6	6	6
Min	59	73	94	102	124
Max	135	137	168	178	215

Pe_{min}	0.01 M	0.02 M	0.05 M	0.1 M	1.0 M
Mean	*1.5*	*1.5*	*1.5*	*1.5*	*1.8*
St. Dev.	0.4	0.3	0.3	0.3	0.4
n	6	6	6	6	6
Min	0.8	0.9	0.9	1.0	1.2
Max	1.9	1.8	1.7	1.8	2.2

Φ	0.01 M	0.02 M	0.05 M	0.1 M	0.2 M	0.5 M
Mean	*0.30*	*0.37*	*0.40*	*0.50*	*0.54*	*0.54*
St. Dev.	0.04	0.06	0.08	0.04	0.04	0.03
n	10	11	11	11	11	11
Min	0.24	0.26	0.28	0.44	0.46	0.47
Max	0.38	0.47	0.55	0.57	0.59	0.59

$\Theta/\Phi-K_c$	0.01 M	0.02 M	0.05 M	0.1 M	1.0 M
Mean	*1.32*	*1.38*	*1.83*	*1.60*	*1.23*
St. Dev.	0.47	0.31	0.40	0.16	0.12

Table C.6 Transport properties (Θ, Φ, κ) for BSA in blank 4v% agarose gels, as a function of ionic strength.

Θ	0.01 M	0.02 M	0.05 M	0.1 M	1.0 M
Mean	*0.93*	*0.92*	*0.91*	*0.91*	*0.93*
St. Dev.	0.03	0.01	0.01	0.00	0.01
n	6	6	6	6	6
Min	0.91	0.90	0.90	0.91	0.92
Max	0.98	0.94	0.92	0.92	0.94

Θ'	0.01 M	0.02 M	0.05 M	0.1 M	1.0 M
Mean	*0.96*	*0.97*	*0.96*	*0.96*	*0.97*
St. Dev.	0.01	0.01	0.00	0.01	0.01
n	6	6	6	6	6
Min	0.94	0.95	0.96	0.95	0.97
Max	0.97	0.97	0.96	0.97	0.98

κ	0.01 M	0.02 M	0.05 M	0.1 M	1.0 M
Mean (nm^2)	*246*	*251*	*251*	*265*	*281*
St. Dev.	38	40	41	42	50
n	6	6	6	6	6
Min	191	196	196	211	209
Max	292	301	298	324	340

Pe_{min}	0.01 M	0.02 M	0.05 M	0.1 M	1.0 M
Mean	*2.0*	*2.0*	*2.0*	*2.1*	*2.2*
St. Dev.	0.3	0.4	0.4	0.4	0.4
n	6	6	6	6	6
Min	1.6	1.6	1.6	1.6	1.6
Max	2.5	2.5	2.4	2.5	2.7

Φ	0.01 M	0.02 M	0.05 M	0.1 M	0.2 M	0.5 M
Mean	*0.66*	*0.65*	*0.60*	*0.61*	*0.63*	*0.67*
St. Dev.	0.05	0.04	0.08	0.06	0.04	0.05
n	9	10	9	9	10	10
Min	0.61	0.59	0.53	0.52	0.55	0.62
Max	0.72	0.71	0.74	0.71	0.68	0.76

$\Theta/\Phi-K_c$	0.01 M	0.02 M	0.05 M	0.1 M	1.0 M
Mean	*1.41*	*1.42*	*1.51*	*1.50*	*1.23*
St. Dev.	0.10	0.08	0.19	0.15	0.08

Table C.7 Transport properties (Θ, κ) for BSA in 3v% agarose – 0.4 v% GAG gels, as a function of ionic strength.

Θ	0.01 M	0.02 M	0.05 M	0.1 M
Mean	***0.50***	***0.65***	***0.80***	***0.86***
St. Dev.	0.05	0.07	0.03	0.03
n	6	6	6	6
Min	0.42	0.51	0.76	0.81
Max	0.56	0.71	0.84	0.91

Θ'	0.01 M	0.02 M	0.05 M	0.1 M
Mean	***0.67***	***0.82***	***0.90***	***0.93***
St. Dev.	0.07	0.07	0.02	0.02
n	6	6	6	6
Min	0.58	0.69	0.86	0.90
Max	0.76	0.89	0.93	0.96

κ	0.01 M	0.02 M	0.05 M	0.1 M
Mean (nm^2)	***207***	***256***	***326***	***363***
St. Dev.	38	56	60	66
n	6	6	6	6
Min	169	204	253	286
Max	261	346	397	444

Pe_{min}	0.01 M	0.02 M	0.05 M	0.1 M
Mean	***1.3***	***1.7***	***1.5***	***1.5***
St. Dev.	0.2	0.3	0.2	0.3
n	6	6	6	6
Min	1.1	1.3	1.2	1.3
Max	1.6	2.1	1.8	1.8

Table C.8 Transport properties (Θ, κ) for BSA in blank 3v% agarose gels, as a function of ionic strength.

Θ	0.01 M	0.02 M	0.05 M	0.1 M
Mean	***0.88***	***0.88***	***0.88***	***0.95***
St. Dev.	0.01	0.03	0.02	0.01
n	6	6	6	6
Min	0.86	0.85	0.86	0.94
Max	0.90	0.93	0.91	0.97

Θ'	0.01 M	0.02 M	0.05 M	0.1 M
Mean	***0.96***	***0.95***	***0.96***	***0.98***
St. Dev.	0.01	0.01	0.01	0.00
n	6	6	6	6
Min	0.95	0.94	0.95	0.98
Max	0.96	0.96	0.96	0.99

κ	0.01 M	0.02 M	0.05 M	0.1 M
Mean (nm^2)	***667***	***683***	***683***	***708***
St. Dev.	64	84	69	79
n	6	6	6	6
Min	587	566	588	608
Max	757	804	781	803

Pe_{min}	0.01 M	0.02 M	0.05 M	0.1 M
Mean	***2.0***	***2.0***	***2.0***	***2.1***
St. Dev.	0.2	0.2	0.1	0.2
n	6	6	6	6
Min	1.8	1.8	1.8	1.8
Max	2.2	2.2	2.2	2.3

Appendix D. EXCLUDED VOLUMES FOR SPHERE-COIL INTERACTIONS

In section 4.4.1, the partition coefficient for a hard sphere into a matrix of GAG was considered for the cases where GAG is a rod or a coil. The derivation for the excluded volume and partition coefficient for a sphere in a an array of coils is based on the continuum method used for the interactions between a freely-jointed chain and a rod (White and Deen 2000). Unlike the coil-rod system, an analytical solution is available for the excluded volume of a coil-sphere interaction. A summary of the derivation, performed by W. M. Deen, is provided here.

Let the sphere have a radius r_s and the coil a radius of gyration r_g; the ratio of them is $\lambda = r_g/r_s$. Define a dimensionless contour length along the chain τ ($\tau = 0$ and 1 at the chain ends) and a dimensionless radial coordinate $\eta = r/r_s$. The probability of finding a point τ at position η, given that no preceding part of the chain overlapped with the fiber, is $P(\eta,\tau)$. The probability density with spherical symmetry is given by

$$\frac{\partial P}{\partial \tau} = \frac{\lambda^2}{\eta^2}\frac{\partial}{\partial \eta}\left(\eta^2 \frac{\partial P}{\partial \eta}\right) \tag{D.1}$$

$$P(\eta,0) = 1 \;;\; P(1,\tau) = 0 \;;\; P(\infty,\tau) = 1 \quad . \tag{D.2}$$

Redefine the probability by

$$P(\eta,\tau) = 1 - \Psi(x,\tau)/(1-x) \tag{D.3}$$

with the new position variable $x = \eta - 1$. Then Equation (D.1) and the boundary conditions in Equation (D.2) are transformed to

$$\frac{\partial \Psi}{\partial \tau} = \lambda^2 \frac{\partial^2 \Psi}{\partial x^2} \tag{D.4}$$

$$\Psi(\eta,0) = 0 \;;\; \Psi(0,\tau) = 1 \;;\; \Psi(\infty,\tau) = 0 \quad . \tag{D.5}$$

This equation is identical to the archetypal example of diffusion into a semi-infinite slab (Section 3.5 in (Deen 1998)). Using a similarity transformation $s = x/g(\tau)$, Equations (D.4)-(D.5) have the solution

$$\Psi(s) = 1 - erf(s) = 1 - erf\left(x / \sqrt{4\lambda^2 \tau}\right) \tag{D.6}$$

where *erf* is the error function. In terms of the original probability density function

$$P(\eta, \tau) = 1 - \frac{erfc\left((\eta - 1) / \sqrt{4\lambda^2 \tau}\right)}{\eta} \quad . \tag{D.7}$$

where *erfc* is the complimentary error function. The probability of fitting the entire chain at a position η (for $\eta \geq 1$) is

$$P(\eta, 1) = 1 - \frac{erfc\left((\eta - 1) / 2\lambda\right)}{\eta} \tag{D.8}$$

while the probability is zero for $\eta \leq 1$.

The excluded volume between the sphere and the coil is the volume integral of the probability of the entire chain *not* fitting, or 1-$P(\eta,1)$:

$$V_{sc} = \int_V 1 - P(\eta, 1) dV = 4\pi r_s^3 \int_0^\infty \eta^2 \left(1 - P(\eta, 1)\right) d\eta \quad . \tag{D.9}$$

Separating the integral into two regions

$$\frac{V_{sc}}{(4/3)\pi r_s^3} = 3\int_0^1 \eta^2 d\eta + 3\int_1^\infty \eta \; erfc\left((\eta - 1) / 2\lambda\right) d\eta \quad . \tag{D.10}$$

Now evaluating the first integral and transforming the spatial variable in the second integral to $t = (\eta\text{-}1)/2\lambda$, Equation (D.10) becomes

$$\frac{V_{sc}}{(4/3)\pi r_s^3} = 1 + 6\lambda \int_0^\infty \left(1 + 2\lambda t\right) erfc\left(t\right) dt \quad . \tag{D.11}$$

The complimentary error function has the following properties:

$$\begin{aligned} &\int erfc(x) dx = \frac{-\exp(-x^2)}{\sqrt{\pi}} + x \; erfc(x) \\ &erfc(0) = 1 \quad ; \quad erfc(\infty) = 0 \\ &\int_0^\infty erfc(x) dx = 1 / \sqrt{\pi} \end{aligned} \quad . \tag{D.12}$$

Equation (D.11) then becomes

$$\frac{V_{sc}}{(4/3)\pi r_s^3} = 1 + \frac{6\lambda}{\sqrt{\pi}} + 12\lambda^2 \int_0^\infty t \; erfc\left(t\right) dt \quad . \tag{D.13}$$

The remaining integral in Equation (D.13) can be evaluated using integration by parts:

$$\begin{aligned}\frac{V_{sc}}{(4/3)\pi r_s^3} &= 1+\frac{6\lambda}{\sqrt{\pi}}+0+\frac{12\lambda^2}{\sqrt{\pi}}\int_0^\infty t^2\exp\left(-t^2\right)dt \\ &= 1+\frac{6\lambda}{\sqrt{\pi}}+\frac{12\lambda^2}{\sqrt{\pi}}\left(\frac{\sqrt{\pi}}{4}\right) \\ &= 1+3\lambda\left(\frac{2}{\sqrt{\pi}}+\lambda\right)\end{aligned} \tag{D.14}$$

The partition coefficient for a solute *i* can be calculated from the excluded volume by

$$\Phi_i = \exp\left[-\sum_j \bar{\gamma}_{ij}\right] = \exp\left[-\sum_j \bar{N}_j V_{ij}\right] \tag{D.15}$$

where $\bar{\gamma}_{ij}$ is the interaction parameter between solute *i* and an object *j*, $\bar{N}_j$ is the number concentration of object *j*, and V_{ij} is the excluded volume between objects *i* and *j* (Lazzara et al. 2000). The partition coefficient for a spherical solute *i* with radius r_s in an array of rigid rods with radius r_f was

$$\Phi_i = \exp\left[-\phi_f\left(1+\frac{r_s}{r_f}\right)^2\right] \quad . \tag{D.16}$$

The number concentration can calculated from the rod volume fraction:

$$\bar{N}_j = \phi_f \big/ \pi r_f^2 L_f \tag{D.17}$$

where L_f is the length of a fiber. Knowing the rigid fiber volume fraction, the equivalent partition coefficient for flexible fibers (coils) is found by combining Equations (D.14), (D.15), and (D.17):

$$\Phi_i = \exp\left[-\phi_f\frac{4r_s^3}{r_f^2 L_f}\left(\frac{1}{3}+\frac{r_g}{r_s}\left(\frac{2}{\sqrt{\pi}}+\frac{r_g}{r_s}\right)\right)\right] \quad . \tag{D.18}$$

As referenced in the text, GAG properties were assumed to be L_f = 105 nm, r_f = 0.5 nm, and r_g = 7.5 nm.

Appendix E. VARIANCE-WEIGHTED STATISTICS

In section 5.3, it was necessary to analyze values of the convective hindrance factor, K_c, which were only known as a statistical mean and variance, not as individual measurements of multiple samples. Since a limited number of samples were used to calculate K_c, the variance at each condition could differ. In order to account for these different variance and place a stronger weight on values of K_c that were known more accurately, variance-weighting was used in the statistical analysis. Thanks to Professor Daniele Veneziano (MIT, Department of Civil Engineering) for a helpful discussion on this topic.

Error Propagation

Assume that two properties, x and y, are measured independently at a condition i, each having n_x and n_y unique measurements. The means (m_x, m_y) and variances (σ_x^2, σ_y^2) of these measurements at each condition i are calculated by standard methods. The following equations give the mean and variance of the quotient of these properties.

$$let\ K_i \equiv \frac{x_i}{y_i} \tag{E.1}$$

$$m_{K_i} = \frac{m_{x_i}}{m_{y_i}} \tag{E.2}$$

$$\frac{\sigma_{K_i}^2}{m_{K_i}^2} = \frac{\sigma_{x_i}^2}{m_{x_i}^2} + \frac{\sigma_{y_i}^2}{m_{y_i}^2} \tag{E.3}$$

Note: The standard deviation is the square root of the variance. For properties with unique measurements, the standard error (or standard deviation of the mean) is the standard deviation divided by the square root of the number of measurements, n.

Weighted Mean

To find the average value of K over all conditions i, it may be desired to more heavily weight those values which are known more accurately. Knowing the mean value and variance of K at each condition i (m_{Ki} and σ_{Ki}^2, respectively), the average value and variance can be calculated by

$$m_K = \left(\sum_i \frac{m_{K_i}}{\sigma_{K_i}^2} \right) \Bigg/ \left(\sum_i \frac{1}{\sigma_{K_i}^2} \right) \tag{E.4}$$

$$\sigma_K^2 = 1 \Bigg/ \left(\sum_i \frac{1}{\sigma_{K_i}^2} \right) \tag{E.5}$$

Weighted Least-Squares Regression

The values of K_i can also be fit to a curve by weighted least-squares regression, which again places more weight on those points known more accurately. Assume that K is measured as a function of c, which are related by the linear form

$$K = \beta_1 + \beta_2 c \quad . \tag{E.6}$$

Assuming that mean values and variance of K are known for i different values of c; c is assumed to be know exactly. Four matrixes are defined:

$$\text{parameter matrix : } \underline{\boldsymbol{\beta}} = \begin{pmatrix} \beta_1 \\ \beta_2 \end{pmatrix} \tag{E.7}$$

$$\text{dependant variable : } \underline{\mathbf{Y}} = \begin{pmatrix} m_{K,1} \\ \vdots \\ m_{K,i} \end{pmatrix} \tag{E.8}$$

$$\text{independent variable : } \underline{\underline{\mathbf{X}}} = \begin{pmatrix} 1 & c_1 \\ \vdots & \vdots \\ 1 & c_i \end{pmatrix} \tag{E.9}$$

$$\text{weighting factor} : \underline{\underline{\mathbf{W}}} = \begin{pmatrix} 1/\sigma_{K1}^2 & 0 & 0 \\ 0 & \ddots & 0 \\ 0 & 0 & 1/\sigma_{Ki}^2 \end{pmatrix} . \tag{E.10}$$

The least-squares fit of the slope and intercept of the line are calculated from

$$\underline{\boldsymbol{\beta}} = \left(\underline{\underline{\mathbf{X}}}^T \underline{\underline{\mathbf{W}}}\,\underline{\underline{\mathbf{X}}}\right)^{-1} \underline{\underline{\mathbf{X}}}^T \underline{\underline{\mathbf{W}}}\,\underline{\mathbf{Y}} . \tag{E.11}$$

The variance of the least-squares parameters are

$$\underline{\underline{\boldsymbol{\sigma}}}_{\beta}^2 = \left(\underline{\underline{\mathbf{X}}}^T \underline{\underline{\mathbf{W}}}\,\underline{\underline{\mathbf{X}}}\right)^{-1} = \begin{pmatrix} \sigma_{\beta 1}^2 & 0 \\ 0 & \sigma_{\beta 2}^2 \end{pmatrix} . \tag{E.12}$$

Note that the method above can be adapted to multiple independent variables by adding additional an additional parameter in Matrix (E.7) and a third column in Matrix (E.9). The method can also be used for least-squares regression of non-linear functions. For example an exponential could be fit by replacing c with $\ln(c)$ in Matrix (E.9); a quadratic expression could include a third column with c_i^2 in Matrix (E.9).

Below is an example of MATLAB code to fit the parameters in a linear system.

```
beta=(X'*W*X)\(X'*W*Y);  % matrix of least-squares linear parameters
sigma2b=inv(X'*W*X);     % variance matrix for beta parameters

intercept=[beta(1), sqrt(sigma2b(1,1))]  % mean, std dev of intercept
slope=[beta(2), sqrt(sigma2b(2,2))]      % mean, std dev of slope
```

Appendix F. ENDOTHELIAL MODELS: 1 VERSUS 2 LAYERS

As noted in section 6.1, the endothelium can be modeled in two ways: as a single layer containing both glycocalyx and fenestrae or as two separate layers in series. The following section discusses the implications of the two approaches for hydraulic permeability and sieving.

Hydraulic Permeability

Flow through a gel is given by Darcy's Law,

$$\mathrm{v} = \frac{\kappa\beta}{\mu\delta}\Delta P \tag{F.1}$$

where β is the correction factor for any hindrances to the flow due to impermeable obstructions. Calculation of β was described in detail in Chapters 3 and 6. For layers in series, the volumetric flux (v) is constant through all layers and the pressure drop across each layer sum to the total pressure drop. If the fiber matrix and liquid are the same in both layers (κ and μ are constant), then the correction factor for two layers (β) is related to the correction factor of each layer (β_1, β_2) by

$$\frac{\delta_1}{\beta_1} + \frac{\delta_2}{\beta_2} = \frac{\delta_1 + \delta_2}{\beta} \quad . \tag{F.2}$$

where the thickness of both layers is the sum of the individual thicknesses, $\delta = \delta_1 + \delta_2$. The assumption in this approach is that the pressure is uniform at the interface between layers 1 and 2.

To check the validity of this assumption, Comsol Multiphysics™ was used to model a single endothelial layer (shown in Figure F.1(a)), as well as model the glycocalyx (layer 1) and fenestra (layer 2) individually. The model of layer 1 assumed that shaded region on the bottom surface in Figure F.1 was impermeable. The models used the endothelial dimensions given in Chapter 6: $R_f = 30$ nm, $b = 60$ nm, $\delta_2 = 60$ nm, and $\delta_1 = 100$-1000 nm. The resulting values are β are summarized in Table 1 for the single-layer model and the two-layer model using Equation (F.2). The correction factors for the one-layer and two-layer models deviated by less than 6%, confirming that the two modeling approaches are equally valid.

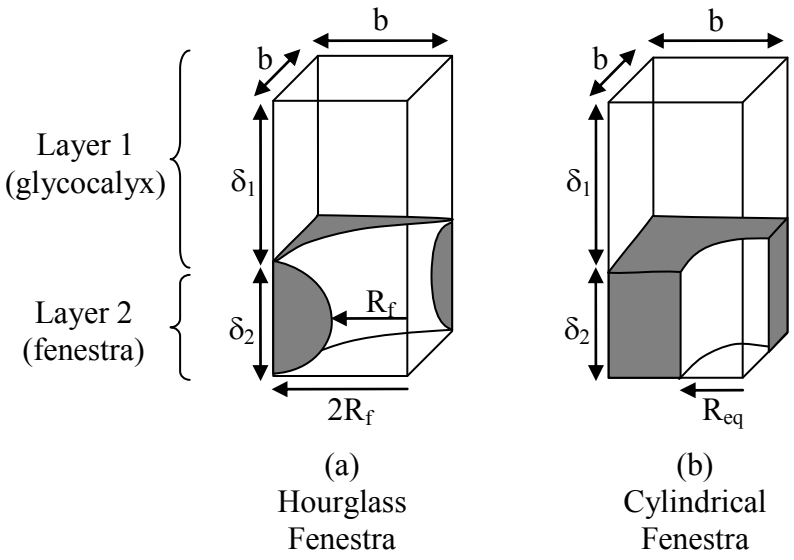

Figure F.1 Diagram of a unit cell of the endothelium. The fenestra can be modeled by (a) a physiologically-based hourglass shape or (b) a simplified straight-walled cylinder. If the endothelium is considered as two layers in series, the glycocalyx (layer 1) is upstream of the fenestra (layer 2). The fluid-filled space in both layers are assumed to have the same Darcy permeability.

Table F.1 Correction factors (β) for endothelial resistance to flow. Results for models of the endothelium with one and two layers, for hourglass and cylindrical fenestra, and for a range of glycocalyx thicknesses.

	Hourglass		**Cylindrical**
δ_1/b	**Single Layer**	**Two Layers**	**Two Layers**
1.5	0.419	0.443	0.404
2.5	0.501	0.527	0.487
5	0.634	0.657	0.621
20	0.857	0.871	0.848

For comparison, the fenestra was also modeled as a straight-walled cylindrical pore, as shown in Figure F.1(b). For the several values of R_{eq} considered, the correction factor β_2 deviated from the pore area fraction $\varepsilon = \pi R_{eq}^2/4b^2$ by less than 0.001%. It was found that a radius of R_{eq} = 33.6 nm gave a correction factor identical to that of the hourglass-shaped fenestra in Layer 2. As shown in Table F.1, using β_1 for cylindrical pores yielded values of β that were within 4 v% of the single-region hourglass simulations, confirming that all three approaches to modeling the fenestra are comparable.

Sieving

In models of sieving through the glomerular basement membrane, it was shown that the sieving coefficient was correctly modeled if the Péclet number included the hydraulic correction factor (Deen et al. 2001, Edwards et al. 1999):

$$\mathrm{Pe} = \frac{K_c \, \mathrm{v} \, \delta}{K_d D_\infty \beta} \quad . \tag{F.3}$$

This result is directly applicable to sieving through the glycocalyx, since both are a uniform slab of material with at least one surface partially blocked with circular openings. The Péclet number for the glycocalyx uses values of β_1 calculated previously for hydraulic permeability.

As shown for hydraulic permeability, the fenestra are equally well modeled by an hourglass shape or a cylindrical pore. For a cylindrical pore, the velocity through the glycocalyx (v) is increased to v/ε ($\approx \mathrm{v}/\beta$) in the pore, such that the Péclet number in the pore is also given by Equation (F.3). It is easily assumed that the Péclet number for an hourglass fenestra would also be accurately described by Equation (F.3), using β_2 and the volume flux, v, based on the entire unit cell cross-sectional area.

As described in Chapter 6, the sieving coefficient of a layer is a function of both the properties of that layer (Φ_i, $K_{c,i}$, and Pe_i) as well as the sieving coefficient of the downstream layers (Θ_n). The sieving coefficient for the endothelium is the product of the glycocalyx and fenestra layers. Using Equation (6.16) for the sieving coefficient of Layer 1, the sieving coefficient of the endothelium is

$$\Theta_{endo} = \Theta_1 \Theta_2 = \frac{\Phi K_c}{\Theta_n \left(1 - e^{-Pe_1}\right) + \Phi K_c / \Theta_2 \, e^{-Pe_1}} \tag{F.4}$$

Assuming that the fiber properties are the same between the layers (ΦK_c is constant) and using Equation (6.16) to substitute for Θ_2, the endothelial sieving coefficient becomes

$$\Theta_{endo} = \frac{\Phi K_c}{\Theta_n \left(1 - e^{-(Pe_1 + Pe_2)}\right) + \Phi K_c e^{-(Pe_1 + Pe_2)}} \quad . \tag{F.5}$$

Again assuming the same fiber properties between the layers, the sum of the Péclet numbers is

$$Pe_1 + Pe_2 = \frac{K_c v}{K_d D_\infty}\left(\frac{\delta_1}{\beta_1} + \frac{\delta_2}{\beta_2}\right) \quad . \tag{F.6}$$

Noticing the similarity of terms in Equations (F.6) and (F.2), the sum of the Péclet numbers is equal to a single endothelial Péclet number based on the single-layer correction factor and overall thickness:

$$Pe_1 + Pe_2 = \frac{K_c v}{K_d D_\infty}\left(\frac{\delta_1 + \delta_2}{\beta}\right) = Pe_{endo} \quad . \tag{F.7}$$

Substituting this result into Equation (F.5) gives the expression expected for treating the endothelium as a single layer:

$$\Theta_{endo} = \frac{\Phi K_c}{\Theta_n\left(1 - e^{-Pe_{endo}}\right) + \Phi K_c e^{-Pe_{endo}}} \quad . \tag{F.8}$$

This result justifies that an accurate sieving coefficient through the endothelium can be obtained by using the hydraulic correction factor for a single layer, as was assumed in the analysis in Section 6.1.

INDEX OF SYMBOLS

a	Radius of boundary layer in Helmholtz model [m]
A_i	Area of fiber region i [m^2]
$[A]_i$	Absorbance of a sample i [-]
A_m	Cross-sectional exposed area of a gel membrane [m^2]
b	Dimensional unit cell radius [m]
B	Dimensionless unit cell width [-]
c'_i	Concentration of species i inside the membrane (Donnan model) [mol/m^3]
c_b	Bulk concentration [mol/m^3]
c_i	Concentration of species i [mol/m^3]
$c_{i,init}$	Initial (t=0) concentration of species i [mol/m^3]
$c_{i,0}$	Bulk solution concentration of species i [mol/m^3]
c_m	Fixed negative charge concentration in the membrane (>0) [mol/m^3]
c_M	Concentration at the upstream surface of a membrane [mol/m^3]
C_i	Dimensionless concentration of species i [-]
Da	Damköhler number [-]
D_i	Diffusivity of species i [m^2/s]
D_∞	Diffusivity in free solution [m^2/s]
$\mathbf{e}_i$	Unit vector in the i-direction [-]
E_{DL}	Double layer characteristic electric field [V/m]
E_s	Flow-induced characteristic electric field [V/m]
$f_i(\Theta_B)$	Bound GAG hindrance function for $i=D_G$, k_1, or Φ_G [-]
$\tilde{f}_i$	Dimensionless force per unit length [-]
F	Faraday's constant [= 9.648 x 10^4 C/mol]
F_i	Force acting on fibers of type i [Pa-m^2]
G_1, G_2	Dimensionless parameters in Helmholtz model [-]
$\mathbf{j}$	Current density [C/m^2-s]
$\langle \mathbf{j} \rangle$	Macroscopic, or area-averaged, current density [C/m^2-s]
k	Hydraulic permeability [m^2/Pa-s]
k_{avg}	Average permeability of multiple fiber types or orientations [m^2/Pa-s]
k_1	GAG-active site binding rate constant [L/mol/s]
k_2	Active site degradation rate constant [s^{-1}]
k_{eff}	Effective permeability of multiple fiber regions [m^2/Pa-s]
k_i	Hydraulic permeability of fiber type i or region i [m^2/Pa-s]
k_{ij}	Electrokinetic coupling coefficients
k_{oc}	Open circuit hydraulic permeability [m^2/Pa-s]
k_{rxn}	General first-order reaction constant [s^{-1}]
K_c	Convective hindrance coefficient [-]
K_d	Diffusive hindrance coefficient [-]
l	Optical pathlength of a sample in spectrometry [m]
$l_{f,i}$	Length of a fiber of type i [m]

L	Length over which a pressure drop occurs [m]
m_i	Mass of species i [g]
m_i	Bound GAG hindrance parameter for $i=D_G$, k_1, or Φ_G [-]
n	Number of data points [-]
n_i	Number of fibers of type i [-]
$\mathbf{n}_i$	Flux of species i [moles/m^2-s]
$\mathbf{N}_i$	Dimensionless flux of species i [-]
p	Pressure [Pa]
P	Dimensionless pressure [-]
Pe	Peclet number = $u_s\lambda_D/D_+ = K_c v\delta/K_d D_\infty$ [-]
Pe_{min}	Minimum Peclet number in a membrane = $v\delta/D_\infty$ [-]
Q	Volumetric flow rate of filtration [m^3/s]
r_f	Fiber radius [m]
$r_{f,i}$	Fiber radius of fiber type i [m]
r_s	Solute hydraulic radius [m]
$r_{s,i}$	Hydraulic radius of solute type i [m]
R	Ideal gas constant [= 8.314 J/mol-K]
R_f	Dimensionless fiber radius [-]
R_m	Mesh fiber radius [m]
R_{tube}	Inner radius of the ultra-filtration cell outlet tube [m]
Re	Reynolds number = $v\delta\rho/\mu$
Sc	Schmidt number = $\mu/\rho D_\infty$
t	Time variable [s]
T	Absolute temperature [K]
$\mathbf{u}$	Dimensionless fluid velocity vector [-]
u_s	Superficial fluid velocity [m/s]
$\mathbf{v}$	Dimensional fluid velocity vector [m/s]
$\langle\mathbf{v}\rangle$	Macroscopic, or area-averaged, velocity [m/s]
v_j	j-component of velocity (j = x, y, z, etc.) [m/s]
V	Voltage [V]
V_{th}	Thermal voltage [V]
V_i	Volume of a sample i [m^3]
V_{total}	Total unit volume [m^3]
W	Center-to-center mesh fiber spacing [m]
x	Independent position variable [m]
X	Dimensionless independent position variable [-]
x_i	Generic abscissa variable
z_i	Valance charge of species i [-]
z_{tube}	Length of ultrafiltration cell outlet tube [m]
α	Dimensionless ratio of electrophoretic to positive ion mobility [-]
α	Dimensionless filtrate velocity through a membrane [-]
α_{dye}	Absorption coefficient of dye in free solution [mol^{-1} cm^2]
α_m	Dimensionless ratio of mesh open area to total area [-]
β	Maxwell parameter for relative permeabilities [-]
β_m	Correction factor for support mesh flow resistance [-]

β_E	Dimensionless ratio of induced to double layer electric fields [-]
δ	Thickness of a gel membrane [m]
δ_1	Thickness of a gel membrane upstream from the mesh [m]
ε	Dielectric permittivity [F/m]
ε_j	Volume fraction of region j [-]
ϕ	Fiber volume fraction [-]
$\hat{\phi}$	Bead-and-string fiber volume fraction [-]
ϕ_A	Fraction of sterically available active sites [-]
ϕ_i	Volume fraction of fiber type i [-]
Φ_i	Partition coefficient of species i [-]
γ	Binding proportion between GAG and dye [-]
γ_G	Ratio of maximum concentration of unbound GAG to active sites [-]
γ_m	Dimensionless fraction of gel upstream of mesh [-]
κ	Darcy permeability [m^2]
λ	Ratio of solute radius to fiber radius [-]
λ_D	Debye length [m]
λ_m	Dimensionless ratio of mesh thickness to mesh fiber radius [-]
μ	Fluid viscosity [Pa-s]
μ_i	Mobility of species i [m^2/V-s]
π_b	Bulk osmotic pressure [Pa]
ρ	Fluid density [kg/m^3]
Θ	Membrane sieving coefficient [-]
Θ'	Apparent sieving coefficient, without concentration polarization correction [-]
Θ_i	Dimensionless concentration of species i [-]
σ_o	Fluid conductivity [C/m-V-s]
σ_s	Surface charge density [C/m^2]
$\tilde{\sigma}_i$	Dimensionless surface charge density of object i [-]
τ	Dimensionless independent time variable [-]
τ_D	Characteristic diffusion (or diffusion+reaction) time [s]
ω	Angular velocity of the bulk fluid [s^{-1}]
ω_{st}	Angular velocity of the stir bar [s^{-1}]
ψ	Electrical potential [V/m]
ψ_D	Donnan potential [V/m]
Ψ	Dimensionless electrical potential [-]
ξ	Dimensionless ratio of electrokinetic properties [-]
∇	Dimensionless gradient operator [-]
$\bar{\nabla}$	Dimensional gradient operator [m^{-1}]

BIBLIOGRAPHY

1. Adamson RH and Clough G. Plasma proteins modify the endothelial cell glycocalyx of frog mesenteric microvessels. *J. Physiol. (Lond).* **445**: 473-486, 1992.
2. Anderson B, Hoffman P, and Meyer K. The o-serine linkage in peptides of chondroitin 4- or 6-sulfate. *J. Biol. Chem.* **240**: 156-167, 1964.
3. Anderson JL, Rauh F, and Morales A. Particle diffusion as a function of concentration and ionic strength. *The Journal of Physical Chemistry* **82**: 608-616, 1978.
4. Andersson L-O, Borg H, and Miller-Andersson M. Purification and characterization of human factor IX. *Thromb. Res.* **7**: 451-459, 1975.
5. Arnott S, Fulmer A, and Scott WE. The agarose double helix and its function in agarose gel structure. *J. Mol. Biol.* **90**: 269-284, 1974.
6. Attwood TK, Nelmes BJ, and Sellen DB. Electron microscopy of beaded agarose gels. *Biopolymers* **27**: 201-212, 1988.
7. Avasthi PS and Koshy V. The anionic matrix at the rat glomerular endothelial surface. *Anat. Rec.* **220**: 258-266, 1988.
8. Axén R, Porath J, and Ernback S. Chemical coupling of peptides and proteins to polysaccharides by means of cyanogen halides. *Nature* **214**: 1302-1304, 1967.
9. Aymard P, Martin DR, Plucknett K, Foster TJ, Clark AH, and Norton IT. Influence of thermal history on the structural and mechanical properties of agarose gels. *Biopolymers* **59**: 131-144, 2001.
10. Balakrishnan M and Agarwal GP. Protein fractionation in a vortex flow filter: I. Effect of hydrodynamics and solution environment on single protein transmission. *J. Membr. Sci.* **112**: 47-74, 1996.
11. Ballermann BJ. Regulation of bovine glomerular endothelial cell growth in vitro. *Am. J. Physiol.* **256**: C182-C189, 1989.
12. Barskii VE, Ivanov VB, Skylar YE, and Mikhailov GI. [dichlorotriazineylaminofluorescein-a new fluorochrome for cytochemical and histochemical detection of proteins]. *Izv. Akad. Nauk SSSR. Biol.* **5**: 744-747, 1968.
13. Bertini S, Bisio A, Torri G, Bensi D, and Terbojevich M. Molecular weight determination of heparin and dermatan sulfate by size exclusion chromatography with a triple detector array. *Biomacromolecules* **6**: 168-173, 2005.
14. Bettelheim FA, Laurent TC, and Pertoft H. Interaction between serum albumin and acidic polysaccharides. *Carbohydr. Res.* **2**, 1966.
15. Bhattacharjee S, Kim AS, and Elimelech M. Concentration polarization of interacting solute particles in cross-flow membrane filtration. *J. Colloid Interface Sci.* **212**: 81-99, 1999.
16. Bitter T and Muir HM. A modified uronic acid carbazole reaction. *Anal. Biochem.* **4**: 330-334, 1962.
17. Blouch K, Deen WM, Fauvel J-P, Bialek J, Derby G, and Myers BD. Molecular configuration and glomerular size selectivity in healthy and nephrotic humans. *Am. J. Physiol. Renal Physiol.* **273**: F430-F437, 1997.
18. Bolton GR, Deen WM, and Daniels BS. Assessment of the charge selectivity of glomerular basement membrane using ficoll sulfate. *Am. J. Physiol.* **274**: F889-F896, 1998.
19. Bonnecaze RT and Brady JF. The effective conductivity of random suspensions of spherical particles. *Proc. R. Soc. London, A* **432**: 445-465, 1991.
20. Buck KKS, Gerhardt NI, Dungan SR, and Phillips RJ. The effect of solute concentration on equilibrium partitioning in polymeric gels. *J. Colloid Interface Sci.* **234**: 400-409, 2001.
21. Bulone D, Giacomazza D, Martorana V, Newman J, and San Biagio PL. Ordering of agarose near the macroscopic gelation point. *Phys. Rev. E: Stat. Nonlin. Soft Matter Phys.* **69**: 041401, 2004.
22. Burns DB and Zydney AL. Effect of solution pH on protein transport through ultrafiltration membranes. *Biotechnol. Bioeng.* **64**: 27-37, 1999.
23. Capila I and Linhardt RJ. Heparin-protein interactions. *Angew. Chem.* **41**: 390-412, 2002.
24. Chammas P. *Electromechanical coupling in articular cartilage: An electrokinetic micromodel and experimental results* (S.M. Thesis). Boston, MA: Boston University, 1989.

25. Chammas P, Federspiel WJ, and Eisenberg SR. A microcontinuum model of electrokinetic coupling in the extracellular matrix: Perturbation formulation and solution. *J. Colloid Interface Sci.* **168**: 526-538, 1994.
26. Chui MM, Phillips RJ, and McCarthy MJ. Measurement of the porous microstructure of hydrogels by nuclear magnetic resonance. *J. Colloid Interface Sci.* **174**: 336-344, 1995.
27. Clague DS, Kandhai BD, Zhang R, and Sloot PMA. Hydraulic permeability of (un)bounded fibrous media using the lattice boltzmann method. *Phys. Rev. E: Stat. Nonlin. Soft Matter Phys.* **61**: 616-625, 2000.
28. Clague DS and Phillips RJ. A numerical calculation of the hydraulic permeability of three-dimensional disordered fibrous media. *Phys. Fluids A* **9**: 1562-1572, 1997.
29. Crone HD. Ion-exclusion effects on the chromatography of acetylcholinesterase and other proteins on agarose columns at low ionic strength. *J. Chromatogr.* **92**: 127-135, 1974.
30. Cuatrecasas P. Protein purification by affinity chromatography. *J. Biol. Chem.* **245**: 3059-3065, 1970.
31. Curry FE, Rutledge JC, and Lenz JF. Modulation of microvessel wall charge by plasma glycoprotein orosomucoid. *Am. J. Physiol.* **257**: H1354-H1359, 1989.
32. Daamen WF, van Moerkerk HTB, Hafmans T, Buttafoco L, Poot AA, Veerkamp JH, and van Kuppevelt TH. Preparation and evaluation of molecularly-defined collagen-elastin-glycosaminoglycan scaffolds for tissue engineering. *Biomaterials* **24**: 4001-4009, 2003.
33. Danishefsky I and Tzeng F. Preparation of heparin-linked agarose and its interaction with plasma. *Thromb. Res.* **4**: 237-246, 1974.
34. Danishefsky I, Tzeng F, Ahrens M, and Klein S. Synthesis of heparin-sepharoses and their binding with thrombin and antithrombin-heparin cofactor. *Thromb. Res.* **8**: 131-140, 1976.
35. De Belder AN and Granath K. Preparation and properties of fluorescein-labeled dextrans. *Carbohydr. Res.* **30**: 375-378, 1973.
36. de Bernardo S, Weigele M, Toome V, Manhart K, Leimgruber W, Böhlen P, Stein S, and Udenfriend S. Studies of the reaction of fluorescamine with primary amines. *Arch. Biochem. Biophys.* **163**: 390-399, 1974.
37. De Keizer A, Van Der Drift WPJT, and Overbeek JTG. Electrophoresis of randomly oriented cylinderical particles. *Biophys. Chem.* **3**: 107-108, 1975.
38. Dea ICM, Moorhouse R, Rees DA, Arnott S, Guss JM, and Balazs EA. Hyaluronic acid: A novel, double helical molecule. *Science* **179**: 560-562, 1973.
39. Deen WM. *Analysis of transport phenomena*. New York: Oxford University Press, 1998.
40. Deen WM. Cellular contributions to glomerular size-selectivity. *Kidney Int.* **69**: 1295-1297, 2006.
41. Deen WM. Hindered transport of large molecules in liquid-filled pores. *AIChE J.* **33**: 1409-1425, 1987.
42. Deen WM. What determines glomerular capillary permeability? *J. Clin. Invest.* **114**: 1412-1414, 2004.
43. Deen WM and Lazzara MJ. Glomerular filtration of albumin: How small is the sieving coefficient? *Kidney Int.* **66**: S63-S64, 2004.
44. Deen WM, Lazzara MJ, and Myers BD. Structural determinants of glomerular permeability. *Am. J. Physiol. Renal Physiol.* **281**: F579-F596, 2001.
45. Deen WM, Satvat B, and Jamieson JM. Theoretical model for glomerular filtration of charged solutes. *Am. J. Physiol.* **238**: F126-F139, 1980.
46. Diakun GP, Edwards HE, Allen JC, Phillips GO, and Cundall RB. A simple purpose-built fluorimeter for the titrimetric assay of glycosaminoglycans. *Anal. Biochem.* **94**: 378-382, 1979.
47. DiLeo AJ. *The augmentation of macromolecular diffusion coefficients by diffusion potentials and the role of diffusion potentials in the ultrafiltration of macromolecular solutions* (PhD Thesis). Cambridge, MA: Massachusetts Institute of Technology, 1982.
48. Djabourov M, Clark AH, Rowlands DW, and Ross-Murphy SB. Small-angle x-ray scattering characterization of agarose sols and gels. *Macromolecules* **22**: 180-188, 1989.
49. Drummond JE and Tahir MI. Laminar viscous flow through regular arrays of parallel solid cylinders. *Int. J. Multiphase Flow* **10**: 515-540, 1984.
50. Drumond MC and Deen WM. Structural determinants of glomerular hydraulic permeability. *Am. J. Physiol.* **266**: F1-F12, 1994.

51. Edge ASB and Spiro RG. Selective deglycosylation of the heparan sulfate proteoglycan of bovine glomerular basement membrane and identification of the core protein. *J. Biol. Chem.* **262**: 6893-6898, 1987.
52. Edwards A, Daniels BS, and Deen WM. Hindered transport of macromolecules in isolated glomeruli. II. Convection and pressure effects in basement membranes. *Biophys. J.* **72**: 214-222, 1997a.
53. Edwards A, Daniels BS, and Deen WM. Ultrastructural model for size selectivity in glomerular filtration. *Am. J. Physiol.* **276**: F892-F902, 1999.
54. Edwards A, Deen WM, and Daniels BS. Hindered transport of macromolecules in isolated glomeruli. I. Diffusion across intact and cell-free capillaries. *Biophys. J.* **72**: 204-213, 1997b.
55. Edwards DA, Shapiro M, Bar-Yoseph P, and Shapira M. The influence of reynolds number upon the apparent permeability of spatially periodic arrays of cylinders. *Phys. Fluids A* **2**: 45-55, 1990.
56. Edwards SL and Dubin PL. pH effects on non-ideal protein size-exclusion chromatography on superose 6. *J. Chromatogr.* **648**: 3-7, 1993.
57. Eisenberg SR and Grodzinsky AJ. Electrokinetic micromodel of extracellular matrix and other polyelectrolyte networks. *PhysicoChem. Hydrodyn.* **10**: 517-539, 1988.
58. Ethier CR. Flow through mixed fibrous porous materials. *AIChE J.* **37**: 1227-1236, 1991.
59. Ethier CR. *Hydrodynamics of flow through gels with applications to the eye* (S.M. Thesis). Cambridge, MA: Massachusetts Institute of Technology, 1983.
60. Fanti LA and Glandt ED. Partitioning of spherical particles into fibrous matrices: 1. Density-functional theory. *J. Colloid Interface Sci.* **135**: 385-395, 1990.
61. Fasman GD. Practical handbook of biochemistry and molecular biology. Boca Raton, FL: CRC Press, 1989.
62. Fissell WH, Manley S, Dubnisheva A, Glass J, Magistrelli J, Eldridge AN, Fleischman AJ, Zydney AL, and Roy S. Ficoll is not a rigid sphere. *Am. J. Physiol. Renal Physiol.* **293**: F1209-F1213, 2007.
63. Foord SA and Atkins EDT. New x-ray diffraction results from agarose: Extended single helix structures and implications for gelation mechanism. *Biopolymers* **28**: 1345-1365, 1989.
64. Fricke H. A mathematical treatment of the electric conductivity and capacity of disperse systems. I. The electric conductivity of a suspension of homogeneous spheroids. *Phys. Rev.* **24**: 575-587, 1924.
65. Funahashi M, Matsumoto I, and Seno N. Preparation of three types of heparin-sepharose and their binding activities to thrombin and antithrombin III. *Anal. Biochem.* **126**: 414-421, 1982.
66. Galambos JT. The reaction of carbazole with carbohydrates. I. Effect of borate and sulfamate on the carbazole color of sugars. *Anal. Biochem.* **19**: 119-132, 1967.
67. Gardell S. Separation on dowex 50 ion exchange resin of glucosamine and galactosamine and their quantitative determination. *Acta Chem. Scand.* **7**: 207-215, 1953.
68. Gold EW. A simple spectrophotometric method for estimating glycosaminoglycan concentrations. *Anal. Biochem.* **99**: 183-188, 1979.
69. Goosen MFA and Sefton MV. Heparinized styrene-butadiene-styrene elastomers. *J. Biomed. Mater. Res.* **13**: 347-364, 1979.
70. Green DF, Hwang KH, Ryan US, and Bourgoignie JJ. Culture of endothelial cells from baboon and human glomeruli. *Kidney Int.* **41**: 1506-1516, 1992.
71. Griess GA, Edwards DA, Dumais M, Harris RA, Renn DW, and Serwer P. Heterogeneity of the pores of polysaccharide gels: Dependance on the molecular weight and derivatization of the polysaccharide. *J. Struct. Biol.* **111**: 39-47, 1993a.
72. Griess GA, Guiseley KB, and Serwer P. The relationship of agarose gel structure to the sieving of spheres during agarose gel electrophoresis. *Biophys. J.* **65**: 138-148, 1993b.
73. Groffen AJ, Ruegg MA, Dijkman H, van de Velden TJ, Buskens CA, van den Born J, Assmann KJ, Monnens LA, Veerkamp JH, and van den Heuvel LP. Agrin is a major heparan sulfate proteoglycan in the human glomerular basement membrane. *J. Histochem. Cytochem.* **46**: 19-27, 1998.
74. Gutenwik J, Nilsson B, and Axelsson A. Coupled diffusion and adsorption effects for multiple proteins in agarose gel. *AIChE J.* **50**: 3006-3018, 2004.
75. Guyton A and Hall J. *Textbook of medical physiology*. Philadelphia, PA: Saunders, 2000.
76. Happel J. Viscous flow relative to arrays of cylinders. *AIChE J.* **5**: 174-177, 1959.
77. Haraldsson B, Johnsson EK, and Rippe B. Glomerular permselectivity is dependent on adequate serum concentrations of orosomuciod. *Kidney Int.* **41**: 310-316, 1992.

78. Haraldsson B, Nyström J, and Deen WM. Properties of the glomerular barrier and mechanisms of proteinuria. *Physiol. Rev.* **88**: 451-487, 2008.
79. Haraldsson B and Sörensson J. Why do we not all have proteinuria? An update of our current understanding of the glomerular barrier. *News Physiol. Sci.* **19**: 7-10, 2004.
80. Hase S. Precolumn derivatization for chromatographic and electrophoretic analyses of carbohydrates. *J. Chromatogr.* **720**: 173-182, 1996.
81. Hasimoto H. On the periodic fundamental solutions of the stokes equations and their application to viscous flow past a cubic array of spheres. *J. Fluid Mech.* **5**: 317-328, 1959.
82. Henry CBS and Duling BR. Permeation of the luminal capillary glycocalyx in determined by hyaluronan. *Am. J. Physiol.* **277**: H508-H514, 1999.
83. Higdon JJL and Ford GD. Permeability of three-dimensional models of fibrous porous media. *J. Fluid Mech.* **308**: 341-361, 1996.
84. Hill RJ. Transport in polymer-gel composites: Theoretical methodology and response to an electric field. *J. Fluid Mech.* **551**: 405-433, 2006.
85. Hirota N, Kumaki Y, Narita T, Gong JP, and Osada Y. Effect of charge on protein diffusion in hydrogels. *J. Phys. Chem. B* **104**: 9898-9903, 2000.
86. Hoare DG and Koshland DE, Jr. A method for the quantitative modification and estimation of carboxylic acid groups in proteins. *J. Biol. Chem.* **242**: 2447-2453, 1967.
87. Huxley VH and Curry FE. Differential actions of albumin and plasma on capillary solute permeability. *Am. J. Physiol.* **260**: H1645-H1654, 1991.
88. Huxley VH and Williams DA. Role of a glycocalyx on coronary arteriole permeability to proteins: Evidence from enzyme treatments. *Am. J. Physiol.* **278**: H1177-H1185, 2000.
89. Iverius PH. Coupling of glycosaminoglycans to agarose beads (sepharose 4b). *Biochem. J.* **124**: 677-683, 1971.
90. Jackson GW and James DF. The hydrodynamic resistance of hyaluronic acid and its contribution to tissue permeability. *Biorheology* **19**: 317-330, 1982.
91. Jackson GW and James DF. The permeability of fibrous porous media. *Can. J. Chem. Eng.* **64**: 364-374, 1986.
92. Jandik KA, Kruep D, Cartier M, and Linhardt RJ. Accelerated stability studies of heparin. *J. Pharm. Sci.* **85**: 45-51, 1996.
93. Jaques LB. Determination of heparin and related sulfated mucopolysaccharides. In: *Methods of biochemical analysis*, edited by Glick D. New York, NY: Wiley, 1977, p. 203-312.
94. Jeffrey DJ. Conduction through a random suspension of spheres. *Proc. R. Soc. London, A* **335**: 355-367, 1973.
95. Johnson EM, Berk DA, Jain RK, and Deen WM. Diffusion and partitioning of proteins in charged agarose gels. *Biophys. J.* **68**: 1561-1568, 1995.
96. Johnson EM, Berk DA, Jain RK, and Deen WM. Hindered diffusion in agarose gels: Test of effective medium model. *Biophys. J.* **70**: 1017-1026, 1996.
97. Johnson EM and Deen WM. Electrostatic effects on the equilibrium partitioning of spherical colloids in random fibrous media. *J. Colloid Interface Sci.* **178**: 749-756, 1996a.
98. Johnson EM and Deen WM. Hydraulic permeability of agarose gels. *AIChE J.* **42**: 1220-1224, 1996b.
99. Johnston ST. *Convective transport of macromolecules in gels* (PhD Thesis). Cambridge, MA: Massachusetts Institute of Technology, 1999.
100. Johnston ST and Deen WM. Hindered convection of ficoll and proteins in agarose gels. *Ind. Eng. Chem. Res.* **41**: 340-346, 2002.
101. Johnston ST and Deen WM. Hindered convection of proteins in agarose gels. *J. Membr. Sci.* **153**: 217-279, 1999.
102. Johnston ST, Smith KA, and Deen WM. Concentration polarization in stirred ultrifiltration cells. *AIChE J.* **47**: 1115-1125, 2001.
103. Kanwar YS, Hascall VC, Jakubowski ML, and Gibbons JT. Effect of β-d-xyloside on the glomerular proteoglycans. I. Biochemical studies. *J. Cell Biol.* **99**: 715-722, 1984a.
104. Kanwar YS, Linker A, and Farquahar MG. Increased permeability of the glomerular basement membrane to ferritin after removal of glycosaminoglycans (heparan sulfate) by enzyme digestion. *J. Cell Biol.* **86**: 688-693, 1980.

105. Kanwar YS, Veis A, Kimura JH, and Jakubowski ML. Characterization of heparan sulfate-proteoglycan of glomerular basement membranes. *Proc. Natl. Acad. Sci. U. S. A.* **81**: 762-766, 1984b.
106. Kanwar YS and Venkatachalam MA. Chapter 1: Ultrastructure of glomerulus and juxtaglomerular apparatus. In: *Renal physiology*, edited by Windhager EE. Washington: American Physiological Society, 1992.
107. Kapur V, Charkoudian JC, and Anderson JL. Transport of proteins through gel-filled porous membranes. *J. Membr. Sci.* **131**: 143-153, 1997.
108. Karlsson M, Edfors-Lilja I, and Björnsson S. Binding and detection of glycosaminoglycans immobilized on membranes treated with cationic detergents. *Anal. Biochem.* **286**: 51-58, 2000.
109. Karst NA and Linhardt RJ. Recent chemical and enzymatic approaches to the synthesis of glycosaminoglycan oligosaccharides. *Curr. Med. Chem.* **10**: 1993-2031, 2003.
110. Kasinath BS. Glomerular endothelial cell proteoglycans - regulation by tgf-β1. *Arch. Biochem. Biophys.* **305**: 370-377, 1993.
111. Kato I and Anfinsen CB. Purification of synthetic ribonuclease s-peptide derivatives by specific complex formation on columns of ribonuclease s-protein bound to agarose. *J. Biol. Chem.* **244**: 5849-5855, 1969.
112. Keller KH and Stein TR. A two-dimensional analysis of porous membrane transport. *Math. Biosci.* **1**: 421-437, 1967.
113. Key PY and Sellen DB. A laser light-scattering study of the structure of agarose gels. *J. Polym. Sci., Part B: Polym. Phys.* **20**: 659-679, 1982.
114. Kjellén L and Lindahl U. Proteoglycans: Structures and interactions. *Annu. Rev. Biochem.* **60**: 443-475, 1991.
115. Klein DJ, Brown DM, Oegema TR, Brenchley PE, Andersson JC, Dickinson MAJ, Horigan EA, and Hassell JR. Glomerular basement membrane proteoglycans are derived from a larger precursor. *J. Cell Biol.* **106**: 963-970, 1988.
116. Kohn J and Wilchek M. Procedures for the analysis of cyanogen bromide-activated sepharose or sephadex by quantitative determination of cyanate esters and imidocarbonates. *Anal. Biochem.* **115**: 375-382, 1981.
117. Kohn J and Wilchek M. The use of cyanogen bromide and other novel cyanylating agents for the activation of polysaccharide resins. *Appl. Biochem. Biotechnol.* **9**: 285-305, 1984.
118. Kon A, Takagaki K, Nakamura T, and Endo M. Application of 2-aminopyridine fluorescence labeling to glycosaminoglycans. *J. Biochem. (Tokyo).* **110**: 132-135, 1991.
119. Koponen A, Kandhai D, Hellén E, Alava M, Hoekstra A, Kataja M, Niskanen K, Sloot P, and Timonen J. Permeability of three-dimensional random fiber webs. *Phys. Rev. Lett.* **80**: 716-719, 1998.
120. Koshiishi I, Takenouchi M, Hasegawa T, and Imanari T. Enzymatic method for the simultaneous determination of hyaluronan and chondroitin sulfates using high-performance liquid chromatography. *Anal. Biochem.* **265**: 49-54, 1998.
121. Kosto KB and Deen WM. Diffusivities of macromolecules in composite hydrogels. *AIChE J.* **50**: 2648-2658, 2004.
122. Kosto KB and Deen WM. Hindered convection of macromolecules in hydrogels. *Biophys. J.* **88**: 277-286, 2005.
123. Kosto KB, Panuganti S, and Deen WM. Equilibrium partitioning of ficoll in composite hydrogels. *J. Colloid Interface Sci.* **277**: 404-409, 2004.
124. Kuberan B, Gunay NS, Dordick JS, and Linhardt RJ. Preparation and isolation of neoglycoconjugates using biotin-streptavidin complexes. *Glycoconj. J.* **16**: 271-281, 1999.
125. Kuwabara S. The forces experienced by randomly distributed parallel circular cylinders or spheres in a viscous flow at small reynolds numbers. *J. Phys. Soc. Jpn.* **14**: 527-532, 1959.
126. LaBarre D, Boffa MC, and Jozefowicz M. Preparation and properties of heparin-poly(methyl methacrylate) copolymers. In: *Transformations of functional groups on polymers*, edited by Overberger CG and Sedlacek B: John Wiley & Sons, Inc., 1974.
127. LaBarre D and Jozefowicz M. Properties of herarin-poly(methyl methacrylate) copolymers. II. *J. Biomed. Mater. Res.* **11**: 283-295, 1977.
128. Lafayette RA, Druzin M, Sibley R, Derby G, Malik T, Huie P, Polhemus C, Deen WM, and Myers BD. Nature of glomerular dysfunction in pre-eclampsia. *Kidney Int.* **54**: 1240-1249, 1998.
129. LaFrance LK and Dapron J. End point attached heparin affinity matrix. *J. Mol. Recognit.* **10**: 748-751, 1997.

130. Lakshminarayanaiah N. *Transport phenomena in membranes*. New York: Academic, 1969.
131. Latta H and Johnston WH. The glycoprotein inner layer of glomerular capillary basement membrane as a filtration barrier. *J. Ultrastruct. Res.* **57**: 65-67, 1976.
132. Laurent TC. Determination of the structure of agarose gels by gel chromatography. *Biochim. Biophys. Acta* **136**: 199-205, 1967.
133. Lazzara MJ, Blankschtein D, and Deen WM. Effects of multisolute steric interactions on membrane partition coefficients. *J. Colloid Interface Sci.* **226**: 112-122, 2000.
134. Lazzara MJ and Deen WM. Effects of concentration on the partitioning of macromolecule mixtures in agarose gels. *J. Colloid Interface Sci.* **272**: 288-297, 2004.
135. Lea PJ, Slilverman M, Hegele R, and Hollenberg MJ. Tridimensional ultrastructure of glomerular capillary endothelium revealed by high-resolution scanning electron microscopy. *Microvasc. Res.* **38**: 296-308, 1989.
136. Lebrun L and Junter GA. Diffusion of sucrose and dextran through agar gel membranes. *Enzyme Microb. Technol.* **15**: 1057-1062, 1993.
137. Lees A, Nelson BL, and Mond JJ. Activation of soluble polysaccharides with 1-cyano-4-dimethylaminopyridinium tetrafluoroborate for use in protein-polysaccharide conjugate vaccines and immunological reagents. *Vaccine* **14**: 190-198, 1996.
138. Levick JR. Review article: Flow through interstitium and other fiberous matrices. *Q. J. Exp. Physiol.* **72**: 409, 1987.
139. Lindahl U and Höök M. Glycosaminoglycans and their binding to biological macromolecules. *Annu. Rev. Biochem.* **47**: 385-417, 1978.
140. Maaloum M, Pernodet N, and Tinland B. Agarose gel structure using atomic force microscopy: Gel concentration and ionic strength effects. *Electrophoresis* **19**: 1606-1610, 1998.
141. MacIntosh FC. A colorimetric method for the standardization of heparin preparations. *Biochem. J.* **35**: 776-782, 1941.
142. Mackplow MB, Shaqfeh ESG, and Schiek RL. A numerical study of heat and mass transport in fibre suspensions. *Proc. R. Soc. London, A* **447**: 77, 1994.
143. Maddox DA, Deen WM, and Brenner BM. Chapter 13: Glomerular filtration. In: *Renal physiology*, edited by Windhager EE. New York, NY: Oxford University Press, 1992, p. 545-638.
144. Manno M, Emanuele A, Martorana V, Bulone D, San Biagio PL, Palma-Vittorelli MB, and Palma MU. Multiple interactions between molecular and supramolecular ordering. *Phys. Rev. E: Stat. Nonlin. Soft Matter Phys.* **59**: 2222-2230, 1999.
145. March SC, Parikh I, and Cuatrecasas P. A simplified method for cyanogen bromide activation of agarose for affinity chromatography. *Anal. Biochem.* **60**: 149-152, 1974.
146. Maroudas A, Mizrahi J, Ben Haim E, and Ziv I. Swelling pressure in cartilage. In: *Intersitional-lymphatic liquid and solute movement*, edited by Staub N, Hogg J and Hargens A. Basel, Switzerland: Karger, 1987, p. 203-212.
147. Masaro L and Zhu XX. Physical models of diffusion for polymer solutions, gels and solids. *Prog. Polym. Sci.* **24**: 731-775, 1999.
148. Mattern KJ and Deen WM. Binding of glycosaminoglycans to cyano-activated agarose membranes: Kinetic and diffusional effects on yield and homogeneity. *Carbohydr. Res.* **342**: 2192-2201, 2007.
149. Mattern KJ and Deen WM. "mixing rules" for estimating the hydraulic permeability of fiber mixtures. *AIChE J.* **54**: 32-41, 2008.
150. Mattern KJ, Nakornchai C, and Deen WM. Darcy permeability of agarose-glycosaminoglycan gels analyzed using fiber-mixture and donnan models. *Biophys. J.* **95**: in press, 2008.
151. Maynard SE, Min J-Y, Merchan J, Lim K-H, Li J, Mondal S, Libermann TA, Morgan JP, Selke FW, Stillman IE, Epstein FH, Sukhatme VP, and Karumanchi SA. Excess placental soluble fms-like tyrosine kinase 1 (sFlt1) may contribute to endothelial dysfunction, hypertension, and proteinuria in preeeclampsia. *J. Clin. Invest.* **111**: 649-658, 2003.
152. Mehta A and Zydney AL. Effect of membrane charge on flow and protein transport during ultrafiltration. *Biotechnol. Prog.* **22**: 484-492, 2006.
153. Meredith RE and Tobias CW. Conductivities in emulsions. *J. Electrochem. Soc.* **108**: 286-290, 1961.
154. Millesime L, Amiel C, and Chaufer B. Ultrafiltration of lysozyme and bovine serum albumin with polysulfone membranes modified with quaternized polyvinylimidazole. *J. Membr. Sci.* **89**: 223-234, 1994.

155. Miyama H, Yoshida H, and Nosaka Y. Negatively charged polyacrylonitrile graft copolymer membrane for permeation and separation of plasma proteins. *Makromol. Chem., Rapid Commun.* **9**: 57-61, 1988.
156. Moussaoui M, Benlyas M, and Wahl P. Diffusion of proteins in sepharose cl-b gels. *J. Chromatogr.* **591**: 115-120, 1992.
157. Nakao S, Osada H, Kurata H, Suru T, and Kimura S. Separation of proteins by charged ultrafiltration membranes. *Desalination* **70**: 191-205, 1988.
158. Ogston AG and Wells JD. The osmotic properties of sulphoethyl-sephadex. *Biochem. J.* **128**: 685-690, 1972.
159. Ohlson M, Sörensson J, and Haraldsson B. Glomerular size and charge selectivity in the rat as revealed by fitc-ficoll and albumin. *Am. J. Physiol.* **279**: F84-F91, 2000.
160. Ohshima H. Streaming potential across a charged membrane. *J. Colloid Interface Sci.* **164**: 510-513, 1994.
161. Oliver JD, III, Anderson S, Troy JL, Brenner BM, and Deen WM. Determination of glomerular size-selectivity in the normal rat with ficoll. *J. Am. Soc. Nephrol.* **3**: 214-228, 1992.
162. Onsager L. Theories and problems of liquid diffusion. *Ann. N. Y. Acad. Sci.* **96**: 241-265, 1945.
163. Parikh I, March SC, and Cuatrecasas P. [6] topics in the methodology of substituted reactions with agarose. In: *Affinity techniques: Enzyme purification part b*, edited by Jakoby WB and Wilchek M. New York, NY: Academic Press, 1974, p. 77-102.
164. Phillips RJ. A hydrodynamic model for hindered diffusion of proteins and michelles in hydrogels. *Biophys. J.* **79**: 3350-3353, 2000.
165. Phillips RJ, Deen WM, and Brady JF. Hindered transport in fibrous membranes and gels: Effect of solute size and fiber configuration. *J. Colloid Interface Sci.* **139**: 363-373, 1990.
166. Phillips RJ, Deen WM, and Brady JF. Hindered transport of spherical macromolecules in fibrous membranes and gels. *AIChE J.* **35**: 1761-1769, 1989.
167. Pieper JS, Hafmans T, Veerkamp JH, and van Kuppevelt TH. Development of tailor-made collagen-glycosaminoglycan matrices: Edc/nhs crosslinking, and ultrastructural aspects. *Biomaterials* **21**: 581-593, 2000.
168. Pieper JS, Oosterhof A, Dijkstra PJ, Veerkamp JH, and van Kuppevelt TH. Preparation and characterization of porous crosslinked collagenous matrices containing bioavailable chondroitin sulphate. *Biomaterials* **20**: 847-858, 1999.
169. Pines E and Prins W. Structure-property relations of thermoreversible macromolecular hydrogels. *Macromolecules* **6**: 888-895, 1973.
170. Pluen A, Netti PA, Jain RK, and Berk DA. Diffusion of macromolecules in agarose gels: Comparison of linear and globular configurations. *Biophys. J.* **77**: 542-552, 1999.
171. Porath J, Axén R, and Ernback S. Chemical coupling of proteins to agarose. *Nature* **215**: 1491-1492, 1967.
172. Pries AR, Secomb TW, and Gaehtgens P. The endothelial surface layer. *Eur. J. Physiol.* **440**: 653-666, 2000.
173. Pujar NS and Zydney AL. Charge regulation and electrostatic interactions for a spherical particle in a cylindrical pore. *J. Colloid Interface Sci.* **192**: 338-349, 1997.
174. Pujar NS and Zydney AL. Electrostatic and electrokinetic interactions during protein transport through narrow pore membranes. *Ind. Eng. Chem. Res.* **33**: 2473-2482, 1994.
175. Ratajska-Gadomska B and Gadomski W. Water structure in nanopores of agarose gel by raman spectroscopy. *J. Chem. Phys.* **121**: 12583-12588, 2004.
176. Rea WJ, Eberle JW, Watson JT, Ecker RR, and Sugg WL. Gas transfer in a heparinized membrane oxygenator. *Surg. Forum* **22**: 188-190, 1971.
177. Reeves WH, Kanwar YS, and Farquahar MG. Assembly of the glomerular filtration surface: Differentiation of anionic sites in the glomerular capillaries of newborn rate kidney. *J. Cell Biol.* **85**: 735-753, 1980.
178. Rossi M, Morita H, Sormunen R, Airene S, Kreivi M, Wang L, Fukai N, Olsen BR, Tryggvason K, and Soininen R. Heparan sulfate chains of perlecan are indispensable in the lens capsule but not in the kidney. *EMBO J.* **22**: 236-245, 2003.
179. Rostgaard J and Qvortrup K. Sieve plugs in fenestrae of glomerular capillaries - site of the filtration barrier. *Cells Tissues Organs* **170**: 132-138, 2002.
180. Roth M. Fluorescence reaction for amino acids. *Anal. Chem.* **43**: 880-882, 1971.

181. Rubinstein A, Nakar D, and Sintov A. Colonic drug delivery: Enhanced release of indomethacin from cross-linked chondroitin matrix in rat cell content. *Pharm. Res.* **9**: 276-278, 1992.
182. Ryan G and Karnovsky MJ. Distribution of endogenous albumin in the rat glomerulus: Role of hemodynamic factors in glomerular barrier function. *Kidney Int.* **9**: 36-45, 1976.
183. Salamone JC. Polymeric materials encyclopedia. Boca Raton, FL: CRC Press, 1996.
184. Sangani AS and Acrivos A. Slow flow past periodic arrays of cylinders with application to heat transfer. *Int. J. Multiphase Flow* **8**: 193-206, 1982.
185. Sasaki H, Hayashi A, Kitagaki-Ogawa H, Matsumoto I, and Seno N. Improved method for the immobilization of heparin. *J. Chromatogr.* **400**: 123-132, 1987.
186. Savage COS. The biology of the glomerulus: Endothelial cells. *Kidney Int.* **45**: 314-319, 1994.
187. Schaefer L, Grone HJ, Raslik I, Robenek H, Ugorcakova J, Budney S, Schaefer RM, and Kresse H. Small proteoglycans of normal adult human kidney: Distinct expression patterns of decorin, biglycan, fibromodulin, and lumican. *Kidney Int.* **58**: 1557-1568, 2000.
188. Schneeberger EE and Hamelin M. Interaction of serum proteins with lung endothelial glygocalyx: Its effect on endothelial permeability. *Am. J. Physiol.* **247**: H206-H217, 1984.
189. Schweers E and Löffler F. Realistic modeling of the behavior of fibrous filters through consideration of filter structure. *Powder Technol.* **80**: 191-206, 1994.
190. Sengolge G, Fine DM, and Ballermann BJ. Sage profiles of glomerular and aortic endothelial cells. *Journal of the American Society of Nephrology* **10**: 388A, 1999.
191. Sepulcre G and Moczar E. The preparation of a glycopeptide-sepharose for affinity chromatography. *J. Chromatogr.* **75**: 114-116, 1973.
192. Shafer DE, Toll B, Schuman RF, Nelson BL, Mond JJ, and Lees A. Activation of soluble polysaccharides with 1-cyano-4-dimethulaminophyridinium tetrafluoroborate (CDAP) for use in protein-polysaccharide conjugate vaccines and immunological reagents. II. Selective crosslinking of proteins to CDAP-activted polysaccharides. *Vaccine* **18**: 1273-1281, 2000.
193. Sheehan DC and Hrapchak BB. *Theory and practice of histology*. Columbus, OH: Battelle Press, 1980.
194. Sintov A, Dicapua N, and Rubinstein A. Cross-linked chondroitin sulfate - characterization for drug-delivery purposes. *Biomaterials* **16**: 473-478, 1995.
195. Smith PK, Mallia AK, and Hermanson GT. Colorimetric method for the assay of heparin content in immobilized heparin preparations. *Anal. Biochem.* **109**: 466-473, 1980.
196. Sörensson J, Björnson A, Ohlson M, Ballermann BJ, and Haraldsson B. Synthesis of sulfated proteoglycans by bovine glomerular endothelial cells in culture. *Am. J. Physiol.* **284**: F373-F380, 2003.
197. Sörensson J, Ohlson M, and Haraldsson B. A quantitative analysis of the glomerular charge barrier in the rat. *Am. J. Physiol.* **280**: F646-F656, 2001.
198. Sörensson J, Ohlson M, Lindström KE, and Haraldsson B. Glomerular charge selectivity for horseradish peroxidase and albumin at low and normal ionic strengths. *Acta Physiol. Scand.* **163**: 83-91, 1998.
199. Spielman L and Goren SL. Model for predicting pressure drop and filtration efficiency in fibrous media. *Environ. Sci. Technol.* **2**: 279-287, 1968.
200. Squire JM, Chew M, Nneji G, Neal C, Barry J, and Michel C. Quasi-periodic substructure in the microvessel endothelial glycocalyx: A possible explanation for molecular filtering? *J. Struct. Biol.* **136**: 239-255, 2001.
201. Stigter D. Electrophoresis of highly charged colloidal cylinders in univalent salt solutions. 2. Random orientation in external field and application to polyelectrolytes. *J. Phys. Chem.* **82**: 1424-1429, 1978.
202. Tamura J-i. Recent advances in the synthetic studies of glycosaminoglycans. *Trends Glycosci Glyc* **13**: 65-88, 2001.
203. Toome V, de Bernardo S, Manhart K, and Weigele M. Preliminary evaluation of fluorescamine as a colorimetric reagent for primary amines. *Anal. Lett.* **7**: 437-443, 1974.
204. Toome V and Manhart K. A simple simultaneous colorimetric determination of primary and secondary amines with fluorescamine. *Anal. Lett.* **8**: 441-448, 1975.
205. Tryggvason K. Unraveling the mechanisms of glomerular ultrafiltration: Nephrin, a key compenent of the slit diaphragm. *J. Am. Soc. Nephrol.* **10**: 2440-2445, 1999.

206. Turner MR, Clough G, and Michel CC. The effects of cationixed ferritin and native ferritin upon the filtration coefficient of single frog capillaries. Evidence that proteins in the endothelial cell coat influence permeability. *Microvasc. Res.* **25**: 205-222, 1983.
207. van Kuppevelt THMSM and Veerkamp JH. Application of cationic probes for the ultrastructural localization of proteoglycans in basement membrane. *Microsc. Res. Tech.* **28**: 125-140, 1994.
208. van Reis R, Brake JM, Chakoudian J, Burns DB, and Zydney AL. High-performance tangential flow filtration using charged membranes. *J. Membr. Sci.* **159**: 133-142, 1999.
209. Varshavskaya MY, Klibanov AL, Goldmacher VS, and Torchilin VP. A simple method for the determination of heparin content in heparin-sepharose. *Anal. Biochem.* **95**: 449-451, 1979.
210. Venturoli D and Rippe B. Ficoll and dextran vs. Globular proteins as probes for testing glomerular permselectivity: Effects of molecular size, shape, charge, and deformability. *Am. J. Physiol.* **288**: F605-F613, 2005.
211. Vilker VL. *The ultrafiltration of biological macromolecules* (PhD). Cambridge, MA: Massachusetts Institute of Technology, 1976.
212. Vilker VL, Colton CK, and Smith KA. The osmotic pressure of concentrated protein solutions: Effect of soncentration and pH in saline solutions of bovine serum albumin. *J. Colloid Interface Sci.* **79**: 548-566, 1981.
213. Vink H and Duling BR. Capillary endothelial surface layer selectively reduces plasma solute distribution volume. *Am. J. Physiol.* **278**: H285-H289, 2000.
214. Volpi N. Purification of heparin, dermatan sulfate and chondroitin sulfate from mixtures by sequential precipitation with various organic solvents. *J. Chromatogr. B. Biomed. Appl.* **685**: 27-34, 1996.
215. Volpi N, Mucci A, and Schenetti L. Stability studies of chondroitin sulfate. *Carbohydr. Res.* **315**: 345-349, 1999.
216. Waffenschmidt S and Jaenicke L. Assay of reducing sugars in the nanomole range with 2,2'-bicinchoninate. *Anal. Biochem.* **165**: 337-340, 1987.
217. Waki S and Harvey JD. Study of agarose gels by electron microscopy of freeze-fractured surfaces. *Biopolymers* **21**: 1909-1926, 1982.
218. Weinbaum S, Tarbell JM, and Damiano ER. The structure and function of the endothelial glycocalyx. *Annu. Rev. Biomed. Eng.* **9**: 121-167, 2007.
219. White JA and Deen WM. Agarose-dextran gels as synthetic analogs of glomerular basement membrane: Water permeability. *Biophys. J.* **82**: 2081-2089, 2002.
220. White JA and Deen WM. Equilibrium partitioning of flexible macromolecules in fibrous membranes and gels. *Macromolecules* **22**: 8504-8511, 2000.
221. Whitley CB, Ridmour MD, Draper KA, Dutton CM, and Neglia JP. Diagnostic test for mucopolysaccharidosis. I. Direct method for quantifying excessive urinary glycosaminoglycan excretion. *Clin. Chem.* **35**: 374-379, 1989.
222. Whytock S and Finch J. The substructure of agarose gels as prepared for electrophoresis. *Biopolymers* **31**: 1025-1028, 1991.
223. Wight TN, Heinegård DK, and Hascall VC. Chapter 2: Proteoglycans: Structure and function. In: *Cell biology of extracellular matrix*, edited by Hay ED. New York, NY: Plenum Press, 1991.
224. Xiong J-Y, Narayanan J, Liu X-Y, Chong TK, Chen SB, and Chung T-S. Topology evolution and gelation mechanism of agarose gel. *J. Phys. Chem.* **109**: 5638-5643, 2005.
225. Yu C and Soong T. Random cell model for pressure-drop prediction in fibrous filters. *J. Appl. Mech.* **42**: 301-304, 1975.
226. Zetter BR. Endothelial heterogeneity: Influence of vessel size, organ localization, and species specificity on the properties of cultured endothelial cells. In: *Endothelial cells*, edited by Ryan US. Boca Raton, FL: CRC Press, 1988.
227. Zugates G. Laboratory notebook & research status report, 2001-2003. - *unpublished results*.